SEISMIC DETECTION OF ROCKFALLS ON RAILWAY LINES

by
Bohdan Nedilko

A THESIS SUBMITTED IN PARTIAL FULFILLMENT OF
THE REQUIREMENTS FOR THE DEGREE OF

DOCTOR OF PHILOSOPHY

in

THE FACULTY OF GRADUATE AND POSTDOCTORAL STUDIES

(Geophysics)

THE UNIVERSITY OF BRITISH COLUMBIA

(Vancouver)

May 2016

© Bohdan Nedilko, 2016

Abstract

Railway operators mitigate the risk of derailments caused by hazardous rocks falling onto the track by installing slide detector fences (SDF). These consist of electrical sensing wires strung on poles located uphill of the track; falling rocks snap these wires and trigger an alarm. Rocks of non-threatening size and migrating animals frequently break the wires causing prolonged false alarms and delaying rail traffic until the SDF is manually repaired, often in a hazardous environment. This thesis is concerned with the development of a prototype of the autonomous Seismic Rockfall Detection System (SRFDS) as a potential replacement for the SDF.

Analysis and classification of natural and anthropogenic seismic signals which have been observed at the SRFDS field installations, is presented. A method for identification of hazardous rocks (>0.028 m^3) using an empirical peak ground velocity attenuation model is outlined. Pattern recognition techniques which are based on cross-correlation and on variations in the short-term / long term averages of the ground vibrations are introduced for rail traffic identification and rockfall detection. The techniques allow the SRFDS to eliminate false activations by rail traffic, report hazardous rocks with minimum (< 3 s) delay, and rearm automatically when a false alarm is revealed.

Performance of the SRFDS field installations was modeled using continuous seismic data recorded at two locations where the SRFDS and the SDF operate in parallel. The SRFDS computer model detected all major rock slides; it was significantly less likely than the SDF to be triggered by animal migration, but may be susceptible to thermal noise in very specific situations. A comparison of the actual number of the train delays caused by the existing SDF with those of the SRFDS computer model, shows that the use of the SRFDS will reduce the average number of delayed trains. The actual reduction of the number of delayed trains is between 3 and 8 times, depending on the location.

Train delays caused by false triggers induced by construction activities and track maintenance could still exist; however, they can be eliminated by the adoption of the appropriate track management procedures.

Preface

This dissertation is original, unpublished, independent work by the author, B.Nedilko.

The pattern recognition algorithms are of my own design and implementation: the matched filtering algorithms for detection of rail traffic using the seismic signals it generates (Chapter 4); the algorithms for low-latency detection of rockfalls in the railway operating environment (Chapter 4); and the 2D grid search algorithm for automatic recognition of hazardous rocks (Chapter 3). I did the modeling of the Seismic Rockfall Detection Systems in Chapter 5 using computer code which I wrote.

The seismic data was collected with the equipment designed and installed by Weir-Jones Engineering Consultants (Vancouver, Canada).

Table of Contents

List of Tables

List of Figures

List of Abbreviations

CANMET-MMSL	Canada Centre for Mineral and Energy Technology - Mining and Mineral Sciences Laboratories
CNR	Canadian National Railway (CN)
CPR	Canadian Pacific Railway (CP)
EMI	Electro-magnetic interference
LDA	Locomotive Detection Algorithm
PGV	Peak Ground Velocity
RGHRP	Railway Ground Hazard Research Program
RMS	Root-mean square, r.m.s.
RTC	Rail Traffic Controller
SDF	Slide Detector Fence
SRFDS	Seismic Rockfall Detection System
STA/LTA	Short-term average *vs* Long-term average
TDA	Train Detection Algorithm
TO	Track occupancy
TW-RFDS	Trip Wire Rockfall Detection System
WD	Wheel detector
WJEC	Weir-Jones Engineering Consultants
ZLCC	Zero lag cross-correlation
ZNCC	Zero-mean normalized cross-correlation

Acknowledgments

I would like to extend my sincerest gratitude to the late Dr. Tadeusz Ulrych, my supervisor, who suggested the topic of this research, for his continuous encouragement and support.

My deepest thanks to Dr. Iain Weir-Jones, my employer and mentor of many years, without whom this project would not have materialized. I am highly appreciative of the efforts by the members of the Supervisory Committee as well as anonymous reviewers for greatly improving the readability of the thesis, including Dr. Ron Clowes, and especially Dr. Michael Bostock who took over as a supervisor after Dr.Ulrych's passing away. I gratefully acknowledge that some ideas and insights about geophysical data analysis used in this work I gained at the courses read by Dr. Michael Bostock, Dr. Felix Herrmann, and Dr. Mark Jellinek at the Department of Earth, Ocean and Atmospheric Sciences (UBC).

Thanks to WJEC / Terrascience Systems Ltd for kindly letting me use their data repository without which this research would be impossible; Dr. Zaicenco for his useful remarks, as well as my colleagues who helped me collect the data for this study.

Last but not least, many thanks to everyone at Canadian Pacific Railways and Canadian National Railways for sharing their expertise with the rockfall monitoring which allowed me to acquire a better understanding of the research topic, in particular Tom Edwards, Mario Ruel (CN), Dr. Chris Bunce, and Eddie Choi (CP), as well as people who provided valuable feedback from the field: Ron Kotylak, Merlin Miskie, Kory Tischler, Michael Wilson, and Brian Goodman. My gratitude also extends to Jerry Specht, Paul Mikols, and Marc Levesque.

Dedication

To Laurie, my beautiful and loved partner, without whose patience and support this work would not have been possible.

1. Introduction

1.1. The problem of rockfalls on railway lines

Transportation routes through mountainous terrain are often susceptible to landslide hazards, particularly rockfalls and rockslides that can cause traffic delays, damage, injury, and death to users of these routes (*e.g.* Peckover and Kerr 1977; Hungr and Evans 1988; Bunce *et al*., 1997; Macciotta *et al*., 2015a). Rockfall is a gravitationally driven geomorphic process that occurs on steep natural or constructed slopes (Higgins and Andrew, 2012a). While usage and definitions of the term *rockfall* vary in the literature, the term generally encompasses the detachment or failure of a rock block or mass and its subsequent downslope movement. Varnes (1978) describes rockfall as a very rapid slope movement in which bedrock material of any size is detached from a steep slope and descends the slope mostly through the air by falling, bouncing, or rolling. In the case of rockslide, the movement consists of shear strain and displacement along one or several surfaces that are visible or may reasonably be inferred (Varnes, 1978). Sharpe (1938) introduced a classification scheme based on type of slope movement, material and movement velocity. Sharpe's work was expanded by Varnes (1978) who used a general term *landslide* to denote the movement of a mass of rock, debris or earth downslope. Landslide movements were classified into five types: falls, topples, slides, spreads and flows; landslide materials included rock, debris, earth and their combinations. Classification presented by Varnes (1978) and Cruden and Varnes (1996) includes a variety of landslide velocities, from extremely slow (millimeters per year) to extremely rapid (meters per second). The classification of landslides devised by Varnes has become the most widely used system in the English language (Hungr *et al.*, 2012).

Hungr and Evans (1988) describe rockfalls of relatively small volumes as "fragmental rockfalls". Hungr *et al.* (1998) used the term *rockfalls* for events involving <10 000 m^3 of material which occur relatively frequently from natural and excavated rock slopes; larger magnitude *rockslides* (<100 000 m^3) occur often in rock cuts at the foot of steep natural slopes. At the upper end of the magnitude spectrum are rock *avalanches* (>1.0×10^7 m^3).

Landslide hazards, particularly rockfalls and rockslides, have been a major problem along the transportation corridors across the Canadian Cordillera (Hungr *et al*., 1999; Evans and Hungr, 1993). These hazards have been the subject of intense mitigative efforts by the operators of the transportation systems utilizing these corridors (*e.g.*, Peckover and Kerr 1977; Hungr and Evans, 1988; Bunce *et al*.

1997). The hazards most frequently reported are rockfalls which are ubiquitous along the steep rock cuts required to accommodate railway alignment (Macciotta *et al*., 2014a; Macciotta *et al*., 2015b). Hungr *et al*. (1999) calculated magnitude – cumulative frequency relationships for bedrock-derived mass movements for each of the two main transportation corridors of southwestern British Columbia: the Fraser-Thompson and the Howe Sound-Lillooet. They concluded that rockfalls in the intermediate magnitude range (1–10 m^3) are the type of rockfalls most likely to cause a fatal injury in this geographic area.

Since trains can be derailed by rocks as small as 30 cm (Piteau and Peckover, 1978), this research is concerned with detection of rocks of this size and larger which will be referred to as *hazardous* rocks (Figure 1.1). By *non-hazardous* rocks we will mean rocks smaller than 0.028m^3. Most of the rockfalls in this study were identified by the seismic signals they produced, and not observed visually. For this reason, we refer to the events discussed here as rockfalls in general, except when it is known specifically what type of event generated the ground vibration.

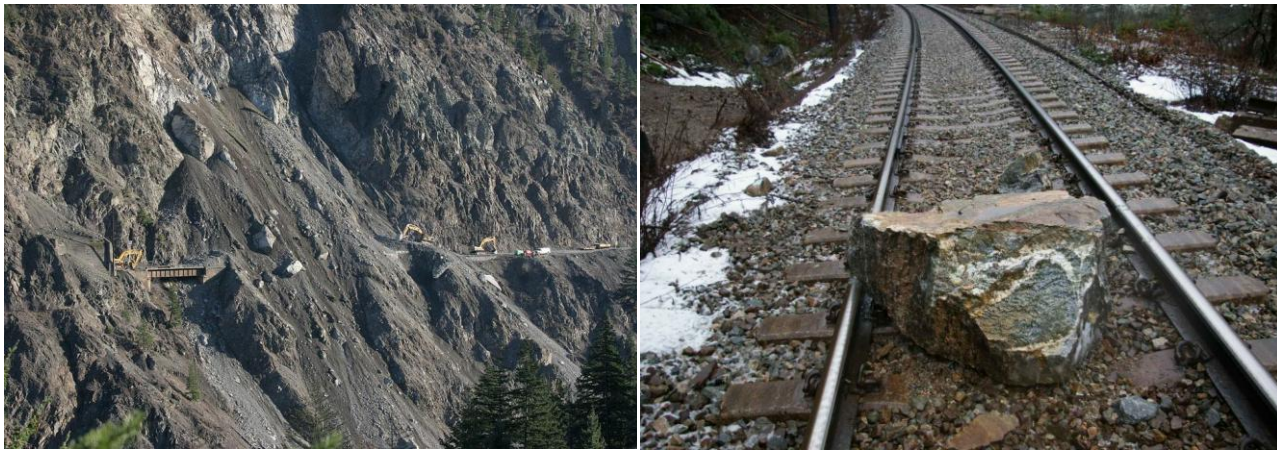

(a) (b)

Figure 1.1. (a) Photo of a rockslide on CN's mainline south of Lytton, British Columbia, Canada (courtesy of Weir-Jones Engineering Consultants (Vancouver, Canada); (b) Photo of a rock that can derail a train (courtesy of Canadian National Railway).

1.1.1. Causes of rockfalls

In a number of studies, basic rockfall types and their typical causes are described with the goal to help evaluate the rockfall hazard and assess the risk to transportation (*e.g.* Peckover, 1975; Varnes, 1978; Brawner and Wyllie, 1976; Higgins and Andrew, 2012a; Higgins and Andrew, 2012b). As a rule, rock

masses are anisotropic and heterogeneous, and they are separated into distinct blocks by numerous discontinuities which are the primary elements that affect the stability of a rock mass (Higgins and Andrew, 2012a). Detachment along discontinuity may be initiated, for example, by external factors such as physical (water pressure, ice, temperature variations, wind, vibration, root growth, excavation of slope, erosion, *etc*.), or chemical weathering of rocks near the surface (DeRoin and McNutt, 2012; Higgins and Andrew, 2012a; Zimmer *et al.*, 2012; Zimmer and Sitar, 2015). Internal factors include: residual stresses from geological influences; orientation; and spacing of rock defects such as joints, faults, bedding planes, and weak zones (Peckover and Kerr, 1977; Cruden and Varnes, 1996; DeRoin and McNutt, 2012). It has been acknowledged in the literature that, though several of these factors may occur together to cause a landslide, only one trigger exists that will cause a near-immediate response, *e.g.* earthquake, volcanic activity, freeze-thaw cycle (Wieczorek, 1996; DeRoin and McNutt, 2012).

The relationship between rockfall occurrences and weather conditions has been confirmed in a number of studies (Peckover 1975; Piteau and Peckover, 1978; Brawner and Wyllie, 1976; Higgins and Andrew 2012a; Macciotta *et al*. 2015a). Thawing water can infiltrate discontinuities in a rock slope, increase the water pressures in them, and trigger rockfalls (Higgins and Andrew 2012a). The presence of water within discontinuities and the geological properties of rock masses are the most significant factors affecting slope failures (Peckover, 1975; Brawner and Wyllie, 1976). For instance, effects of seasonal weather on movement of rock slopes in the Yale Subdivision of CN (southwestern British Columbia, Canada) were studied by Peckover and Kerr (1977). They reported that over the period of 1933-1970 the maximum frequency of rockfalls occurred in November-March when the mean temperature is at or slightly below 0°C. In another study at CN's Squamish Subdivision (southwest British Columbia), over 75% of rockfalls were recorded between November and March (Macciotta *et al.*, 2015a).

1.1.2. Mitigation of risks posed by rockfalls

In order to reduce the risks to users as well as minimize incurred costs and traffic disruptions, carefully selected maintenance techniques are required. Costs incurred by railway operators due to rockfalls include: alignment[1] maintenance work such as scaling and clearing ditches; cost of patrols in bad weather at particularly dangerous locations; delays and rerouting of traffic, and damage claims due to accidents

[1] Alignment is the route upon which a train travels and the track is constructed (AREMA, 2003).

(Peckover and Kerr, 1977). In extreme cases, rockfall can result in injuries and loss of life (Bunce *et al.*, 1997; Bunce, 2008). Dangerous rockfall locations can be addressed by one of the four principal approaches or their combination: (a) relocation of the alignment to avoid or minimize the hazard; (b) slope stabilization, *i.e.* by preventing rocks from detaching, *e.g.* through rock scaling, bolting and shotcreting; (c) protection, *i.e.* keeping rocks that do move out of place from reaching the roadway, as with walls, tunnels, rock sheds or catchment ditches; and (d) warning, *i.e.* signaling the rail traffic when rocks fall in the vicinity of the track (Peckover and Kerr, 1977; Brawner and Wyllie, 1976; Piteau and Peckover, 1978).

Relocation of the alignment is a very costly and rarely available option. Slope stabilization is justified where the cause and extent of potential slope failures can be determined. Expensive protection procedures such as construction of tunnels or rock sheds can be followed where landslides are likely to involve large volumes of falling rocks. Development of deep catchment ditches on the inner side of the track is considered one of the most effective protection measures (Brawner and Wyllie, 1976; Peckover and Kerr, 1977). Warning systems are used where occasional falls are expected but the anticipated protection or stabilization measures would be extremely difficult or expensive (Peckover, 1975; Peckover and Kerr, 1977). Warning methods involve no reduction and sometimes an increase in maintenance costs, and have no effect on the source of danger (Peckover and Kerr, 1977). The most reliable warning system is a two-man, radio-equipped patrol ahead of trains in the most hazardous sections of track; however, the warning device most widely used by North American railway operators is the electric slide detector fence, SDF (Peckover and Kerr, 1977). SDFs are often installed along very high slopes where the cost of stabilization would be extreme (Brawner and Wyllie, 1976).

1.2. Detection of rockfalls with electric slide fences

In order to mitigate the risks caused by rockfalls, in areas that are not protected by structures such as tunnels, concrete walls, and rock sheds, slide detector fences (SDF)[2] are installed. The SDF is composed of multiple wires strung at 100 to 300 mm spacing and supported on 2 to 10 m timber poles spaced 10 to 20 m apart, as shown in Figure 1.2. The SDF is deployed between the track and the rock slope and it can be anywhere between tens of meters and hundreds of meters long. When a rock falls and breaks one or more wires, an electrical circuit opens and activates the warning system located beyond the stopping distance of the train. A warning signal, for example a flashing light, is displayed for all approaching trains, which must then proceed at a slower speed until a signal maintainer reconnects the wires to reset the system. This speed is called Restricted, and it is the speed that a train driver is instructed to maintain within the track section protected by the SDF; the normal speed is called Track Speed. The Restricted Speed is specific to each location prone to rockfall and must be slow enough so that a train can stop, thereby avoiding a possible derailment. The Restricted Speed is slower in the areas where the visibility is obstructed by track curvature. Slide detector fences are commonly used on freight railways where the traffic is controlled by signal systems, and the trains' speed allows them to stop within about 1-2 km distance (Wyllie, 2015).

The signal maintainer has to manually reset all triggered fences, which means that he has to physically attend to the fence to reconnect the wires. This could compromise the safety of signal maintainers if they were to enter an active rockfall area. Maintenance of the SDF can be expensive; because of delays reaching remotely located fences, it takes eight hours on average to repair an activated signal fence (Transport Canada, 2007). Train delays can be further exacerbated by seasonal fluctuations in SDF activation rates. SDF activation rates usually surge in the fall and winter months and oftentimes leave railway Signals and Communications (S&C)[3] maintenance crews shorthanded. In areas with high rockfall activity, the ratio of slowed down trains can exceed 20% of rail traffic (Carlson, 2010). As a result, in busy rail corridors SDF activations can create a bottleneck effect which can slow down dozens of trains

---

[2] Slide Detector Fence (SDF) is also called Trip Wire Rockfall Detection System (TW-RFDS). These two acronyms will be used interchangeably; Canadian Pacific Railway (CP) prefers to use the former acronym, while Canadian National Railway (CN) uses the latter.

[3] Signals and Communications (S&C) departments are responsible for the maintenance of slide detector fences.

daily. In addition, 40% to 70% of SDF triggers are false alarms (Transport Canada, 2007). Discussing the SDF weaknesses, Peckover and Kerr (1977) reported that SDFs give false alarms as much as 80% of the time, as well as cause difficulties with snow clearance. Some of the most frequent causes of wire breakages are animals, pebble-size (less than 20 mm), and cobble-size (more than 20 mm but less than 200 mm) rocks none of which pose a risk of derailment for rail traffic. Furthermore, sagging SDF wires can be short-circuited by wind or corrode and break. In some areas, SDFs are subject to copper theft. Installation of a standard railway slide detector fence can cost as much as $1,000 per running meter (Hatch *et al.*, 2009). Finally, not all rocks that can potentially cause a derailment are detected; SDF is known to miss hazardous rocks, for example when a rock passes between electric wires without breaking them. Regardless of the SDF deficiencies, North American railway operators continue to install them in areas with high rockfall risks in the absence of better alternatives (CN and CP, personal communication).

Figure 1.2. A slide detector fence installed along CN's alignment in White Canyon (near Lytton, Canada).

Electrical slide detector fences were preceded by mechanical systems. For example, a 6,450 m long rockfall detection system called the Pass of Brander Stone Signals was deployed in Scotland in 1882 (Edmund Nuttall Ltd, 2007); the system was still in operation as of 2010[4]. A screen of wires, linked to semaphore signals, was erected on the mountainside alongside the railway. The system has given early warnings of many boulders on the track, but two derailments have occurred where boulders evaded the screen. Weaknesses of this type of detector fence are similar to those of electrical ones. According to research carried out by Network Rail (UK) in 2003-2007, the majority of stone signal triggers (75%) were due to non-hazardous factors: signal failures, animals, or encroaching vegetation. In some areas of Canada, railway operators continue to use mechanical slide detector fences consisting of wire mesh which were installed more than 40 years ago (Figure 1.3).

Figure 1.3. A mechanical slide detector fence (Quebec, Canada).

[4] http://www.westhighlandline.org.uk/index.php/news/79-new-technology-for-the-pass-of-brander. Last checked on October 1, 2015.

1.3. Rockfall warning technologies used along railways

For historical reasons, North American railways have developed a strong interest in alternative technologies for rockfall warning. Peckover and Kerr (1977) investigated the usage of electric fences in eight railway companies: one from North America (CNR); seven from Europe, including West Germany, Switzerland, Sweden, Norway, Czechoslovakia, and Austria; and one company from Japan. According to this survey, electric slide detector fences were not used at all in five out of seven of these railways including the ones from West Germany, Switzerland, Sweden, Czechoslovakia, and Austria, while the operators in Norway and Japan did use electric fences. The reason for this difference was that many of the railway lines in Europe were built between the late-19th and early-20th centuries when skilled labour was relatively inexpensive (Peckover, 1975). At the time of initial construction, many rock slope stabilization and alignment protection structures were built with the intent that no rocks should reach the track. These structures continue to serve today and are maintained and added to as required, making warning systems redundant. The emphasis in those countries has thus been on remedial work rather than on warning systems, which contrasts with the traditional approach of the US and Canadian railways (Peckover, 1975; Peckover and Kerr, 1977).

In addition to slide detector fences, another method of monitoring rail lines currently in use involves detecting a problem by sensing a loss of electrical continuity through the rail. A break may occur for a number of reasons including: service stresses induced by trains and maintenance equipment; thermal contraction in the wintertime; the road bed subsidence; or because a rock strikes one of the rails with sufficient force. If either of the rails breaks, the loss of electrical continuity activates the trackside signals (Andrew *et al.*, 2012). However, rocks may fall onto the track without breaking the rails and affecting the electrical continuity. Another weak spot of this technology is that rocks large enough to derail a train can miss the rail and therefore go undetected.

The imperfections of the currently used rockfall warning technologies have prompted railway operators in Canada and abroad to seek more reliable and cost-effective alternatives to the slide fences. Sophisticated warning systems, *e.g.* TV monitoring, radar and laser detection systems, were studied in the 1970s (Peckover, 1975). CNR has been testing the effectiveness of geophones buried at intervals along the roadway shoulder to detect vibrations from falling rocks since the mid-1970s (Peckover, 1975; Peckover and Kerr, 1977).

A comprehensive review of potential rockfall detection technologies is in a report by Edmund Nuttall Ltd (2007, not published). A variety of intrusion detection technologies have been suggested for the purpose

of rockfall monitoring, *e.g.* a pressure sensitive cable, including: fibre optic cables used for strain measurements; a coaxial cable to detect electromagnetic field disturbance (Brackett, 2002); obstacle detectors based on microwave technology; as well as optical emitters. Digital cameras have been used to monitor mine slopes and debris flows (*e.g.* Prochaska *et al.*, 2008); however, video cameras need to be absolutely steady to provide motion detection, and are sensitive to weather conditions.

Available or potential real-time track hazard detection technologies were critically assessed in a report prepared for the Canadian Railway Ground Hazard Research Program (RGHRP) by Maloney and Miller (2004). The assessment criteria included the ability to identify the hazard in real time; the extent of the monitored area; the ability to operate in poor weather conditions as well as withstand maintenance zone operations and vandalism; the ability to detect hazardous rocks and resolve slow movement of debris; the automatic/ remote reset capability; chances of false triggers; and cost. In this report, seismic monitoring was ranked one of the most promising ones.

Remote sensing (*e.g.* light detection and ranging, LiDAR) has been successfully applied to produce displacement maps of ground movement. Since LiDAR surveys are conducted relatively infrequently and require a line-of-sight, this technology may be impractical in many operating environments. Other conventional geotechnical methods of monitoring slope stability (GPS, InSAR, inclinometers) either lack the necessary resolution and / or coverage, or are sensitive to the harsh operating environment. The use of rock movement gauges, extensometers and tilt meters as warning devices is discussed by Andrew *et al.* (2012). Among other technologies suggested for rockfall detection by Maloney and Miller (2004) are unmanned aerial vehicles (UAV) and heli-patrols. However, with regard to the performance criteria most of the non-seismic technologies have one or more disadvantages which rule them out as a potential replacement for the electric slide fence. These disadvantages include: the sensitivity of the monitoring equipment to inclement weather conditions, vulnerability to falling rocks and track maintenance; non-zero chances of missing a hazardous rock; as well as the impossibility of being reset remotely or automatically in case of a false trigger.

1.4. Overview of the thesis structure

Chapter 2. Previous work on seismic monitoring of rockfalls. A review of the literature has been completed in the following areas: seismic rockfall monitoring; modeling of peak amplitude decay of seismic signals over travel distance in geotechnical engineering and earthquake early warning systems;

methods of slope movement monitoring used in geotechnical engineering; event detection techniques used in seismology for single stations and sensor arrays; pattern recognition techniques utilized within this research for detection of rail traffic and rockfall; and trajectory modeling techniques relevant to the current study. Then we proceed with the overview of previous feasibility studies of seismic rockfall monitoring along transportation routes, after which the goals of this study are formulated.

Chapter 3. Collection of seismic data and identification of hazardous rockfalls. In this chapter, the test sites and data acquisition instrumentation used in the research are described. Based on the observed amplitude decay properties of seismic waves generated by natural and simulated rockfalls, a method of automatic identification of hazardous rocks (> 0.028 m^3) will be introduced. Examples of anthropogenic and natural seismic signals encountered at the test sites are presented; these ground vibrations are characterized by typical peak amplitudes, dominant frequencies, and spatio-temporal patterns which can be used for automatic event identification.

Chapter 4. Implementation of the autonomous Seismic Rockfall Detection System. We will describe the approach to designing an autonomous SRFDS which was worked out to address the properties of observed ambient seismic signals and meet the system's functional requirements. The concept of SRFDS automatic rearming using the rail traffic signals as a probe into the track's condition will be introduced. In a typical operating environment, the strongest and the most frequently occurring seismic signals (other than rockfalls) are related to anthropogenic sources, rail traffic and track maintenance. We will explain how these event categories will be handled within the suggested approach. Several train detection algorithms that utilize seismic signals generated by rail traffic will be suggested. Also, an algorithm for the rapid detection of rockfalls in the presence of train noise will be described.

Chapter 5. Performance comparison of the SDF and the SRFDS at the test site. In this chapter, performance of the test SRFDS installations will be evaluated against the existing slide fences. It will be explained how the statistics of slide fence activations and associated train delays was collected and processed. Then the methodology of collection and analysis of seismic data is discussed followed by the results of computer modeling of the SRFDS behaviour. The computer modeling was performed based on several years of continuous seismic data collected at two tests sites in British Columbia (Canada). Based on the results of computer modeling, it is concluded that the autonomous SRFDS is a more efficient rockfall warning technology compared to the existing electric slide fences.

Chapter 6. Summary and Conclusions. This chapter summarizes the observations made and the results achieved in the course of the research project.

2. Previous Work on Seismic Monitoring of Rockfalls

This thesis is concerned with the development of an autonomous Seismic Rockfall Detection System (SRFDS) as a potential replacement for the SDF. The SRFDS relies on information about rockfalls as well as natural and anthropogenic ground vibrations that is obtained from seismograms. In this chapter we will overview the main concepts used in seismic monitoring studies, including event detection and pattern recognition analysis, and previous work on seismic rockfall detection. The goals of this study will be formulated at the end of this chapter.

Two factors set this research apart from the majority of previous work. Firstly, it is the scale of the events of interest: while the bulk of studies have been directed at events involving hundreds of cubic meters of rock, the North American railway operators are concerned with rocks as small as 0.028 m^3 (in one study in Australia, the critical size boulder was defined as 0.2 m^3, *e.g.* Lee and Jones, 2004). There does not seem to be much scientific literature on real-time identification of rockfall of this size; rather, research efforts have targeted modeling rockfall trajectory for the purpose of risk assessment. Secondly, the SRFDS is a rapid response system meant to identify and report hazardous events in real time, which is different from the *a priori* risk evaluation models, and *a posteriori* damage assessment studies which combine seismic records with remote sensing data. This imposes performance constraints similar to those faced by the automatic earthquake early warning systems (EEWS): the ability to discriminate between hazardous events and background noise in real time with minimum false positives and no false negatives.

2.1. Seismic waves

Seismic waves are an elastic strain response of the medium to physical stress. Rockfall impacts, road traffic, movement of tectonic plates, explosions, and construction site vibrators excite seismic waves which can be divided into two main categories: body waves (compression, or P-wave; and shear, or S-wave) and surface waves (Rayleigh wave and Love wave) (Aki and Richards, 2002; Shearer, 2009). These waves have been observed in studies of rockfalls (*e.g.* Zimmer *et al.*, 2012; Vilajosana *et al.*, 2008; DeRoin and McNutt, 2012). Figure 2.1 illustrates body and surface waves excited by a vertical point source acting on the surface of a homogenous, isotropic, linear elastic halfspace.

The P-wave particle motion is in the direction of the wave propagation; the S-wave particle motion is transverse; the Love wave is horizontally polarized; and the Rayleigh wave is elliptically polarized in the

vertical plane. Rayleigh waves are always generated when a free surface exists in a continuous body. Horizontally polarized Love waves can occur at a range of scales whenever waveguides are present, *e.g.* whenever shallow velocities are lower than deeper velocities. In the presence of a soft superficial layer over a stiffer halfspace, multiple reflections Love waves are produced by energy trapped in the softer layer (Gibowicz and Kijko, 1994).

Lamb (1904) provided the basic theory for the ground vibration in a homogenous elastic half-space. It can be shown (Richart *et al*.,1970; Foti, 2000) that in a linear elastic half-space the following power laws can express the changes in seismic wave amplitude which result from geometrical spreading. Change of amplitude A over distance r from the source is described by $A \sim r^{-1}$ for compression and shear waves. For the Rayleigh wave that is excited by a point force and propagates with a cylindrical wavefront, a geometrical spreading relationship of $A \sim r^{-0.5}$ is expected based on the energy conservation for the elastic cylindrical surface wave. It must be noted that in reality, even at very low strain levels, soil behaviour cannot be considered elastic: cycles of loading and unloading show energy dissipation which is due to the friction between particles and the motion of the pore fluid. Hence, energy dissipation occurs for very small strains (Foti, 2000).

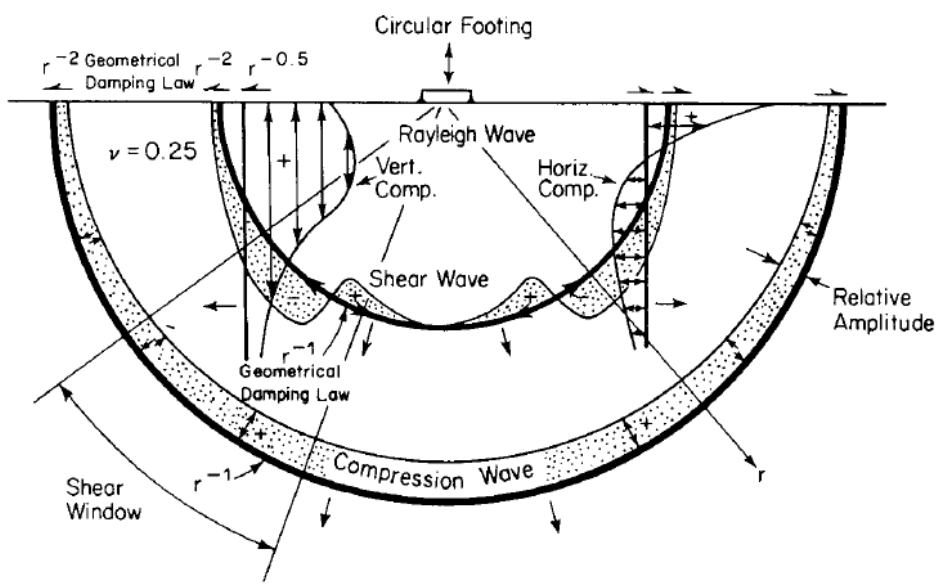

Figure 2.1. Vertical point source acting on the surface of a homogenous, isotropic, linear elastic half-space (from Foti, 2000).

For circular footing vibrating harmonically at low frequency over a homogeneous isotropic linear elastic halfspace, 67% of the total input energy goes into Rayleigh waves and the remaining fraction is divided between shear (26%) and compression (7%) waves (Gutowski and Dym, 1976). Combining these results with the geometrical spreading laws, the conclusion is that at a certain distance from the source, usually in the far-field which begins one wavelength from the source, the wavefield is essentially dominated by the Rayleigh waves (Aki and Richards, 1980).

The geometrical spreading of the Rayleigh waves with a small exponent of 0.5 is rarely observed in measurements (Gutowski and Dym, 1976; Kim and Lee, 2000; Auersch and Said, 2010); Gutowski and Dym (1976), Kim and Lee (2000) observed higher rate of amplitude decay in measurements of body waves in the near field. This formula, $A \sim r^{-0.5}$, can be improved by introduction of a material (hysteretic) damping of the soil which adds an exponential multiplier $A \sim exp(-\alpha\, r)$, which, however, is rarely confirmed by measurements (Auersch, 2010a). Huang *et al.* (2007) applied the far field asymptotic behaviour of the zeroth-order Hankel function, $A \sim r^{-0.5} exp(-\alpha\, r)$, in their study of ground vibration produced by debris flow. Wiss (1981) discovered that for many types of technically induced vibrations, a strong power law is observed, $A \sim r^{-q}$, $q >> 0.5$.

Auersch (2010a) suggested that the best explanation of the strong amplitude decay observed in experiments is the scattering phenomena: waves that pass through randomly inhomogeneous media experience scattering in addition to geometrical spreading and material damping effects. He concluded that these effects are more pronounced in engineering situations than in the strong motion investigations as the damping is lower and the wave velocities are higher.

If the soil mechanical properties vary with depth, the solution of the Rayleigh wave equation will be frequency dependent and hence the resulting wave field is dispersive, meaning that its phase velocity will be a function of frequency. One assumption about the variation of the soil mechanical properties with depth is that the soil column is a stratified medium with homogeneous linear elastic layers. With this simplification, a number of numerical methods have been developed to model the wave propagation, *e.g.* the transfer-matrix method (Thompson, 1950; Haskell, 1953), and its modifications (Kausel and Roesset, 1981; Kennett, 1974, 1979). An important consequence of surface wave dispersive behaviour in layered media is the existence of group velocity. A typical feature that can be experimentally observed in surface waves' traces is the spreading of the signal. At short distances from the source, the signal is composed essentially of a narrow impulse, in which the different modes are combined, while as the wave travels along the surface the modes separate because of their different velocities.

Configurations of the surface seismic arrays used in the studies of surface wave propagation and seismic P-wave refraction are basically the same: the diagram in Figure 2.2 shows paths of direct, reflected, and refracted waves for a two-layer velocity model which will be used to explain field observations later in the text.

To interpret seismic records presented in the following chapters it is important to know that the P-wave is the fastest and is polarized in the direction of propagation. The S-wave is polarized in the vertical and horizontal planes, and its velocity ranges from 0 to 70% of the velocity of the P-wave (Sheriff and Geldart, 1995). The Rayleigh wave velocity is typically 92% of the S-wave (Gibowicz and Kijko, 1994).

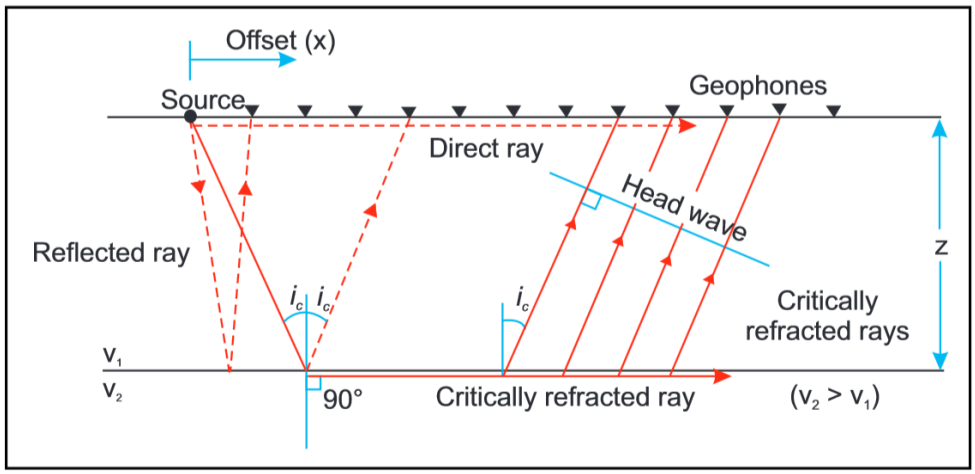

Figure 2.2. Raypath diagram showing the respective paths for direct, reflected, and refracted rays[5].

2.2. Previous seismic studies of natural and simulated rockfalls

Seismic studies of landslides have been conducted on a wide range of scales, usually involving hundreds of cubic meters or larger. Seismic recordings have been analyzed to identify, for example, rockfalls and rockslides movements (Lacroix and Helmstetter, 2011; Roth and Blikra, 2007), snow avalanches (Bessason *et al*., 2007), slope failures in open pit mines, and rock bursts in underground mines. Amitrano

[5] http://www.reynolds-international.co.uk/uploads/files/10tssseismicrefraction.pdf (last checked on July 31, 2015)

et al. (2007) monitored an active earth slide with a broadband seismometer and discovered strong signals within 0.1-10 Hz band. Seismic monitoring has been performed based on the assumption that future catastrophic events can be predicted by detecting precursor ground motion. For example, Amitrano *et al*. (2005) analyzed the statistical patterns of seismicity before a cliff collapse involving more than 10^3 m^3 of rock, and reported a power law acceleration of seismicity rate and energy shortly before the collapse. In a similar study, Senfaute *et al*. (2009) noticed a progressive decrease of the frequencies as the rock approached failure; it was hypothesized that the decreasing spectral frequency patterns are associated with seismic events progressing toward a rockfall. In a passive seismic monitoring study of the dynamics of an unstable limestone cliff, Got *et al.* (2010) concluded that for the purpose of early warning systems both total seismic energy release and base noise level should be inspected.

The differences in the polarization properties, frequency, velocity and geometrical spreading laws of the waves can be used to identify the seismic phases and to estimate the direction of incoming waves (Jurkevics, 1988). Vilajosana *et al.* (2008) used three-component seismometers to estimate the direction of the source using the wave polarization and locate a rockfall. Wave identification through polarization estimation can be difficult for moving sources in complex media, because the resulting polarization is a superposition of different waves coming from different sources delayed in time (Deparis *et al.*, 2008).

Deparis *et al.* (2009) and Dammeier *et al.* (2011) were able to identify P and S arrivals induced by rockfalls and active rockslides. The distance to a seismic event can be calculated by using the velocity difference between P and S waves. Epicenter location can help to define the active part of a rockslide which sometimes can be confirmed by geomorphological observations (Tonnellier *et al.*, 2013). When the distance between sensors and sources is small, the P, S and surface waves can be mixed and difficult to identify, which makes picking first arrivals impossible (Lacroix and Helmstetter, 2011).

Seismic signatures of rockslides and rockfalls have been analyzed to distinguish the type of failure (*e.g.* rockfall, rockslide or earthquake), as well as to estimate the size and the triggering mechanism of failure. Signal characteristics typical of debris avalanches include emergent onsets, low maximum amplitude relative to duration, and indistinct phases (Norris, 1994) while seismic signals from explosions and rock impacts onto the ground were observed to appear suddenly and to decrease rapidly (Vilajosana *et al*., 2008; DeRoin and McNutt, 2012). Hibert *et al.* (2014) describe a technique for automated volume estimation of rockfalls which occur near a volcano crater; the technique utilizes the estimated slope length and the correlation between the seismic and the potential energies of a rockfall. Norris (1994) investigated links between the source volume, source materials, track materials, and failure modes, as well as seismograms of 14 large volume ($>10^4$ m^3) rockfalls and avalanches in the Cascade Range of

Washington. He found that rockfalls that have the same source areas and descent paths show a linear or nearly linear relation between source volume and signal amplitude, and it was concluded that the volume of rockfalls occurring in these circumstances may be predictable from seismic records. Dammeier *et al.* (2011) developed quantitative estimates of the fundamental rockslide properties based on several simple metrics, *e.g.* peak value of the ground velocity, velocity envelope area, and duration; all volume estimates of known rockslides with volumes between 10^3 and 10^6 m^3 were found to be reasonably close to the actual values. However, other researchers found poor correlation between the volume of rockfalls and the duration of their seismic signals (Tilling *et al*., 1975). Deparis *et al.* (2009) found no relation between the rockfall parameters and seismic magnitude, except for the rough correlation between the duration and runout distance. Deparis *et al.* (2009) compared the seismic energy and the potential energy of rockfalls and concluded that only a small amount of kinetic energy is transmitted as seismic waves which is due to non-linear effects during the impact.

Vilajosana *et al*. (2008) studied an artificially triggered rockfall using two three-component seismic stations. It was found that each impact of the rock onto the ground produced strong, mainly linearly polarized P-waves. The estimates of seismic energy correlated with the kinetic energy of the impacted mass; it was concluded that determination of the rockfall size based on the detailed analysis of seismograms is feasible. Lacroix and Helmstetter (2011) describe a beam-forming method used for event location within a progressive rock slide; they used a video camera to estimate the volumes and calibrate seismic signals. Helmstetter and Garambois (2010) developed a pseudo-automatic method for detecting and classifying events based on intercorrelaiton of signals at different sensors.

DeRoin and McNutt (2012) observed an increase of surface rockfall activity which occurred at nearly the same time as precursory earthquake activity increased beneath a volcano; they concluded that seismic monitoring of rockfalls can provide real-time hazard assessment at volcanoes.

The monitoring efforts have been aimed at reporting hazardous landslides and avalanches in real time. An automatic system based on seismic measurement has been used as an early warning system to detect and analyze avalanches (Bessason *et al.*, 2007). Identification is performed by comparing new events with old known events; a number of signal parameters are used to classify events as avalanches, rockfalls, earthquakes, traffic induced signals or maintenance work. Power of the recorded signal is used as an indicator of the event size. Huang *et al.* (2007) describe an advanced system for debris flow monitoring based on measurements of ground vibrations; the authors investigated frequencies, wave speeds and amplitude decay patterns of signals induced by debris flows.

2.3. Seismic wave generation by impact loading

The correlation between the mass of the rock and the peak ground velocity is intuitive and was consistently observed during the rockfall tests performed in the course of this research. However, there do not appear to be many studies of ground response to impact sources recorded with (sub)surface transducers with respect to the rock size. As far as the railway operators are concerned, a rock as small as 0.028 m^3 can cause a derailment; while the studies of naturally occurring rockslides and rockfalls typically deal with the events which involve much larger volumes (*e.g.* Deparis *et al.*, 2008; Norris, 1994; Hibert *et al.*, 2014; Dammeier *et al.*, 2011). For automatic event recognition, reliable travel time information is not always available because a rockfall can involve many rocks (*e.g.* DeRoin and McNutt, 2012; also see seismogram in Figure 3.63) and induce multiple seismic phases, including body and surface wave which complicates the task of singling out individual phases for subsequent travel time computation. Instead, the research of previous work was focused on PGV (peak ground velocity) decay models as a means to estimate the rock size.

Application of amplitude decay models in geotechnical engineering

Vibrations generated by various construction activities can be detrimental to adjacent facilities. As a result, a significant amount of experimental data on the rates of amplitude decay of mechanically induced surface waves has been accumulated. Ground vibration propagation tests which involve dropping a weight can be used to assess the rate of decay of amplitude with distance from the vibration source.

Attempts to statistically correlate PGV with the weight size and elevation were made in the studies of dynamic soil compaction and vibration propagation. A number of relationships between the impact energy and peak ground velocity in various soil profiles have been suggested (Richart *et al.*, 1970; Wiss, 1981; Woods and Jedele, 1985; Jedele, 2005). For instance, a commonly used method to express the decay of ground vibrations with distance which includes geometrical spreading and material damping was suggested by Bornitz (1931) (Kim and Lee, 2000):

$$w_2 = w_1 \left(\frac{r_1}{r_2}\right)^n e^{-\alpha(r_2 - r_1)} \tag{2.1}$$

where w_1 and w_2 are vibration amplitudes at distance r_1 and r_2 from the source of vibration; n is a geometrical spreading coefficient; α is a material damping coefficient. Sometimes, this model incorporates dependency between the material damping coefficient and the frequency (Richart *et al.*, 1970) in the form

$$\alpha_2 = \alpha_1 (f_2 / f_1)$$

where α_1 – is known value of α at frequency f_1;
α_2 – unknown value of α at frequency f_2.

Wiss (1981) suggested that energy and distance could be combined in a "scaled distance" format:

$$V = k\,(D/E^{1/2})^{-N} \tag{2.2}$$

where V = peak particle velocity, k = intercept at 1 energy unit; D = distance from the vibration source; E = energy of the source; N = pseudo-attenuation factor.

Model (2.2) was tested by Jedele (2005) who reported site-specific N- pseudo-attenuation factors and material damping coefficients (α) for thirteen construction sites with different soil types. Energy sources included, for the most part, a 63 kg (140 lb) Standard Penetration Test donut-type weight dropped from 2.4m elevation. Mayne *et al.* (1984) used this model in their summary of field measurements from over 120 locations where dynamic compaction was performed for site improvement. Kim and Lee (2000) used eq. (2.1) to approximate the PGV decrease of various ground vibration sources, including train and hydraulic hammer, and investigated the contributions from geometrical spreading and material damping.

The general trend is for the amplitude of ground vibrations to have a linear drop off in the far field on log-log scale (Mayne, 1984; Auersch, 2010a; Jedele, 2005) whereas in many studies the PGV trend is not reported for the first 10 meters, *i.e.* in the near field. In the report on a series of dynamic compaction experiments at a site near a seashore, Hwang and Tu (2006) observed a steeper drop off in the near field for larger weights, *i.e.* in the near field the difference in PGV between smaller weight and larger weights is more significant than in the far field. Ground vibration was induced by dropping a 25 ton weight from 5, 10, 15 and 20 m elevations. A shallow trench between the drop location and sensors had practically no isolation effect on the peak amplitudes. Another interesting conclusion was that when the elevation is higher than a certain height limit, the influence of tamping energy on the induced vibrations becomes insignificant.

It must be noted that dynamic compaction involves treating unconsolidated soils, sometimes reclaimed land as well as heterogeneous fill materials, with high-energy tamping (up to 5-20 tons, 10-20 meters elevation). Therefore, the amplitude decay rates obtained in this field of study may not be readily transferrable to rockfall detection. However, the log-log linear law has been observed in a number of studies of surface waves in consolidated soils which, for example, involved explosive sources, weight drops, and hammer excitation (Gutowski and Dym, 1976; Auersch and Said, 2010; Auersch 2010a). The practical conclusions based on the above studies which will be used in the following discussion are that a) though the amplitude change law depends on the soil properties at a specific site, ground response to the impacts of the same energy is consistent, at least statistically; b) PGVs correlate positively with impact energy.

The same value of impact energy can correspond to different combinations of rock mass and falling height. Correlation between the impact energy and the impact force was observed by Calvetti *et al.* (2005) and Roesset *et al.* (1993). Calvetti *et al.* (2005) studied impacts of an 850 kg reinforced concrete sphere on granular soils both experimentally (impact energy was in the range of 40-150 kJ) and numerically (with energy up to 5000 kJ). The influence of block mass, falling height, and thickness of the cushion on the impact force acting on the horizontal plate were analyzed numerically using the Discrete Element Method. They used a combination of weights and heights with the same kinetic energy; it was concluded that for the same impact energy, impacts of a smaller mass and larger falling height induce larger vertical stress. With regard to analytical models, Gucunski (1991) suggested a procedure to estimate the values of the mass and drop height required to produce the desired amplitudes. Gucunski (1991) and Roesset *et al.* (1993) modeled the impact of weight falling onto elastic half-space by means of a simple mass-damper system. However, Roesset *et al.* (1993) admitted that the model is not satisfactory when inelastic collision takes place, which is the case when rocks fall onto the railway embankment. Farin *et al* (2015) derived scaling laws which relate the mass and the speed of an impactor to the radiated elastic energy and the frequency content of the emitted seismic signal. They used elastic, viscoelastic and elastoplastic impact models which were tested in lab experiments, and concluded that the impactor's mass and speed can be estimated from the seismic signal generated by an impact on a thin plate and on a thick block.

2.4. Real time seismic monitoring

Operation of the seismic rockfall detection system is similar to that of an Earthquake Early Warning System (EEWS): both use seismic signals to estimate the potential damage and forward this information

to the end users in real time. EEWS uses an alert on an impending earthquake damage based on measurements of P-wave ground motion (P-wave propagates faster and is less destructive than S-wave). Operational EEWS are currently running in Japan (UrEDAS), USA, Taiwan, Mexico, Turkey, Canada (*ShakeAlarm*®) , and some other countries (Kanamori, 2007; Zaicenco *et al.*, 2010; Zollo, 2010). For example, UrEDAS (Japan) has been used for controlling the speed of Japanese high-speed train. Most EEWS developed so far are conceived as either 'regional' (network-based) or 'on-site' (stand-alone) systems; response time of EEWS varies between 2-10 seconds depending on the epicenter location and network density. In one example, UrEDAS located in the epicentral area issued a warning 1 second after the P-wave arrival at the site, which resulted in power shutdown and activation of emergency brakes on the train moving at a speed of 200 km/h near the epicenter (Kanamori, 2007). Though the train eventually derailed a few seconds later, no casualties occurred.

A number of empirical log-linear relations between the earthquake magnitude M, peak acceleration a_p and hypocentral distance R have been proposed. For example, Hasegawa *et al.* (1981) developed the following ground motion attenuation model for western Canada: $a_p = 10\, e^{1.3M}\, R^{-1.5}$. Examples of other ground motion relations can be found in (Hasegawa *et al.*, 1981; Macciotta *et al.*, 2015a).

The California Integrated Seismic Network (CISN) uses three EEW algorithms, two for regional networks, and one for a single-sensor (Bose *et al.*, 2009; Kuyuk *et al.*, 2013). The algorithms are based on two parameters: period τ_c and high-pass filtered displacement amplitude P_d ; as well as an empirical scaling relationship between τ_c , P_d, moment magnitude, and the peak ground velocity. The empirical relationship was obtained from a large number of historical earthquake records from seismically active areas, *e.g.* Japan and California. Test users of the CISN include the San Francisco Bay Area Rapid Transit.

In strong motion seismology, empirically derived scaling relationships between the earthquake magnitude, frequency, peak ground motion amplitude and hypocentral distance have been used for rapid magnitude estimation and earthquake early warning (*e.g.* Allen and Kanamori, 2003). In the ElarmS algorithm described by Kuyuk *et al.* (2013), after a multi-station trigger has been detected and located using arrival times and analyzed by a simple grid-search algorithm, the earthquake's magnitude is estimated using the scaling relationship empirically determined from the past earthquake records. The trigger criteria depend on site conditions and are different, generally speaking, for stations at rock sites and those built on soft soils (Bose *et al.*, 2009).

Micro-seismic monitoring has been used in the fields of underground mining, slope stability monitoring, and reservoir monitoring (*e.g.* Hardy and Kimble, 1991). Mine monitoring efforts are aimed at predicting

and preventing catastrophic failures in underground mines, and usually involve placing extensometers in the areas of low stability, as well as deployment of seismic arrays in order to analyze acoustic emission/micro-seismic activity (AE/MS). Micro-seismic monitoring provides information about the response of the rock mass to the mining activities, *e.g.* longwall caving, rock bursts, and triggered seismicity (*e.g.* Hatherly, 2013; McGarr and Simson, 1997; Fritschen, 2010; Brink *et al.* 2002). Hard rock mining often occurs in environments with inherently unstable rock masses because the removal of the rock causes perturbations in the existing stress field, leaving the mine prone to catastrophic failures (Zimmer, 2011). Increases in acoustic emission levels can be associated with the onset of fracturing that could lead to a roof fall, *i.e.* gradual failures of poorly-supported blocks of rock in low stress mines.

Similar to earthquake seismology, the use of a suitable array of sensors and recording equipment allows one to determine event locations and the nature of the failures (tensile or shear), direction of slip and its magnitude. Existing micro-seismic monitoring systems usually utilize advanced sensor networks which can evaluate the timing, location, and energy level of individual events (*e.g.* Gibowicz and Kijko, 1994; Gibowicz, 1990). Background noise and equipment sensitivity may impose limitations on the magnitude of detectable events and location accuracy. Micro-seismic techniques have also been developed to allow the location of trapped miners. If the miners trapped underground strike the roof of the workings and generate seismic waves, the ground vibration can be detected by sensors installed on the surface (Durkin and Greenfield, 1981). Successful micro-seismic monitoring studies have been conducted in some open pit mines (Shiotani, 1998).

2.5. Pattern recognition and sensor array methods

It is not hard for a human observer to recognize a rockfall pattern in a seismic array record and distinguish it from rail traffic, as it will be demonstrated in the following chapter. Manual analysis can be time-consuming, whereas an early warning system requires real-time processing of seismograms. We will review the concepts used in automatic processing of individual seismic records as well as seismic array methods.

2.5.1. Detection of seismic events

The problem of automatic recognition of seismic events of interest and false alarms is not new. For example, post-detection processing was introduced by Stewart (1977) who computed a characteristic function for a recorded seismic event to filter out undesired signals. The implementation of automatic analysis procedures is motivated by the existence of large global digital seismic data bases. In the early 1970s when relatively inexpensive and powerful computers became increasingly available, researchers developed automatic phase pickers for on-line detection of P and occasionally S arrivals (Allen, 1982).

Overview of triggers used for individual stations can be found in (Joswig, 1990; Withers *et al.*, 1998). Several trigger algorithms are presently known and used, from a very simple amplitude threshold type to sophisticated pattern recognition, adaptive methods and neural network based approaches. Previous work on seismic phase and event detection can be generally categorized into time domain (*e.g.* Allen, 1978; Trnkoczy, 2002), frequency domain (Gledhill, 1985; Dowla *et al.*, 1990), particle motion processing, and pattern matching (Withers *et al.*, 1998). These algorithms are based on the amplitude, the envelope, or the power of the signal(s) in time domain, or on the frequency domain content of seismic signal. Chen (1978) discussed the efficiency of various discriminants used for automatic discrimination of natural earthquakes and nuclear explosions.

In the time domain, STA/LTA (short-term average *vs* long-term average) phase picker is the most popular in seismology (for reviews, see Allen, 1982; Joswig, 1990) and it comes in many different variants (*e.g.*, Ambuter and Solomon, 1974; Stevenson, 1976; McEvilly and Majer, 1982; Baer and Kradolfer, 1987; Zimmer and Sitar, 2015). Earl and Shearer (1994) applied the STA/LTA detector to an envelope function. Among the more sophisticated ones, trigger algorithms of Allen (1978) and Murdock and Hutt (1983) are among the most common. A number of other event-detection methods have also been proposed by various researchers, and the most popular are listed in (Tselentis *et al.*, 2012) with the application to passive seismic monitoring. Many of these algorithms function in association with the seismic phase time picking.

Several authors have suggested the polarization approach to signal detection based on the premise that the wave-field spatial coherence increases when a signal is present. This idea has been applied for isolated three-component sensors (Rudd and Husebye, 1992). Wagner and Owens (1996) outline a signal detection approach for multi-channel seismic data; the method uses sample covariance matrix (principal-component analysis, PCA) which can be applied to three-component data as well as vertical-component sensor array. The goal is to identify those points in time that contain coherent signals. Compared to

conventional and minimum-variance vertical-component beamforming, the method essentially forms all possible beams without the computational load of an equivalent beamforming detector.

Algorithms for seismic array detection fall into a special field of research. The idea of using the number of network triggers as a discriminant has been widely used in seismology (*e.g.* Stewart, 1977; Allen, 1978). This array technique (the coincidence trigger algorithm, available either in seismic networks or within a multichannel stand-alone seismic recorder, or in a group of interconnected seismic recorders) uses a voting scheme for triggering. Only if the total number of votes exceeds a given pre-set value, does the system actually trigger (*e.g.* Hardy *et al.*, 1988; Hardy and Kimble, 1991; Zimmer *et al.*, 2012; Zimmer and Sitar, 2015). Rost and Thomas (2002) reviewed various array techniques developed since the 1960s. Most array methods use the ability of seismic arrays to measure the vector velocity of an incident wave front, *e.g.* the so-called vespa process (velocity spectral analysis, Davies *et al*., 1971), sonograms (Joswig, 1990), beamforming, three-component analysis, and migration. This information can be used to distinguish between different seismic phases, to separate waves from different seismic events and to improve the signal-to-noise ratio. Savard and Bostock (2015) developed a cross-station correlation approach based on waveform coherence and travel time consistency to locate low-frequency earthquakes using seismic network data. In surface micro-seismic monitoring, zero time-lapse cross-correlation of a noisy time-series with a known signal was used by Eisner *et al.* (2008) for detecting weak signals induced by hydraulic fracturing; this technique is known as a matched filter. Withers *et al.* (1998) describe an automated, near-real-time, waveform correlation event detection and location system (WCEDS) to operate on 150 channels of telemetered data in real time. This is a matched filter algorithm that detects events by correlating envelope function with theoretical or empirical seismogram envelopes; phase picks, automatic or otherwise, are not used. An STA/LTA algorithm incorporating adaptive window lengths was found to provide an output that best met the requirements of a global WCEDS. In earthquake seismology, array-based waveform correlation of strong events with noisy time-series is used to detect weaker events (*e.g.*, Gibbons and Ringdal, 2006). Almendros *et al.* (1999) combined the zero lag cross-correlation (ZLCC) of windowed seismograms, a technique used to detect plane waves, with the 3D grid search to locate coherent seismic signals and estimate the back-azimuth and the apparent velocity; they presented a modified method which allows the wave front to be circular. Frankel *et al.* (1991) used the average of the cross-correlations between all pairs of stations in an array. In reflection seismology, a source-time function, known as chirp or sweep, is correlated with the recorded waveform to deconvolve medium response (Sheriff and Geldart, 1995).

The problem of automatic recognition of anthropogenic noise was addressed by Allen (1978) who appears to be the first researcher to describe a computer program capable of distinguishing earthquakes from noise

sources such as wind or vehicular traffic using a single seismometer trace. Besides the event picking capability, the algorithm used a separate post-detection process and stored sufficient information during the event to enable it to decide at the end whether the event was an earthquake and worth recording, or merely noise that should be ignored. To simplify the recognition problem, results were cross-referenced between stations.

Pattern recognition

If a simple amplitude threshold is used, each pulse with energy above the threshold will trigger a preliminary detection which subsequently must be evaluated by some post-detection logic. Pattern recognition implements a positive decision logic: only a sufficient similarity with the event pattern will trigger the monitoring system. In seismology, a number of automatic pattern recognition techniques have been designed. Early pattern recognition detectors were based on syntactic sentence analysis (*e.g.* Lui and Fu, 1983; Anderson, 1982). Joswig (1990; 1993; 1995) introduced the idea of pictorial representation of individual seismograms combined with pattern recognition performed by standard computer vision methods. He used sonograms which display spectral energy *versus* time in order to identify teleseismic events and known noises, and likened the process of automatic earthquake detection to the visual inspection of seismograms by an observer who compared them to a mental image of an event. This allowed him to apply computer vision techniques to seismograms transformed into mental images.

In the field of machine learning, two different approaches are available. For supervised learning, labeled training data with known class-memberships are required to introduce the patterns to be recognized by the algorithm. Unsupervised learning uses unlabelled training data for automatic pattern identification; this machine learning technique automates the recognition of wavefield patterns with a minimum of domain knowledge. Esposito *et al.* (2006) used supervised (multilayer perceptron, MLP) and unsupervised (self-organizing maps, SOM) neural networks (NN) to detect and discriminate between landslide, explosion-quake and volcano micro-tremors, reporting up to 99% of events as classified correctly. To characterize different type of events, spectral features as well as amplitude-versus-time information was used. Köhler *et al.* (2010) implemented a classification system based on SOM which correctly distinguished tectonic and rockfall events as well as background noise patterns due to human activity. In their case study, ground motion induced by microseisms was dominated by frequencies below 1 Hz whereas anthropogenic noise was mainly above 1 Hz. An overview of literature about the origin and the nature of the ambient seismic noise can be found in (Bonnefoy-Claudet *et al.*, 2006).

Summarizing the applicability of the reviewed techniques for automatic recognition of hazardous rockfalls along railway alignments, it should be noted that, in this research the NN approach was not tried for a number of reasons, including the small training set, less than 100% detection rate, and overlapping spectra of rockfalls and ambient noises. Regarding current research, the use of beam forming methods (averaging) for S/N improvement by stacking was found unproductive because of non-uniform sensor operating environments, whereas for a successful stack of the waveforms across the array, the waveforms must be coherent (Rost and Thomas, 2002). In addition, the number of seismic sensors in the rockfall monitoring array can be relatively small (10-30 transducers), while the amplitude of ground vibration induced by anthropogenic sources (trains) can be many times that of a hazardous rock.

One can also search for linear particle motion in detecting body-wave phases, but near-surface scattering, multiple surface impacts, and superimposed seismic background noise can have a deleterious influence on linearity. Furthermore, particle-motion methods are generally more computationally intensive than time domain methods. This, as well as a significantly larger cost of deployment of three-component arrays, are some of the reasons why the polarization techniques were not used in the current study.

2.5.2. Detection of rail traffic

The scientific literature does not appear to contain much information about detection of trains using seismic or acoustic sensors. This may be because there are more reliable and cost-effective techniques available for railway operators. In addition to electro-magnetic wheel counters and electric track occupancy relays, trains can be detected using radar, cameras, infrared sensors (hot box detectors), optical and ultrasonic sensors. However, the goal of this research has been to accomplish the task of seismic rockfall monitoring with minimum overhead and maximum system robustness.

Studies of the acoustic and the seismic excitations associated with railway operations have been directed towards noise and vibration reduction rather than detection of trains over a distance or classification of vehicle types. Ground vibrations induced by rail traffic have been widely studied with regard to the environmental effects of the accompanying noise. The cause of wheel-rail noise is thought to be wheel and rail structural vibrations excited by a combination of the wheel and rail surface roughness. The most comprehensive and widely used wheel/rail noise model is that developed by Remington (1987) and Thompson (1993). Sources such as the track, the ties, or the vehicle body may be present; however, these are only of secondary importance (Thompson, 1993). Experimental evidence indicates a linear relationship between roughness and noise (Thompson, 1996).

High-speed trains can generate strong vibrations that propagate at large distances from the track and cause annoyance to the public or even structural damage, for example, through resonance of an arch bridge. Analytical solutions for ground response under varying train speeds have been developed (Krylov *et al.*, 1996; Ditzel *et al.*, 2001; Kenny, 1954; Fryba, 1972) which are valid for a narrow range of track conditions and excitation sources. Krylov (1996) investigated the effect of track dynamics on the vibrations due to high-speed trains; an increased effect on the level of ground vibration occurs for trains travelling at speeds larger than Rayleigh wave velocity in the supporting ground. Ditzel *et al.* (2001) presented a method to calculate the displacements generated by a moving train which takes into account reflection and transmission properties of the layers. The theoretical model was compared to the experimental measurements with two lines of vertical geophones, one perpendicular and one parallel to a railway track. Sheng *et al.* (1999) used the propagator matrix method of Thomson (1950) and Haskell (1953) based on wave number theory to model propagation of vibration generated by a harmonic or a constant load moving along a layered beam resting on the layered half-space.

Numerical modeling techniques allow one to create accurate models of the complex geometries associated with the track components. Kouroussis *et al.* (2009), Connolly *et al.* (2013) and Costa *et al.* (2012) developed models of the generation and propagation of ground vibrations induced by railway traffic which are based on the finite-element method (FEM) and the boundary-element method (BEM). A dynamic FEM-model capable of simulating non-linear excitation was developed by Connolly *et al.* (2013); in particular, the model was used to compute PGV decrease with increasing distance from the track with 80% correlation between the simulated and experimental results. Kouroussis *et al*. (2012) attempted to quantify the effect of vehicle and track parameters on the ground vibrations levels. It was found that the Young's modulus and damping characteristics of the soil had a significant effect on vibration levels (Kouroussis *et al.*, 2013). Connolly *et al.* (2013) developed a site-specific three dimensional numerical model to investigate the effect of embankment constituent material on ground borne vibration levels at various distances from the track. The model can calculate the propagation and transmission of ground vibration in the vicinity of high speed railways.

With regard to the identification of railway vehicles, Ni *et al.* (2011) proposed an *a posteriori* method based on the automatic isolation of the dominant excitation frequencies generated by the carriage periodicity in order to calculate train speed. This automatic procedure assumes the train speed to be constant and requires the analysis of the dominant frequencies induced by trainload (Ju *et al.*, 2009). Kouroussis *et al.* (2014) proposed a number of improvements to this method which rely on *a priori* information about the distance between tracks, wheels, and the carriage length. Because ground vibration contains transient events, their method uses the running root mean square (r.m.s.) in addition to the

original signal; the original signal was smoothed in order to fully resolve the carriage periodicity at 300 km/h. However, with regard to the typical operating environment of the SRFDS, this method has a limited applicability as it uses *a priori* parameters and assumes that the vehicle velocity is constant; also, this method does not apply to high-rails (a vehicle that can operate both on rail tracks and a conventional road). In addition, the *a posteriori* method will delay vehicle identification, especially in the case of slowly moving trains.

The task of identification of moving vehicles with seismic sensors has been addressed in military applications and intrusion detection. Anderson *et al.* (2001) performed finite-difference time domain (FDTD) simulation of moving armored vehicles. Spectral analysis has been used for target discrimination and classification. Moran and Greenfield (1997) utilized spatial coherence (coherence is a frequency domain measure between two signals that varies between 0 and 1) computed across a sensor array to estimate the bearing to a seismic source. Moran *et al*. (1998) demonstrated that knowledge of the spatial variation of wave field amplitude could be used to estimate the distance to a moving target. Succi *et al.* (2000) used surface Rayleigh waves to track both personnel and vehicles using a Kalman filter to improve the signal-to-noise ratio.

Seismic array methods

Time-delay surges of seismic energy induced by a train's progress from geophone to geophone look similar to a wave front impinging onto a linear array (sample seismograms are presented in the next chapter). Several methods have been derived for estimating wave parameters using observations from a discrete spatial array of sensors; beam-forming is one of them. Assuming that one plane wave (the source is at large distance) propagates with a certain velocity in a certain direction across an array of sensors, each one senses essentially the same signal, but time-shifted according to the respective position. If the signals are shifted by the correct propagation delays and summed, they superpose coherently and background noise is reduced. If the time shifts do not fit to the actual wave direction and velocity, the signal fit is worse and the sum amplitude is smaller. For an unknown propagation velocity v and direction θ, v and θ are varied systematically; the resulting two-dimensional distribution of sum-signal amplitude will show a peak around the correct values of velocity and direction.

For example, Barsikow *et al*. (1987) used 1-D phased microphone array mounted along wayside to investigate sound emission of high-speed trains; the sensitivity of line array depends upon the incident

angle of the impinging waveforms. By summing recorded signals, a beam pattern can be formed that describes the response of the array.

Transients in train signals, which can be particularly strong near rail expansion joints, result in poorly correlated signals. This is the reason why the beam-steering/ stacking technique was not attempted in this study: adding train signals is unlikely to cancel local transients. In addition, one cannot expect a rail vehicle to maintain precisely the same speed across a 400-1,000 m long array of sensors.

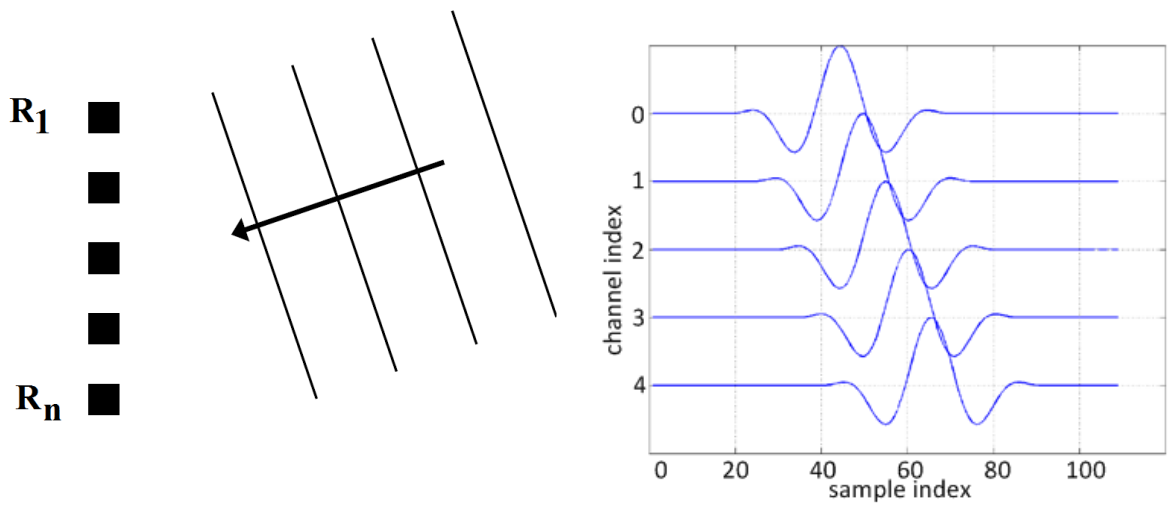

Figure 2.3. A wave front impinging onto a sensor array R_1, R_2, …, R_n [6].

Besides beam-forming, algorithms based on correlation or coherence techniques are often used if the number of instruments is small, and the signals are well separated in time (Denholm-Price and Rees, 1999). The goal of these methods is to maximize the weighted sum of either the cross correlation in the time domain, or cross-coherence in the frequency domain, for all possible pairs of instruments. This yields the time delay of the signal between each of the sensors, from which the speed and direction of the waves can be determined. Several authors (Barsikow, 1996; Altmann, 2004) reported that sensor-array processing of vehicle noise by beam forming works well in the acoustic realm, due to the similarity of

[6] Modified from S.P. Näsholm's presentation on conventional beamforming: http://www.uio.no/studier/emner/matnat/ifi/INF5410/v12/undervisningsmateriale/foils/conventional_beamforming_part_1.pdf. Last checked on February 10, 2016.

signal form measured at different locations. However, for ground vibrations this approach gives inaccurate results, because the seismic signals are dissimilar even at neighbouring positions due to dispersion of Rayleigh surface waves, soil inhomogeneity, and multiple sources (Altmann, 2004).

For train identification, a combination of beam-forming and correlation methods will be used. The beam-forming approach will be applied to compute time-shifts of the r.m.s. envelopes of train signals assuming a steady velocity; then, windowed pairs of r.m.s. signals will be correlated and the product, rather than the sum, of individual correlations will be computed. Because of strong transient noises coming from rail joints and wheel surface roughness, as well as multiple sources of excitation, envelope signals will be compared. The product of correlations, or the *cost function*, will be evaluated against a threshold to identify the train pattern.

Cross-correlation analysis, or matched filtering, is a well-known technique for time-delay estimation, widely used, for example, in seismology (Gibbons and Ringdal, 2006), radar (Knapp and Carter, 1976), image processing (Briechle and Hanebeck, 2001), and medical imaging (Bonnefous and Pesque, 1986; Luo and Konofagou, 2010). In pattern recognition, a reference signal is defined in one time/space frame and subsequently compared with different candidate windows from another frame/space of data, within a pre-defined search range. In the one-dimensional case, the reference signal, or template, is shifted in discrete steps along the time axis and then the cost function is calculated over the template area to quantify the similarity between the reference and comparison windows. Numerous cost functions have been developed for different methods of estimation of the position of a given pattern in an image, including, but not limited to, non-normalized cross-correlation (CC), normalized cross-correlation (NCC), zero-mean normalized cross-correlation (ZNCC, *i.e.*, normalized covariance), sum of absolute differences (SAD), and sum of squared differences (SSD) (*e.g.* Viola and Walker, 2003).

A ZNCC-based time-delay estimator will be used in the train detection algorithm later in the text to detect a vehicle by searching for a time-delay pattern in the seismic data. The train velocity is estimated from the temporal shift between the reference window and the best-match comparison window which gives the maximum cost function value. Two basic cases can be differentiated: when the position of the region of interest is unknown and when an estimate for the position is given (Briechle and Hanebeck, 2001). The former is usually the case when train detection is performed because the arrival time of a vehicle is one of the unknowns. The latter case is known as feature tracking. As an example (*e.g.* Walker and Trahey, 1995), zero-mean normalized cross-correlation of two continuous signals, $s_r(t)$ and $s_c(t)$, is defined as:

$$R_{ZNCC}(\tau) = \frac{\int_{-T/2}^{T/2}(s_r(t)-\overline{s_r})(s_c(t+\tau)-\overline{s_c}(\tau))dt}{\sqrt{\int_{-T/2}^{T/2}(s_r(t)-\overline{s_r})^2 dt}\sqrt{\int_{-T/2}^{T/2}(s_c(t+\tau)-\overline{s_c}(\tau))dt}}$$

where

$$\overline{s_r} = \frac{1}{T}\int_{-T/2}^{T/2} s_r(t)dt$$

$$\overline{s_c}(\tau) = \frac{1}{T}\int_{-T/2}^{T/2} s_c(t+\tau)dt$$

$s_r(t)$ - reference signal; $s_c(t)$ - comparison signal; τ – temporal shift; T – correlation window. Selection of the reference signal within the train detection algorithm will be discussed in the following chapters.

The direct method of an exhaustive search can be computationally intensive. Various optimization techniques can be added to the trial-and-error search algorithm in order to improve its real-time performance. For instance, if two or more comparison signals are used, computation of the product of ZNCCs can be aborted as soon as ZNCC falls below the cost function threshold. If a train pattern has been identified at a reference sensor, the same conclusion can be applied to the comparison sensors. Also, if the smoothed signal is of low frequency (as is the case with surges of seismic energy induced by railcars rolling past a seismic sensor), the envelope of signal acquired at 1 kHz can be sub-sampled at 10-100 Hz, depending on the train velocity.

2.6. Landslide monitoring methods used in geological engineering

In geological engineering, the current state of practice is to monitor known unstable rock slopes and document the displacements or morphological changes over time. This task can be accomplished with displacement sensors, permanent real-time GPS stations, seismic, acoustic emission/ micro-seismic monitoring, visual inspection, conventional geotechnical instrumentation, *e.g.* extensometers, as well as

remote sensing (Macciotta *et al.*, 2014b; Bobrowsky *et al*., 2014). The latter includes InSAR, terrestrial and airborne LiDAR systems, and photography (Collins and Sitar, 2007; Jaboyedoff *et al.*, 2012; Gauthier *et al.*, 2012a; Gauthier *et al.*, 2012b; Lato *et al*., 2015; Kromer *et al.*, 2015; Hutchinson *et al*., 2015). Roth and Blikra (2007) used a laser ranging system to study the movement rate of an unstable rock slope, which was estimated at several centimeters a year.

Slope monitoring plays an important role in the risk management of open pit mines. Historically, displacement data derived from measuring geodetic prisms have been used to delineate the boundaries of potential slope hazards. The geodetic measurements are susceptible to uncertainty which can result in an early warning of impending failure or a false alarm related to highly localized movements. New technologies such as ground-based radar can provide high resolution, full area coverage of a slope in combination with near real-time acquisition and millimeter precision (Severin *et al.*, 2014). However, because of the catastrophic character of rockfalls and the susceptibility to inclement weather, the rockfall monitoring techniques based on remote sensing which relies on line-of-sight measurements cannot be used in many practical situations.

Using terrestrial LiDAR scans helps to identify the location, volume and mobility of rocks down the slope. Since 2012, terrestrial LiDAR and photogrammetry have been applied in White Canyon (near Lytton, Canada) in order to assess the railway ground hazards; quarterly measurements were taken with LiDAR which allowed the researchers identify the loss of blocks as small as 0.5 m^3 (Hutchinson *et al*., 2015). In another experiment in White Canyon, Kromer *et al.* (2015) observed slope deformation in the seven months preceding the collapse on June 5, 2013, with a distinct pattern of smaller rockfalls around the perimeter of the deforming block. It was concluded that LiDAR monitoring can help detect precursors to rock slope failures. Rosser *et al*. (2007) used LiDAR to identify a relatively small rockfall which occurred prior to larger slope failure in sedimentary rocks. In addition to differential monitoring of rock movement or failure over time, LiDAR can help manage and assess rockfall hazards, including kinematic stability (joint identification/ orientation), obtain rock discontinuity spacing, and assess the likely size of potentially unstable blocks (Lato *et al.*, 2012). Mobile terrestrial LiDAR equipment can collect, at traffic speed, roadside data along highways and rail lines (Lato *et al.*, 2009); Digital Elevation Maps (DEM) obtained with LiDAR data can be applied to rockfall modeling, *e.g.* to statistically evaluate potential rockfall paths and final positions.

2.7. Rockfall trajectory modeling

Because of the strong correlation between the peak amplitude of seismic signals excited by surface impacts and the kinetic energy of rock, a brief review of the concepts related to rockfall trajectory modeling will be provided.

When the resources available to minimize natural hazards are limited, a method is required to assess the best strategy for resource allocation. Before the best method of alignment protection can be chosen at a particular spot, it is important to have an estimate of the size of rocks and the manner by which they will arrive at the roadway. Design of protective structures such as a rockfall barrier requires knowing rockfall trajectory heights and kinetic energies in order to determine its strength, as well as the location of impact points and trajectory paths to determine the optimum location and dimensions of the barrier or fence (Wyllie, 2014). An adequate geological model for a slope of limited area and uniform gradient may be developed from an investigation consisting of a relatively quick and simple reconnaissance study and prediction of rockfall behaviour from backanalysis of past events or by empirical methods (Higgins and Andrew, 2012b). In a general case, a more detailed risk assessment of the rockfall area is required. The first engineering treatment on rockfall problems was completed by Ritchie (1963) based on full scale tests; since then, many numerical analyses have been designed.

Methods of modeling and prediction of rockfall trajectory, as well as available software tools, have been reviewed in a number of publications, *e.g.* by Turner and Duffy (2012), Lan *et al.* (2007), Chen *et al*. (2013), and Li and Lan (2015). The use of computer programs has become popular for creating rockfall susceptibility maps, hazard and risk maps (Chen *et al*., 2013). Many modeling programs are available to simulate rockfall behaviour, and these are widely used to design protection measures, *e.g.* reviews in Turner and Duffy (2012), Li and Lan (2015), Lambert and Nicot (2011).

Trajectories of individual rocks are computed using Newtonian mechanics, *e.g.* Wyllie (2014) discusses the application of impact mechanics theory to the behaviour of rockfalls. Rockfall simulation models can be grouped by their spatial dimensions (2D and 3D); rock shape (lumped mass, hybrid and detailed shape model); kinematics (rebound models, incorporation of sliding and rolling motion); and deterministic *vs* stochastic (Chen *et al*. 2013; Macciotta *et al*., 2014a; Gischig *et al.*, 2015)**.** Rockfall dynamics are defined by many variable factors, for instance source locations and surface roughness. Minor inaccuracies in model inputs, including the necessary simplification in modeling rock shapes or terrain maps, can lead to significant uncertainties in the modeling of trajectories (Li and Lan, 2015). Single calculations of height and energy are not adequate for rockfall protection design; instead, complexities in the modeling

that are best handled by stochastic analyses are addressed by simulating a large number of trajectories (Turner and Duffy, 2012). Li and Lan (2015) demonstrate an example of probabilistic modeling of rockfall bounce heights on the railway. Macciotta *et al*. (2014a) used Monte Carlo simulation for risk assessment of slope hazards in CP Cascade subdivision Mile 6.9 (Canada); in the same study area, Lan *et al.* (2007) used probabilistic model to assess distribution of rocks.

Probabilistic models can be calibrated with historical rockfall records. Bunce *et al*. (1997) used rock fall impact-mark mapping supplemented by documented rock fall records to establish a rock fall frequency and magnitude. Wyllie (2014) provides carefully documented data on actual rock events that can be used to calibrate modeling programs. Distribution of rock volumes can be estimated from historical records (*e.g.* Hungr *et al.*1998; Macciotta, 2015b).

Adopting extreme rockfall trajectory values generated by stochastic models for the design of protective structures is typically conservative and costly; decisions need to be made on confidence levels. Macciotta *et al*. (2014a) presented a method to calculate rockfall trajectory heights and velocities based on three-dimensional, lumped mass Monte Carlo simulations; the selected distribution fits were chosen so that they best fitted the data at the extreme upper values. The model obtained by Macciotta *et al*. (2014a) suggests that about 70% of rocks are rolling when they intersect the track at the study area.

In the following chapter a technique for computation of the SRFDS trigger threshold will be presented which utilizes the minimum peak ground velocity amplitudes obtained in SRFDS calibration tests. This approach is similar to the stochastic method used in the rockfall modeling in that a) a number of rock drop experiments needs to be carried out, and b) the system trigger threshold is computed as an extreme value. The difference is that, unlike the design of protective structures, the extreme lower values, rather than the upper ones, of the estimated peak amplitudes need to be used. Also, the SRFDS calibration tests are carried out with the minimum hazardous rock (*i.e.* 0.028 m^3) dropped from the minimum elevation that is of concern to the railway operator. It is apparent that the minimum bounce height estimated using the trajectory modeling methods should be chosen for SRFDS calibration tests.

2.8. Previous seismic rockfall detection systems

A number of experimental seismic monitoring installations which include either geophones or fibre optic cables as sensors have been deployed in North America, Europe, and Australia (Plouffe *et al.*, 2007;

Cleave *et al.*, 2009; Akkerman and Prahl, 2013; Schweigl, 2015; Hardy *et al.*, 1988; Hardy and Kimble, 1991; Collins *et al.*, 2014; personal communication). Rockfall warning systems that use geophones were discussed as far back as the early 1970s (Robb, 1971; Peckover, 1975; a review in Hardy *et al.*,1988), and the initial feasibility studies of the Seismic Rockfall Detection System (SRFDS) were carried out in the late 1980s and the early 1990s. The SRFDS uses an array of geophones in order to convert seismic signals to analog outputs which are subsequently digitized and processed by a central computer. These geophones, spaced about 10-20 m apart, are buried in the ground along the track, or installed on the rails or on the ties, and are connected to one or more data acquisition systems. The idea is that when a rock falls (or another event occurs, such as a train or vehicle passing the site, or an animal walking along the track, *etc*.) the analytical software running on the central computer will apply a set of criteria in order to determine whether a rockfall has occurred. If a hazardous rockfall has been identified, the SRFDS will send a message to the railway signaling system to display a warning signal for approaching trains. Once the rock has been cleared off the track or an inspection reveals the alarm was a false trigger, the system can be reset electronically, without requiring the signal maintainer to be on site to physically repair the system (Bunce *et al.*, 2005).

Hardy (1992) experimented with an autonomous rockfall monitoring system deployed along a highway (Hardy *et al.*, 1988; Hardy and Kimble, 1991). An array of 10 geophones was permanently installed in holes drilled at the top of the slope, and a six geophone linear array was temporarily installed in the soil along the toe region. Acoustic Emission/ Micro-seismic (AE/MS) signals were monitored over a wide range of frequencies using geophones (10 Hz-500 Hz), an accelerometer (0-2 kHz) and an AE transducer (15 kHz-45 kHz). The experiment involved sliding and falling blocks. It was concluded that the ability to detect AE/MS signals at a distance from their source is dependent on the source spectrum, the degree and frequency dependence of the associated intrinsic attenuation, the distance of the transducer from the source, and the band-width and sensitivity of the transducer and the associated monitoring system. Unwanted micro-seismic activity was found to be a major problem, including traffic noise and wind loads on trees. Two methods of preventing false triggers of the rockfall monitoring system were designed. The first one used a guard transducer (A) located upstream in the traffic flow, some distance from the highway slope being monitored by a second transducer (B). Signals from the guard transducer were used to render the rockfall monitoring system inoperative during the time that transducer (B) was activated by vehicular traffic. An obvious shortcoming of this method was that while the system was under the influence of traffic it was not capable of sensing debris falling from highway slope cuts. The second method utilized frequency discrimination to identify signals generated by falling debris and to distinguish these from signals generated by vehicular traffic; however, truck traffic sporadically triggered the system. Hardy *et*

al. (1988) concluded that future studies should consider the use of adaptive filtering, and pattern recognition.

The Railway Ground Hazard Research Program was established in Canada in the mid 1990s in an attempt to lower the risks and costs associated with train derailments (Bunce *et al.*, 2006). The RGHRP has been supported by Canada's two Class I railway operators [Canadian National Railway (CNR) and Canadian Pacific Railway (CPR)], Transport Canada, Natural Resource Canada and the University of Alberta. It has undertaken a series of investigations to identify technologies which have the potential for replacing slide fences. The applicability of seismic monitoring for the detection, interpretation, and location of hazardous rockfalls occurring along railways was initially investigated by CANMET-MMSL in the late 1990s. In 2006, CANMET summarized their findings in a report which outlined a suggested protocol for development of seismic rockfall monitoring system (Plouffe *et al.*, 2007; Lemay, 2007).

CANMET's experiments started in 1998 and involved simulated rockfalls. Empirical relationships showed the peak ground velocity (PGV) and energy values of rock-fall induced vibrations to be proportional with weight and inversely proportional with distance. Sensors installed on the rails were more sensitive to vibrations induced by dropped rocks compared to sensors installed in the ballast. In 1999, CANMET carried out field tests near Hope (BC, Canada) using rail-mounted sensors which also included analysis of records obtained during scaling. It was concluded that it might not be the heavier rock that generated the dominant signal when several rocks fell on the railroad, but rather a smaller rock with a larger energy. The third series of tests was carried out in 2006. Drop tests included hazardous and non-hazardous (below 70 kg) rocks dropped from elevations between 2.5 and 4 meters. It was concluded that by choosing appropriate levels of PGV and energy it was possible to filter out signals from non-hazardous rockfalls without missing signals from larger rocks. However, arrival times had to be used first to obtain the epicenter location and calculate sensor-to-epicenter distances. No method of automatic identification of vehicles was suggested: it was assumed that railway companies are aware of the location of their vehicles, and false alarms could be easily detected by correlating their location and time with the vehicle fleet coordinator.

In 2003, the Norges Geotekniske Institutt (Norway) carried out research similar to that of CANMET-MMSL (Cleave *et al.*, 2009). The test site is exposed to ice and rockfalls, and the new warning system was designed to replace the existing SDF. The warning system was in operation continuously for 5 years. The automatic event identification system produced a relatively small number of false positives (which was acceptable), and missed several rockfalls.

In 2007, a continuous monitoring system consisting of three geophones directly located on the rock was implemented in Austria (Schweigl, 2015). A simple pre-set threshold was used to detect events. The system displayed a high level of false alarms: most of the recorded events were ground vibrations produced by wild animals touching the plastic cables, or by thunderstorms. The experiment was terminated following repeated hardware damage caused by lightning.

Agioutantis *et al.* (2014) performed feasibility tests of a seismic rockfall monitoring system on the the assumption that the rockfall is a free fall, and observed that higher impact energies correspond to higher values for the measured peak particle velocity, and that the major factors controlling the amplitude are the impact energy and ground conditions. It was estimated that a spacing of 15–30 m is adequate to capture rockfall incidents with an impact energy above 30 J, which corresponds to a rock of 0.3 kg falling from 10 m. Collins *et al*. (2014) presents examples of two micro-seismic railway monitoring systems installed in the US, including seismograms of rockfalls and trains.

Seismic signals can be detected with sensors other than geophones. Distributed acoustic sensing (DAS) is an emerging technology which uses Rayleigh scattering in an optical fibre to detect seismic energy. DAS systems can detect seismic noise by utilizing fibre optic cables buried within the ground and connected to an optical interrogator. DAS systems have been used to provide encroachment warning along pipelines as well as to prevent theft of copper cables installed on the wayside. DAS systems installed for the purpose of rockfall monitoring are based on the same principle as described above with regard to SRFDS; however, instead of individual geophones the DAS system produces measurements at virtual sensor locations. Akkerman and Prahl (2013) describe a DAS system used for rockfall monitoring; the average rate of nuisance (non-threat) alarms is one per day, except during change of seasons when wide temperature swings result in thermal movement of the track causing 80% of the nuisance alarms. In recent years rockfall monitoring systems which use Distributed Acoustic Sensing (DAS) were installed by BNSF (Akkerman and Prahl, 2013), Queensland Rail (Australia), and Network Rail (UK) (personal communication).

2.9. Goals of this research

The Slide Detector Fence (SDF) is the most widely used technology for the detection of rockfalls along railways, but it has a number of weak points: non-hazardous rocks or animals can cause false alarms

delaying rail traffic for extended periods of time; the percentage of false alarms in the total number of SDF activations can be as high as 70%. In order to repair a broken trip wire, signal maintainers have to visit the site which could compromise their safety.

The main reason for developing and implementing a seismic rockfall monitoring technology is to provide an improvement to slide detector fences currently installed wherever rockfall hazards are considered severe. This system is expected to have a number of advantages over the existing slide fences, including:

- The SRFDS geophones would sense the rocks falling onto the track without being damaged or incapacitated by rocks, wild life, track maintenance equipment or bad weather;
- It will not miss hazardous rockfalls, unless strong ambient noise temporarily renders the system insensitive (this concern will be addressed in the following chapters);
- It should be able to discriminate rockfalls from other sources of nuisance activations and report them in real time;
- After the system has been activated, it can be reset remotely or automatically, without requiring an onsite repair. Trains will be required to proceed at Restricted Speed less frequently, and signal maintainers will be required to complete fewer repairs compared to the existing system.
- It will eliminate bottlenecks caused by prolonged SDF activations and increase the efficiency of the rail system in busy transport corridors.

This improvement could also have a positive side effect for the environment. According to Hydro Quebec[7], with the exception of pipelines, rail is the most energy-efficient method of moving freight over land, up to 3-4 times more efficient than shipping by truck in terms of energy consumption and CO_2 emission. However, consumers may still prefer trucking companies to rail when a timely delivery of shipment is important.

A number of feasibility studies of seismic rockfall detection systems have been carried out since the early 1970s. Based on the review of available literature as well as feedback from CN and CP, none of these attempts have succeeded yet, *e.g.* because the test installations were subject to strong anthropogenic noise, or were unable to correctly identify hazardous rocks. The goals of this research are:

---

[7] http://www.climatechange.ca.gov/events/2007-06-12_mac_meeting/public_comments/transport_en_2006.pdf (last checked on July 29, 2015).

- Using previous work on seismic monitoring of rockfalls, develop a method for automatic recognition of hazardous rocks falling onto railway track;
- Study ground vibrations encountered along railroads and, if necessary, design filters to remove the undesired signals;
- Develop traffic detection and other relevant algorithms in order to design an autonomous SRFDS;
- Carry out field tests and compare the performance of SDF and SRFDS in busy rail corridors.

3. Collection of Seismic Data and Identification of Hazardous Rockfalls

In this chapter, the first two goals of this research will be addressed. Firstly, we will use experimental data and previous work on seismic detection of rockfalls to develop a technique for automatic recognition of hazardous rocks falling onto railway track. We will describe the test sites, the test equipment and the data acquisition instrumentation used by Weir-Jones Engineering Consultants (WJEC) to collect experimental data. This research project grew out of the feasibility study initiated by the Railway Ground Hazard Research Program in the mid 1990s and carried out by CANMET-MMSL[8]. Following the positive results obtained by CANMET, the RGHRP invited a number of companies to express their interest in the development of a SRFDS prototype. Weir-Jones Engineering Consultants (Vancouver, Canada) was one of the companies whose proposal was approved by the RGHRG. The author joined the project at Phase 1 as a data analyst and principal developer of pattern recognition algorithms and SRFDS data processing software.

The second goal addressed in this chapter is a study of ground vibrations encountered along railways. In the previous experiments on seismic rockfall monitoring, unwanted ambient signals were found to be a major problem (*e.g.* Hardy *et al.*, 1988). The concept of an autonomous SRFDS (Chapter 4) is based on the analysis of seismic signals observed at the test sites.

3.1. Simulated rockfalls

Cruden and Varnes' (1996) definition of a rockfall highlights two stages of the phenomenon: the detachment of a rock block from a slope and the subsequent downslope movement through flying, bouncing and rolling. Micro-seismic monitoring of rock slopes allows one to detect precursory activity (cracking) as well as rockfalls (Hardy *et al.*, 1988; Hardy and Kimble, 1991; Amitrano *et al*., 2005; Senfaute *et al*., 2009; Got *et al.*, 2010; Zimmer *et al.*, 2012; Zimmer and Sitar, 2015). Though both stages

[8] (Natural Resources Canada) Canada Centre for Mineral and Energy Technology - Mining and Mineral Sciences Laboratories.

induce seismic signals, in this study we used seismic signals associated with rockfalls impacting the track area. In accordance with CANMET recommendations (Plouffe *et al.*, 2007), as well as for considerations of signal quality and protection from falling rocks, in all test installations discussed in this chapter seismic sensors were deployed under the grade within 1.0 – 2.0 m of rail track, rather than on the slope as was done in some previous studies (*e.g.* Hardy *et al.*, 1988; Hardy and Kimble, 1991).

WJEC conducted the feasibility research on the CPR rail track south of West 16th Ave in Vancouver (Phase 1) followed by field tests at CN's site near Squamish, BC (Phase 2). In 2009-2011, WJEC installed three SRFDSs in Canada, two in British Columbia and one in Quebec. The three systems have been used to collect event data and test the SRFDS data analysis algorithms. Subsequently, additional systems have been installed.

3.1.1. Phase 1. Test site in Vancouver (BC, Canada)

The purpose of the Phase 1 tests in Vancouver (BC, Canada) was to determine the number and type of geophone assemblies, as well as signal gains of the acquisition system, necessary to measure the vibrational signals produced by hazardous rockfalls. Figure 3.1 demonstrates the test site, the weight drop tripod, and the geophone assemblies installed near the track.

Figure 3.1. Photo of the drop apparatus and free-field and ballast geophones (courtesy of WJEC).

The test site

Selection of the Phase 1 test site, a 250 m section of unused CPR rail track, was motivated primarily by its proximity to the WJEC main office in Vancouver. The site was located at a busy intersection exposed to continuous ambient noise with strong transients induced by city traffic. The layout of the test site together with the associated sensor names, drop locations and placement of the geophones is shown in Figure 3.2.

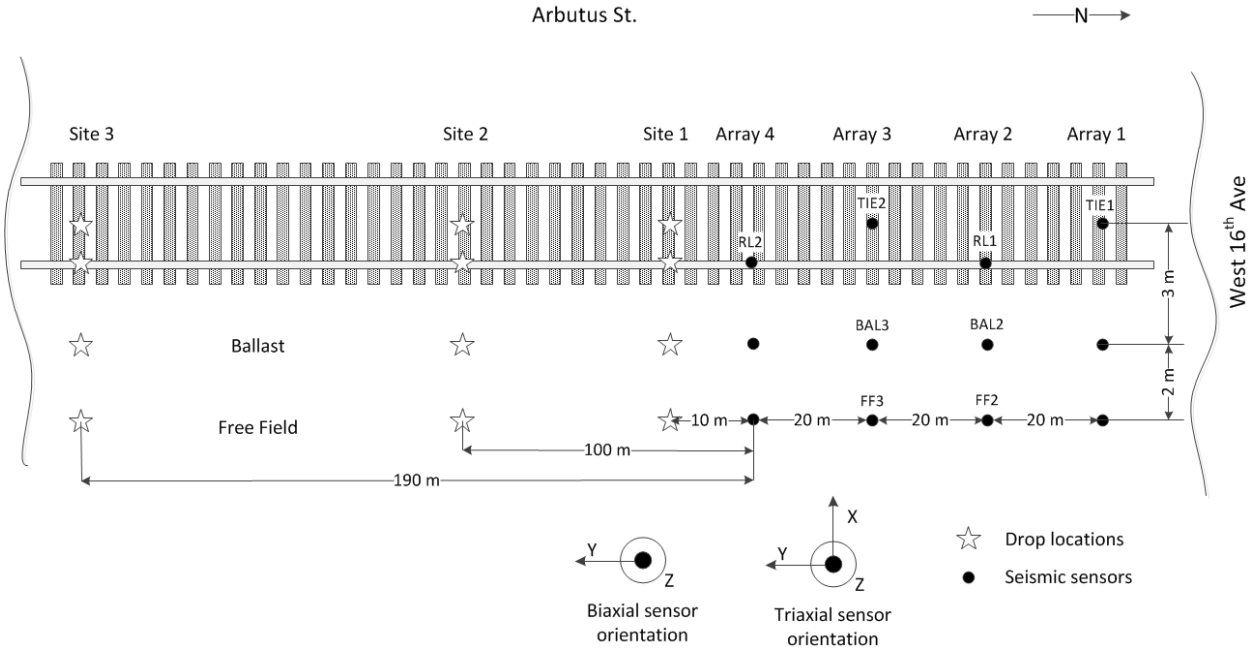

Figure 3.2. Layout of the test site at West 16th Avenue (Vancouver, Canada).

The ground conditions at the Phase 1 site differed from those at the three subsequent installations in BC (Squamish, White Canyon and Hope) in that it did not have shallow bedrock. No detailed information is available on the geological profile; however, based on the observations at two excavated construction sites within 100 meters of the test site, it consisted of at least 10 meters of glacial till. According to Turner *et al*. (1998) in this area of Vancouver till is up to 25m thick consisting of heterogenous glacial deposits of clay, silt sand and stones.

Data acquisition equipment

A total of 12 multi-element geophone sensor packages assembled by WJEC were installed at various locations along a 60 m section of track. Two 24-bit, 24 channel data acquisition systems from TerraScience Ltd were used to record seismic data, complete with a GPS antenna and a laptop PC equipped with WJEC's proprietary data acquisition software, AutoTAR™. A combined hardware/ software gain of 100 was used to amplify the geophone signals prior to converting them into binary data; a 2 kHz sampling rate was used. The geophone packages were arranged into four arrays installed 20 m apart, and oriented perpendicular to the track (Figure 3.2). In the layout diagram, the rail sensors are named "RLx", the tie sensors are named "TIEx", and the free field sensors are named "FFx". In the Vancouver/ West 16th tests, the three-component sensor's Y-axis was approximately parallel with the transverse direction of wave propagation; while the X-axis was parallel with the radial direction.

Test drops

A tripod mechanism with a winch and appropriate weights was used to simulate rockfalls (Figure 3.1) which involved dropping a weight vertically from a height of approximately 2.5 m. Two different types of weights were used to simulate rockfalls, the first was a steel cylinder weighing approximately 115kg; the second one consisted of a number of canvas sacks containing 115kg of lead shot. In the original requirement specifications, the RGHRP desired the SRFDS to be able to detect one cubic foot rock falling from the elevation of 4 meters and higher. According to CP, "a single 1 cubic foot (0.03 m^3) rock was selected because there are no recorded cases where rockfalls smaller than 1 cubic ft. are known to have sufficient energy upon impact to break a rail or be large enough to derail a train.<...> The 4 m height was used because this is the height which is generally considered the minimum height that a rockfall could originate from and still reach the near rail." (personal communication).

Since transportation of a 4 m high portable tripod mechanism presented a logistical challenge, it was decided to use a smaller tripod in combination with a heavier weight. The canvas sacks were used to simulate impacts of soft material which were expected to induce lower peak ground velocities compared to the steel cylinder. Also, in the subsequent field tests the canvas sacks were used to simulate rocks-on-ties and rocks-on-rail events because of the risk of breaking rails by dropping the steel cylinder.

The drop locations were grouped into three sets, referred to as Site 1, Site 2 and Site 3 in the site layout diagram, and located 10 m, 100 m and 190 m away from Array 4. Two additional drop locations were added to the test program, located at 40 m and 70 m away from Array 4.

The majority of data samples presented in this research are displayed in the engineering units of the velocity transducers (meters per second). The conversion factors used in this research were provided by WJEC.

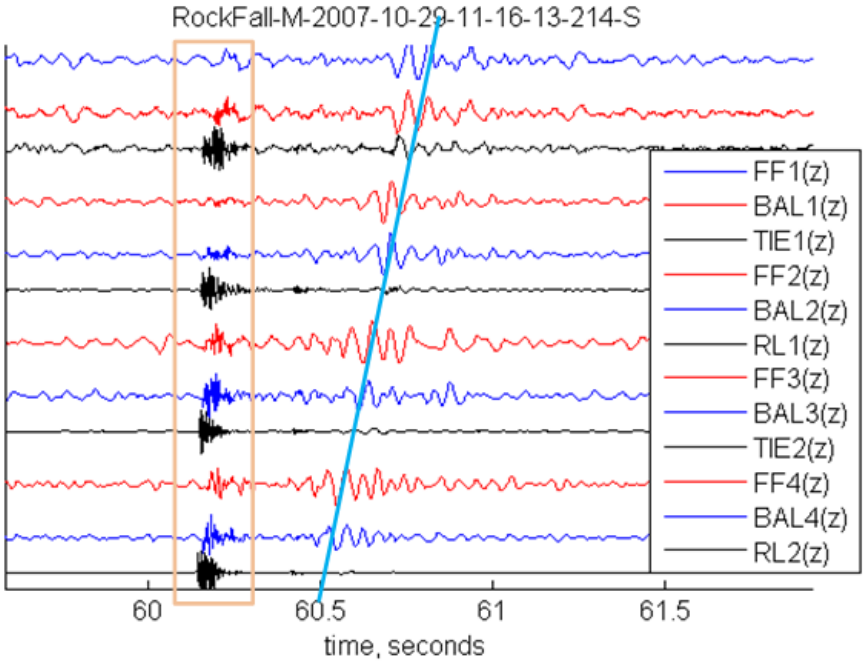

Figure 3.3. Z-components of rail and ground vibrations. The signals were induced by the 115 kg steel weight dropped onto the rail at Site 2 located 100 meters away from the geophone Array 4.

Analysis of the Phase 1 drop test data

Because of the elevated background noise at this location, the maximum detection range of surface impacts was 150 m – 200 m. However, the high gain (*i.e.* *x*100) often resulted in saturated signals when the weights were dropped within 40 m of the sensors, and for the subsequent field installations the combined gain was reduced to 2.0, which is the minimum gain level available for this model of data logger.

Analysis of vibrations induced by dropping weights on the ties and the rails demonstrated that both the rail and tie sensors detect signals whose amplitude spectrum is dominated by high frequencies (>100 Hz) and which precede the arrivals of seismic waves (Figure 3.3). These precursor signals have an estimated propagation velocity of 5 km/s which suggests that the signals were transmitted along the rail rather than through the ground since this is a reasonable approximation of the velocity of sound in steel. Peak amplitudes of the Y-axis responses of the rail sensors to the rail vibration were consistently larger than those of Z-axis, possibly because the Y- sensors were oriented along the rail and were more sensitive to longitudinal wave motion than the vertically oriented Z- sensors. The high velocity, high frequency arrivals were followed by much slower seismic waves travelling at approx. 250 m/s.

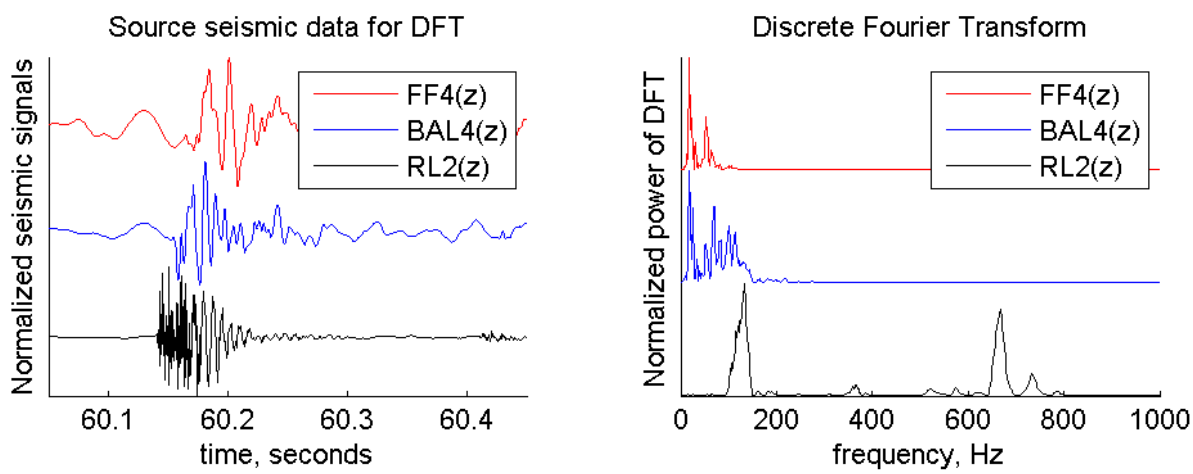

(a) (b)

Figure 3.4. (a) Z-components of rail vibrations; (b) FFT.

The seismogram in Figure 3.4(a) demonstrates that, as the sound wave propagates along the rail, it excites ground vibration in the ballast. The signal is first detected by the rail-mounted sensor (RL2); as the vibrational energy is transmitted into the ground, it is detected by the ballast sensor (BAL4) and then, with more delay, by the free-field (FF4) sensor located several meters away from the track. The response of RL2 has stronger high frequency content than BAL4 and FF4. Therefore, in the presence of multiple propagation media, automatic interpretation of ground and rail vibrations induced by falling rocks and associated multiple arrivals of vibrational energy can be challenging.

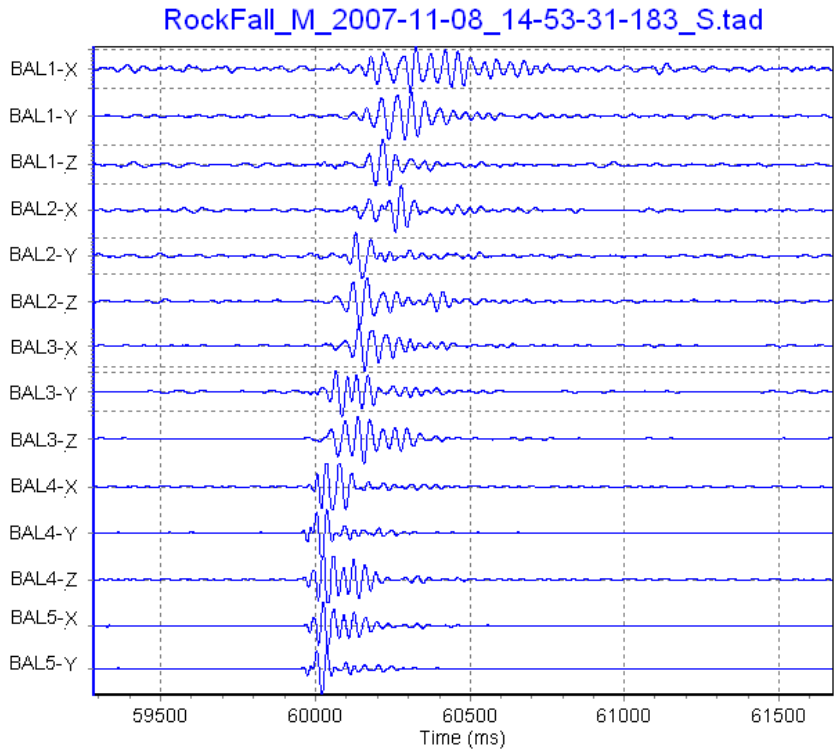

Figure 3.5. Seismic record of 115 kg of lead shot dropped from 2.5 meters elevation 10 meters outside the seismic array (drop tests in Vancouver, 2007). The wave front remains relatively narrow over the 70 m travel path. Sample polarization plots of sensor BAL-2 response are in Figure 3.6 and Figure 3.7.

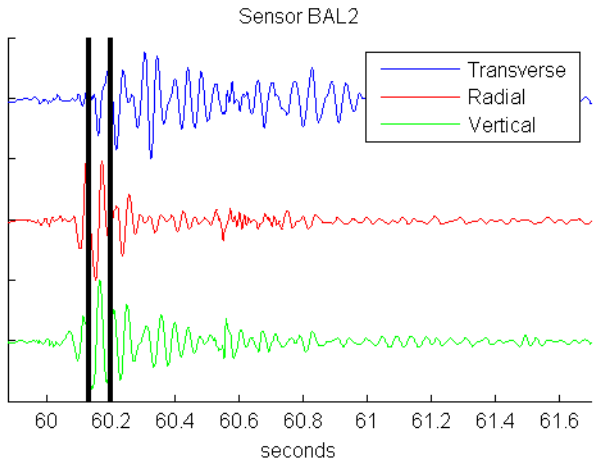

Figure 3.6. The time windows used for polarization plots of BAL-2 signals in Figure 3.7.

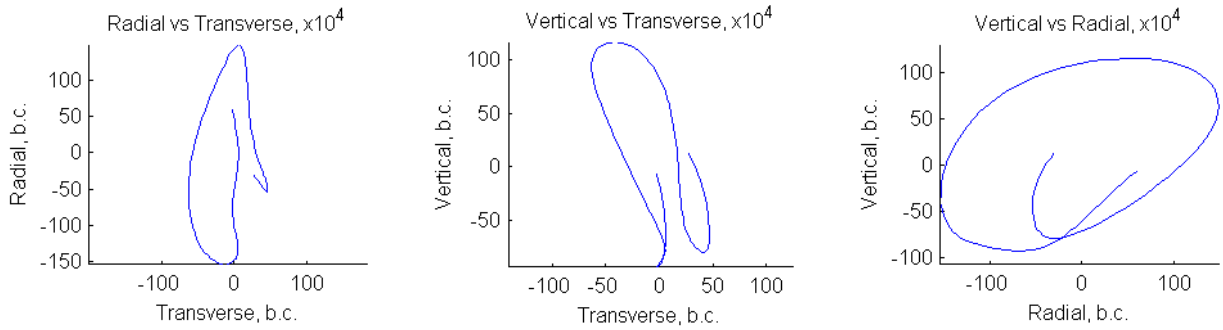

(a) (b) (c)

Figure 3.7. Polarization plots of a three-component sensor, BAL-2, response to a simulated rockfall ~30 m away. The time window is 70 milliseconds and is shown in Figure 3.6. (a) Radial *vs* transverse; the particle motion is polarized in the direction of wave propagation; (b) vertical *vs* transverse; and (c) vertical *vs* radial. These data samples are in binary counts (b.c.) generated by the A/D boards. In order to convert binary counts into the engineering units, these values must be multiplied by $3.026 * 10^{-10}$ m/s/b.c. This conversion factor is specific to GS-32CT, the type of geophone used at the test sites, the type of data logger used, as well as the gain of the data logger. The conversion factors used in this research were provided by WJEC.

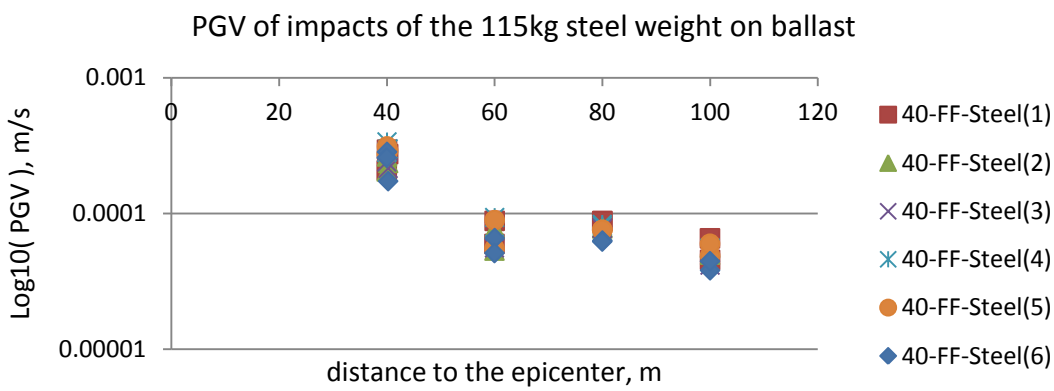

Figure 3.8. Example of PGV(z) of the ballast sensors; the seismic signals were induced by dropping the 115 kg steel weight onto the ballast from 2.5 m elevation 40 meters away from the nearest sensor. The plot demonstrates the PGV decay with distance, as well as PGV variability between tests.

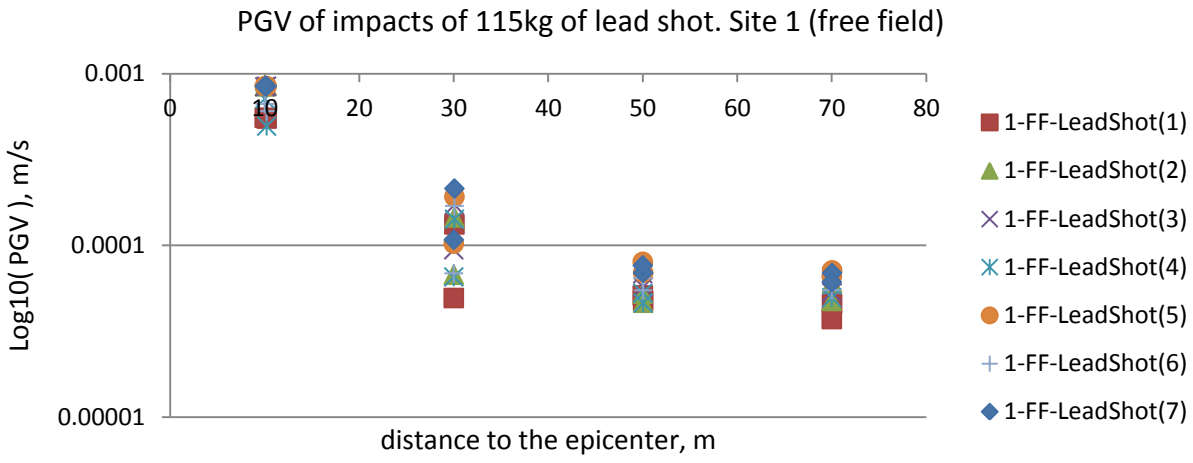

Figure 3.9. Example of PGV(z) of the ballast sensors. Ground vibration was induced by dropping 115 kg of lead shot onto the ballast from 2.5 m elevation 10 meters away from the nearest sensor.

3.1.2. Phase 2. The test site near Squamish (BC, Canada)

In early 2008, WJEC carried out a series of drop tests, referred to as Phase 2, at CN's experimental site at Squamish subdivision Mile 55.5 which is located near Squamish (BC, Canada). The 250 km long Howe Sound – Lillooet corridor is one of the two main transportation corridors in south-western British Columbia. It is occupied by BC Highway 99 (the Squamish Highway) and the former BCRail track currently operated by CN. The goals were to collect seismic records of simulated rockfalls and rail traffic, and to develop a technique for automatic recognition of rockfalls which would activate the monitoring system when hazardous rockfalls occur.

At the Squamish site, a basalt flow formation lies above the rail tracks, and movements of the vertical columns can be a source of rockfalls (Figure 3.10). The monitored area extended over 50 meters and was equipped with an electrical slide fence; no information about the ground conditions at this site was available.

Figure 3.10. Photo of the experimental site at Squamish/ Brackendale (BC, Canada) looking north (courtesy of WJEC).

Compared to the subsequent installations near Hope (BC, Canada) and in White Canyon (BC, Canada), this site was relatively uneventful, with 2-4 trains and high-rails (rail-mounted maintenance vehicles) per day, usually without stops. No track maintenance was carried out by CN during the tests except when the railway operator used a ballast tamping machine which damaged most of the rail mounted sensors while leaving the ballast sensors unscathed. The ballast tamper lifts the rails-and-ties assembly off the ground during its operation. This clearly demonstrated the susceptibility of rail mounted sensors to operational damage, and in the subsequent rockfall monitoring installations only ballast sensors were used.

Data acquisition equipment

Fifteen tri-axial sensor packages were installed in five groups approximately 14 m apart and 0.5 m below the grade (Figure 3.11). Three groups were installed on the uphill side of the tracks, the other two on the downhill side. The intent of having up- and down-slope sensors was to investigate the SRFDS sensitivity to rockfalls when the sensors and the epicenter are on the opposite sides of the rail track. Each group of sensors included one triaxial single element rail sensor ("RLx"), one triaxial single element ballast sensor ("BLx-T1"), and one triaxial three-element ballast sensor ("BLx-T3").

Seismic data were acquired using two 24-bit data loggers and stored onboard. In order not to run out of onboard storage space, the sensors installed in ballast were sampled at 500 Hz, the sensors mounted under the rails were sampled at 1 kHz. The latter resulted in under-sampling of train signals. The Squamish seismic monitoring installation was run in a continuous data acquisition mode for a few months in order to study seismic signals encountered in the SRFDS operating environment. The data files were periodically retrieved from this location by a technician. The subsequent simulated rockfalls confirmed that with a combined gain of 2.0, the 24-bit data loggers provide enough resolution to record both weak background signals and vibrations induced by rockfalls and freight trains without saturation. Ground vibration induced by the 115 kg weights dropped within 2 m of ballast sensors was recorded without clipping.

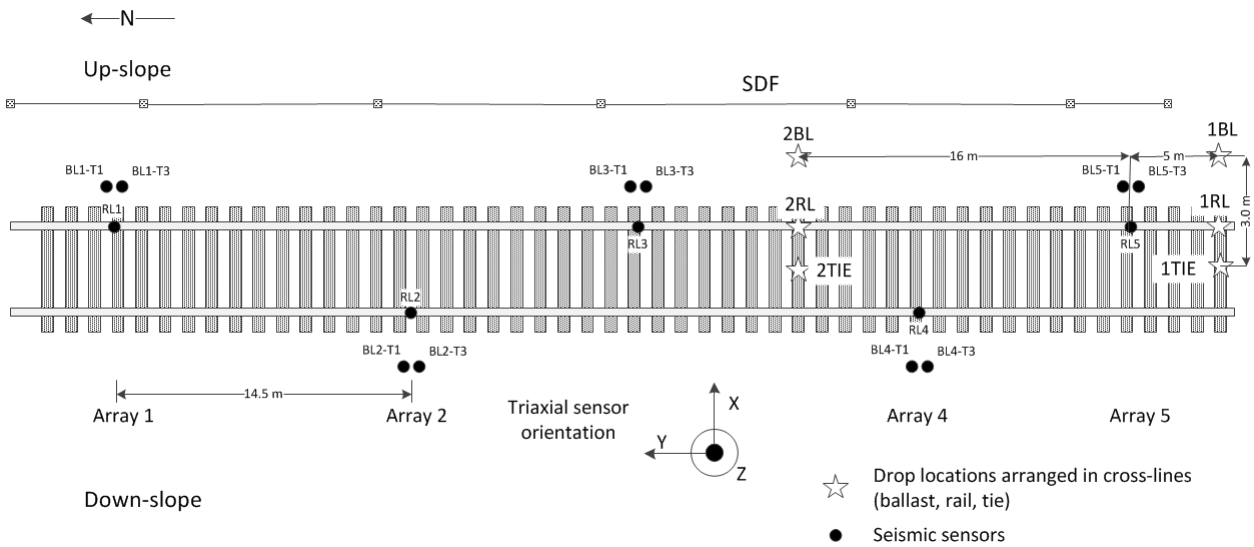

Figure 3.11. Layout of the test site near Squamish.

Test drop locations

The tripod and the drop weights were the ones designed for the Phase 1 tests. Impacts on the rails and ties were performed with a 5 kg sledgehammer and 115 kg of lead shot in order not to damage them. The weights were dropped on 0.5 m of snow as well as on dry ground; no significant difference in peak amplitudes was observed.

Compared to the Phase 1 tests which were performed in the walkaway pattern outside the geophone array, the Phase 2 drop locations were both inside and outside the sensor array which provided a more detailed picture of the PGV decay within 20 meters of the source.

Test results

An example of peak amplitude decay observed in a series of three drops at the Squamish site is shown in Figure 3.12. In the legend, "1-BL" and "1-TI" indicate drop location, including the index of the cross-line (*e.g.* "1") and whether the impact was on tie, rail or ballast. Though the plot displays consistent PGV decay trends, some variability is noticeable which can be explained by minor differences between tests in impact locations and elevations. It was concluded that the horizontal channels of the sensors did not provide much information about the ground response in addition to the output of the Z-channels; the subsequent installations in White Canyon and near Hope (both in British Columbia, Canada) used only vertically oriented uniaxial sensors.

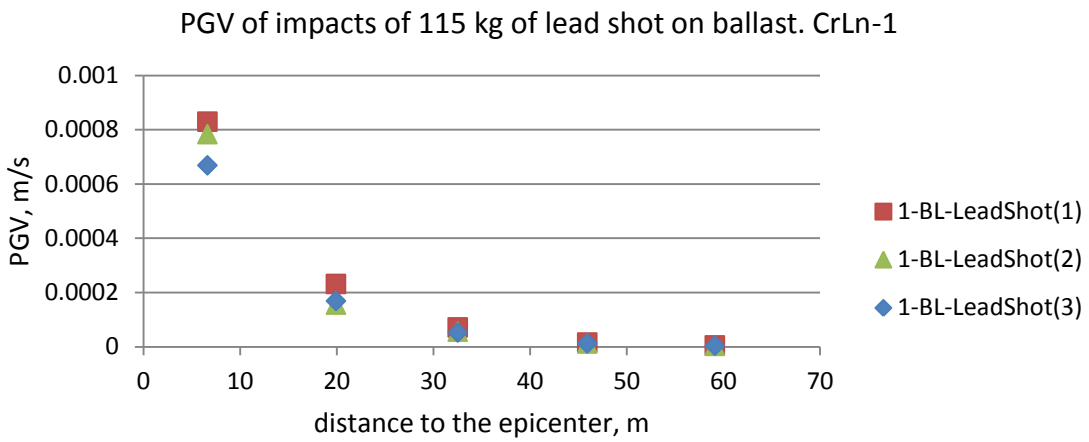

Figure 3.12. The PGV measured on Z-channels of five one-element geophone sensor packages installed in ballast. In this series of three tests, the weight was dropped on ballast at cross line #1 from the same elevation.

Data analysis

A seismogram of a test drop of the 115 kg steel cylinder from 2.5 meters elevation is shown in Figure 3.13. Compared to the Phase 1 tests, the wave duration increases with the distance due to multiple reflections and the difference in velocity between various seismic phases. Time separation between the relatively fast P and the slower Rayleigh waves is not clearly visible because of the short array length. At sensor BL-1, which is the farthest from the drop location and closest to the tunnel portal (Figure 3.10) the arrival of head wave occurs 2-3 m/s earlier than at sensor BL-2, probably because of the shallower bedrock in this area. The Rayleigh wave amplitude dominates the amplitude of the refracted P-wave

within the first 40-50 meters; however, at BL-1 the refracted wave is stronger than the surface wave, possibly due to the track curvature and inhomogeneous propagation medium.

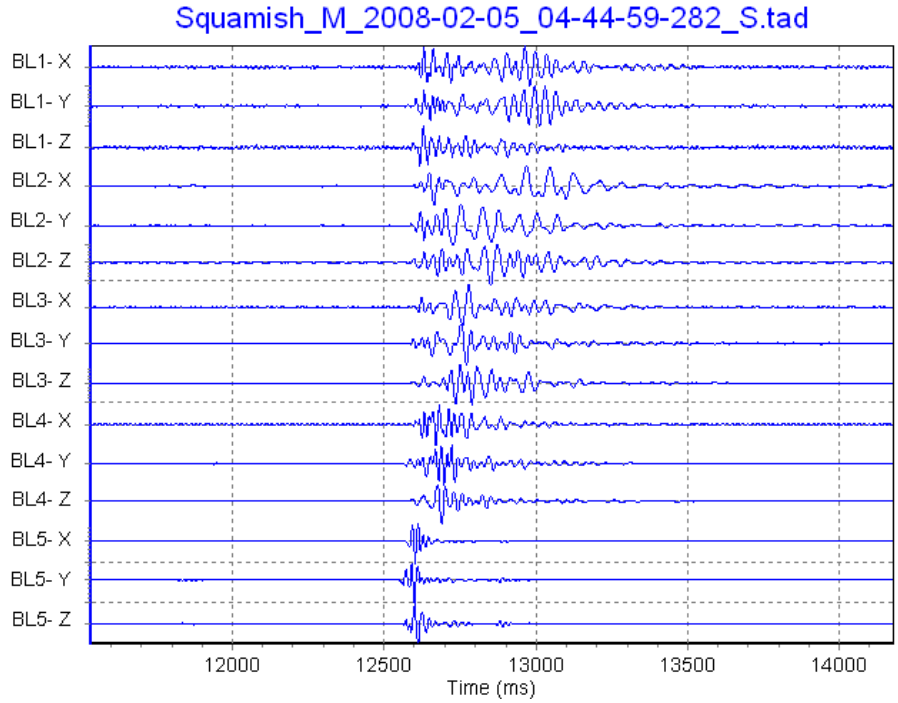

Figure 3.13. Seismic record of the 115 kg steel cylinder dropped on ballast from 2.5 meters elevation 5 m outside the Squamish seismic array (cross-line #1 in Figure 3.11) The sensors are 14.5 meters apart.

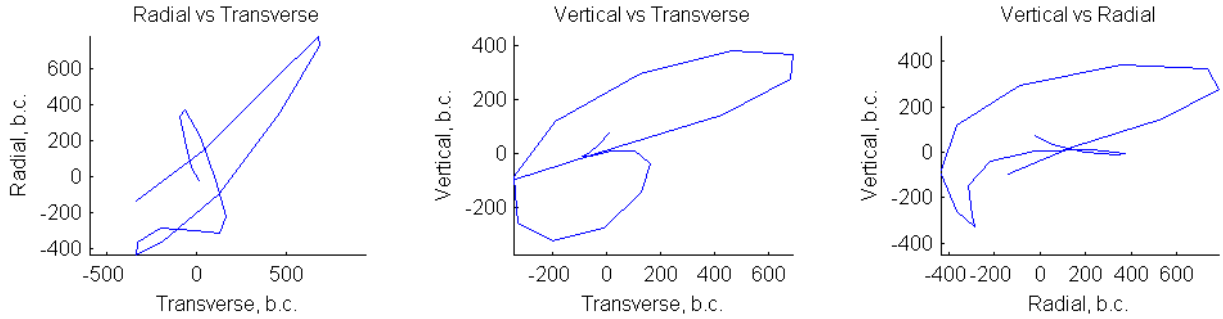

(a) (b) (c)

Figure 3.14. Polarization of a 40 ms segment of the three-component seismic record which begins after the first arrival of the seismic energy at sensors BL-1 (see Figure 3.15) located approx. 60 m from the epicentre. (a) radial *vs* transverse; (b) vertical *vs* transverse; and (c) vertical *vs* radial.

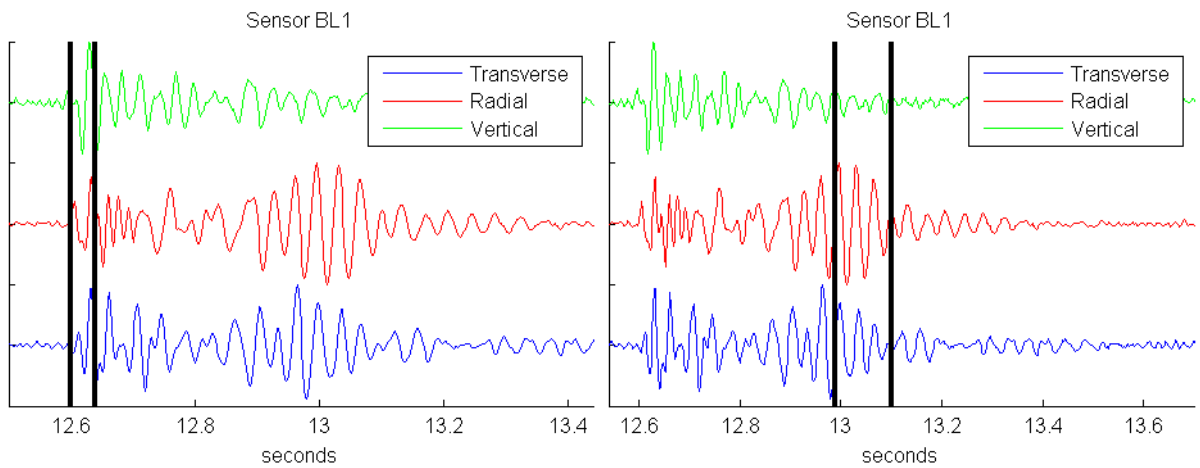

(a) (b)

Figure 3.15. The time windows used for polarization plots in Figure 3.14 and Figure 3.16. In the Squamish tests, the three-component sensor's Y-axis was parallel with the transverse direction of wave propagation; the X-axis was parallel with the radial direction.

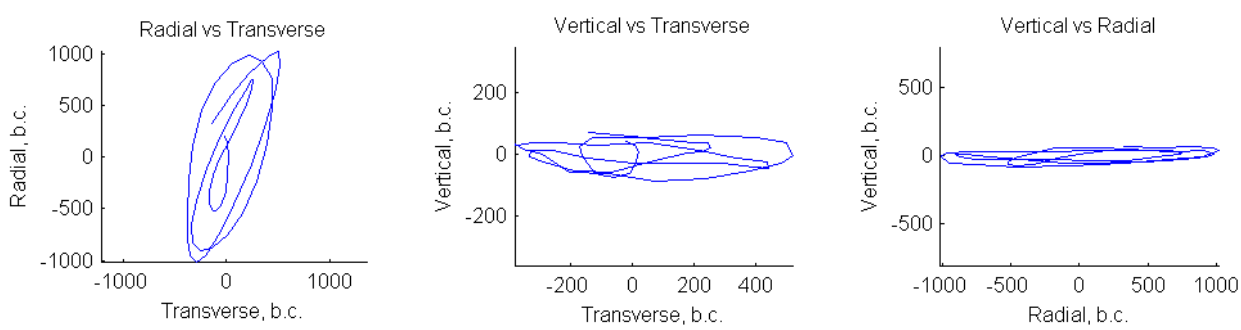

(a) (b) (c)

Figure 3.16. Polarization plots of the three-component seismic record that starts 0.4 s after the first arrival (Figure 3.15 (b)). Based on the polarization properties and arrival time of the windowed signal it contains surface waves. (a) radial *vs* transverse; (b) vertical *vs* transverse; and (c) vertical *vs* radial.

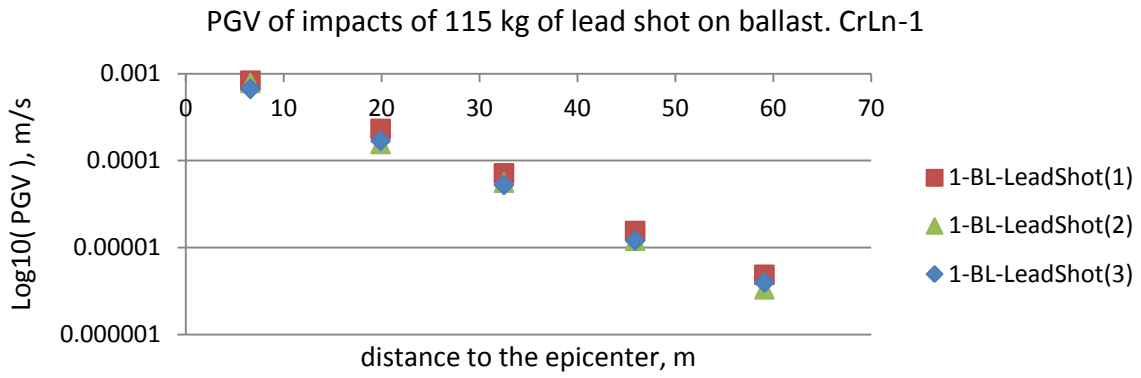

Figure 3.17. PGV(z) of ground vibration induced by dropping 115 kg of lead shot on ballast from 2.5 m elevation (cross-line #1). The PGV values are displayed in Log10 format. The PGV falls off one order of magnitude every 25 m (approx.). The sensor locations (uphill and downhill) do not appear to affect their sensitivity to the induced vibrations. Sensitivity of the velocity transducers does not appear to depend on their location, either up-hill or down-hill.

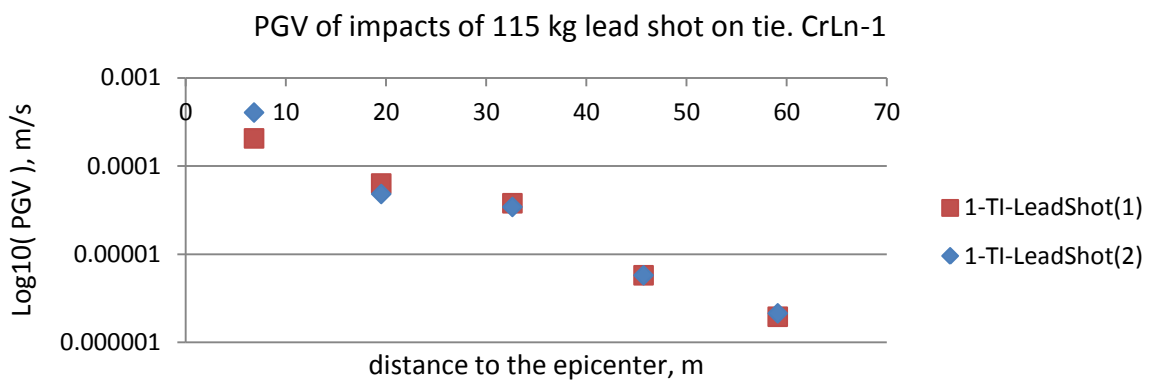

Figure 3.18. PGV(z) of ground vibration induced by dropping 115 kg of lead shot on tie from 2.5 m elevation (location 1TIE in the test layout diagram). The PGV falls off one order of magnitude every 25 m (approx.).

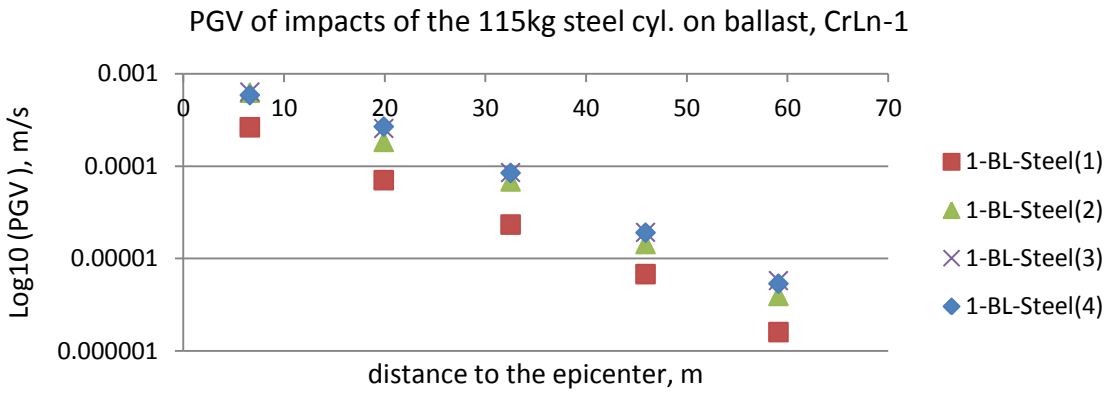

Figure 3.19. PGV(z) of ground vibration induced by dropping the 115 kg steel weight on ballast from 2.5 m elevation (location 1BT). The PGV falls off one order of magnitude every 25 m (approx.). Though the signals display noticeable variability between drops, the up-hill and down-hill sensors appear to be equally sensitive to the seismic signals.

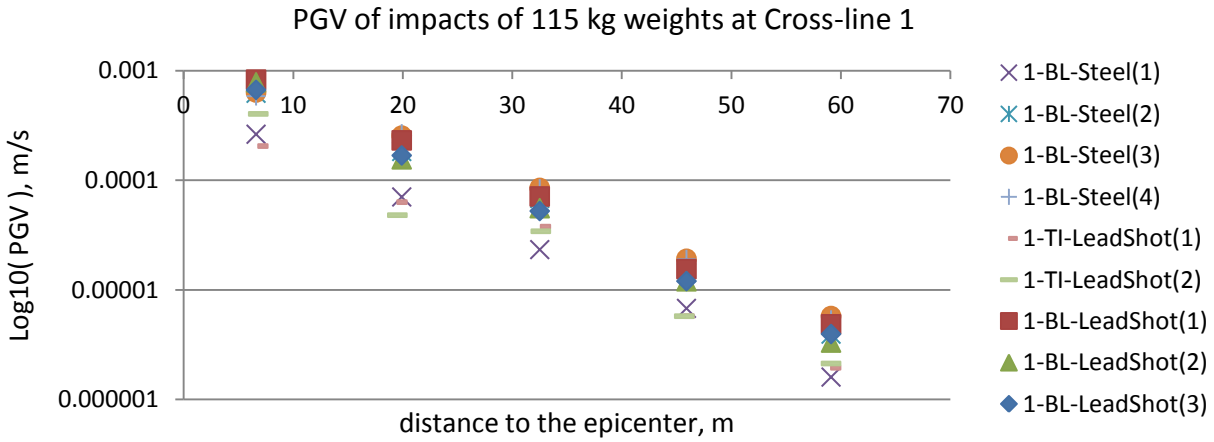

Figure 3.20. Combination of drop-on-tie and drop-on-ballast results from Figure 3.17 to Figure 3.19. The PGV falls off one order of magnitude every 25 m (approx.). Though the combined plot displays some PGV variability, the consistency PGVs generated by the same weight dropped from the same elevation is evident.

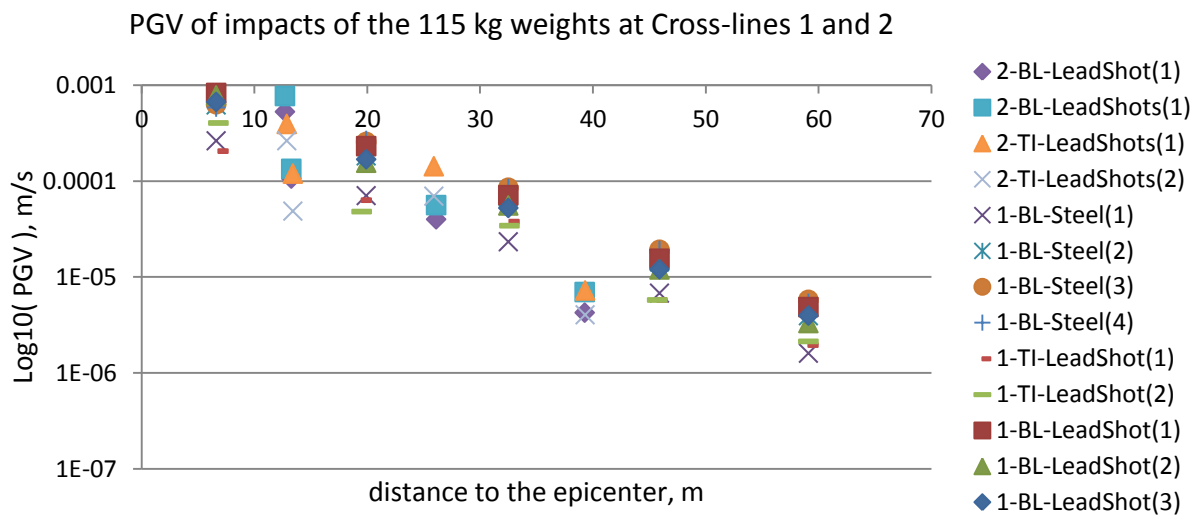

Figure 3.21. Combination of drop test results from Cross Line #1 and Cross Line #2, located approx. 22 m apart. Compared to Figure 3.20, more variability is present in the measurements, perhaps because of the differences in ground properties at the two test locations.

Summary of the Squamish tests

Based on the simulated rockfalls, the following observations can be made, assuming that dropping 115 kg from 2.5 m elevation was an adequate proxy for the original requirement of detecting $V \geq 0.028$ m^3 rocks falling from $h \geq 4$ m elevation:

- In absolute terms, the most significant drop in peak amplitude occurs within the first 5-10 meters from the epicenter, *i.e.* in the near field. The test crew tried to be as consistent as possible with the experimental setup, including the drop weight, its elevation and the tripod location; however, sometimes the recorded peak amplitudes varied by more than 100% between test drops;

- Drops on ties tended to induce weaker peak amplitudes compared to drops on ballast, perhaps because, in the latter case, the impact energy was concentrated in a smaller area. The base of the steel cylinder was approx. 0.13 m^2, while the rail tie area is estimated 0.3 m^2. Therefore, the SRFDS should apply the threshold obtained for the weaker ground response which, at this site, was observed in drops on ties. Given the variability of peak amplitudes between test drops, the worst case scenario field conditions should be used for calibration tests;

- Seismic records of ground vibrations induced by rockfalls and recorded with ballast geophones can be quite complex and seem to include direct and refracted body waves, surface waves, as well as rail vibrations. Extracting travel time information from seismograms automatically will be prone to errors, especially if several surface impacts occur within a short time window (*e.g.* seismogram of a rockfall in Figure 3.63). Therefore, it was decided to avoid using the arrival times and epicenter location techniques for identification of hazardous rockfalls;

- Consistent log-linear amplitude decay was observed in all experiments, approximately one order of magnitude every ~25-30 meters. Because the maximum epicentral distance was about 60 m, amplitude measurements beyond that distance were not available;

- Location of sensors up/down slope did not have observable effect on their sensitivity to surface impacts.

Table 3.1. The trigger threshold used for automatic differentiation between hazardous and non-hazardous rocks (Chapter 5). The threshold values were obtained by dropping 115 kg of lead shot on ties at the Squamish test site.

Distance to epicenter	PGV, m/s	Log10 (PGV), m/s
5	0.0002117932	-3.674088082
18.3	0.0000484099	-4.315066139
31.6	0.0000347946	-4.458488282
45	0.0000057487	-5.240432521

In July 2008, the Squamish test installation underwent field trials which involved rock scalers dislodging a few rocks from the basaltic formation 15-20 meters above the track (Figure 3.22(b)). In Figure 3.22(a) the peak amplitudes of ground vibrations generated by falling rocks are compared to the trigger threshold obtained with the 115 kg weight. During the scaling exercise, no detailed records were kept about the timing of surface impacts, nor about the sizes of dislodged rocks. The rocks varied in size; some were hazardous (*i.e.* approx. 0.028 m^3), some were not. The rocks fell on the ground predominantly in the vicinity of sensor BL-2. In Figure 3.22(a) the peak amplitudes decrease faster in the direction of sensor BL-1 located near the tunnel portal (Figure 3.10), and the peak ground velocity of many seismic signals observed at BL-1 is below the PGV threshold. In the absence of detailed information about the ground conditions at the site, this observation was attributed to the fact that the track, which is straight between

sensors BL-4 and BL-5, begins to curve north of BL-4 (Figure 3.10, Figure 3.11). Based on this hypothesis, a one-sided (*i.e.* truncated) PGV threshold model was later used for the SRFDS test installation at the Hope site where the rail track has two relatively sharp curves (Chapter 5). The maximum epicentral distance of the one-sided PGV model is 45 m, rather than 90 m (Table 3.1). With regard to sensors BL-2 to BL-5, the majority of peak amplitudes in Figure 3.22(a) exceed the PGV threshold. In one case the peak amplitude fell below the threshold at BL-5 (Figure 3.22 (a)) which was probably due to a non-hazardous rock.

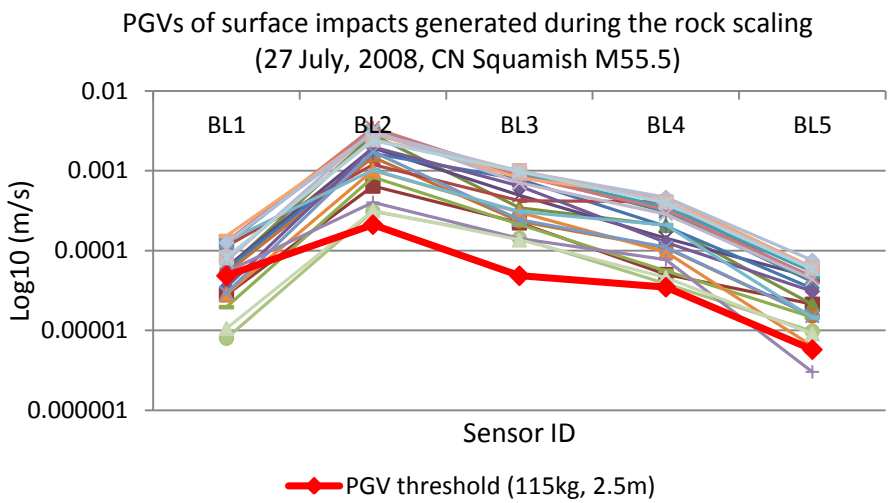

(a)

(b)

Figure 3.22. (a) Comparison of the PGV threshold obtained with the 115 kg weight and the peak amplitudes of the first 21 surface impacts generated by the rocks dislodged by the scalers at the Squamish site. (b) The scaling of the columnar basalt at the test site near Squamish. The threshold PGV (red line) is plotted on the assumption that the epicenter is at sensor BL-2.

In the early stage of the research project, the system's ability to identify rail traffic signals was not prioritized: it was expected that the monitoring system would follow the CANMET/ RGHRP suggestion and interact with the RTC (Rail Traffic Controller) in order to ascertain the presence of trains and maintenance vehicles at the site (Plouffe *et al.*, 2007). The event analysis software was programmed to use the signal duration to differentiate between rocks and trains, assuming that the train and high-rail signals are longer than rockfalls. This decision was based on the preliminary analysis of rail traffic signals available at the time: the seismic signals generated by the simulated rockfalls lasted only 1-2 s and were significantly shorter than the high-rail and, especially, train signals. Once sample records of

naturally occurring rockfalls were obtained later in this study, which oftentimes lasted for more than 10-15 s, the duration-based approach turned out to be over-simplified and prone to failures, and it was abandoned in favour of matched filtering.

3.2. Field tests

The Fraser–Thompson corridor is one of the two main transportation corridors in south-western British Columbia. It extends from Vancouver to Kamloops via Hope and Lytton for a distance of 420 km and is utilized by CP and CN main lines. One of the two sites where a SRFDS prototype was tested is located near Hope, British Columbia at CP Cascade subdivision, Mile 38.9; the other was deployed in White Canyon near Lytton. Slope movements occurring in this area have been studied previously, *e.g.* Hungr *et al*. (1999) reported the frequency and magnitude (expressed in rock volume) of rockfalls along CP Rail route in the Fraser-Thompson corridor. They concluded that high-frequency, low-magnitude slope movements in this area show spatial clustering due to slope geometry and geological factors, and that rockfall frequency depends on the slope stabilization measures. Quantitative risk assessment of hazards related to rockfalls within CP Cascade subdivision Mile 2.0 to Mile 15.0 as a function of spatial and volumetric distribution was analyzed by Macciotta *et al.* (2015b). Based on CP historical records available for the study area, in approx. 52% of event records, the slope movement involved 0.3 to 2.0 m^3 of material.

3.2.1. The SRFDS test site in White Canyon (BC, Canada)

CN's core mainline within British Columbia, known as the BC South Line, is routed along the banks of the Thompson River from Kamloops to Lytton, and along the Fraser River from Lytton into Vancouver. East of Lytton, it passes through a section of the Thompson River Valley called White Canyon, which is characterized by extensively altered metasediments which have undergone significant weathering (Figure 3.23). These rock formations on the north side of the track are a source of frequent rockfalls which make the White Canyon area one of the most problematic sections of the nationwide network of railway lines (Hutchinson *et al.*, 2015). Much of the material that tumbles down is gravel and small cobbles (Carlson, 2010); however, occasionally (twice per year on the average, according to CN) larger volumes of material

fall, which pose a risk of derailment for passing trains. Some of the rockfalls that occurred within the area of White Canyon instrumented with geophones are illustrated in Appendix E. Although the SDF installed in White Canyon protects trains from rockfalls effectively, it is frequently activated under conditions that do not pose a hazard to trains. Rocks of non-threatening size, or animals activate the system up to several times a week, requiring trains to proceed at Restricted Speed (about 10 km/h) because the sharp curves around cliffs, tunnels and rock sheds in the area do not permit long sight lines. As required by the Canadian Rail Operating Rules, a train proceeding at Restricted Speed must be prepared to stop within half the range of vision (Carlson, 2010). During the rainy season and in the spring when snow begins to melt, the build-up of rock fragments occurs at a higher rate, increasing the number of SDF activations that are due to non-hazardous causes.

Figure 3.23. View of the Thomson River Canyon between M94.4 rock shed and M94.0 tunnel portal.

Traditional geo-hazard modeling techniques, developed for mining engineering and highway cuts, evaluate the regional and site-specific settings to obtain a probabilistic assessment of overall rockfall risk, often with a high degree of success (Bunce *et al.*, 1997; Abott *et al.*, 1998). When such techniques are applied to White Canyon, most of the area is identified as being high hazard, a result that is not practical for rockfall prediction (Carlson, 2010). For example, in 2012-2013 three major rockfalls occurred in White Canyon outside the existing rock sheds (*e.g.* Figure 3.61, Figure E.11). Given that the cost of

installing rock sheds or building tunnels along the entire CN mainline within White Canyon would be prohibitive, other stabilization and protection measures are used. In areas where the continued risk of rockfalls exists and/or the effects of a derailment are potentially higher (such as when the track is in close proximity to the river) SDFs are also installed.

(a) (b)

Figure 3.24. Track maintenance can generate ground vibration whose seismic signature is indiscernible from rockslides (courtesy of WJEC).

This site is accessible only by high-rail vehicles from the Lasha service yard west of the site. According to CN, the Lasha Slide Fence between miles 93.1 and 94.7, called Fence B, is activated for an average of 2,300 hrs/year, this is 23.3% of the annual total (Carlson, 2010). For the most part, these prolonged activations are false alarms due to wire breakage when there are no rocks visible on the track, as well as delays to repair due to traffic volume and poor site conditions (because of darkness, poor weather, *etc.*) which results in the maintenance crews being unable to work.

CN geotechnical engineers are investigating the potential benefits of using rockfall warning technologies other than the SDF. In 1998, a prototype of the Electromagnetic Field Disturbance (EMFD) Rockfall Detection System was installed along Fence B. The experiment was not successful because the system showed a high rate of random triggering (Brackett, 2002); at the time CN used a 0.04 m^3 rock to test the prototype. A number of landslide monitoring studies have been carried out in this part of White Canyon (*e.g.*Gauthier *et al.*, 2012a; Gauthier *et al.*, 2012b; Kromer *et al.*, 2015), as well as the Thompson River valley using LiDAR, GPS, InSAR, piezometers, inclinometers and optic fibre (*e.g.* Eshraghian *et al.*, 2007; Eshraghian *et al.*, 2008; Macciotta *et al.*, 2014b; Bobrowsky *et al*., 2014).

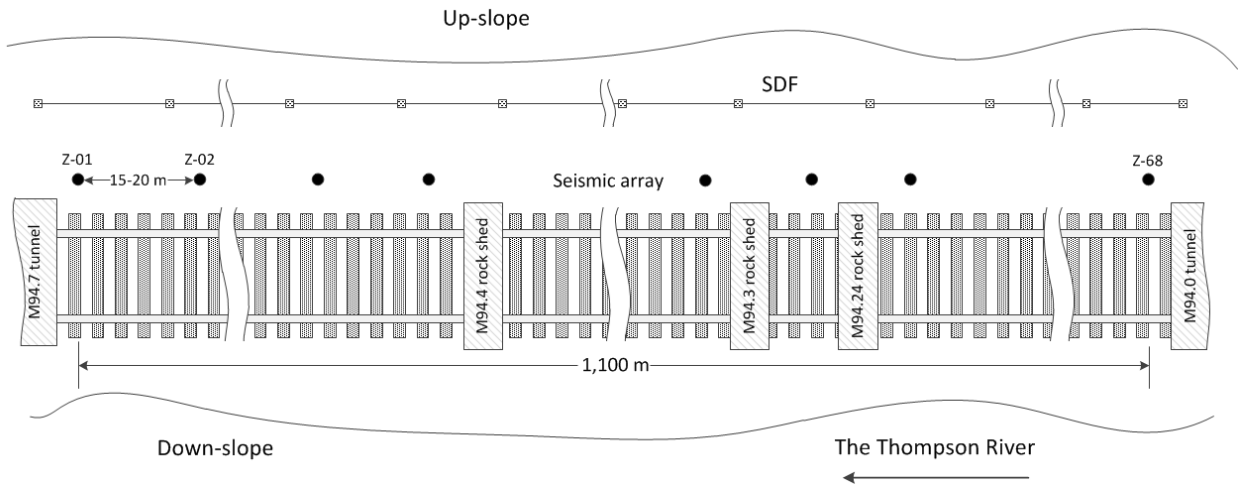

Figure 3.25. Layout of the seismic monitoring test site in White Canyon.

Data acquisition equipment

In 2009-2010, WJEC instrumented the uphill side of CN's rail track, along Fence B, with 68 single channel vertical geophones, spaced 15-20 meters apart (Figure 3.25). A plan view of the geophone array is in Figure 3.44. Though there exist three separate cables on the track's up-slope side, for geomechanical reasons this was the preferred location for the geophone array. The amount of electro-magnetic interference (EMI) noise at this location was not known at the time when the first group of 32 sensors was deployed. This resulted in the installation of unshielded sensors cables which are widely used in geophysical exploration. Such cables are much more susceptible to EMI than the shielded ones. In the data samples used in this research the sensors are numbered Z-01 to Z-68, west to east starting at Mile 94.70 tunnel. Though the installation crew tried to deploy geophones as consistently as possible, there are some fluctuations in the sensors' vertical and lateral distances with respect to the rail track (Figure 3.26).

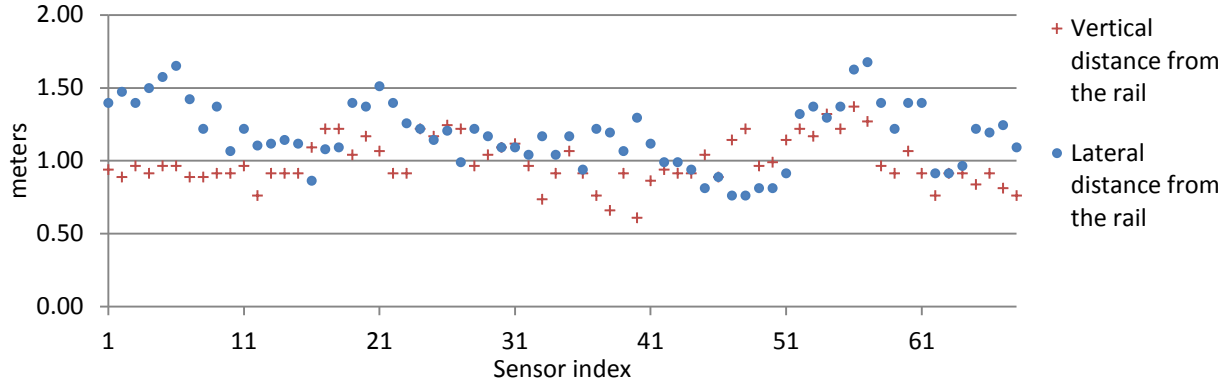

Figure 3.26. Elevations and lateral distances of the geophones with respect to the upslope rail.

In early 2009, a temporary digital camera complete with an infra-red illuminator was added to the seismic monitoring system and synchronized with the data acquisition software: every time a seismic event was detected, a digital photo of the site was taken. This allowed a correct interpretation of seismic signals that looked ambiguous on the seismograms, for instance ones generated by track maintenance and stationary trains (Figure 3.24 (a)).

Being 1,100 m long, the White Canyon site which is located at CN Ashcroft Subdivision Mile 94.5 is significantly larger than the one at Squamish. Due to the on-going slope sloughing and the proximity of the CP line on the opposite bank of the Thompson River, the White Canyon site is subject to a variety of anthropogenic seismic signals (Figure 3.24). Continuous sloughing means that maintenance crews need to visit the area periodically to clean up debris. It also experiences a high volume of rail traffic, 24 trains a day on average including frequent train stops.

Data collection and analysis

Detailed evaluation of ground response to simulated rockfalls similar to that near Squamish was not performed at this site. Instead, research efforts were focused mainly on collection, analysis and classification of anthropogenic and naturally occurring seismic events in order to develop an automatic monitoring system.

Before the first version of the SRFDS/Data Analysis module became available in late 2010, AutoTAR™ was used to obtain samples of seismic events. AutoTAR™ has basic event detection capabilities based on the STA/LTA algorithm that can be configured for individual channels as well as combined into array triggers. Seismic records of the events detected by AutoTAR™ were automatically stored on a hard disk drive and subsequently downloaded over the Internet for in-depth investigation. In this manner, typical seismic events occurring in the instrumented section of White Canyon were identified.

Figure 3.27. Photo of the study area in White Canyon. Site view looking east from the Mile 94.4 rock shed with cobble-size rocks on the track.

In the early stages of the White Canyon project, the system activation threshold was set relatively low for the system evaluation and event detection purposes which resulted in many false positives induced by non-hazardous rocks, *e.g.* Figure 3.27. After the first year of field tests, the importance of identification of slow and stationary trains became obvious because trains stop in this area several times a week.

Activations of the slide detector fence (SDF)

At the White Canyon site, the railway operator provided a contact closure (a device that detects the open or closed status of a circuit) that indicates the SDF status. Activations of the Lasha SDF (Fence B) were

monitored using a digital relay connected to the Main PC. A software tool was developed in this study which was continuously checking the status of the SDF output line. The incidences and timing of SDF activations and deactivations were recorded in a log file, and used to compare the performance of the two rockfall warning systems.

Track occupancy signal

CN provided a contact closure called Track Occupancy that indicates the presence of a train. Time-stamped Track Occupancy signals were logged in the same manner as the SDF activations, and used to count trains slowed-down by SDF activations. The block (an electrically isolated part of rail track) monitored by the contact closure only partially overlaps the seismic array; thus, the track occupancy signal available at the White Canyon site cannot be used to reliably locate a train in order to ignore the associated ground vibration. The track occupancy system does not report the presence of high-rails because their wheels are electrically isolated and do not close the electric circuit.

3.2.2. The SRFDS test site near Hope (BC, Canada)

The site is located east of Hope, BC on the north bank of Fraser River in CP Cascade subdivision commencing at Mile 038.90. While the White Canyon SRFDS is frequently subject to ground vibration related to track maintenance, the Hope site is relatively quiet. Though as many trains pass the Hope site daily (24 trains on the average), train stops are less frequent here compared to the White Canyon site. In the past, two SRFDS prototypes were installed at the Hope site including the CANMET's temporary installation (all seismic sensors were mounted on the rails) and a system designed by an undisclosed engineering company contracted by the RGHRP (sensors were installed in the ballast).

Figure 3.28. This photo shows the study area at CP Cascade M038.90 site looking west from the instrumentation enclosure. The rock slope is near-vertical in this part of the CP Cascade subdivision.

In 2011, a seismic array was installed at Mile 038.90 of CP Cascade Subdivision alongside 360 meters of existing electrical fence (Figure 3.28, Figure 3.29). Hazardous rockfalls are rare at this location compared to the White Canyon site (according to one estimate, 2-4 per month), however, nuisance rock and ice falls break slide fence wires several times a year (Figure 3.30, Table 5.3, Table 5.4). According to the study of Macciotta *et al.* (2011) who reported the distribution of rockfalls along CP Cascade subdivision, this area is one of the most active within the subdivision because a steep cut was required here to accommodate the railway alignment.

Feedback from the field is important for validation of the rockfall alarms generated by the SRFDS in real time; it helps one to learn more about the site conditions and improves the overall reliability of the system. Three sources of such feedback have been used in this study:

- Site visits. Given the remoteness of the SRFDS installations, regular visits are not possible. In the course of this project, the test sites were visited only a few times per year, whereas events of interest occur up to several times a week;
- Field reports from S&C maintainers. If a maintainer visits the site to repair a broken slide fence wire, he may (or may not) have time to photograph the rocks(s). The field reports available for analysis were irregular and somewhat subjective since it was not always possible to identify the

rock that caused the alarm, especially in the areas where rockfall activity is on-going. These reports are summarized in Appendix E and Appendix D.

- Web cameras.

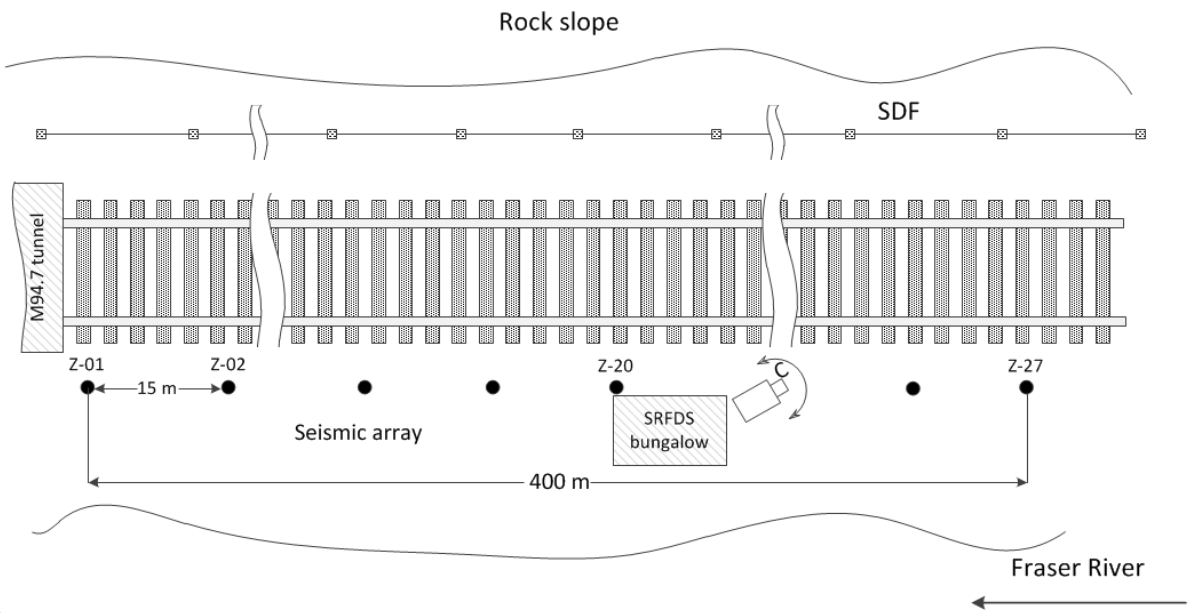

(a)

(b)

Figure 3.29. (a) Layout of the SRFDS test site near Hope. (b) Plan view of the as-built sensor array; the seismic sensors follow the track curvature.

A significant advantage of the Hope site as the SRFDS evaluation tool is that it is the only operational site in this research project equipped with a web camera[9]. Another important feature of the Hope test site is that the rock face here is near-vertical along the entire span of the seismic array. Thus, rocks tend to fall

[9] As of August, 2015. Subsequently cameras have been installed on new SRFDS systems in Quebec, BC, and Washington State.

onto the rail track in a manner consistent with the assumptions on which the Squamish drop tests were based. The rail track has two relatively sharp curves, one beginning near Z-06, another near Z-20. The web camera is located near Z-20; sensors Z-01 to Z-05 are within the web camera's blind spot.

Figure 3.30. Photo of the area in the middle of the CASC 038.90 SDF.

Subgrade

Figure 3.31 shows the ground surface (which could be rock, fill, *etc*.) that existed at the time when the CP railway was built in the late 19th century. The broken line follows the change of grade for the rail track. When the excess rock was blasted off, troughs were filled with rocks and debris. The drawing illustrates the inhomogeneous ground conditions at this site, including significant, up to several meters, fluctuation of the bedrock depth along the 360 m seismic array. Because of these factors, instead of attempting to model the site velocity profile, a statistical approach was adapted in this research towards modeling the ground vibrations generated by rockfalls.

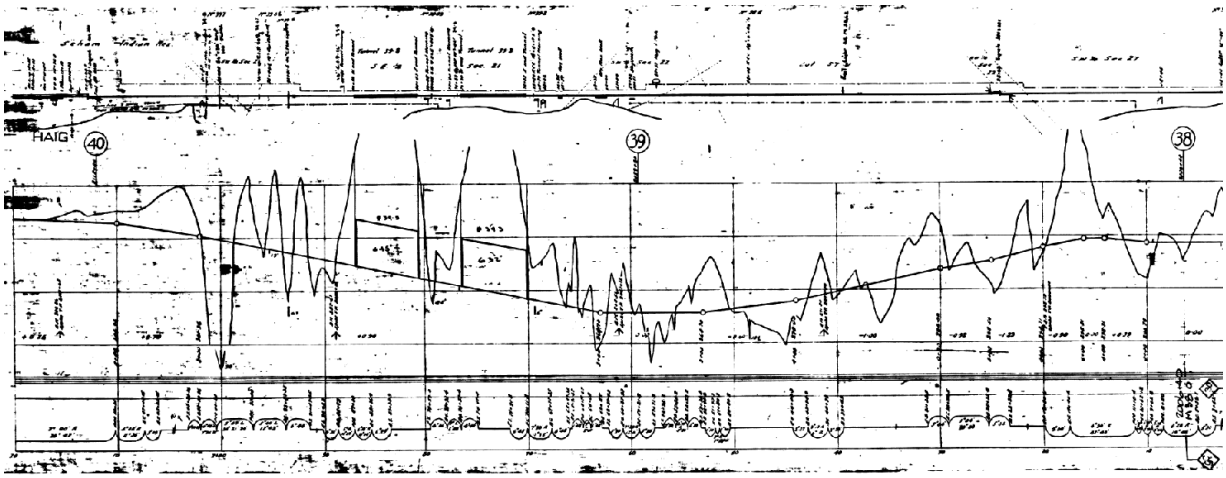

Figure 3.31. A copy of the drawing of track profile survey near CP CASC 038.90, XIX c. (courtesy of Canadian Pacific Railway).

Data collection

The Hope SRFDS includes 27 vertical geophones spaced 15 m apart deployed along the down-slope side of the track. Sensor elevations are shown in Figure 3.32.

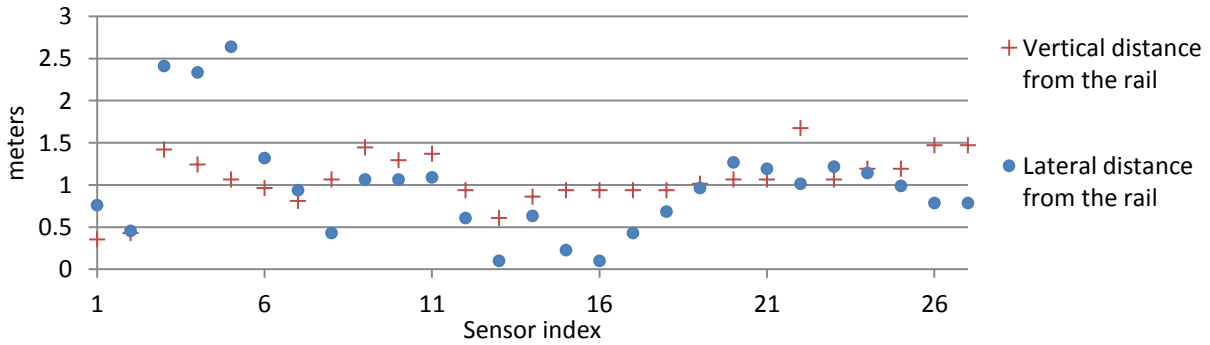

Figure 3.32. Elevations and lateral distances of the seismic sensors with respect to the down-slope rail.

Between December 2011 and mid-2015, the Hope SRFDS processed seismic data in real time in the same way as it was performed in White Canyon. When a seismic signal was detected that met the trigger criteria, the SRFDS emailed a notification including the event time, location, peak amplitude, and the

number of triggered sensors. The Hope SRFDS recorded the timing of SDF activations for subsequent comparison of the SRFDS and the SDF based on the number of train delays. Field tests stopped after a hardware failure in 2015.

3.2.4. The SRFDS test site near La Tuque (Quebec, Canada)

This site is located at CN St-Maurice Subdivision Mile 7.4, about 15 km north-west of the town of La Tuque (Quebec, Canada). As of October 2015 the La Tuque SRFDS was dormant due to damage to the data logger caused by lightning strikes. The system consists of nine vertically oriented geophones installed 15 m apart along the up-slope side of the track, and two wheel detectors extending about 20 m past each end of the geophone string. While the system was operational it recorded useful data samples of ambient seismic signals (*e.g.* Figure 3.79).

Figure 3.33. Study area at CN's St-Maurice Sub Mile 7.4 looking north (courtesy of CN).

3.2.3. Ground vibrations induced by naturally occurring rockfalls

Seismic records of naturally occurring rockfalls are shown in Figure 3.34 - Figure 3.36. In Figure 3.34, in addition to the seismic waves, high frequency rail vibration can be seen propagating at ~5,000 m/s. The

wave duration increases with the distance, probably due to the time separation of body and surface waves, and the effects of layered, inhomogeneous medium. Since the ground vibration dies out before the time separation between the body and surface waves becomes evident, seismic phases appear continuous and can be a superposition of body and surface waves.

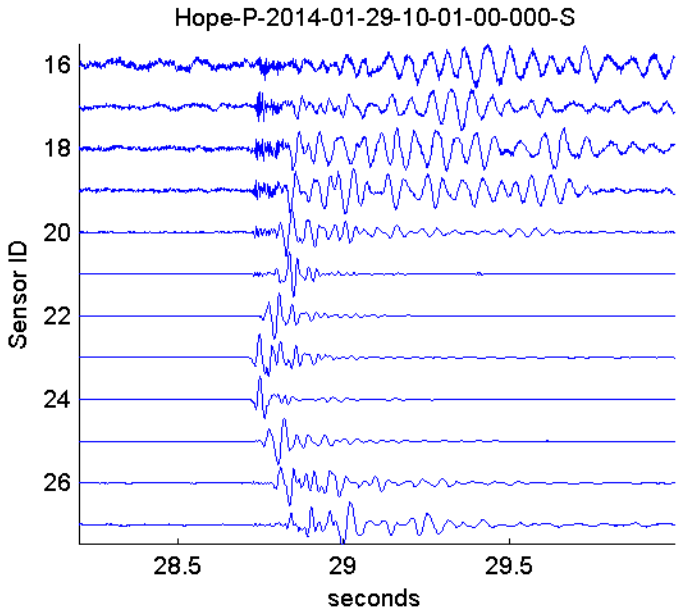

Figure 3.34. Response of the Hope seismic array to a natural rockfall. In addition to the seismic waves, high frequency rail vibration which propagates at ~5,000 m/s can be seen in the seismogram at 28.750 s (sensors Z-16 to Z-21).

In Figure 3.34, the slower phase is dominated by lower frequencies, and its velocity is 120 m/s (estimated); this appears to be the Rayleigh wave. The much faster wave that travels at 2,200 m/s (estimated) can be the refracted P-wave propagating in the bedrock. The amplitudes of P-wave and Rayleigh wave drop off asymmetrically with respect to the impact location, probably because of the ground conditions and site topography (track shoulder is approx. 6-7 m wide, and there are steep curves near Z-20 and Z-06). However, this could also be due to the radiation pattern; this analysis of rockfall signals is based on the assumption that rocks have essentially a vertical trajectory. Also, though the Rayleigh wave exceeds the P-wave amplitude within 40-50 meters of the impact location, it quickly dies out beyond that distance. In addition to the site topography, a possible explanation for this is the variations in the depth of bedrock as well as an inhomogeneous medium which consists of gravel, sand, large boulders *etc*. An example of ground vibration induced by a rockfall in White Canyon is in Figure 3.36.

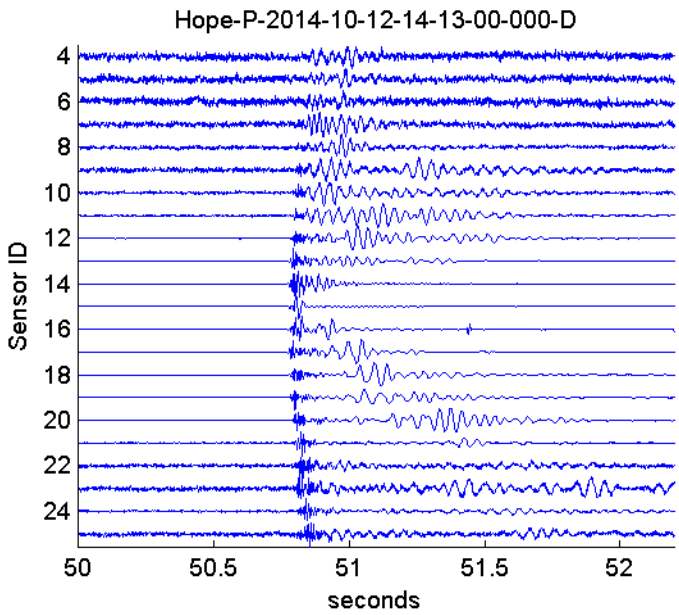

Figure 3.35. Response of the Hope seismic array to a natural rockfall at 50.750 s. The waveforms are asymmetric with respect to the epicenter sensor Z-15. The amplitude of the high velocity, high frequency signal, apparently caused by rail vibration, falls off at a higher rate west of Z-15 (sensors Z-04 to Z-14) compared to the opposite direction (Z-16 to Z-25).

The following observations can be made about the seismic signals induced by natural rockfalls. The vibration energy propagates in several media, including the rails, bedrock and ballast, along different paths and at different velocities. In the Hope seismograms, head wave arrivals were observed that occurred earlier at the sensors located farther away from the impact location, which is similar to the observations about simulated rockfalls at the Squamish test site. These sensors are located closer to the tunnel portals, which suggests that the bedrock is shallower under these sensors. Contrary to theoretical predictions, the Rayleigh wave amplitude does not necessarily dominate P-waves in the far field, possibly because of the site topography and inhomogeneous near-surface propagation medium.

Summarizing the analysis of seismograms of simulated and natural rockfalls, it should be noted that automatic identification of individual seismic phases induced by surface impacts, including arrival times and impact location, can be challenging and, if attempted, would be prone to error. Therefore, it was decided not to calculate rockfall location in real time; instead, an approach with the intention of detecting hazardous rocks has been adapted that is based only on the analysis of peak amplitudes.

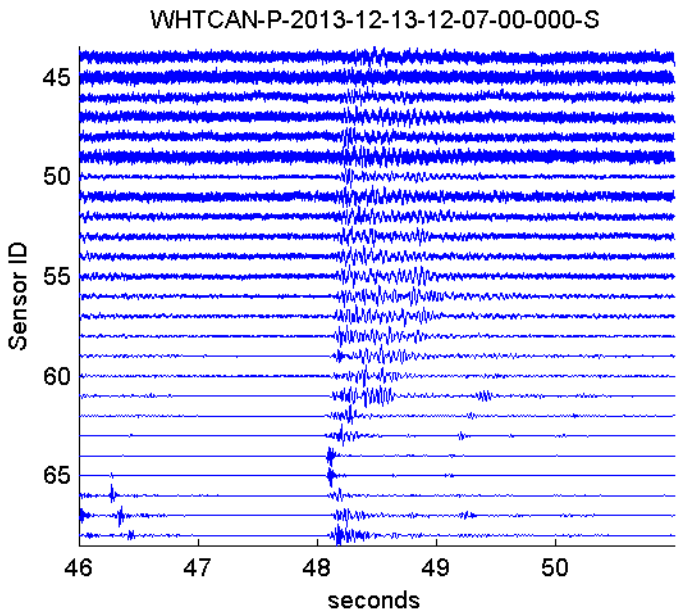

Figure 3.36. Ground response to a rock impact (the White Canyon SRFDS). The ground vibration was detected 250 m away from the impact location; the wave duration increased with the distance, probably because of the time separation between the body and surface waves. The first arrivals at >50 m distance from the epicenter occur at ~1,200 m/s and appear to be related to the body waves propagating in bedrock.

3.3. Identification of hazardous rocks

The system calibration procedure described below is based on the assumption that of two rocks dropped from the same height, the heavier one will generate stronger ground vibration, provided that the ground conditions are the same in both cases. For example, in the Squamish experiments, the amplitude of ground vibration induced by the 5 kg sledge hammer dropped onto a tie decayed below the system noise level within 45 m from the epicenter. Ground vibration induced by 115 kg of lead shot dropped on ballast was detectable at least 60 m from the epicenter (Figure 3.37). For comparison, the trace marked "05Jun2013 rockfall" contains PGV induced by the June 5, 2013 rockfall in White Canyon which covered 100 meters of rail track (Figure 3.63); the associated ground vibration was detected by the geophones 0.5 km east and west from the epicenter.

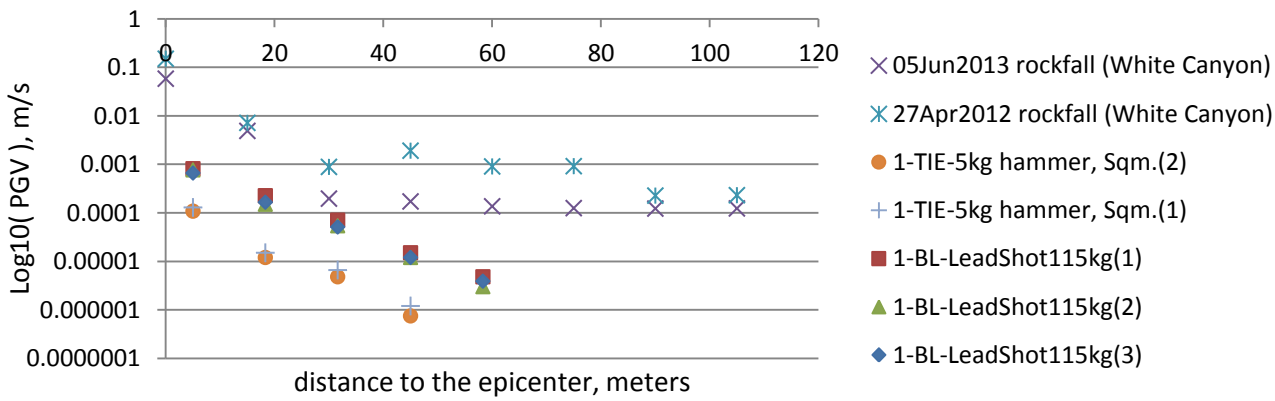

Figure 3.37. Comparison of peak amplitudes: the June 5, 2012 and the April 27, 2012 rockfalls (White Canyon); 115 kg of lead shot dropped on ballast from 2.5 m elevation (Squamish); and a 5 kg sledge hammer dropped on a tie (Squamish).

The plot in Figure 3.37 demonstrates that the PGVs induced by the sledgehammer are consistently below the PGV induced by the 115 kg weight. Therefore, if the PGV decay relationship obtained for the 115 kg weight were used as the trigger threshold, the rockfall monitoring system would be triggered by the rockfall, and it would ignore the sledgehammer event as insignificant. The system calibration concept is depicted in Figure 3.38, where it is assumed that the same PGV *vs* source distance relationship applies to all locations along the seismic array. After a number of drop tests, the empirical threshold $\boldsymbol{PGV^T(d)}$ is obtained as a function of distance d between the impact location and the sensor. In Figure 3.38, the segments of polyline interpolate the minimal PGVs observed at each sensor S-01, S-02, and so on. Thus,

$\boldsymbol{PGV^T}(d)$ can be used to calculate threshold value at an arbitrary distance d between the sensor and the rockfall epicenter. It is further assumed that if the system is calibrated with the minimum-size hazardous rock (0.028m^3), bigger rocks that fall from the same minimum elevation or higher will induce ground vibration with larger PGVs. Several test drops involving the same minimum weight and elevation have to be performed along the rail track to confirm uniform (one-dimensional) response of the geophone array to the excitations. If the ground response turns out to be dependent on the drop and/or sensor location, the threshold model will depend on the drop location (x,y) as well as the sensor location $\{S(x), S(y)\}$, *i.e.* $\boldsymbol{PGV^T}(S, x, y)$. In this case the system calibration procedure will have to involve multiple test drops along the geophone array.

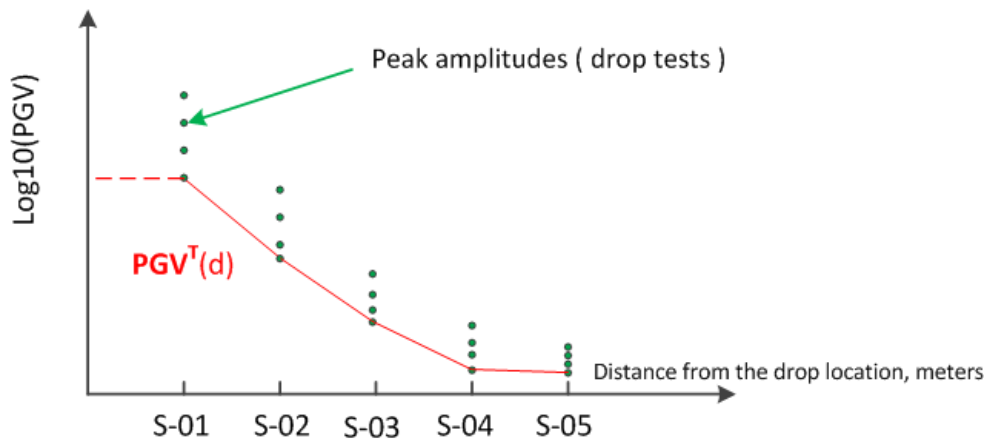

Figure 3.38. The threshold PGV model, $\boldsymbol{PGV^T}(d)$, is obtained in a series of drop tests. The polyline describes the PGV threshold as a function of epicentral distance.

For processing seismic data in real time, a time window of specific length Δt is used to scan the data channels for network triggers, *e.g.* Δt = 2 s (Figure 3.39). For each time interval $(t;\ t+\Delta t)$ and each sensor S_i (where $i=1, ..., N$ is the sensor index) $PGV(S_i)$ are computed and compared to the system activation threshold $\boldsymbol{PGV^T}(d)$. Figure 3.40 demonstrates the grid search procedure which locates all potential rockfall epicenters $H^j(x,y)$**.** Between every pair of sensors, $(S_i; S_{i+1})$ 2D grid is computed using specific steps Δx and Δy, for instance Δx=1 m and Δy=1 m. For every point on the grid, $H^j(x,y)$**,** epicentral distances $d^j_i = d(\ H^j(x,y), S_i\ )$ between and H^j and sensors $\{S_i, i=1,..,N\}$ are calculated. Then, $\{\ d^j_i\ \}$ are used to obtain the threshold PGVs, $\boldsymbol{PGV^T}(d^j_i)$, $i = 1, ..., N$.

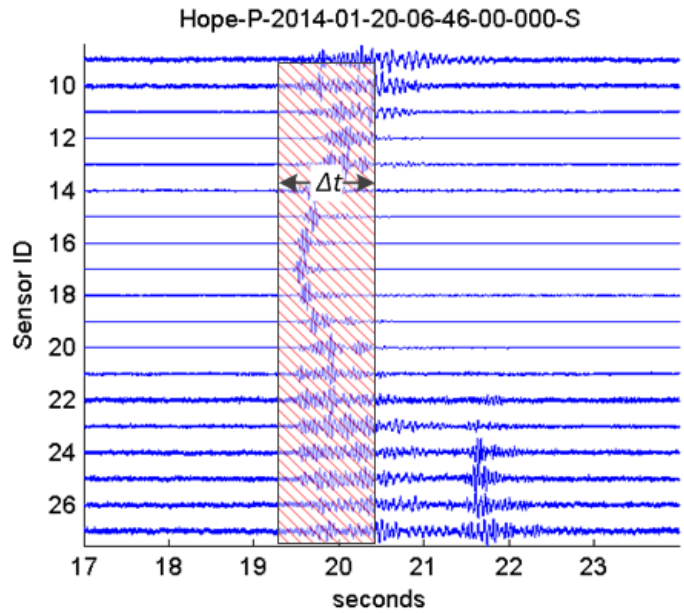

Figure 3.39. A moving time window is used to detect an array trigger in real time.

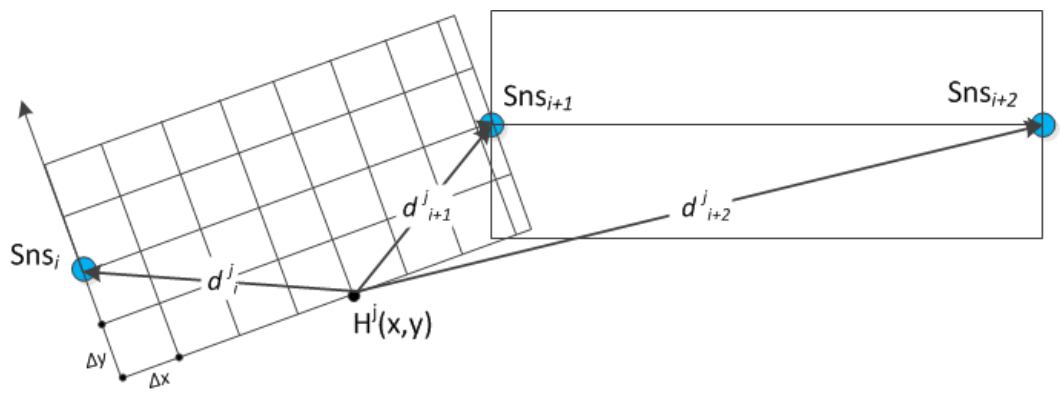

Figure 3.40. Illustration of the 2D grid search procedure used to compute epicentral distances $H^j(x,y)$.

In order for the system to trigger, the measured peak ground amplitudes $PGV(S_i)$ must exceed all computed amplitudes $\boldsymbol{PGV}^T(d_i^j)$, $i=1, ..., N$ at some location $H^j(x,y)$ (Figure 3.41):

$$PGV(S_i) \geq \boldsymbol{PGV}^T(d_i^j),\ i = 1, ..., N$$

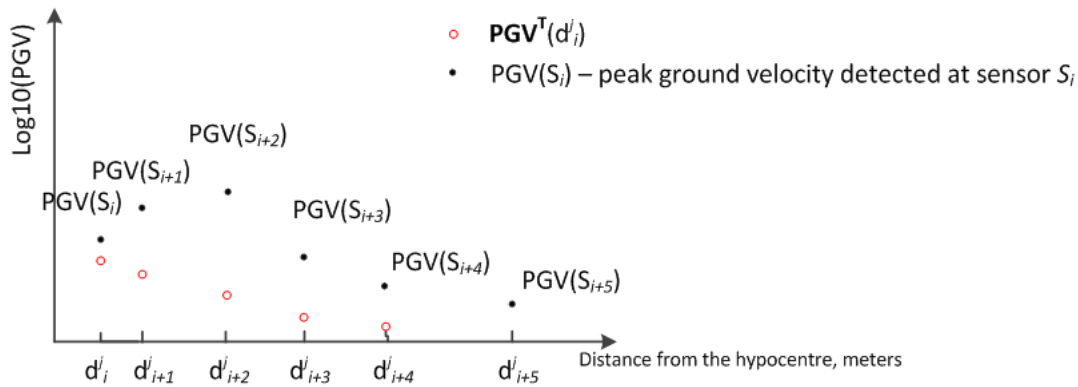

Figure 3.41. Comparison of the measured PGVs and $\boldsymbol{PGV^T}(d^j_i)$ computed for a hypothetical location $H^j(x,y)$. In this example, all measured PGVs exceed the threshold.

If a rockfall involves rock(s) larger than 0.028 m^3, a number of locations $H^j(x,y)$ along the sensor array can pass the threshold test (Figure 3.37, Figure 3.42). To illustrate this, in Figure 3.43 and Figure 3.44 the PGV threshold obtained in the series of tests at the site near Squamish is compared to the PGVs of some of the largest rockfalls recorded in White Canyon.

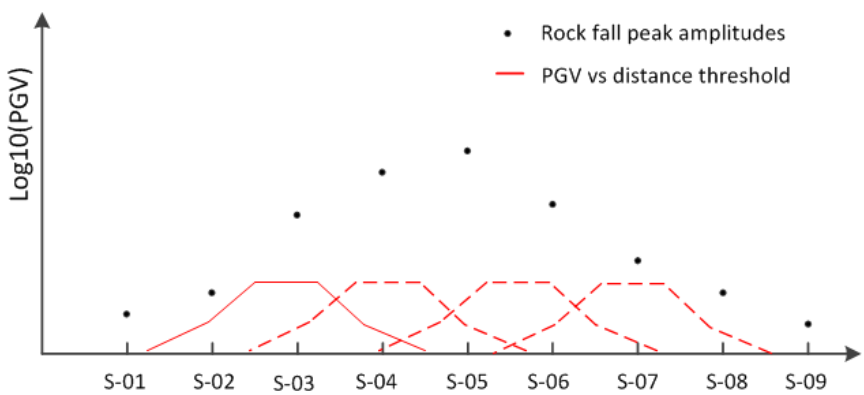

Figure 3.42. A number of locations along the sensor array can pass the threshold test.

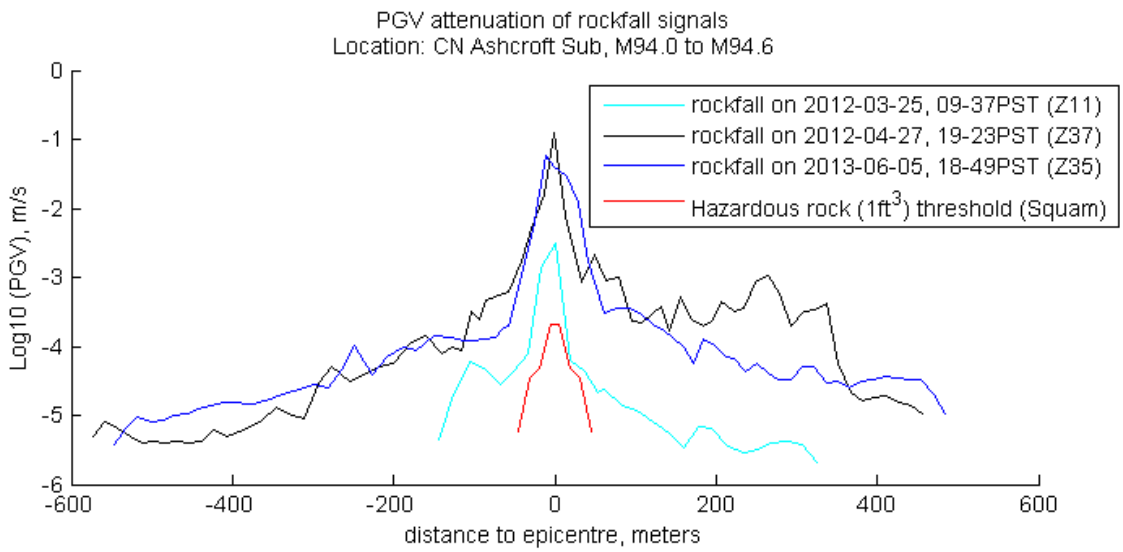

Figure 3.43. PGVs obtained from seismic records of the three largest rockfalls recorded in White Canyon in 2012-2013. The rockfall PGVs are compared to the trigger threshold (the red polyline) used for automatic detection of hazardous rocks. In Figure 3.44, the locations within the geophone array are plotted where the peak amplitudes of seismic signals generated by the June 5, 2013 rockfall exceeded the trigger threshold.

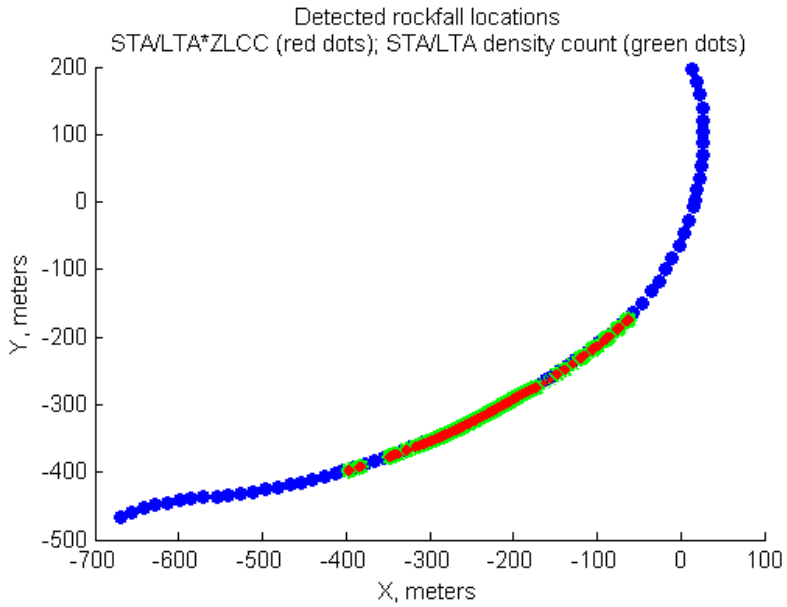

Figure 3.44. Locations within the White Canyon geophone array where the PGV of the June 5, 2013 rockfall passed the threshold test. The locations of 68 geophones are marked with blue dots; the rockfall epicenters that satisfy the trigger criteria are marked with green and red dots. The rockfall pattern recognition algorithms will be discussed in Chapter 4.

3.4. Case study: calibration of a 400 m rockfall monitoring array

The following case study describes a preliminary site characterization and as-built system calibration tests at a site in Eastern Quebec (Canada) where a 400 m long / 27 geophone seismic rockfall monitoring array was going to be deployed. Weir-Jones Engineering who performed the tests preferred not to disclose details about the site location, and it will be referred to as the SRFDS-EQ. The site is protected with a mechanical slide detector fence which the railway operator found inadequate for the task. No information about the ground condition at this site is available. The first, preliminary set of rock drop tests was performed using surface geophones temporarily installed on metal spikes. After a permanent sensor array was installed it was calibrated in another series of drop tests.

3.4.1. Preliminary site tests using temporary geophones

One of the goals of the preliminary test was to investigate the consistency of the peak amplitudes of ground vibrations induced by surface impacts of the same energy. The second goal was to confirm that, with the planned distance between the sensors (15 meters) the seismic array will be able to detect hazardous rocks.

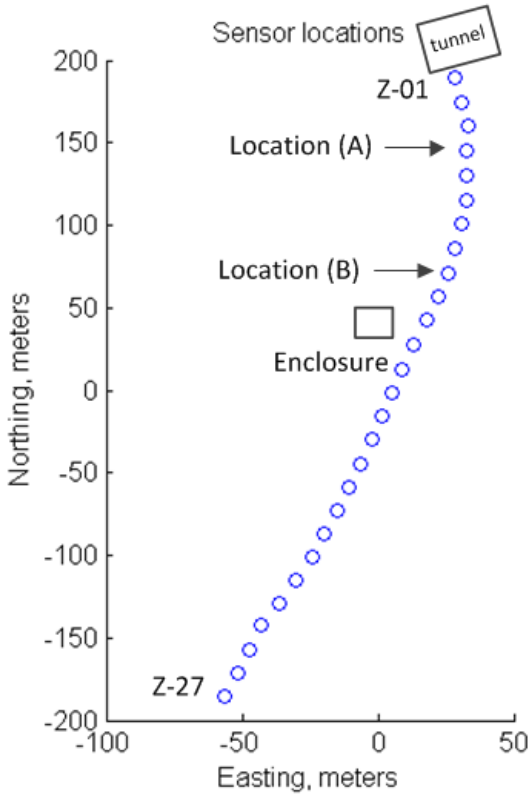

Figure 3.45. Schematic layout of the permanent seismic array and test locations with respect to the tunnel (*not to scale*).

The test locations

Two locations were selected randomly for the comparison tests (Figure 3.45): the high-rail mounting area (a timber grade crossing) which in this case study will be referred to as location (A); and location (B) where an instrumentation enclosure was installed a few weeks before the tests. Location (A) had been used by high-rail and heavy construction equipment and the ground here looked well compacted; whereas area (B) near the enclosure had been built-up with soil and fresh ballast several weeks before the tests to provide a foundation for the enclosure, and it did not bear signs of treatment by soil compaction equipment. The high-rail mounting area is about 30 meters south of a tunnel portal; the enclosure is about 180 meters south of the portal.

Data acquisition equipment

For the preliminary tests, a 24-bit battery-powered data logger manufactured by TSL (Terrascience Systems Ltd, Vancouver, Canada) was utilized, together with six vertical velocity transducers

(geophones) from OYO Geospace GS-11D (4.5Hz corner frequency, 4000Ω coil resistance, and 18.2 KΩ damping resistor for 70% damping, intrinsic sensitivity ~2.1 V/in/sec). The geophones were equipped with ~10 cm spikes to allow them to be vertically mounted in the ballast.

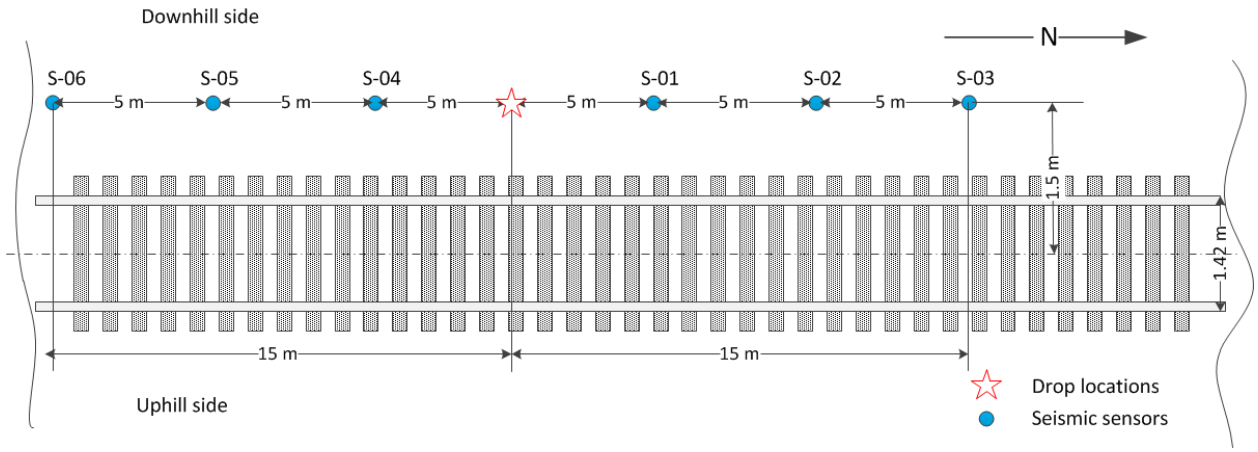

Figure 3.46. Layout of the temporary seismic arrays at locations (A) and (B). At (A), the temporary array started approx. 15 meters south of the tunnel.

Test procedure

In both locations, six sensors were positioned symmetrically with respect to the drop location spaced at 5 meters (Figure 3.45, Figure 3.46). Coordinates of sensors S-1, S-2, and S-3 with respect to the drop location were 5 m, 10 m, and 15 m; coordinates of S-4, S-5 and S-6 were -5 m, -10 m and -15 m respectively. The sensors were installed along the downslope side of the track, approx. 1.5 m off the centerline, arranged in a line. Test rocks were dropped on ballast exactly between S-1 and S-4. In order to obtain tolerance estimates for the ground response, two rocks were used: one of the rocks was selected to be smaller while the other was larger than 0.028 m^3 (1 ft^3). The larger rock measured 75 cm x 30 cm x 30 cm, and was dropped using an excavator; its estimated weight was 170 kg. The smaller rock was approx. 22 cm x 10 cm x 10 cm and it was dropped by hand; its estimated weight was approx. 8 kg.

(a) (b)

Figure 3.47. Photos of the two rocks used for the drop tests. (a) The smaller rock was approx. 22 cm x 10 cm x 10 cm, 8 kg; (b) the larger one was approx. 75 cm x 30 cm x 30 cm, 170 kg.

The rocks were dropped from two elevations, 1 meter and 2 meters. The actual elevations at which the excavator released the large rock were up to 0.5 m off the target, mostly because of the rock's elongated shape. At location (A), the 170 kg rock was dropped 6 times from 1 m elevation and 3 times from 2 m elevation; the 8 kg rock was dropped 3 times from 1 m elevation and 3 times from 2 m elevation. At location (B), the 170 kg rock was dropped 3 times from 1 m elevation, and only once from 2 m elevation. Unfortunately the series of tests at location (B) was abbreviated because the data logger ran low on power having been collecting data during the previous night. As a result, only four drops were performed at location (A) compared to fifteen drops at location (B); no test data for the smaller rock was available at location (B).

Test results

The plot in Figure 3.48 contains summaries of PGVs (peak ground velocities) observed at location (A) grouped by the drop elevation and the rock size. Test results were averaged for each sub-category, *e.g.* PGVs induced by the larger of the two rocks dropped from 1 m elevation were averaged for six sets of measurements. As one would expect, the larger rock induced ground vibration with significantly larger amplitude; also, the peak amplitude increased with the elevation (Figure 3.48). The plot in Figure 3.49 contains summaries of PGVs observed at location (B) grouped by the drop elevation and the rock size. Only one record was available for the 2 m drop of the large rock; test results for the smaller rock were not

available. The difference in ground responses at location (A) and (B) to the impacts of similar energy are shown in Figure 3.50 (the larger rock, 1m and 2m elevations).

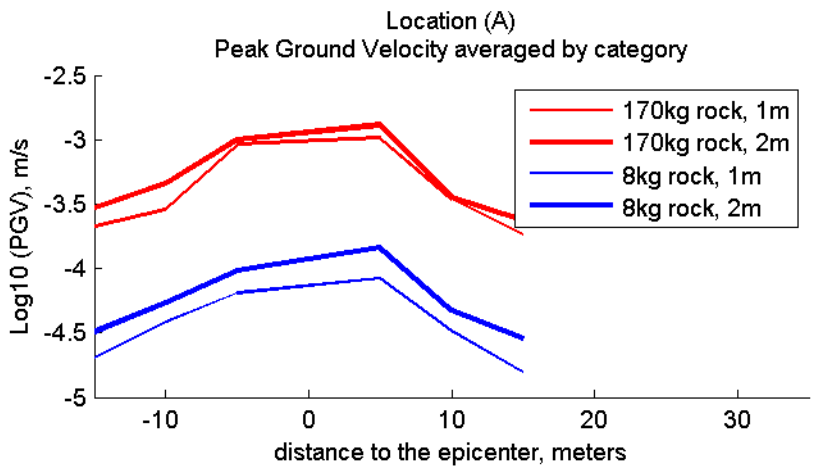

Figure 3.48. Summary of the PGV observed at location (A) and averaged by category. The positive direction of the X-axis is towards the tunnel.

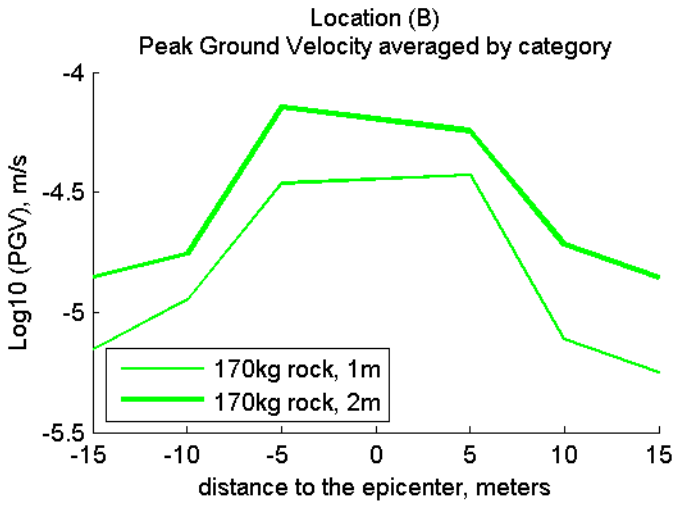

Figure 3.49. Summary of the PGV observed at location (B) and averaged by category.

Conclusions

[1] The geophones detected ground vibration induced by the rocks at both locations. Thus, the experiment confirmed that at 15 m spacing, the test impacts would be detected at 3-4 sensors minimum.

[2] Seismograms acquired at location (A), using the larger rock as well as the smaller one, indicate that the amplitude decrease towards the tunnel is less pronounced (Figure 3.48); the PGVs fall off more rapidly in the southerly direction (away from the tunnel). This pattern is visible both in the averaged records (Figure 3.49) as well as within the individual records. It is possible that the drop locations were consistently closer to the northern three-sensor sub-array; another explanation is that the bedrock is shallower in this direction, given the location of the tunnel.

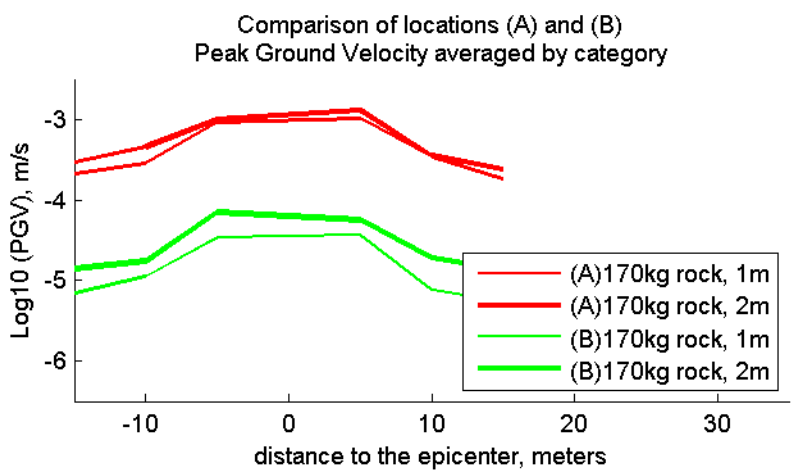

Figure 3.50. Location (A) *vs* location (B): comparison of the ground response to the impacts of the 170 kg dropped from 1 m and 2 m elevations.

[3] The most important observation concerns the strikingly different ground responses to drops of the same weight at locations (A) and (B) (Figure 3.50): the PGVs at (B) are approx. 20 times smaller compared to (A). The amplitude of the excavator noise at location (B) was also significantly smaller: at location (A), the r.m.s. (root-mean square) of ground vibration at the sensor closest to the excavator was ~2,200 binary counts (b.c.) or 0.000008 m/s *vs* ~250 b.c., or 0.0000009 m/s at location (B). The one order of magnitude difference in PGVs can be explained by assuming that unconsolidated soil/ ballast at (B) absorbed a higher proportion of the impact energy and had a stronger material damping effect on the amplitude. During the tests, the weight released by the excavator actually seemed to leave deeper depressions in the ground at location (B) indicating that impact energy release was of longer duration.

This assumption about the ground condition at location (B) was later confirmed based on the calibration tests of the permanently installed geophone array.

[4] The preliminary site characterization tests demonstrated that the ground response at this site is highly inconsistent, and there is a possibility that this inconsistency depends not only on the location but also on the direction of measurements. At the time of preliminary tests it was not clear whether the high rate of amplitude decay at location (B) is the worst case scenario within the entire 400 m long site, or whether there are areas with an even higher rate.

3.4.2. System calibration tests

The permanently installed seismic monitoring array consists of 27 vertical geophones referred to Z-01 to Z-27, which cover approx. 350 m of track (Figure 3.45). The same geophone model was used for both the preliminary tests and the permanent installation, Geospace GS-11D. However, for the permanent installation the sensors were grouted in place downslope 15 m apart about 0.5 m below the grade. Geophone Z-10 is the closest to the instrumentation enclosure containing the monitoring equipment.

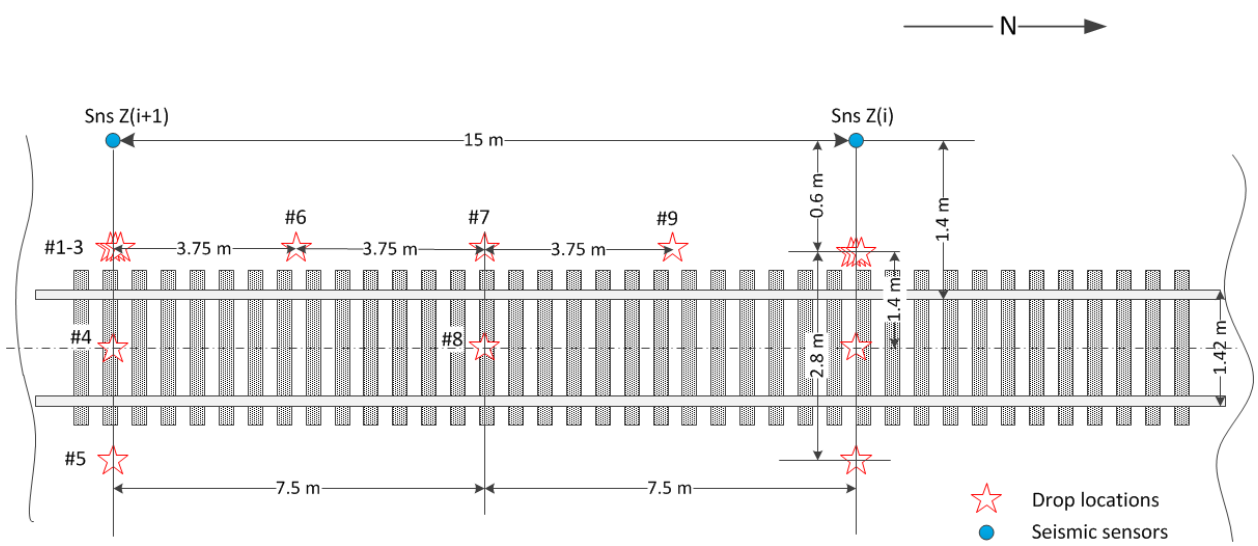

Figure 3.51. Locations of the nine rock drops performed between each pair of geophones.

Seismic data on the ground response to rockfalls were obtained by manually dropping a 15 kg rock in a consistent manner along the geophone array; the test crew released the rock mass from the same elevation, 1.75 m. The calibration data have been used to establish the system activation threshold and to configure the analytical software to distinguish hazardous rocks from non-hazardous in real time. Another purpose of the calibration test was to investigate the consistency of ground response within the instrumented area. The sketch in Figure 3.51 demonstrates the layout of test drops, as well as the approximate distances with regard to the sensors and the rail track.

Nine drops were carried out between each pair of sensors. Drops #1-3 were performed onto the ballast about 0.6 m from the geophone on the downhill side; drop #4 was performed at the track centerline. Drop #5 was onto the ballast on the uphill side; drop #6 was performed on the down hill side about 3.75m towards the next sensor; drop #7 was performed on the down hill side at 7.5m towards the next station. Drop #8 was onto the rail centerline at 7.5m towards the next sensor; and drop #9 was on the down hill side at 11.25 m toward the next sensor. Drops #4 and #8 were aimed at the nearest gap between ties. The tests started at Z-27 (drops #1-8) and continued north towards Z-01.

A	B	C	K	L	M	N	O	P	Q	R	S	T	
Sensor ID	Drop ID	hh:mm:ss	Z06	Z07	Z08	Z09	Z10	Z11	Z12	Z13	Z14	Z15	Z16
	2	11:17:15	0	172	535	2259	640561	527	204	162	0	0	
	1	11:17:11	0	149	418	1400	600603	248	138	0	0	0	
Z11			0	0	0	0	0	0	0	0	0	0	
	9	11:15:19	0	0	258	1487	8354	591	234	147	0	0	
	8	11:15:07	0	0	294	838	3157	2244	446	363	207	0	
	7	11:14:59	0	0	191	446	1977	975	335	0	0	0	
	6	11:14:48	0	0	0	285	972	4446	414	161	0	0	
	5	11:14:37	0	0	146	266	565	6188	341	0	0	0	
	4	11:14:27	0	0	279	369	1246	25365	566	513	219	0	
	3	**11:14:19**	**0**	**0**	**152**	**213**	**1028**	**258630**	**640**	**302**	**180**	**0**	
	2	11:14:15	0	0	0	163	588	219871	375	170	140	0	
	1	11:14:11	0	0	127	163	757	183901	375	207	182	0	
Z12			0	0	0	0	0	0	0	0	0	0	

Figure 3.52. Illustration of the tabulated calibration data stored in a spreadsheet. The data is in binary counts (b.c.) of the A/D board; the conversion factor between b.c. and the engineering units (meters per second) is 1.454 x 10^{-8} m/s/b.c. For example, drop #3 was performed beteween Z-11 and Z-10 at 11:14:19 (local time), and the ground vibration was detected at sensors Z-08 to Z-15. The highest PGV=258,630 b.c. was observed at Z-11 because this sensor was the closest to the epicenter (impact point).

Data processing

Altogether, the system calibration procedure involved 243 drops. A sample seismogram of ground vibration induced by dropping the 15 kg rock is demonstrated in Figure 3.53. For each of the 243 seismograms the observed peak ground velocity was tabulated (Figure 3.52). If the PGV was below the system noise level, it was assumed to be zero which usually was the case for sensors located more than 50-70 m away from the drop location.

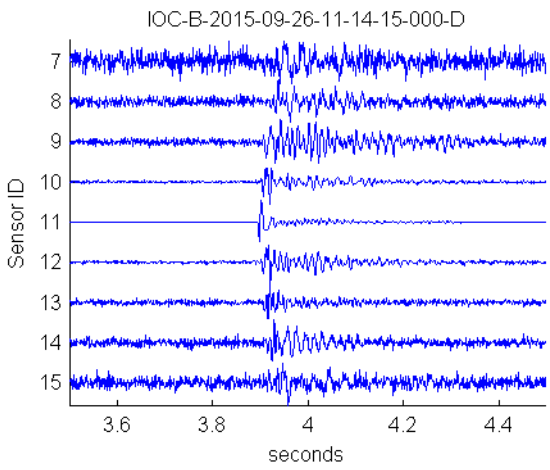

Figure 3.53. This seismogram demonstrates seismic signals induced by dropping the test rock (15 kg) at location #8 between sensors Z-13 and Z-14. The induced seismic signals are detectable ~45 m from the epicentre.

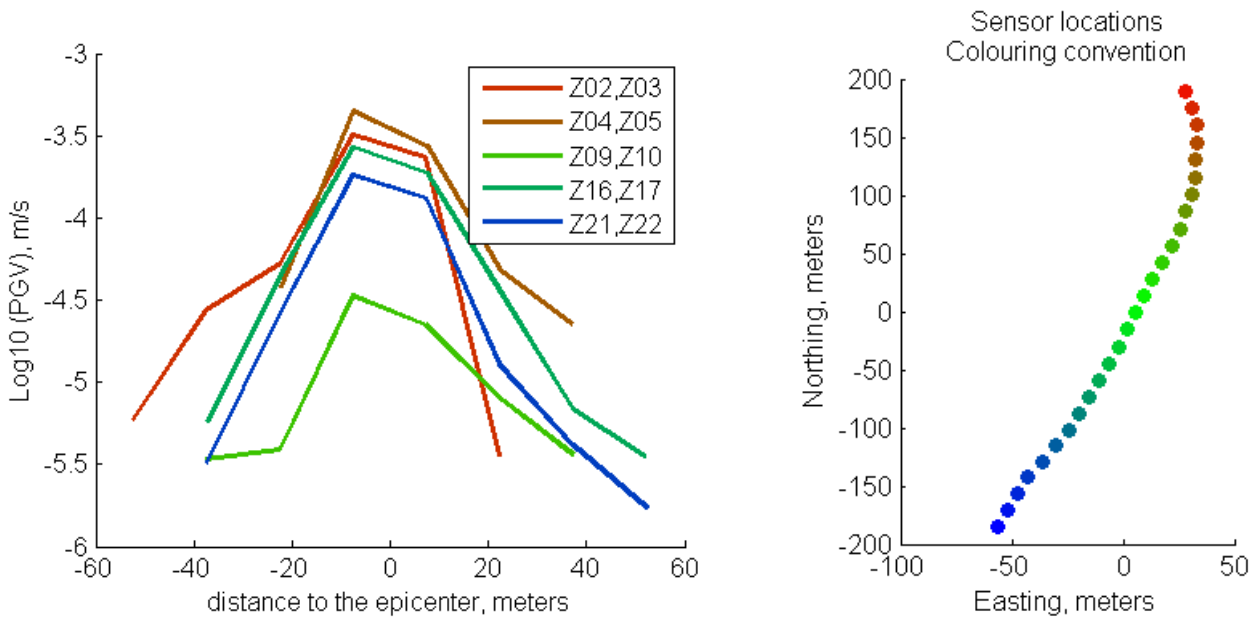

(a) (b)

Figure 3.54. (a) Examples of the PGV decay over distance from the epicenter; the data is displayed in log10 scale. For each pair of sensors indicated in the plot legend, the ground response data were obtained at drop location #7, located halfway between the sensors. The positive direction of the X-axis is towards the North. (b) The drop location coloring convention used in (a) as well as Figure 3.55.

Examples of the ground response data are in Figure 3.54(a). The coloring of the PGV curves is based on the following convention: sensor Z-01 is red; sensor Z-14 (in the middle of the array) is green; sensor Z-27 is blue; between sensors Z-01, Z-14 and Z-27 colors change in the linear manner (Figure 3.54(b)). The same convention is used in Figure 3.55.

In Figure 3.55, PGVs *vs* epicentral distance (the distance between the impact point and the sensor) are plotted for all 243 rock drops. Here, the majority of weak ground responses (*i.e.* low amplitude) are colored light-green. In accordance with the coloring convention, such drop tests cluster near Z-14. The stronger ground response is, for the most part, colored red and dark green as well as off-blue, and therefore was observed around Z-05 and Z-27 (locations are approximate). The non-uniform ground response to surface impacts is due to the non-homogeneous nature of the ballast and sub-grade along the instrumented area; the softer material in the middle of the array had a more pronounced material damping effect on the amplitude (Figure 3.56). The red curve highlights the weakest ground response to the calibration drops. This empirical PGV *vs* distance curve was used to configure the analytical software for automatic discrimination between hazardous and non-hazardous rocks in real time. Beyond 40-50 meters

from the drop point, the PGVs of seismic signals decrease to and below the system noise floor[10] (Figure 3.54) which is approx. 100 b.c., or 1.454 x 10^{-6} m/s.

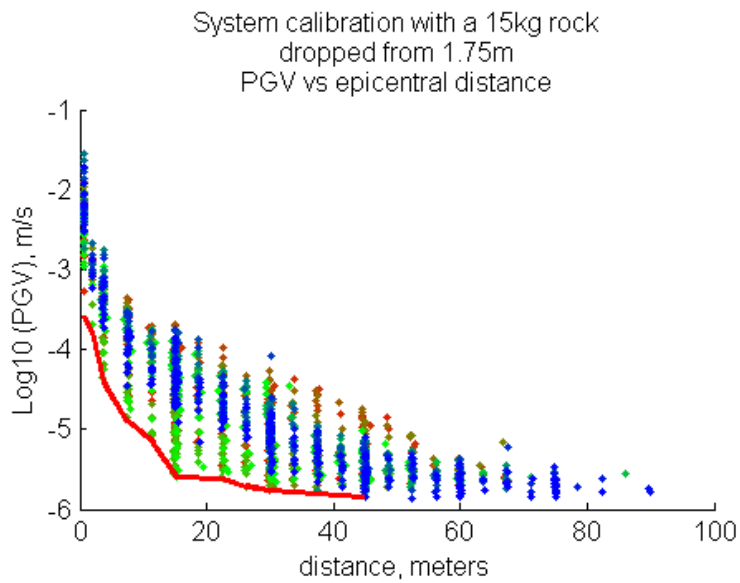

Figure 3.55. Aggregate plot of PGV *versus* epicentral distance observed in the 243 calibration tests. The red polyline highlights the system trigger threshold obtained from the calibration data as the weakest ground response to the impacts of the test rock.

The two-dimensional plot of the PGV data obtained for the 243 site calibration drops is shown in Figure 3.56. This is essentially a visualization of the tabular data illustrated in Figure 3.52. The plot contains 243*x*27 PGV measurements in log10 format. The calibration drops are plotted along the vertical axis. Line 1 contains the PGV measurements from Drop #9 north of Z-01; line 2 contains the PGV measurements from Drop #8 north of Z-01, *etc.* Line 243 of the image in Figure 3.56 contains the results from Drop #1 near Z-27.

[10] Noise floor is the measure of the signal created from the sum of all the noise sources and unwanted signals within a measurement system, where noise is defined as any signal other than the one being monitored https://en.wikipedia.org/wiki/Noise_floor. Last checked on February 1, 2016.

The image in Figure 3.56 contains an apparent anomaly in the area roughly stretching from Z-09 to Z-12, where the peak ground response is significantly weaker (1-2 orders of magnitude) compared to, for example, the high-rail mounting area immediately south of the tunnel, or the area near Z-18. This observation correlates well with the preliminary conclusions. According to Figure 3.56, the weakest ground response is actually 30-50 m south of the enclosure, or approx. 40-60 m south of location (B) used in the preliminary tests.

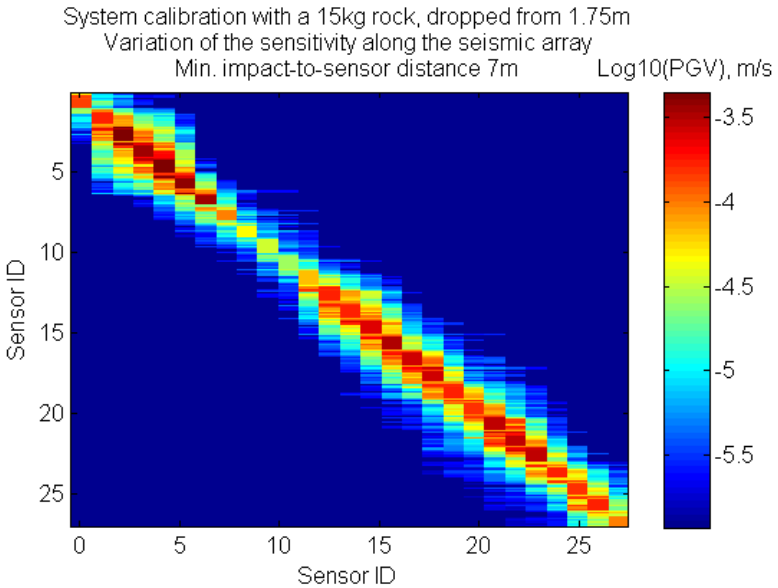

Figure 3.56. PGV *vs* epicentral distance of the 243 site calibration drops (log10 scale). The horizontal axis displays IDs of the array sensors: Z-01, Z-02, …, Z-27. The vertical axis displays indices of the sensors nearest to each of the 243 drop locations. An arbitrarily selected minimum sensor-to-epicentre distance of 7 m was used to remove PGV readings obtained near the drop location in order to enhance the resolution of the peak amplitudes in the far field.

Comparison of the two tests

In Figure 3.57, the peak amplitudes obtained in the preliminary site characterization tests are plotted together with the system trigger threshold used in the Hope and White Canyon installations. Location (A) used in the preliminary tests is near Z-05; while location (B) is near Z-11.

The preliminary tests in location (B) induced a slightly weaker response compared to the SRFDS-EQ trigger threshold (15 kg, 1.75 m), even though the preliminary tests involved a much heavier rock

released from about the same elevation, and dropped in roughly the same area where the weakest response threshold was obtained for the permanent sensor array. This is a not totally unexpected outcome because the sensor installation conditions differ. In the preliminary tests, the sensors were mounted temporarily on the ballast surface, while the system calibration tests involved buried sensors which were coupled to the medium. Among the variables are also the difference in sensor placements and the changes in the ground conditions before and after the seismic array was installed.

The ground response data obtained before the permanent array had been deployed was used to design the layout of geophone array; the data obtained for the permanent installation were used to calculate the actual system trigger threshold.

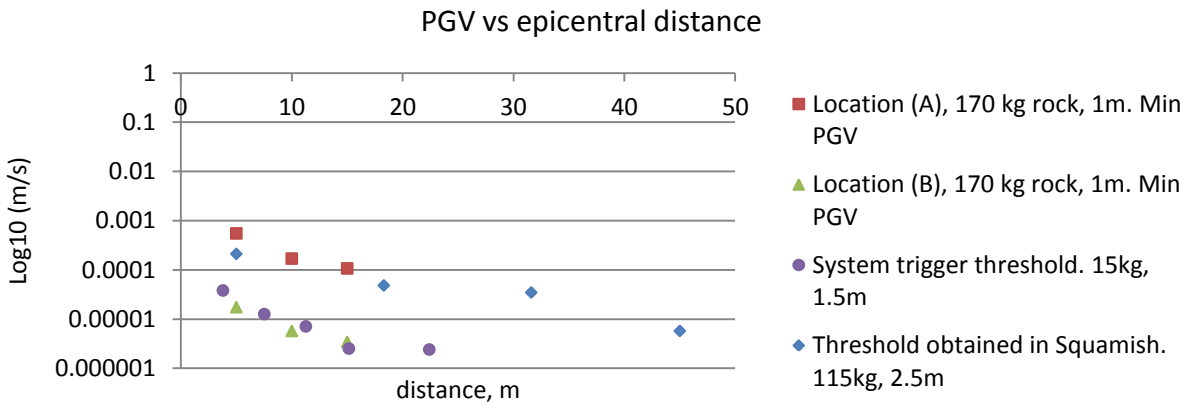

Figure 3.57. Comparison of the peak amplitudes observed in the preliminary site characterization tests, and the system trigger threshold obtained with a 15 kg rock.

The system activation threshold *vs* **train precursor noise**

For real time rockfall monitoring, the SRFDS activation threshold has been adjusted to use the weakest ground response obtained in the calibration tests (the red line in Figure 3.55). This is based on the assumption that both the rock used in the calibration tests and the manner in which the weight was released are typical of the minimum-size rocks that pose a derailment hazard for rail traffic. The disadvantage of using the relatively low threshold is that the rockfall detection system will be excessively sensitive in the areas outside the Z-11 to Z-14 section, both to falling rocks and seismic signals induced by non-hazardous events, *e.g.* rail traffic.

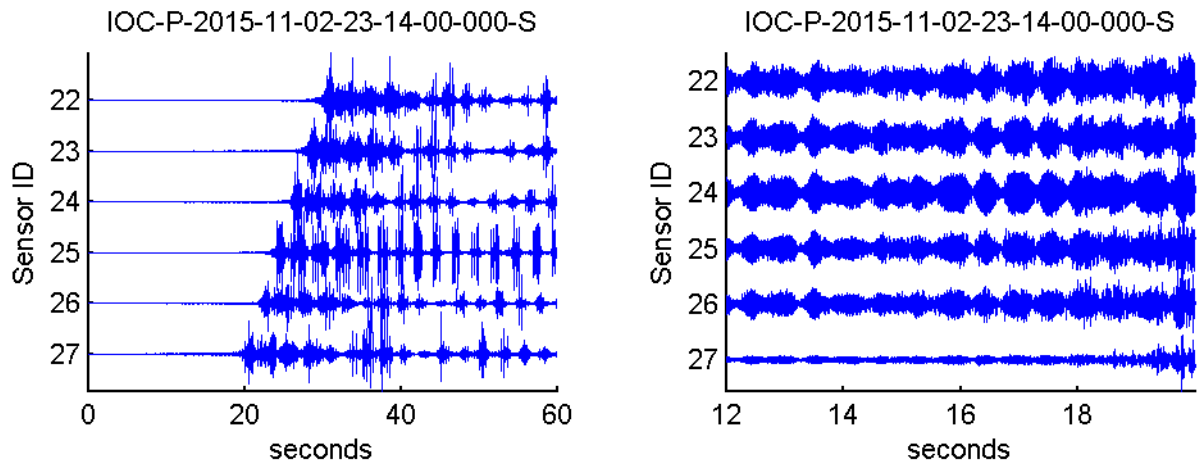

(a) (b)

Figure 3.58. (a) Example of train signals at sensors Z-24 to Z-27; the train is going north at ~30 km/h; the X-axis displays timing, in seconds, with respect to the beginning of the data file. The train signal begins after 20 s. (b) A zoomed-in view of (a) which highlights the precursor ground vibration. This signal appeared 20-40 seconds before the train arrived at the seismic array. The Z-27 signal is scaled with the PGV induced by a locomotive at 19 s which is why the precursor signal appears to be of smaller amplitude compared to the rest of the channels.

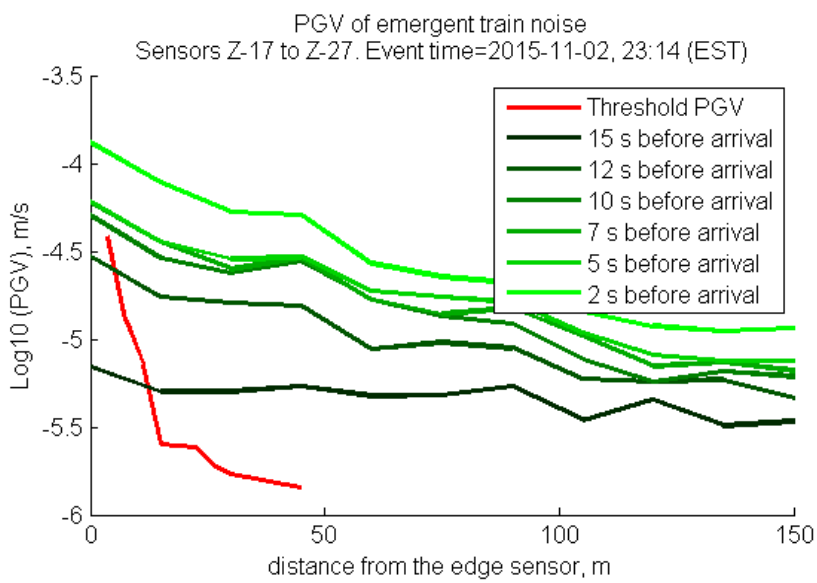

Figure 3.59. PGV of the emergent precursor vibration as a function of train arrival time at the nearest sensor of the seismic array. In this example, the sensor nearest to the approaching train is Z-27. The red polyline is the threshold obtained in the calibration tests.

The emergent ground vibration induced by a train approaching the seismic array ("precursor noise") is illustrated in Figure 3.58 and Figure 3.59. Seismic signals of approaching trains can have relatively high amplitudes and therefore must be ignored by the analytical software in order not to raise a false positive. If the PGV of the precursor signal exceeds the trigger threshold, the event is considered hazardous and the system will activate. The SRFDS analytical algorithms discussed in the next chapter identify regular rail traffic and ignore the strong ground vibration induced by it. In Figure 3.59, the sample precursor noise measured at Z-19 to Z-27 is compared to the system trigger threshold.

According to the plot in Figure 3.59, the precursor ground vibration can activate the SRFDS as early as 10-12 s before the train arrival at Z-27 (*i.e.* when it is 100 m away). This effect is not desirable and results from a combination of two factors: the relatively strong train precursor signal that emerges far ahead of the train; and the relatively low trigger threshold necessitated by the zone of high material damping which is located between sensor locations #11 and #14. Similarly, the amplitude of receding noise induced by a train that is moving away from the geophone array remains high enough for 10-12 s to exceed the current threshold.

3.5. Anthropogenic and natural sources of ground vibration encountered along railroads

In this section, natural and anthropogenic sources of ground vibration which have been observed at the SRFDS test sites will be discussed. Examples of ground vibrations caused by natural factors are rockfall, thunder, and animal migration; examples of anthropogenic sources are trains and track maintenance. Regarding their consequences, events can be hazardous (falling rocks and trees) or non-hazardous (track maintenance, remote traffic). Some seismic signals display regular patterns (rail traffic). Their peak amplitudes can be high enough to activate the SRFDS (rocks, trains), or fall below the threshold (*e.g.* earthquakes). Some of the events occur daily (trains); others are rare. For instance, there have been no activations by pedestrians other than railway personnel, likely because of the remoteness of the test sites.

3.5.1. Rockfalls and their equivalents

A seismogram of a non-hazardous rockfall is shown in Figure 3.60; the rock size is estimated from the induced peak amplitudes. It does not seem to be possible to distinguish the seismic record of a rock hitting the ground from the seismic signatures of other falling objects, for example trees and pieces of ice, which is why these events are in the same category.

The seismic signals in Figure 3.60 are normalized to the Peak Ground Velocity; the horizontal axis displays time in seconds. The traces are ordered by the sensor's numeric Ids, Z-01 to Z-27. Traces Z-01 to Z-12 have no detectable seismic events; rather, they display the white noise of the A/D boards. The noise appears as a solid line because, at 1 kHz sampling rate, each trace contains 60,000 data samples which cannot be resolved on a computer screen. Sensors Z-13 to Z-27 detected the ground vibration generated by the rockfall near Z-20.

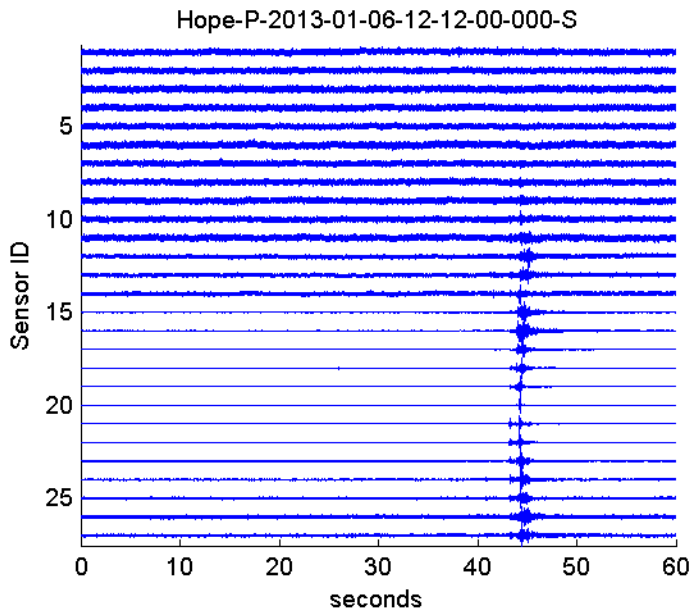

Figure 3.60. A 60 s seismic record of a rockfall near Z-20 (45 s) at the Hope test site.

Between early 2009 and mid-2015, several relatively large rockfalls occurred within the instrumented section of White Canyon some of which involved hundreds of cubic meters of material. In two cases,

CNR was able to provide photographs which allowed the author to compare the seismic records with the amount of deposited material (Figure 3.61, Figure E.11 in Appendix E). There have been no hazardous rockfalls at the Hope site since the SRFDS was installed in 2011 (excluding the material dislodged during the three-month long rock scaling program in 2014).

(a) (b)

Figure 3.61. Photos of the location of the June 5, 2013 rockfall before (a) and after (b) the event (courtesy of CN).

The June 5, 2013 rockfall in White Canyon

One of the largest rockfalls recorded by the White Canyon SRFDS occurred on June 5, 2013 west of the Mile 94.4 rock shed. Photos of the area before and after the event are in Figure 3.61 and Figure 3.27. According to CN's preliminary estimate, 100 m of track was buried under 4 m of rock (personal communication). Based on the subsequent LiDAR scan, the slope failure involved an estimated 2,600 m^3 of rock (Figure 3.62). CN lost six slide fence poles (the poles are 20 m apart) and there was extensive damage to the track roadbed. An analysis of seismic data indicates that there was a series of precursor events of various scales, culminating in the rockfall at 18:49 PST that was detected at all 68 sensors of the White Canyon geophone array (Figure 3.63). This is the strongest seismic event on record since the White Canyon SRFDS project commenced in early 2009 in terms of the peak amplitudes and the range at

which the event was detected. Detailed analysis of this rockfall based upon the LiDAR data has been published elsewhere (Kromer *et al.*, 2015).

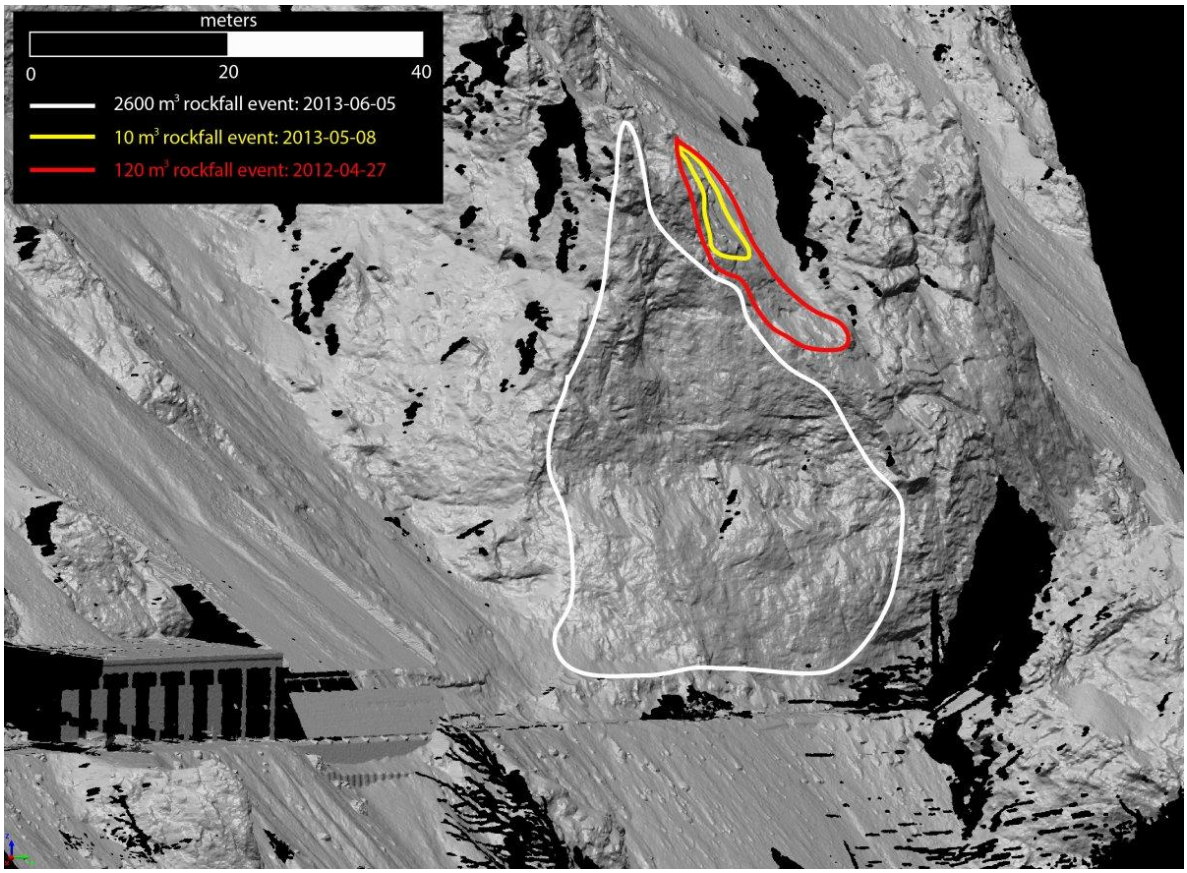

Figure 3.62. LiDAR image produced by RockSense Geosolutions Inc[11] shortly after the June 5, 2013 rockfall.

[11] http://rocksense.ca/ActiveProjects/TrasporationCorridors.html. Last accessed on June 5, 2015.

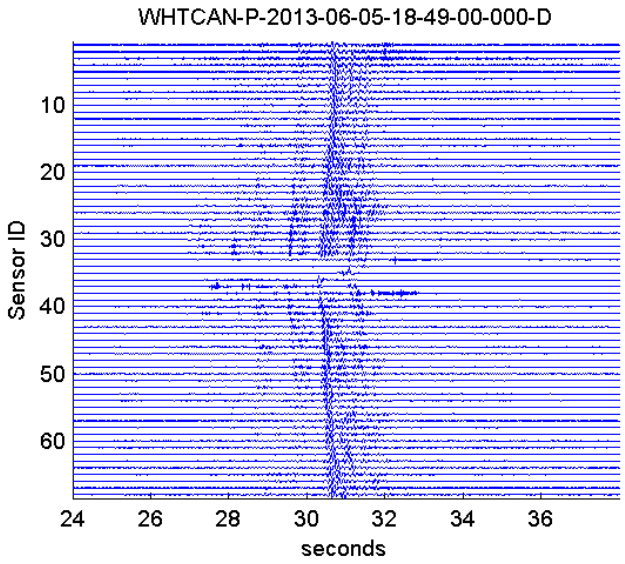

Figure 3.63. Seismic record of the strongest event, in terms of the number of triggered sensors, in the series of rockfalls which occurred between 16:53 PST and 18:56 PST on June 5, 2013.

3.5.2. Rail traffic

Regular trains and high-rails

Train seismograms display a characteristic pattern of periodic, spatially correlated signals whose time shift is proportionate to the train speed (Figure 3.64).

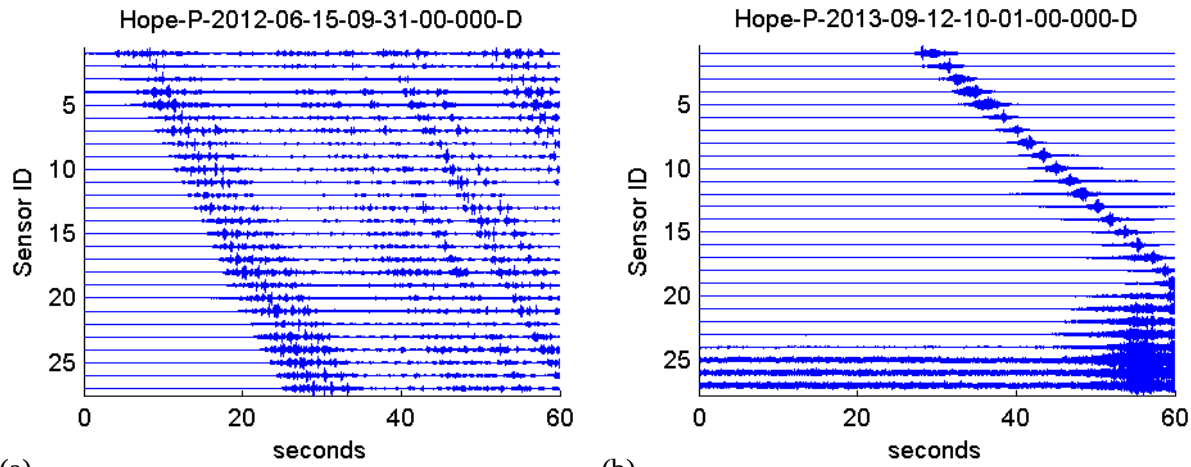

(a) (b)

Figure 3.64. (a) Seismogram of a train; (b) example of high-rail signal. Each trace is individually normalized with its peak amplitude.

Ground vibrations induced by steadily moving trains and high-rails are consistent in terms of duration and sensor-to-sensor travel time. In this research they will be referred to as "regular", whereas accelerating, decelerating and stopping vehicles display irregular signal patterns. Some high-rail signals are a combination of multiple frequencies, probably generated by the vehicle's engine, *e.g.* Figure 3.65. The example in Figure 3.65 also demonstrates that the characteristic ground and/or rail vibration induced by the high-rail was detected more than 10 s before the vehicle arrival at the sensor location (roughly equivalent to 100 m).

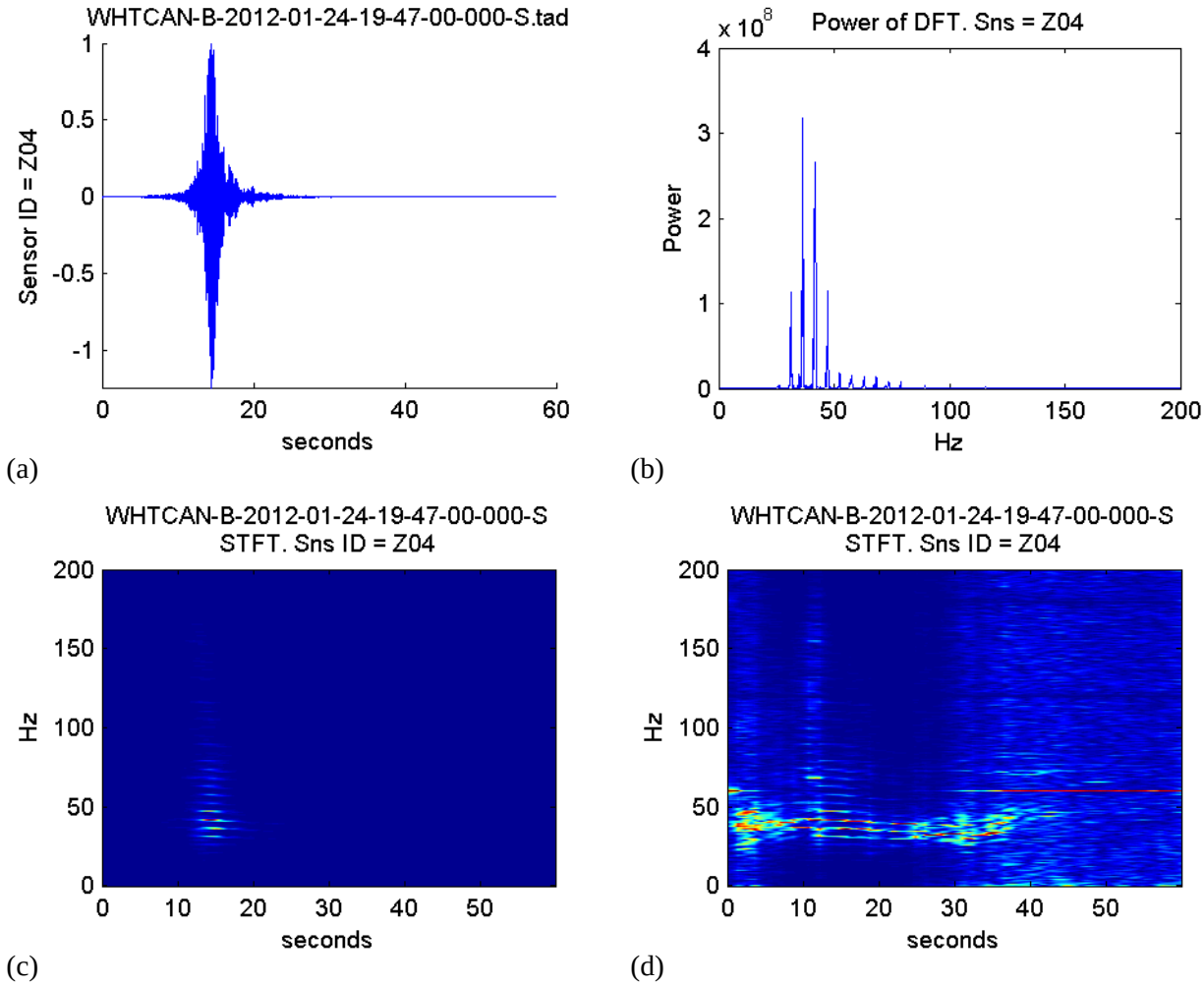

Figure 3.65. Example of high-rail signal with comb spectrum. (a) Source data; (b) FFT is dominated by 5 Hz multiples; (c,d) STFT (short-time Fourier transform). STFT was computed using 5 s time windows. The windowed FFT in plot (c) are globally normalized, while in (d) is they are individually normalized.

The seismic signal in Figure 3.66 is an example of an "organ pipe" signal induced by a westbound train and observed at the west portal of M94.0 tunnel in White Canyon. This type of coherent precursor signal is usually detected at the 3-4 sensors closest to the tunnel portal, *e.g.* within 40-60 meters. The tunnel is 226 m long, and the timing at which this signal emerges ahead of the train is proportionate to the train's speed. For example, if a train is moving at 5 m/s, the signal is detected by the geophones located next to the portal 40-45 s before the train's arrival. These are typically narrow-band signals dominated by 1-3

frequencies; in the example in Figure 3.66, the dominant frequency is 50 Hz. An adaptive notch-filter can be applied to this kind of noise which will detect and remove the strongest frequencies. Peak amplitudes of these signals are inconsistent, but can exceed the peak amplitude of ground vibration generated by high-rails.

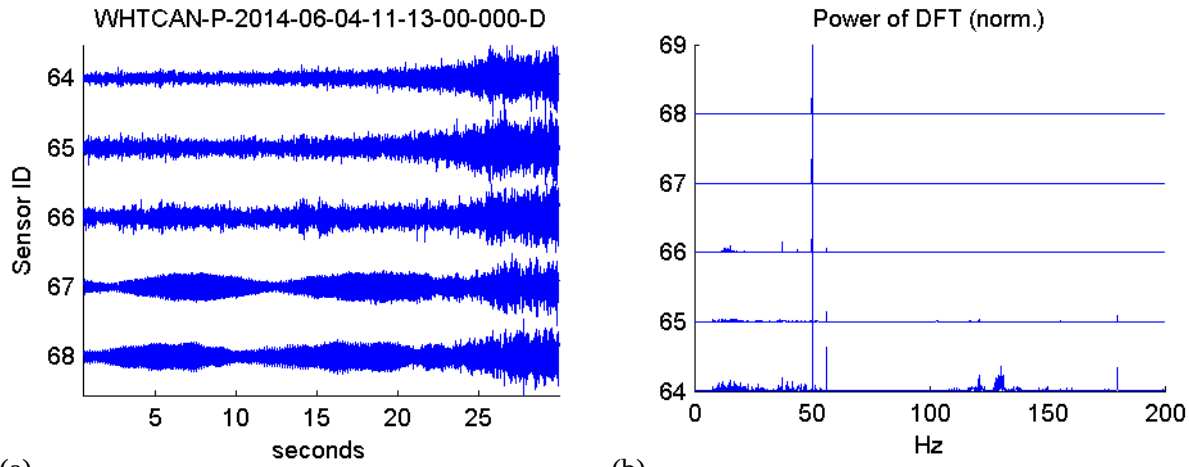

(a) (b)

Figure 3.66. (a) Example of an "organ pipe" signal recorded at the tunnel portal at CN Ashcroft Mile 94.0 a few seconds before a train arrival (Z-67 and Z-68). (b) This signal is dominated by 50 Hz.

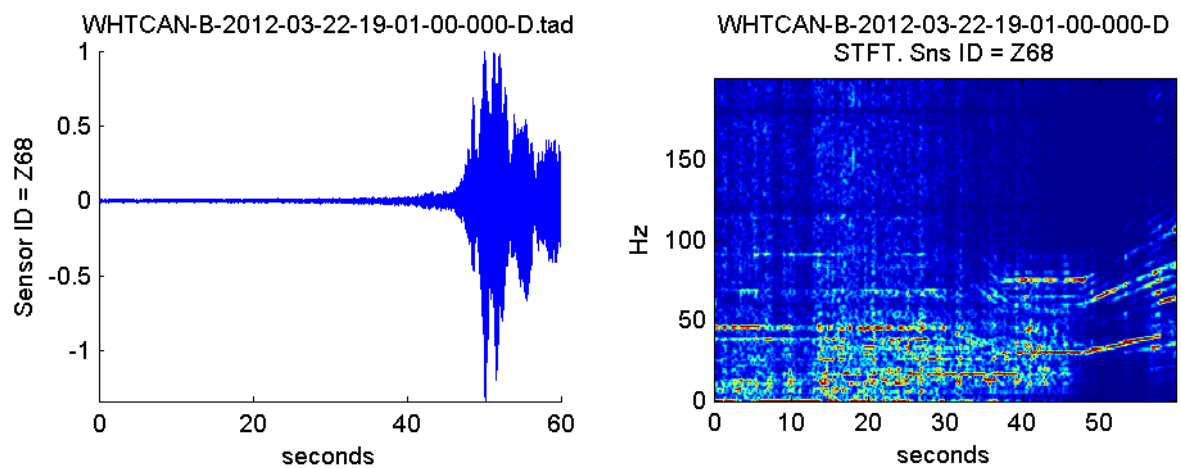

(a) (b)

Figure 3.67. (a) Normalized seismic trace recorded at Z-68 which is installed within 3 m of the M94.0 tunnel portal; (b) short-time FFT. Narrow-band seismic signal emerges about 20 s before the locomotive arrival at 50 s. In plot (b) the dominant frequencies shift up on the frequency scale (~50 to 60 seconds) as the locomotive is approaching the end of the tunnel which may be indicative of the train's acceleration.

An example of a train precursor signal at CP Cascade Mile 039.30 tunnel portal is shown in Figure 3.68. Between 20 s and 45 s (Figure 3.68 (a)) this signal is irregular and can make the seismogram of an approaching train look like that generated by rockfall. The peak amplitude of the tunnel noise at the Hope site is usually lower than that in White Canyon, likely because the tunnel is slightly shorter.

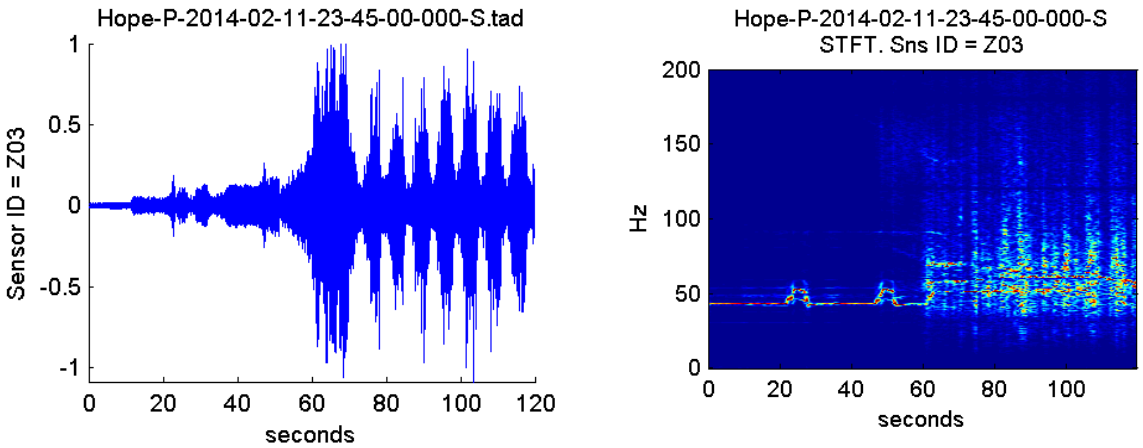

(a) (b)

Figure 3.68. (a) Normalized seismic record of train-induced ground vibration complete with precursor signal (the Hope SRFDS at CP Cascade Mile 039.30); (b) Short-time FFT of the train precursor noise in sample (a). In this example, narrow band tunnel noise preceded the train arrival at 60 s by more than 60 seconds. This property can be potentially used to identify approaching trains in order to ignore the associated ground vibration.

Effects of rail joints on train seismograms

There are a number of rail expansion joints within the instrumented section of White Canyon; such a joint leaves a 1-2 cm gap between the ends of the rails. Transient signals generated by train wheels rolling over the gap result in dissimilar seismic signals induced by the vehicle at different locations along the seismic monitoring array (Figure 3.69). In turn, this can degrade the performance of train identification algorithms discussed in the next chapter. At the White Canyon site, the strongest transients are excited by the rail expansion joints at sensor Z-12 and sensor Z-21. The welded joint near Z-60 also generates transients, likely because of minor imperfections on the rail surface. In order to diminish the negative effect of the transients related to rail joints, all train detection algorithms discussed later use r.m.s.-averaged seismic data.

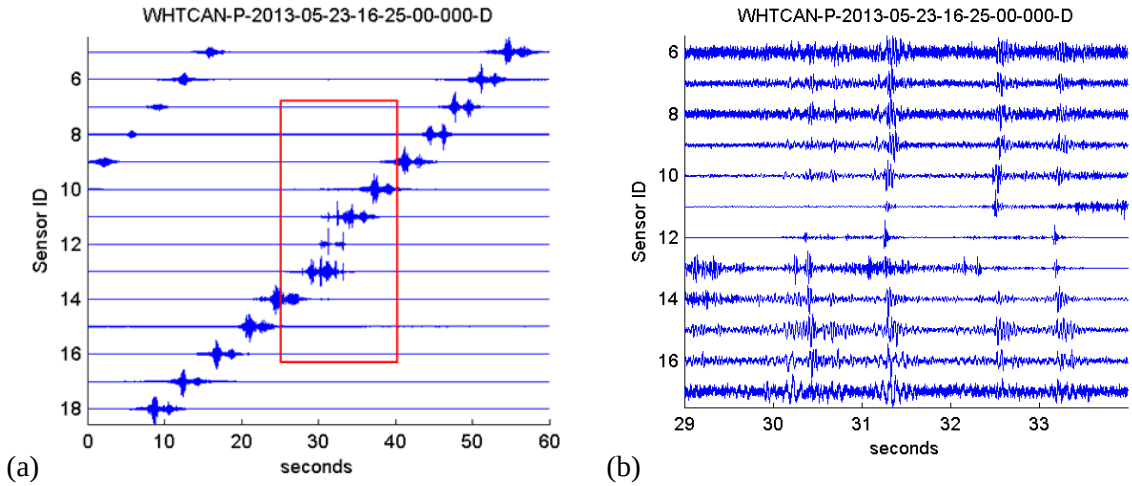

Figure 3.69. (a) Seismogram of a high-rail rolling over the rail expansion joint near Z-12 (the White Canyon SRFDS); (b) in the zoomed-in view, the high-rail signal is dominated by the rockfall-like signals generated by the high-rail wheels rolling over the gaps. This similarity in signal patterns is not surprising because it does not matter whether the rails are hit by a rock or by train wheels.

A seismogram of a high-rail rolling over the expansion joints is illustrated in Figure 3.69. In this example, the seismic signals generated by the wheels hitting the rails are detectable 100-120 meters away; at the sensors that are closest to the rail joint the peak amplitude exceeded 0.0015 m/s which is larger than the system activation threshold. Not only do the rail expansion joints make high-rail signals acquired near Z-12 look unlike a high-rail and correlate poorly with adjacent records, the patterns of seismic signals excited by wheel-rail interaction are the same as the patterns of rockfalls. In another example in Figure 3.70 the peak amplitude of the rail joint noise at Z-12 is almost ten times greater than the peak amplitude of the train signals at Z-14 located 40 m away.

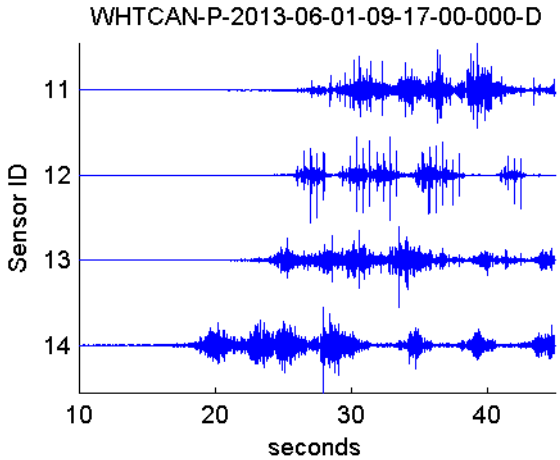

Figure 3.70. An example of transient signals excited by train wheels hitting the rail expansion joints near Z-12.

Train stops and starts

When a train is slowing down, its seismic signature begins to look irregular (Figure 3.71 a, b). After the train stops it disappears from the seismic "radar". A stationary or a slowly moving train (< 8-10 km/h) generates irregular seismic signals that look similar to rockfalls (*e.g.* 80-110 s in Figure 3.71 (a)); the amplitude of such signals can exceed the system activation threshold.

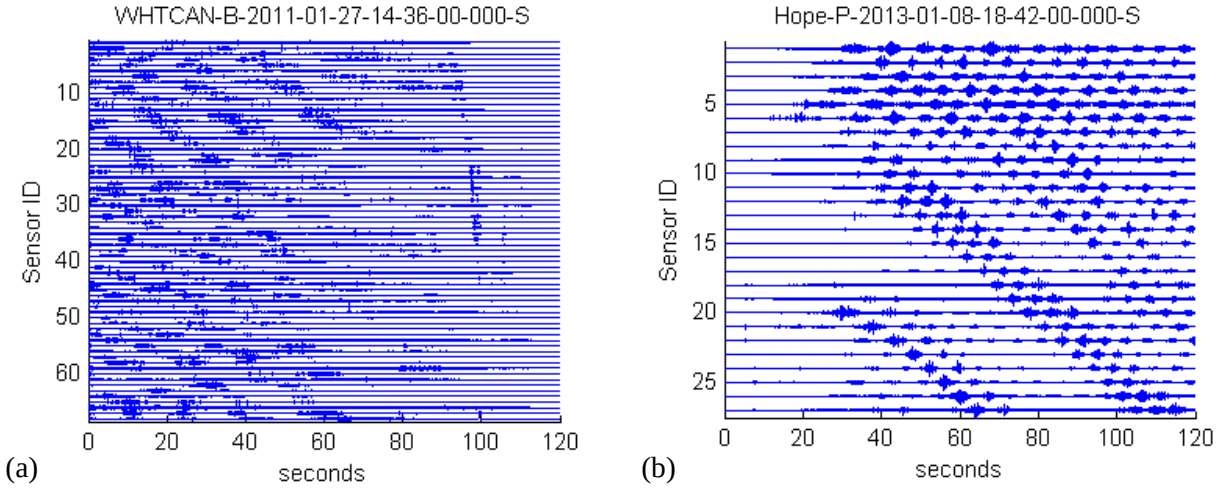

Figure 3.71. (a) Seismogram of a train coming to a complete stop. (b) Seismogram of a starting train.

3.5.3. Track maintenance

In this dissertation, *track maintenance* is used as a broad term which includes ballast cleaning, rail grinding, SDF repairs, debris removal, *etc*. Seismic signals excited by these activities display unpredictable patterns which are almost impossible to identify automatically. For instance, high-rail[12] vehicles operated by track maintenance crews oftentimes perform unpredictable manoeuvres, from idling to changing direction and speed. On the seismogram in Figure 3.72 three high-rails follow in close formation, slow down and then stop. This unpredictability complicates the task of automatic identification of rail traffic.

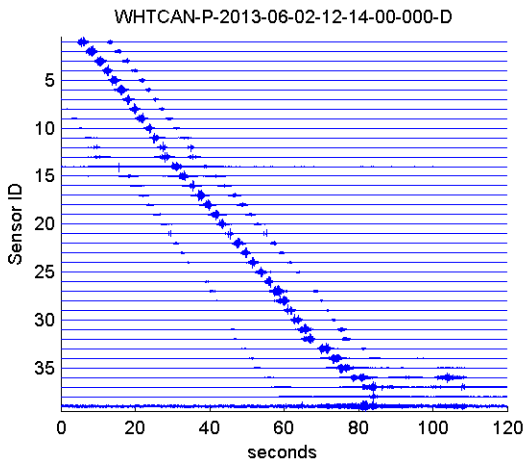

Figure 3.72. An example of irregular signal pattern induced by three high-rails coming to a stop within the area monitored by the White Canyon seismic array (80-100 seconds).

Oftentimes these events are of the same nature as rockfalls, *e.g.* an excavator dumping gravel on the ground. Field observations suggest that the amplitude of such signals can be high enough to activate the monitoring system. It should be noted that the Rail Traffic Controller (RTC) is aware of the location of track maintenance activity; should it result in a system trigger, it can be ignored as a false alarm. The crew can rearm the monitoring system upon completion of their work. Examples of ground vibration generated by track maintenance are in Figure 3.73 and Figure 3.74.

---

[12] A photo of a light duty high-rail is in Figure 3.28.

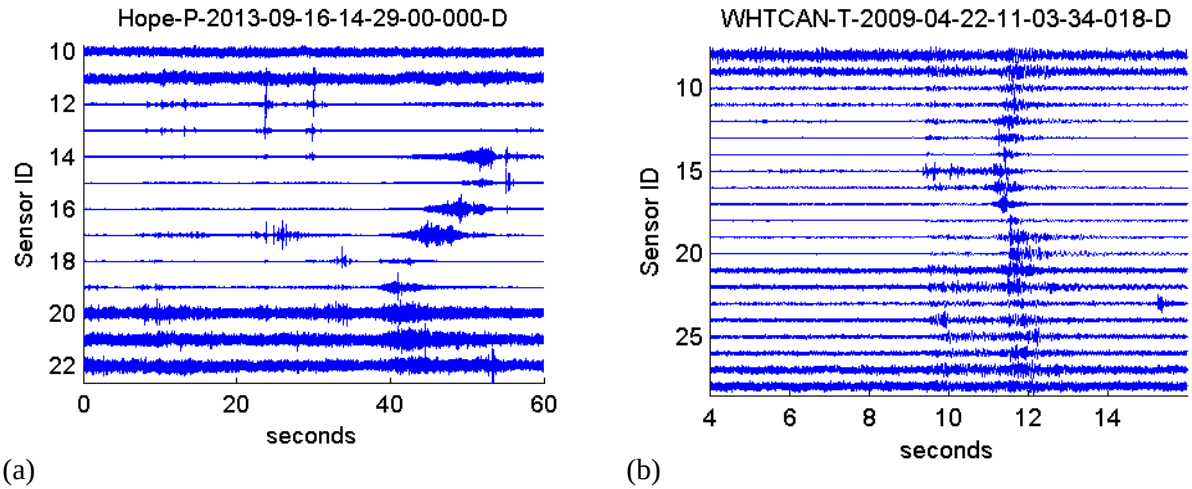

(a) (b)

Figure 3.73. (a) An example of seismic signals induced by walking maintenance personnel (10 to 35 seconds) and high-rail manoeuvres (40 to 45 seconds). (b) Seismic signals induced by the maintenance crew dumping a load of gravel (see Figure 3.24).

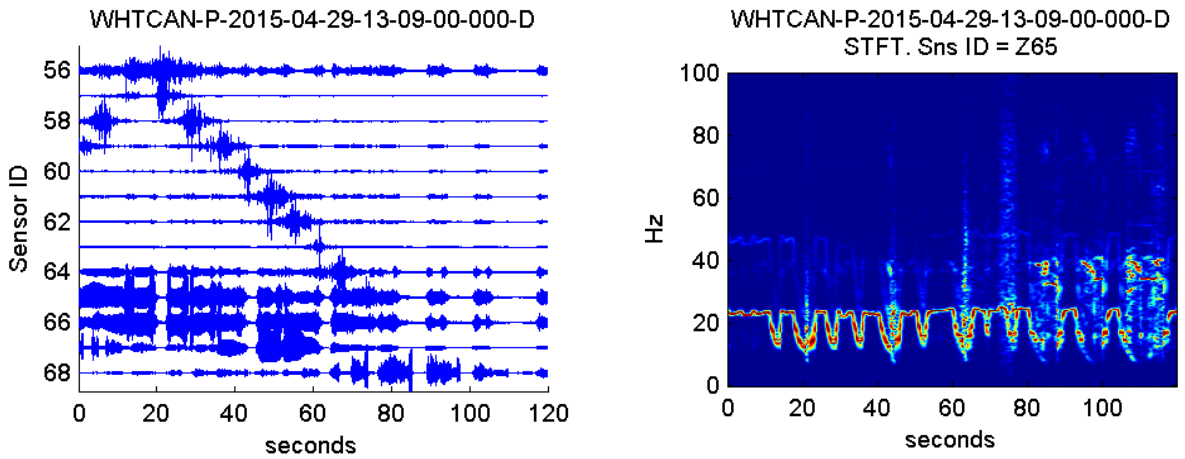

(a) (b)

Figure 3.74. (a) An example of ground vibration generated by a ballast tamping machine near Z-64 in White Canyon. The ground vibration was felt more than 1 km away. (b) Short-time FFT of the vibration recorded 30 meters away from the ballast tamper. The ST-FFT highlights low-frequency, quasi-periodic tamping cycles.

3.5.4. Animals

Ground vibration excited by animals displays signal patterns similar to a series of rockfalls (if the animal is walking), or a high-rail (if the animal is running). An example of such seismic signal is in Figure 3.75: a succession of quasi-periodic spikes. The animal's progression from sensor Z-13 to sensor Z-03 is clearly visible within the first 30 seconds of the record; the animal was running at 7 m/s. The signals picked by Z-01 and Z-02 around 50-60 s were induced by an approaching train.

Although the electric slide fence at the White Canyon test site is tripped on average 1-2 times per month by the local population of bighorn sheep (Table 5.7, Table 5.8), activations of the SRFDS by seismic signals related to animal migration have been rare, 2-3 times a year (Table 5.13, Table 5.14). Analysis of these SRFDS activations suggests that they were triggered by several animals spread out over 40-60 m distance which resulted in an array trigger; one animal is not heavy enough to trigger the seismic monitoring system.

It is desirable for the SRFDS data analysis software to be intelligent enough to detect the encroachment of animals into the monitored area in order to differentiate animal migration from rockfall automatically. However, an attempt to model animal migrations is not likely to be of any practical use. There will always exist the possibility of a rock of hazardous dimensions getting dislodged by animals and landing on the track; such a rock then will be ignored by the system as a part of a flock migration event. This is why, in this research, no attempt was made to design a method of identification of migrating animals by their seismic signatures; instead, all such signals are treated as potential rockfalls.

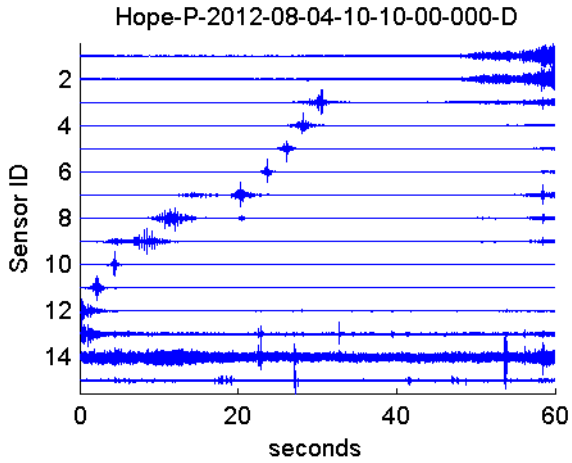

Figure 3.75. An example of signal pattern typical for a running animal: 1 to 30 seconds, sensors Z-03 to Z-13.

3.5.5. Seismic signals with low signal-to-noise ratio

Seismic signals with low signal-to-noise ratio are unlikely to trigger the monitoring system. Below are examples of such signals encountered at the test sites.

Remote traffic

In Figure 3.76(a) an example is demonstrated of the ground vibrations excited by acoustic signals coming from a railway line on the opposite bank of the Thompson River, more than 200 meters away from the seismic array. The signal amplitude is only 2-4 times above the system noise floor; it cannot be a source of false positives. Short-time FFT of the signal is dominated by 10 Hz multiples (Figure 3.76(b)).

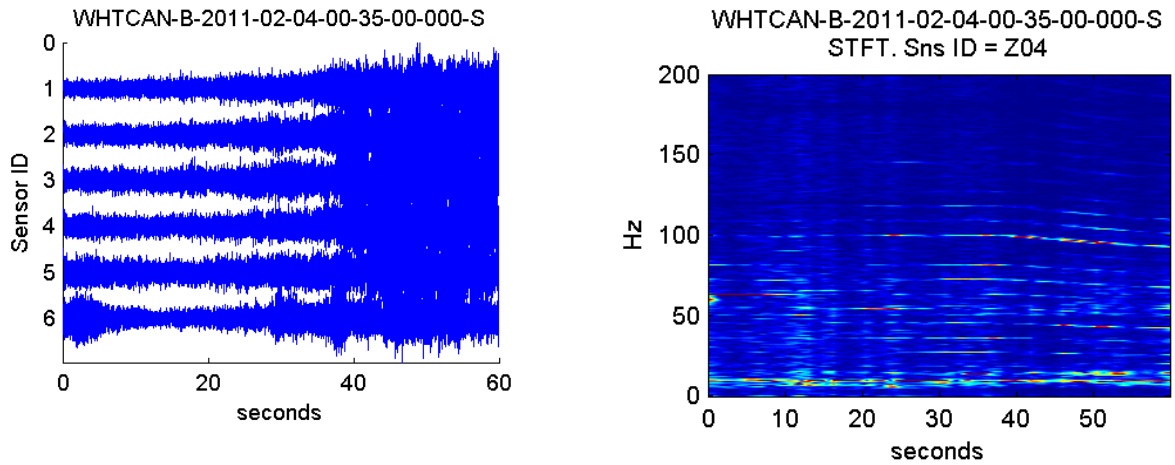

(a) (b)

Figure 3.76. (a) An example of acoustic noise generated by trains on the opposite bank of the Thompson River (White Canyon) . (b) Short time FFT of the remote train noise.

Figure 3.77 and Figure 3.78 display examples of seismic signals, possibly induced by a motorboat or an aircraft, which were recorded at the La Tuque and Hope sites. Both signals have low peak amplitudes and are unlikely to cause false alarms.

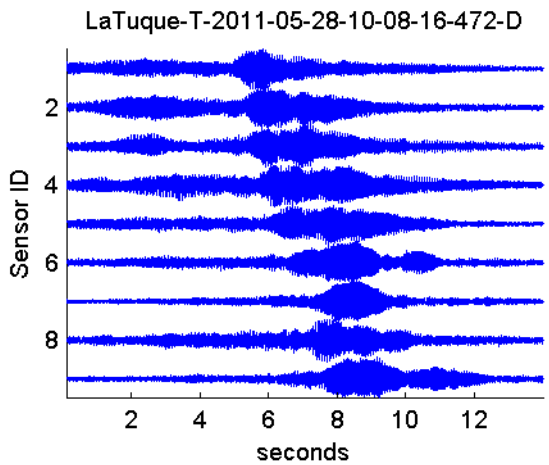

Figure 3.77. An example of low-amplitude background noise, likely generated by a motorboat, which was recorded at the La Tuque site.

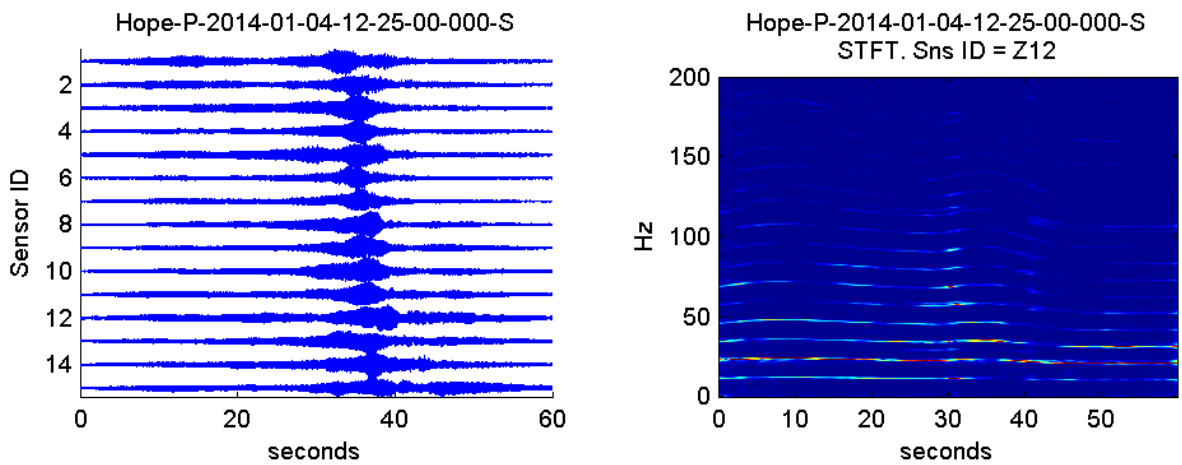

(a) (b)

Figure 3.78. (a) Unidentified signal, probably induced by a motor vehicle, recorded at the Hope site. (b) Short-time FFT of the motor vehicle signal computed with 5 s window and locally normalized. The ST-FFT looks similar to that of the remote train in Figure 3.76.

Road traffic

At the La Tuque site, an unpaved road used by SUVs runs parallel to the rail track; seismic records of the road traffic and high-rails display the same pattern (Figure 3.79). However, high-rails tend to generate higher amplitude signals compared to SUVs, probably because the geophone array is deployed on the

upslope side of the track, 4 meters from the unpaved road. In this example, the high-rail PGVs are within 1.5 x 10^{-5} to 1.5x10^{-5} m/s range, depending on the location of the geophones; SUV PGVs are within 7.6 x 10^{-7} to 3.0 x 10^{-6} m/s range which overlaps the amplitude range of high-rail signals. In this case the SUV signal can be identified by the absence of characteristic spikes on the wheel detector channels, as well as by the absence of transients caused by the rail expansion joints.

With regard to automatic event recognition, ground vibration generated by SUVs presents two concerns: firstly, they can be a source of false triggers; secondly, an SUV signal can be mistaken for a high-rail and interpreted as a sign that the track is clear of obstructions and safe (automatic rearming of the SRFDS is discussed in the next chapter). If there is a need to differentiate rail traffic from road traffic for the purpose of a SRFDS automatic reset, one can either use wheel detectors, or utilize train signals which are much longer and whose PGV is 1-2 orders of magnitude greater than those of SUVs.

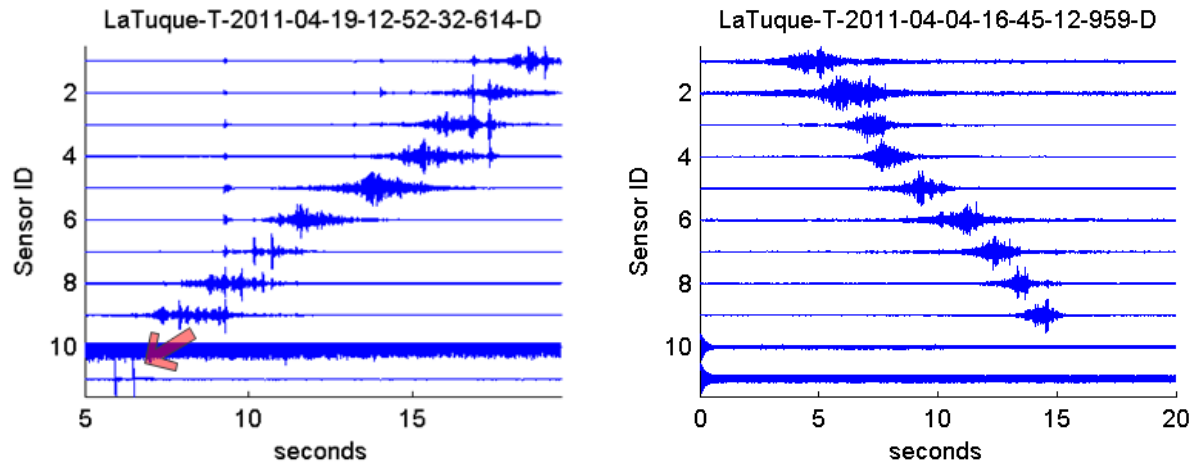

(a) (b)

Figure 3.79. (a) An example of a high-rail signal. Transients generated by the rail joints are visible within the seismogram at 9 s, 14 s and 17 s. The wheel detector channel (#11) displays two surges at 6 s excited by the high-rail wheels (red arrow). (b) Ground vibration induced by a vehicle on the unpaved gravel road parallel to the rail track (Figure 3.33).

Seismic signals generated by wind

The seismic sensors used in this research were buried 0.5-1.0 m deep, and they do not seem to be susceptible to seismic noise from wind gusts and precipitation. However, surface structures can become a source of ground vibration when shaken by wind bursts. Figure 3.80(a) displays an example of ground vibrations coming from two instrumentation enclosures at the La Tuque site being shaken by wind. This interpretation is based on the observation that the seismic sensors closest to the enclosures usually have

the highest signal amplitude. Though there does not seem to be a reliable way to differentiate signals coming from surface structures located in the vicinity of a geophone array (*e.g.* enclosures and commlink antennas), this issue can be resolved by stabilizing these structures with guy wires.

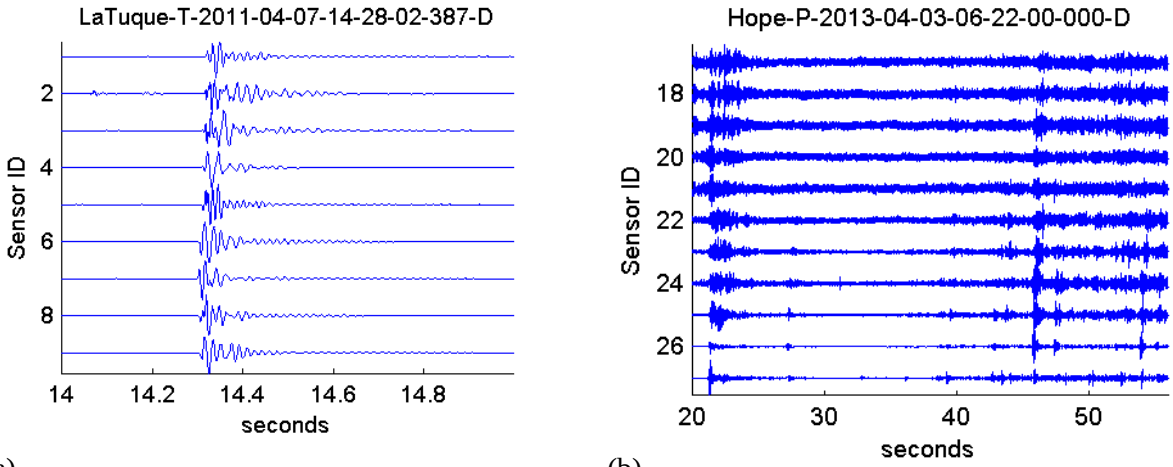

(a) (b)

Figure 3.80. (a) An example of ground vibration apparently induced by the wind shaking two instrumentation enclosures at the La Tuque site, PGV ~ $2.6*10^{-4}$ m/s. (b) An example of what appears to be seismic noise induced by tree roots at the Hope site, PGV ~ $2.0*10^{-4}$ m/s.

Figure 3.80 (b) demonstrates an example of a seismic signal which looks similar to rockfalls but which was probably induced by the movement of tree roots. Multiple events occur within short time intervals and seem to originate from the same area east of the sensor array. Because of their frequency, events of this kind are unlikely to be caused by rockfalls because the rock slope at the CASC 038.90 site is not subject to progressive and ongoing deterioration. The seismogram was recorded in April, which rules out ice falls.

Thunder claps

A seismogram of a thunderclap is shown in Figure 3.81 which is typically preceded by an electric spike caused by electro-magnetic interference between the geophone cables and lightning. Peak amplitudes of these events usually do not exceed $1.5 * 10^{-5}$ m/s, which is about ten times below the system trigger threshold. However, the amplitude of an EMI spike on the unshielded channels can be high and can result in a false alarm.

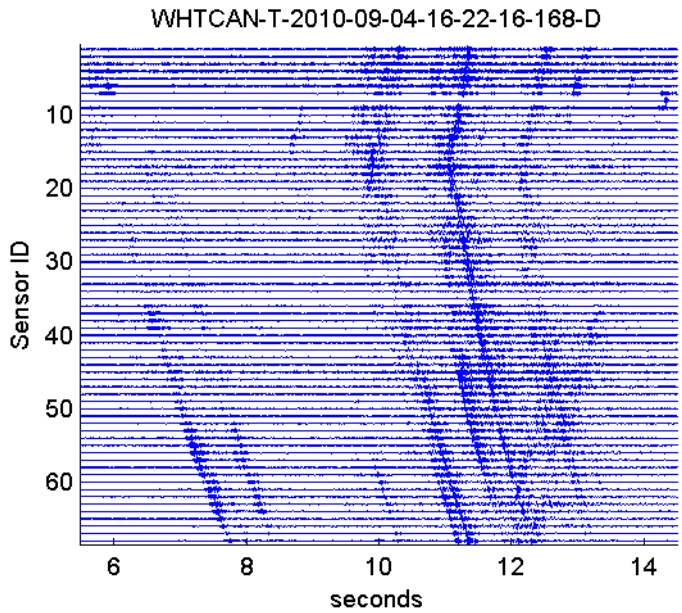

Figure 3.81. Seismic record of a thunder clap (White Canyon).

Earthquakes

Since the dominant frequencies of strong motion events lie below the corner frequencies of the transducer models used in the test installations (10 Hz for GS32-CT and 4.5 Hz for GS-11D), the recorded earthquake signals are of very low amplitudes, 2-3 times above the system noise floor. However, the correlation properties of such signals are of interest as far as rockfall detection techniques are concerned (see Figure 3.83 for the record of the Haida Gwaii earthquake, and Figure C.9 in Appendix C for the zero-lag cross correlation of the seismogram).

Local seismicity. The June 5, 2013 17:17 PST earthquake

In Figure 3.82(a) and Figure 3.82 (b) seismic events are illustrated which were recorded in White Canyon SRFDS and near Hope within a few seconds of each other. The Hope signal was weaker, and occurred 13 seconds after the White Canyon one, which suggests that the event was about 50 km closer to the White Canyon SRFDS site. The geophone responses are dominated by 10 Hz which would be the case when a low frequency event (*e.g.* an earthquake) is recorded using geophones with 10 Hz corner frequency. Within each geophone array the energy arrivals were detected at all sensors practically simultaneously. The event did not initiate any immediate debris falls onto the track; however, a major rockfall occurred in White Canyon 1.5 hr later (Figure 3.61). For the timing of the event the United States Geological Survey

(USGS) database contains no natural seismic events in this area of BC; rather, the event registered by the White Canyon and the Hope sensor arrays may have been a local, relatively weak earthquake in the vicinity of the Fraser Canyon which is not listed in the national nor international earthquake catalogues.

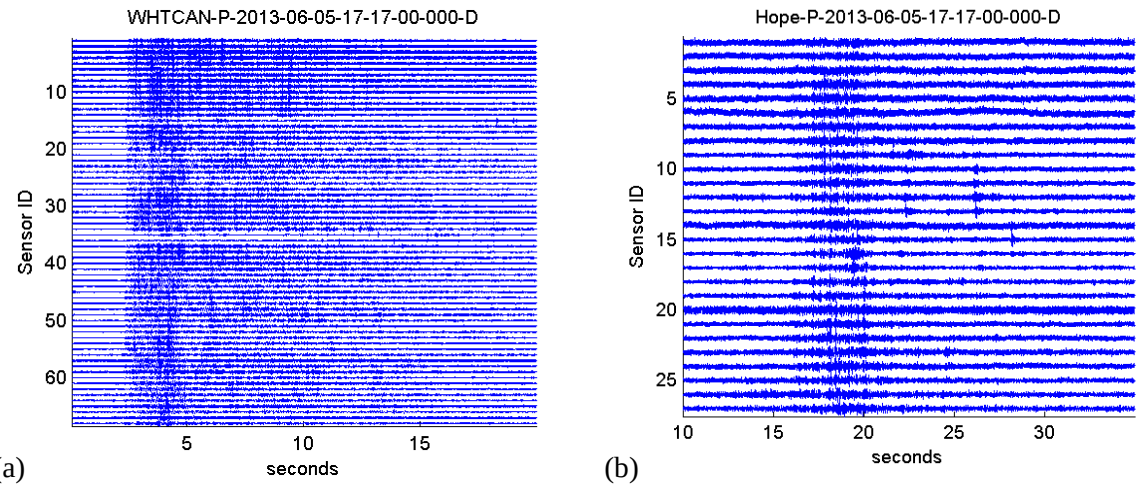

Figure 3.82. (a) Seismogram of a seismic event which could be a response of the geophone array to a local earthquake. (b) Seismogram of an event which could be a response of the Hope SRFDS to the June 5, 2013 17:17:03 PST event detected in White Canyon.

Compared to hazardous rockfalls, the peak amplitudes of teleseismic events are low and energy arrivals occur near-simultaneously. During the four years of continuous seismic monitoring in White Canyon and Hope such events were identified only a few times, usually randomly, and only because they stand out from the background noise rather than exceed the SRFDS activation threshold (*e.g.* Figure 3.82).

The Haida Gwaii earthquake (October 27, 2012)

The 2012 Haida Gwaii earthquake was a magnitude 7.7 earthquake that occurred at 3:04 AM UTC on October 28, 2012[13]. The earthquake's epicentre was on Moresby Island of the Haida Gwaii archipelago, about 800 km from White Canyon. The seismogram in Figure 3.83 illustrates the second minute of the Haida Gwaii earthquake recorded by the White Canyon SRFDS. The first arrival occurred about 2.5 min after the event's start reported by USGS. However, the signal spectrum is dominated by 0.5 Hz which means that the signal is significantly distorted by the geophone transfer function which acts as a high-pass filter with 10 Hz corner frequency. The event was also detected by the Hope SRFDS.

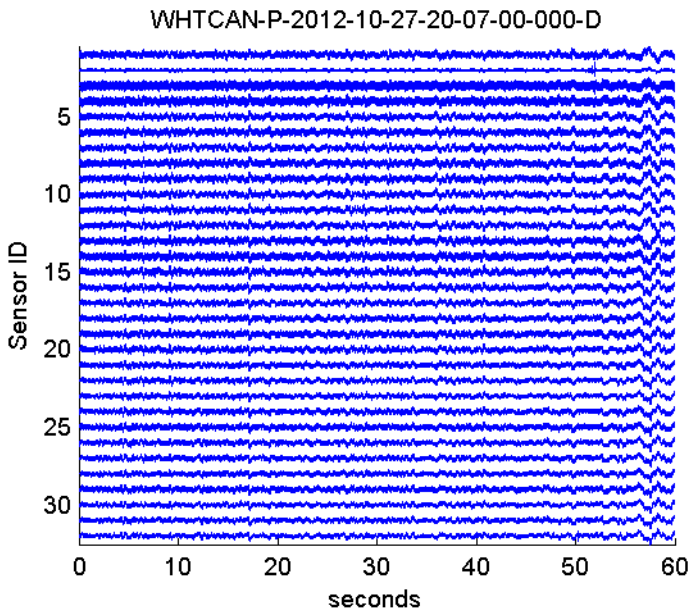

Figure 3.83. The second minute of the October 28, 2012 Haida Gwaii M7.7 earthquake recorded by the White Canyon SRFDS. The epicentral distance is approx. 800 km. The individual arrivals of the earthquake phases are obscured by the long duration of the source time function and the low sensitivity of the GS32-CT velocity transducers to the signal's dominant frequencies. The arrival of S_1 phase is at 57 s. The arrival of P_1 phase appears to occur approx. 80 s earlier (not shown)[14].

[13] http://en.wikipedia.org/wiki/2012_Haida_Gwaii_earthquake. Last accessed on July 6, 2015.

[14] The author would like to thank Prof. M.Bostock for his clarification of the expected travel times of the Haida Gwaii earthquake phases.

3.5.6. EMI spikes

Electric spikes are induced by electromagnetic interference (EMI) of velocity transducers and cables with power lines or lightning strikes. Spikes have significantly lower peak amplitudes on the shielded channels (Z-33 to Z-68) compared to the unshielded ones (Z-01 to Z-32, Figure 3.84). There is a tendency for the spike amplitudes to increase with the length of sensor cable; the unshielded cables act like an antenna picking up EMI noise. A strong EMI spike lasts for tens of milliseconds, and has a peak amplitude which typically exceeds that of a hazardous rockfall. As a result, some EMI spikes can trigger the SRFDS.

Seasonal surge in EMI spikes

Each spring the White Canyon SRFDS would experience an increase in the number of EMI spikes (Figure 3.84). Though the nature of spikes is not completely clear, in part it may have to do with the operation of the relays installed in the nearby signal control bungalow. Although, in the majority of cases, the peak amplitude of EMI noise was below the trigger threshold of the SRFDS, on occasion it exceeded the threshold which resulted in a false alarm. In the majority of cases EMI spikes display regular patterns which can be identified automatically using outlier detection algorithms. Several techniques based on outlier detection were designed to identify such patterns and interpolate affected data samples in order to reduce the chances of false positives.

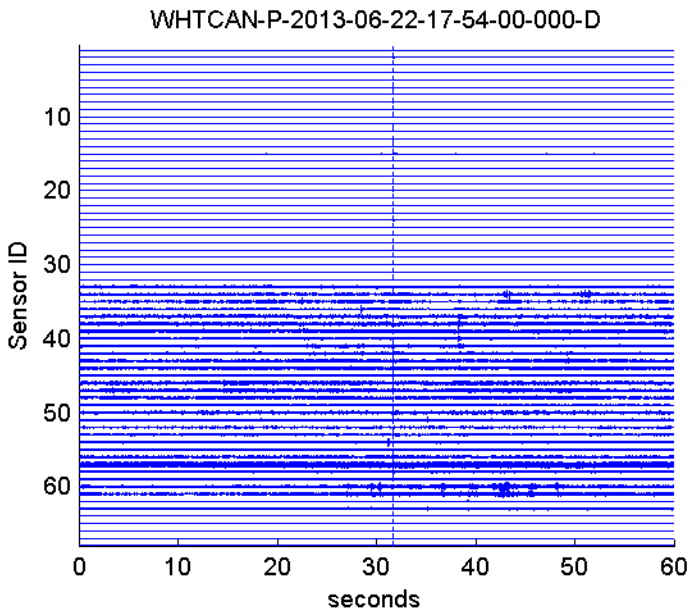

Figure 3.84. Example of an electric spike which affected all 68 channels.

EMI spike filter

In seismic records EMI spikes appear as outliers (Figure 3.84). Hawkins (1980) defines an outlier as an observation that deviates so much from other observations as to arouse suspicion that it was generated by a different mechanism. One can find over 100 outlier detection techniques in applied statistics (Knorr *et al.*, 2000; Maimon and Rockach 2005; Barnett and Lewis, 1994). Electro-magnetic interference induces abrupt changes which are not typical for relatively smooth seismic signals: weak EMI spikes have low amplitude, last a few milliseconds (usually 1 ms) and affect only a few data channels; strong ones can last for tens of milliseconds. Within the SRFDS, EMI spikes are identified using the following distance-based method that combines analysis of individual channels with detection of simultaneous spikes across the sensor array. Individual traces are analyzed using this criteria:

$$\frac{|x_j(i)|}{|x_j(i \pm k)|} \geq N \text{ , } k = 1, 2, \ldots, K,$$

where $x_j(i)$ is *i*-th sample on *j*-th data channel within a file.

In other words, the amplitude of an anomalous data sample, $x_j(i)$, has to exceed the amplitudes of *K* preceding samples as well as *K* following samples at least *N* times. In the beginning of a data file, where *K* data samples immediately preceding an outlier are not necessarily available (unless the data are buffered), a modified detector can be used:

$$\frac{|x_j(i)|}{|x_j(i+k)|} \geq N$$

A similar idea applies to the end of the data file:

$$\frac{|x_j(i)|}{|x_j(i-k)|} \geq N$$

Empirically obtained value of $N = 7$ has been used. For the two-sided detector, $K= 2;$ for the one-sided detectors $K= 4$. Since EMI spikes occur simultaneously and affect a number of adjacent data channels, an array-wide trigger must be detected in order to positively identify an EMI spike:

$$\frac{|x_j(i)|}{|x_j(i\pm k)|} \geq N, \frac{|x_{j+1}(i)|}{|x_{j+1}(i\pm k)|} \geq N, \ \ldots, \frac{|x_{j+m}(i)|}{|x_{j+m}(i\pm k)|} \geq N,$$

where $m \geq M$, the minimum number of array triggers at data index i. The minimum number of array triggers, $M = 6$, has been used because a rock of hazardous size typically triggers $M \geq 6$ sensors. When spikes $x_{j+l}(i)$ are detected at channels $\{ j+l: l=0,\ldots m \}$ the outlier samples are replaced with $min\{x_{j+l}(i \pm k)\}$. Since a strong EMI spike can last a few milliseconds, the described detector can be applied iteratively in order to interpolate the outliers.

3.6. Summary

Test sites

In the course of this study, simulated rockfalls and field experiments were carried out at several test sites, and a number of adjustments were introduced into the configuration of the seismic monitoring systems. The experiments started in Vancouver (BC, Canada) where the ground conditions were different from the subsequent installations in the Canadian Cordillera and consisted of 10-25 m of glacial till (est.). A 24bit data acquisition system, TMA by Terrascience Systems Ltd (Vancouver) was used with 10 Hz, 70% damped geophones (GS-32CT). A combined hardware/ software gain of 100 was used to amplify the geophone signals prior to converting them into binary data; a 2 kHz sampling rate was used. Based on the simulated rock drops it was concluded that rail-mounted sensors are the most sensitive to surface impacts, and that the sampling rate can be reduced to 1kHz. The weight impacts on the rails and ties excited

vibrations which propagated along the rails for approx. 190 m from the source. However, the combined gain of 100 resulted in undesirable signal clipping, and the gain was reduced to 2 in the subsequent SRFDS installations.

The next installation near Squamish (BC, Canada) included the same geophone model, GS-32CT; seismic signals were sampled at 500 Hz (ballast sensors) and 1 kHz (rail sensors). Geophones were assembled into tri-axial sensor packages and deployed every 15 m up- and down-slope. The main lesson learned from the Squamish experiments was the susceptibility of rail mounted sensors to operational damage: in the subsequent rockfall monitoring installations sensors were placed only in ballast. The PGVs correlated well with the impact energy and, at this location, dropped off approximately one order of magnitude every 25 m. The sensors mounted uphill and down-hill appeared to be equally sensitive to the seismic signals. This consistency was used to conceptualize a technique for automatic recognition of hazardous rocks with a PGV threshold obtained in a series calibration drops. Only vertically oriented geophones were used to estimate the trigger threshold. Though no detailed information was available on the ground condition, because of the site's topography, bedrock was expected to be only a few meters deep. Compared to the Phase 1 tests in Vancouver, the duration of waves induced by weight drops increased with the distance, probably due to reflections of seismic waves from the velocity interface and the difference in velocity between various seismic phases. Seismograms of simulated rockfalls included direct and refracted body waves, surface waves, as well as rail vibrations. Time separation between the relatively fast P wave and slower Rayleigh wave was not clearly visible because of the short length of the geophone array combined with low-energy impacts and fast amplitude decay. Because of this complexity it was decided not to use arrival times and epicenter location techniques for identification of hazardous rockfalls in real time. At the early stage of the research project, the event analysis software was programmed to use the signal duration to differentiate between rocks and trains, assuming that the train and high-rail signals are significantly longer than rockfalls. The duration-based approach to automatic event recognition turned out to be over-simplified and prone to failures, and was later replaced with pattern recognition techniques (Chapter 4).

The SRFDS installations in White Canyon and near Hope (both in British Columbia, Canada) also utilized GS-32CT sensors together with the 24 bit TMA data logger model (Terrascience Systems Ltd) configured to apply 2.0 gain and sample signals at 1 kHz. The SRFDS installations were programmed to use the system activation threshold obtained in the series of tests performed near Squamish. Unlike the test site at Squamish, these installations were subject to a number of sources of natural and anthropogenic seismic signals, including train stops, track maintenance, rockfalls involving hundreds of cubic meters of rock, animal migration, ice falls, rail expansion joints *etc*. Analysis of these events, especially the high rate of false alarms experienced by the White Canyon SRFDS due to frequent visits by track maintenance

personnel, has helped to conceptualize the autonomous Seismic Rockfall Detection System described in the following chapter. The monitoring systems were accessible over the Internet which greatly simplified data interpretation; the web camera connected to the Hope SRFDS was particularly useful.

The railway operators provided contact closures that indicated the SDF activation status and helped to collect data for comparison of the performance of the two rockfall warning systems. Following several large rockfalls (>100 m^3) within the instrumented section of White Canyon in 2012-2013, the decision was made to use GS-11D velocity transducers (4.5Hz corner frequency, 4000Ω coil resistance, and 18.2 KΩ damping resistor for 70% damping, intrinsic sensitivity ~2.1 V/in/s) in the subsequent SRFDS installations instead of GS-32CT.

Detection of hazardous rockfalls using the amplitude threshold

Amplitude of the seismic signals induced by rockfall as they propagate away from the source depends on a number of factors which are not always possible to model accurately, including the surface and sub-surface ground conditions. Correlation between the impact energy and the peak ground velocity has been consistently observed in this research, and a statistical approach to modeling of the PGV has been used. In a number of previous studies of dynamic soil compaction and construction site vibration, log-linear regression models were applied to describe the decrease of amplitude as a function of epicentral distance.

An approach to the identification of hazardous rocks in real time has been developed that uses an empirical PGV threshold model obtained in a series of calibration tests. A 115kg weight approx. equivalent to a 0.046 m^3 rock dropped from 2.5 m elevation was used to obtain the PGV threshold for automatic recognition of hazardous rocks. The trigger threshold is applied in a 2D grid search procedure and, if a location is found at which the recorded PGV exceeds the threshold, the SRFDS reports a hazardous rock. This procedure was implemented in the SRFDS/ Data Analysis software that was tested in the field in real time, and used to model SRFDS based on historical data (Chapter 5).

It is assumed that impacts of hazardous rocks can be modeled in the system calibration tests; and that the consistent ground response to the surface impacts can be ascertained experimentally. In practice, a near-vertical rock face appears to be the only type of geology that meets these expectations. To illustrate the opposite example, a debris flow carrying pebbles can potentially cause a derailment; yet, it does not seem to be possible to model such a scenario. It is also expected that a) the selected calibration rock and the minimum drop elevation are representative of the hazardous conditions that the SRFDS has to report; and that b) larger rocks will induce ground vibrations with larger amplitude. It is further assumed that, once

the system trigger threshold has been established in a series of calibration tests, the geotechnical conditions of the site will not change in such a way as to weaken the ground response to hazardous rocks, *e.g.* due to weather (precipitation, temperature) or accumulation of soft deposits at the bottom of the slope. If the ground response is found to depend on the location, the lowest PGV observed across the test site should be utilized as the empirical PGV threshold. For this purpose, test drops need to be carried out along the entire site. In order to plan the system calibration procedure, trajectory models (*e.g.* free-falling, rolling), minimum elevation, and rockfall volume distribution are required for the instrumented site.

Field observations of natural and anthropogenic seismic signals are summarized in Table 3.2 which contains their peak amplitude (column [2]) and the number of triggered sensors (column [3]). Frequency of the events (column [4]) is estimated as *high* if, in the worst case scenario, they occur more than once a day; otherwise this parameter is *low*. Columns [2] and [3] give a qualitative estimate of the chances of the SRFDS becoming triggered by the specific seismic signal. Col.[4] describes the annoyance factor associated with the SRFDS raising a false alarm.

The ground vibrations can be caused by anthropogenic or natural factors; with regard to the propagation media, seismic, electro-magnetic and acoustic events have been observed. Electro-magnetic interference can be efficiently reduced with proper cable shielding and equipment grounding with the exception of unusually strong sources, *e.g.* lightning strikes. Acoustic noises induced by remote traffic, aircraft, or motorboats propagate as pressure waves in the air, and, when acoustic waves excite the ground, are detected by geophones; typically, these signals are too weak and rare to be of concern. The most important of the event categories in Table 3.2 are rockfalls, railway traffic, track maintenance, and electro-magnetic interference. These events occur frequently and have high amplitudes that can cause the rockfall monitoring system to raise an alarm.

EMI spikes in seismic records display regular patterns which can be identified automatically using the outlier detection algorithm. Most of the naturally occurring seismic signals related to non-hazardous events can be filtered out by applying the PGV threshold. Regular rail traffic generates periodic, time-shifted, spatially correlated seismic signals; this characteristic pattern will be used in Chapter 4 to identify trains and high-rails automatically. This task becomes more completed when trains slow down or accelerate. To suppress transients excited by train wheels hitting rail joints, the train detection algorithms described in the next chapter will use r.m.s.-averaging of train signals.

There does not seem to be a way to identify track maintenance signals in a reliable and consistent manner because they display irregular, unpredictable patterns. However, the Rail Traffic Controller is always

aware of the location of maintenance crews. Hence, these alarms can be ignored and the rockfall monitoring system can be reset by the crew before leaving the site.

In the next chapter an approach to the design of an autonomous SRFDS will be presented which will target these event categories in its decision-making logic.

Table 3.2. Summary of typical peak ground velocities observed at the SRFDS test sites in 2010-2015.

	Event type	**Number of triggered sensors[15]**	**Typical peak amplitude[16], m/s**	**Frequency of occurrence**
	[1]	**[2]**	**[3]**	**[4]**
1	Hazardous rock, ice falls	>10	1.0e-004…1.0e-002	Low
2	Non-hazardous rocks	1 to 6	1.0e-004	High
3	Trains	All	1.0e-004 …1.0e-002	High
4	Train starts and stops	All	1.0e-004 …1.0e-002	High
5	Track maintenance vehicles	1 … 10	1.0e-004 …1.0e-002	High
6	Track maintenance	Any	1.0e-004 …1.0e-002	High
7	Animals, pedestrians	3 … 8	1.0e-006…1.0e-004	Low
8	Remote railway line	All	1.0e-006…1.0e-005	High
9	EMI noise	Any	1.0e-005 …1.0e-002	High (seasonal)
10	Earthquakes	Any	1.0e-006	Low
11	Thermal noise	1..20	1.0e-005…1.0e-004	High (site-specific)
12	Tree roots	1..10	1.0e-005…1.0e-004	Low (site-specific)
13	Surface structures	5..10	1.0e-005…1.0e-004	High
14	Road traffic, aircraft, motorboats	1-10	1.0e-005	Low (site-specific)

[15] Assuming 15-20 meters between sensors.

[16] Numbers in this column are approximate, and are meant to indicate the order of magnitude for each signal category.

4. Implementation of the Autonomous Seismic Rockfall Detection System

In this section, the concept of an autonomous Seismic Rockfall Detection System will be described. The autonomous SRFDS was conceptualized based on the properties of the seismic signals observed in the field, and explain how the proposed system will process these signals automatically. Ground vibrations induced by rail traffic and track maintenance require special attention because these are the strongest and the most frequently occurring seismic events. We will introduce the concept of SRFDS self-rearming which allows the SRFDS to rearm automatically if a false alarm is revealed.

In describing the methodology, the terms *false positive event* and *false negative event* will be used which are explained in Table 4.1.

Table 4.1. The SRFDS response to the real events (modified from Cleave *et al.*, 2009).

		What happened in the reality	
		Hazardous event	**Non-hazardous event**
SRFDS response to the event	**Activated**	True Positive	False Positive
	Not activated	False Negative	True Negative

Examples of *true positive* events are rockfalls that were correctly identified and reported as hazardous as well as adverse system health conditions that were automatically identified and reported. A *false positive* event means that the system was activated by a nonhazardous event; examples of such events are trains and track maintenance signals misidentified as hazardous rockfalls, and non-hazardous rocks reported as hazardous. Trains and high-rails correctly identified and ignored by the SRFDS, as well as non-hazardous rocks correctly identified as such and ignored are examples of *true negative* events. Examples of *false negative* events are a hazardous rock misidentified as non-hazardous and not reported; and a hazardous rock misidentified as a railway vehicle and not reported.

4.1. Overview of the proposed approach to the design of an autonomous SRFDS

The key performance requirements for the rockfall detection system which are summarized below are based on the original system specifications composed by the RGHRP (Transport Canada, 2007), as well as the input from CNR and CPR received in the course of the research project:

- No false negatives: the SRFDS must not miss a hazardous rockfall;
- Some false positives are tolerated, but the number of train slow-downs should be smaller than the number of trains slowed down by SDF activations;
- The system latency should be within a few seconds and must not exceed 15 seconds; in other words, the delay between a hazardous rockfall and the SRFDS reporting it should not exceed 15 s. If the system takes too long to identify and report a hazardous rock, chances are that a train will pass the warning signal and will fail to slow down to the Restricted Speed;
- No need to identify ground vibrations generated by track maintenance. Such ground vibration, oftentimes being of the same nature as rockfall, is indistinguishable from rockfall (Figure 3.24). However, even though track maintenance may be a frequent cause of false positives, train delays can be avoided. Firstly, the RTC is aware of the presence of track maintenance personnel and their vehicles in a specific block, and until the personnel clear the block, trains are not allowed to enter it. Secondly, the maintenance crew can rearm the rockfall monitoring system before leaving the site.

It must be noted that if the SRFDS correctly identifies a hazardous rock but for some reason fails to report it (*e.g.* if the hardware or software of the data analysis PC begins to malfunction immediately after the rockfall), the adverse effects of this can potentially be as serious as the consequences of the system missing this rock altogether. This kind of situation has to do with the system health rather than with the correct performance of the rockfall detection algorithms. In the SRFDS field installations described in the previous chapters this matter was addressed by using two PCs: the Main PC programmed for data acquisition and analysis, and the WatchDog PC. Having dedicated redundancy management hardware and software that allows each computer to judge the health condition of the other, is a basic design technique which was implemented, for example, in Space Shuttle computers (Sklaroff, 1976; Lee and Anderson, 1981). The author programmed the PCs to collect and exchange system health information in

real time as well as control two sequentially wired relays independently. The output signal of the SRFDS was "1", or "Rearmed", only when both PCs had the relay contacts closed.

4.1.1. Automatic rearming of the SRFDS using train signals

The peak amplitude of the signal induced by a hazardous rockfall is typically smaller than the PGV of ground vibrations induced by rail traffic, which means that the rockfall monitoring system is incapacitated every time a train passes. However, according to CN/CP, the railway operators who supported this research, they are prepared to tolerate this deficiency. The reason is that even if the SRFDS were able to identify a hazardous rockfall within much stronger train noise, this information would be practically useless because it takes a train several hundred meters to stop (CN/CP personal communication). If such a rockfall were going to result in a derailment, it would have been impossible to avoid. On the other hand, if a train continues its journey it means that either there were no hazardous rockfalls before the train entered the block, or that the rocks were not large enough to derail the train. Thus, it is desirable for an autonomous SRFDS to be able to identify railway traffic for two reasons: firstly, not to raise a false alarm, and secondly, to confirm that there is no obstruction on the track.

In the beginning of the rockfall monitoring project it was expected that the SRFDS would be rearmed remotely after a train operator notified the RTC of the false alarm who would then reset the signal (Bunce *et al.*, 2005; Plouffe *et al.*, 2007). After it became obvious that the SRFDS could be programmed to identify regular rail traffic using seismic signals, the concept of self-rearming was introduced into the SRFDS in order to reduce the number of trains slowed down by SRFDS activations. The SRFDS uses its ability to detect the passage of a train as an indication that the track is clear. The system's self-rearming procedure is illustrated in Figure 4.1. This concept was approved by CN and CP, the railway operators involved in this research project, and implemented in the test installations.

In the previous sections it was indicated that there are two important categories of anthropogenic seismic signals that cannot be reliably identified and ignored automatically: the ground vibrations induced by track maintenance, as well as trains stops. A stationary or a slowly moving train induces seismic signals that can exceed the system trigger threshold. At the early stages of the SRFDS project, the idea of using wheel detectors for this purpose was suggested; wheel detectors offer a way to identify a train’s position within the seismic array in order to ignore the ground vibration. However, because of large gaps between wheel detectors and the need to mount them on the rails, they are not practical and do not offer an effective solution to the problem. Field tests and computer modeling have demonstrated that wheel

detectors are not required to achieve a significant reduction in the number of slowed down trains compared to SDF (Chapter 5). Instead, the SRFDS/Data Analysis module has been programmed to rearm itself when it detects a safe passage of a vehicle, either a train or a high-rail. The advantages of this approach are that the system will not require human intervention to become rearmed, and that no more than one train will be delayed by any activation. The latter means no bottleneck effects typical for SDF activations.

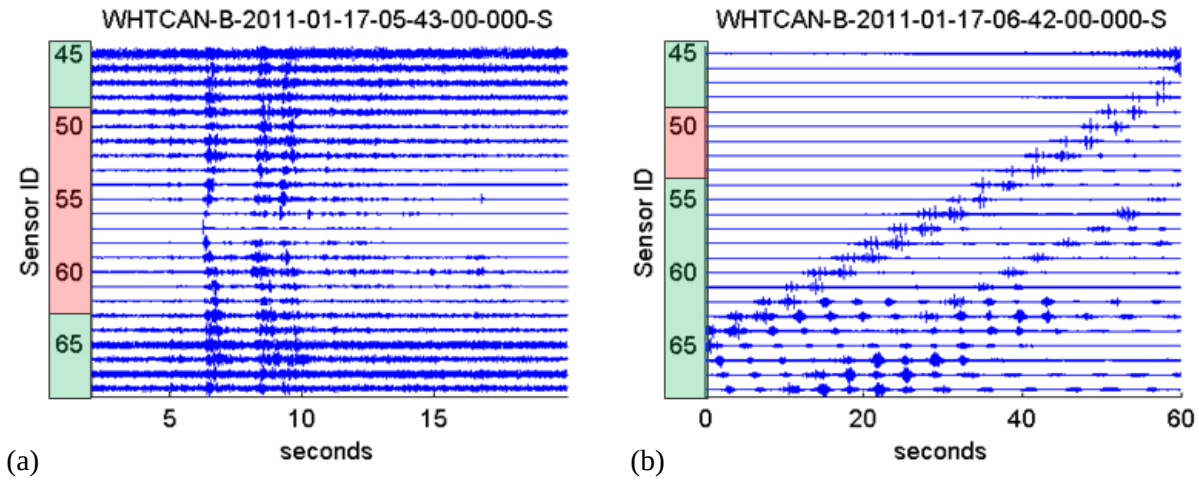

Figure 4.1. In a seismic record (a), numeric IDs of the sensors triggered (activated) by a rockfall are shown in red; the IDs of the de-triggered (or, rearmed) sensors are in green. Image (b) demonstrates how the activated sensors are de-triggered (rearmed) by a passing train.

It is safe for the SRFDS to rearm itself without a signal maintainer first inspecting the track: when the SDF is activated trains still keep coming, though at a reduced speed. The SRDFS will use regular rail traffic to assess the track condition after a hazardous event has been detected (Figure 4.1).

Similar to the SDF, the SRFDS can only be in one of two states, either Rockfall Alarm (activated/ triggered) or Clear to Pass (armed/rearmed). In the SRFDS/Data Analysis software implemented in current research, the system's alarm state is computed based on the states of the individual seismic sensors. As long as one or more sensors are in the Rockfall Alarm state, the SRFDS remains activated. For the SRFDS to be in the Clear-to-Pass state, all sensors have to be rearmed. Using sensor-based activation ensures traffic safety; the SRFDS will continue to monitor the site even after some of the sensors have been activated, for instance, by a track maintenance crew working at the site's east end. If a hazardous rockfall occurs at the site's west end, the crew's patrol high-rails will not be able to rearm the system unless they inspect the area where the rockfall occurred. In other words, a vehicle has to pass through the activated section to rearm it. Keeping track of the activations of individual sensors will also

reduce the amount of effort needed to rearm the system activated by track maintenance personnel; only the sensors where the event was detected are activated. Therefore, in order to rearm the system, a patrol high-rail does not have to travel all the way across the seismic array when the crew activity triggered only a few sensors.

The technical challenge of informing the signal maintainer of the system status can be resolved using a radio-talker broadcasting a message about system activations which can also include the extent and the location of the activated part of the SRFDS. Alternatively, he can simply let the oncoming train cause the system to rearm; however, this procedure has a specific incident cost because the train will be travelling at a reduced speed. Train stops are treated in the same way: if, after starting, the train rolls past all the sensors it has just activated, the sensors will be rearmed causing no delay for the next train. This way, the rockfall monitoring system can be operated in an autonomous mode which will rule out false negatives due to human error.

4.1.2. Identification of rockfall in the presence of ground vibration induced by rail traffic

The problem of noise, or interference of signals of interest with unwanted anthropogenic and natural signals, is ubiquitous in geophysical applications that use (sub)surface seismic sensors (*e.g.* Hardy *et al.*, 1988; Hardy and Kimble, 1991; Zimmer and Sitar, 2015). Unlike strong motion seismic arrays, a noisy environment is hard to avoid in micro-seismic monitoring because undesirable signals lie in the same frequency bands as the signals of interest, and the signal-to-noise ratio can be less than one. In addition, both the events of interest (rockfalls) and unwanted signals (*e.g.* induced by trains or pedestrians) occur in the same area. However, seismic rockfall monitoring systems have the advantage of usually being deployed along railway lines in remote areas where sources of anthropogenic noise are few and can be identified relatively easily. Some of these signals frequently display distinct patterns which can be used for their identification (*e.g.* railway traffic); others are too weak to be confused with a hazardous rockfall (*e.g.* tree roots, aircraft, animal migration). Typical peak amplitudes are summarized in Table 3.2 in the end of Chapter 3.

Hazardous rockfall can produce seismic signals with unpredictable and therefore hard-to-identify patterns. It would be risky to tune up the event detection algorithm to identify the hazardous events using past seismic events because future events may have different time-frequency patterns which can be similar to non-hazardous events, *e.g.* rail traffic. Therefore, if a signal cannot be reliably identified as non-

hazardous one, it must be considered a potentially hazardous event, or a “rockfall”, and reported to a railway operator if the event meets the trigger criteria.

The proposed approach to automatic event discrimination can be summarized in the following step-by-step algorithm executed by the SRFDS for every incoming data file:

Step [0]. Run the EMI spike detection algorithm, and remove all identified spikes;

Step [1]. For every data channel, if ground vibration is detected, run the train detection algorithms (the algorithms will be discussed later in this chapter). Typically only the rail vehicles that proceed at constant speed can be unambiguously identified using seismic sensors. If the seismic signal was not identified as having been induced by rail traffic, is it considered to have been induced by a rockfall. Proceed to Step [3].

Step [2]. If the signal is identified as having been a rail traffic event, rearm the sensor; store a traffic event record for subsequent analysis by the Traffic Tracker algorithm; skip the vehicle signal, and proceed to Step [4].

Step [3]. Utilize the Rockfall Detector procedure (Section 3.3) to analyze all signals that are not identified as rail traffic. If the signal parameters exceed the system trigger threshold, report a hazardous rockfall and put the SRFDS sensors where the rockfall was detected in Rockfall Alarm state.

Step [4]. When a rail traffic event is over, run the Traffic Tracker algorithm to ensure that the traffic events are consistent from sensor to sensor. If any inconsistencies are detected (*e.g.* a vehicle path is too short, or there are too many discrepancies between the train velocities computed at individual sensors) put the system in Rockfall Alarm state.

Below are expected responses of the proposed SRFDS to various sources of strong ground vibration.

Rockfall. Rockfalls are identified in Step [3], unless the associated ground vibration was overwhelmed by rail traffic noise.

Trains and high-rails. Regular traffic is identified in Step [1]. If the SRFDS fails to identify a train it will most likely activate because strong ground vibration induced by trains will be interpreted as a hazardous rockfall.

Track maintenance. Because of the high amplitudes and irregular signal patterns of ground vibrations induced by track maintenance, the SRFDS is likely to become activated. However, the maintenance crew can be instructed to rearm the monitoring system before leaving the site.

Train stops and starts. Train stops will be detected by the Traffic Tracker algorithm which will activate the system. However, in most cases the SRFDS will rearm itself after the train gains enough speed (Step [2]) and becomes identifiable by the SRFDS.

Electric spikes. Weak EMI spikes can be identified and removed from raw seismic data, which will occur in Step [0]. However, unusually strong spikes are likely to slip through the noise filter and activate the SRFDS in Step [3].

Animals. Typically, these signals display irregular patterns, and can be confused with actual rockfalls or high-rails, but they are rare and relatively weak. Based on the field observations, such ground vibrations usually do not exceed the system activation threshold in Step [3]. However, the SRFDS can be activated by several animals especially if they walk close to seismic sensors. The signal pattern of a running animal can look similar to that of a high-rail: the major concern about this scenario is that seismic signals induced by a moving animal can be mistaken for a high-rail and the sensors activated previously by a rockfall will be rearmed. In order to distinguish between these two event categories, the Traffic Tracker filter can be configured to pass only vehicle events of a specific minimum length, for instance, 300 m, and reject other signals (Step [4]).

4.2. Pattern recognition analysis of train signals

The need to have a technique for location and tracking of rail traffic is apparent due to the fact that trains and high-rails induce strong ground vibrations, which, if not correctly identified, will activate the system. This technique is also required in order to implement the concept of SRFDS automatic rearming, one of the main advantages of the SRFDS over the SDF. There were a number of initial attempts in this project to filter out traffic noise which involved using wheel counters and magnetometers. Both were deemed impractical because of the need to install multiple wheel sensors adjacent to the track where they would be exposed to track maintenance equipment, rockfalls and precipitation. Below we will describe several train detection algorithms which combine beam-forming, zero-mean normalized cross-correlation, and STA/LTA techniques to detect patterns of moving rail vehicles within seismic data. These algorithms will be supplemented by several techniques for detection of the end-of-train. Since trains and high-rails can start and stop anywhere within the geophone array, the identification of traffic events will be done at

the individual sensor level. Individual traffic events will then be analyzed for consistency at the seismic array level.

In the early stages of this research project an approach to vehicle detection was investigated which relied on detection of energy arrival at a sensor with a preset amplitude threshold. This is a standard detection technique in strong motion seismic systems where high sensitivity to ambient noise is mostly not an issue because these signals lie within different frequency bands, and the amplitudes of unwanted anthropogenic and natural seismic signals are much smaller than the signals which are supposed to trigger the instrument. Once a number of arrival times obtained at a group of sensors became available they were analyzed for consistency assuming that a vehicle was moving at a constant speed. This approach turned out to be impractical for several reasons, mainly because of the ambiguity of threshold selection; peak amplitudes induced by the rail traffic vary by several orders of magnitude. It is not unusual for a high-rail excavator operating 20-40 meters away from a seismic sensor to induce ground vibration that is stronger than the signal of a lightweight high-rail truck moving next to the sensor. Precursor ground vibration which propagates ahead of a train has been found to be a source of significant errors in the arrival time estimates, especially near rail expansion joints. Finally, vehicle accelerations, decelerations and starts from within the geophone array made this approach inapplicable to a large percentage of traffic events.

With regard to the frequency domain methods, seismic signals induced by train wheels and detected by rail-mounted sensors do contain high frequencies (>300 Hz) compared to those induced by rocks falling onto the embankment. However, it turned out to be impractical to mount seismic sensors under rails as it leaves them vulnerable to damage by rockfall and track maintenance equipment. Also, it is not unusual for rocks to hit ties or rails which would also result in high-frequency rail vibration. As a result, frequency domain techniques were not used in this research for train detection; instead, time-domain pattern recognition methods were developed.

The train detection algorithms presented in this chapter detect trains and high-rails by comparing seismic signals recorded at two or more sensors. This means that the SRFDS has to wait until enough data have been acquired in order to attempt vehicle identification. If it were possible to perform traffic analysis by comparing a seismogram of a moving vehicle to a template signal, we would need only one train record at a time. Unfortunately, there does not seem to be such a thing as a typical train signal: trains include

railcars of various lengths[17], railcars are coupled together in an arbitrary order; and trains change their speed arbitrarily. Based on field observations, CP and CN trains can be up to 3 km long; whereas a high-rail truck, being ~5 m long, is the shortest type of rail vehicle. In this study the length of a vehicle is not factored into the pattern recognition algorithms. Individual railcars seem to have their unique seismic signatures, perhaps, caused by imperfections on their wheels and the rail surface. In addition, each geophone operates in a unique environment, including its depth, lateral distance to the rail, proximity to rail joints and so on. All these factors have lead to the development of a vehicle detection technique based on cross-correlation of smoothed seismic signals acquired at adjacent sensors, rather than comparing them to a template signal.

Rail traffic signals will be identified within two categories:

- *Irregular*, *i.e.* trains starting within the geophone array. The identification algorithm will make no assumption as to whether the locomotive signal is available. The generic Train Detection Algorithm (TDA) described later in this chapter will target the middle part of the train signal, which comes after the locomotive;

- *Regular*, *i.e.* when a complete seismic record of a moving train is available, including the locomotive. In this case, there is less uncertainty about a vehicle's direction and speed, and fewer comparison signals are needed. This assumption will be used in the locomotive detection algorithms referred to as LDA(1) and LDA(2).

4.2.1. Identification of irregular train signals

The train detection algorithm, TDA, will utilize a trial-and-error procedure in order to detect similarities in seismic signals. The SRFDS has to identify a vehicle as soon as possible, without waiting for 3-7 min until a full train record becomes available which leads to a number of practical challenges. Rail vehicles change their speed arbitrarily, and can stop anywhere within the seismic array. Therefore, the point in time when the train signal starts together with the train's velocity are the variables of the pattern search

[17] According to CN's signal maintainers, a typical railcar is approx. 70 ft/ 20 m long; there are also 40 ft/ 13 m, 50 ft/ 16 m, and 90 ft / 30 m railcars (personal communication).

algorithm. Within this algorithm, seismic signals are correlated using 3-5 s time windows advanced in 0.25-1.0 s time increments Δt; the time delay between the correlated signals is inversely proportional to the train velocity. Since we compare the structures of seismic signals, the time window must be long enough to cover at least one structural element of the train signal. In the case of an r.m.s.-smoothed train signal such structural elements are periodic surges of seismic energy induced by railcar tracks rolling past the sensor, each surge lasting 0.2-1.0 seconds depending on the train speed.

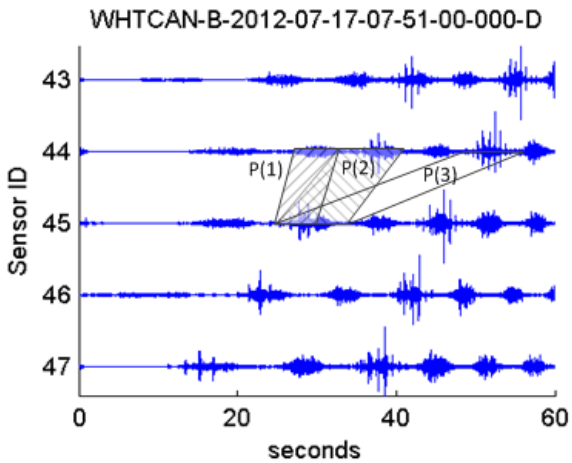

Figure 4.2. Illustration of the effect of spatial aliasing on identification of train velocity which results from using only one comparison sensor and a relatively short correlation window. This is a seismogram of a train starting within the monitored area of White Canyon. The seismogram displays an irregular signal pattern for the first 15-20 s; after the train accelerates to 11-12 km/h, the seismic signals begin to look typical for a moving vehicle. The *X*-axis displays time in seconds; the *Y*-axes are individually scaled and marked with the numeric ID of the sensor where the records were acquired, *e.g.* "47", "48".

Selection of comparison sensors

The slower the velocity used by the TDA, the longer the SRFDS has to wait until enough data is accumulated before it can attempt train detection. The length of the time window increases the overall delay in train identification. The number of comparison sensors is also important; using two or more comparison sensors greatly improves the accuracy of train velocity estimation (Figure 4.2). The trade-off is a longer delay, especially when a train is moving slowly. In order to complete the identification of a vehicle within a reasonable amount of time, the TDA performs vehicle identification using 2-5 comparison traces selected depending on the hypothetical velocity. The higher the hypothetical velocity, the larger the aperture of the sub-array needs to be to resolve the vehicle pattern.

The TDA searches for a time-delay pattern in the seismic data by computing ZNCC (zero-mean normalized cross-correlation) of the r.m.s.-smoothed reference and comparison signals within the sliding time window. If more than one comparison signal is used, individual ZNCC coefficients are multiplied. We will use mZNCC as the acronym for the cost function (a measure of similarity between the reference and the comparison signals) obtained as a product of *m* cross-correlation coefficients. The pattern identification procedure is based on the assumption that, though individual seismic signals excited by vehicles may look similar to multiple rockfalls, the arrival time delays of a vehicle signal as it moves from sensor to sensor are significantly larger compared to seismic signals induced by rockfall (Figure 4.3). In the areas prone to rockfall, trains and high-rails usually operate at speeds below 50 km/h, whereas seismic waves propagate at 100-200 m/s or faster. If, at a certain combination of vehicle speed and arrival time, the records of seismic events are found to be highly correlated (*i.e.* the cost function exceeds a pre-set threshold), this speed and arrival time are considered to be an acceptable solution of the pattern recognition routine.

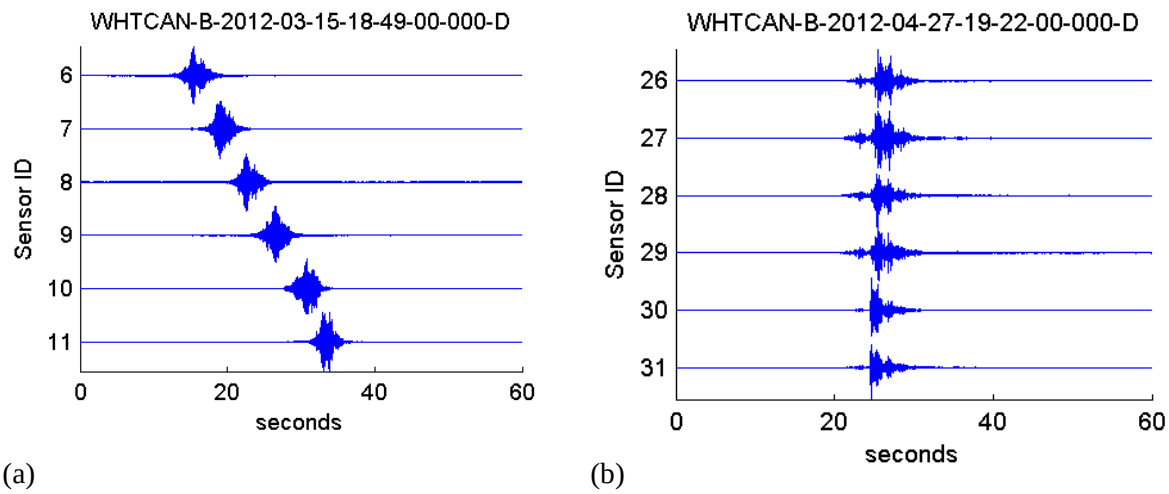

(a) (b)

Figure 4.3. Sample seismic records of a high-rail (a), and a rockfall (b), demonstrate the difference in the timing of energy arrivals. The sensors are 20 m apart.

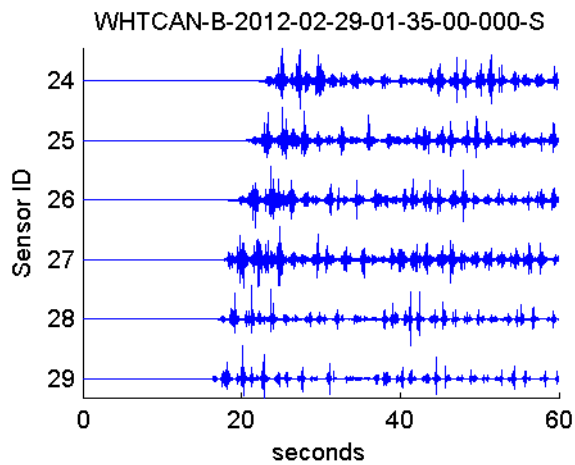

Figure 4.4. Seismic record of a train used in this section to illustrate the TDA (Figure 4.5, Figure 4.6). The *X*-axis displays time in seconds with respect to the beginning of the data file; the *Y*-axis coordinates represent sensor IDs, *e.g.* "27" is Z-27. The amplitudes are individually normalized to [-1; 1] range using each trace's PGV.

The seismic records of the train which will be used in this section to illustrate the TDA are in Figure 4.4. The data were acquired at the White Canyon site where the sensors' IDs increment in the eastern direction; thus, the train is westbound, moving from Z-29 towards Z-24. Using the distance between sensors, the estimated train speed is 12 m/s.

Signal smoothing

In order to suppress high amplitude transients that are generated by rail expansion joints while preserving low frequency surges of seismic energy induced by train wheels, two r.m.s. smoothing windows will be used (eq. 4.1), 0.2 s for detecting trains whose velocity is above 20 km/h [~5.6 m/s], and 1.0 s window for slower trains. In Figure 4.5 the first few seconds of r.m.s. -smoothed train signals are shown; the peak amplitudes of r.m.s. values are normalized to [0; 1] range.

$$x_{RMS}(i) = \sqrt{\frac{1}{N^{RMS}} \sum_{j=i-N_{RMS}+1}^{i} \left(x_j\right)^2} \tag{4.1}$$

where N^{RMS} is the number of data samples within the smoothing window.

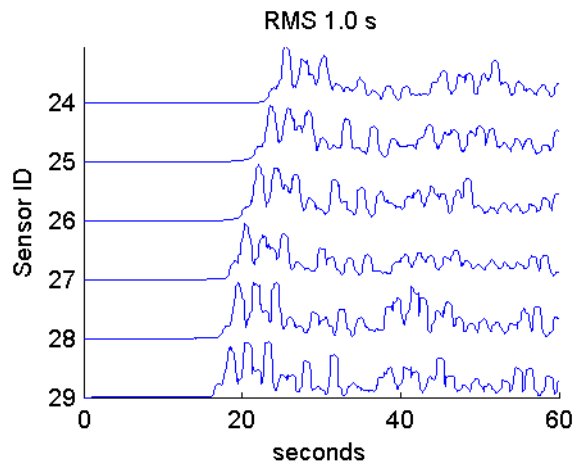

Figure 4.5. The r.m.s.- smoothed locomotive signals used for train detection analysis in Figure 4.6.

The width of the cross-correlation window depends on the tested velocity; for faster trains shorter windows are used. A linear relationship based on the average railcar length was obtained for calculation of the cross-correlation window $w^{ZNCC}(v)$ as a function of train velocity:

$$w^{ZNCC}(v) = w_{min}^{ZNCC} + \left(v_{max} - v\right) * \frac{\left(w_{max}^{ZNCC} - w_{min}^{ZNCC}\right)}{\left(v_{max} - v_{min}\right)}$$

where v_{min} = 2.5 m/s; v_{max} = 19 m/s; w_{min}^{ZNCC} = 3 s; w_{max}^{ZNCC} = 5 s.

The vehicle pattern

In Figure 4.6 a velocity *vs* time plot of mZNCC coefficients computed for westbound traffic is shown. The cost function was computed by advancing the cross-correlation window at Δt = 0.25 s increments, and varying velocities between v_{min} = 2.5 m/s and v_{max} = 19 m/s in 0.25 m/s increments. Sensor Z-24 was used as the reference.

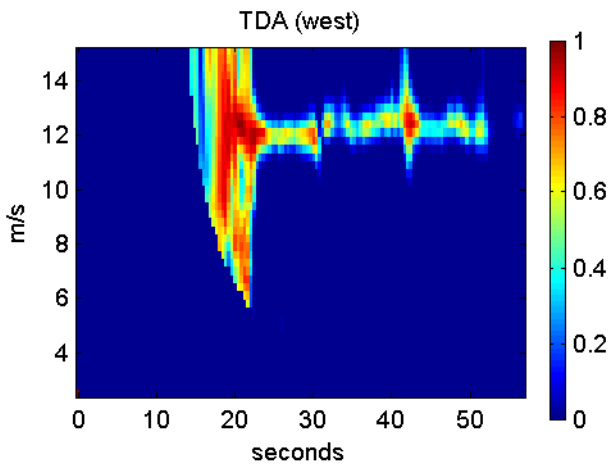

Figure 4.6. Velocity *vs* time plot of cost functions (mZNCC) of a train signal in Figure 4.4 and Figure 4.5. Each cell contains a product of the ZNCC computed assuming a westbound train; five comparison traces were used. The train precursor pattern demonstrates the signal blurring effect of r.m.s.-smoothing onto the precursor ground vibration. Between 30 s and 50 s the train pattern is slightly bent upward which is indicative of the train's acceleration.

Using Figure 4.6 as an illustration, a correlation coefficient contained in the ||mZNCC|| matrix cell with coordinates {time = 21 s; speed = 12 m/s} is 0.6. Based on the field tests, if a pair of r.m.s. signals correlates at 0.85 or better, this is indicative of a traffic pattern. Since five comparison sensors were used in this example (m = 5), the threshold becomes $0.85^5 = 0.37$. Thus, all elements of ||mZNCC|| matrix in Figure 4.6 that are greater than 0.37 mean that a corresponding pair of {time; speed} values can be a potential solution of the Train Detection Algorithm. If we compare this plot to the source data in Figure 4.4 we will see that 21 s is the arrival time of the locomotive at Z-24.

In the cost function image in Figure 4.6 two distinct patterns can be observed: horizontal and vertical. The predominantly horizontal pattern which starts around 21 s and continues at v = 12 m/s across the mZNCC plot, is composed of relatively high correlation coefficients (the “train pattern”). It should be noted that there are gaps in the train pattern due to inconsistencies in the source signals, for instance, due to train acceleration and different operating environments of individual sensors. The train pattern is surrounded by near-zero mZNCC values that correspond to speeds faster than 13 m/s and slower than 11 m/s. After two matrices of mZNCC cost functions have been computed, one based on the hypothesis of an

eastward train, and the other for a westward train, the TDA algorithm scans them along the time and velocity axes, looking for the characteristic train pattern[18]. This pattern has to be at least several seconds long and no more than 2-4 m/s wide in order to be indicative of a moving vehicle.

The vehicle precursor pattern

The second observation about the mZNCC plot concerns the vertically oriented pattern of high mZNCC coefficients that precedes the train pattern. The area is several seconds wide extending from 17 s to 21 s along the time axis, and from 5 m/s to 19.5 m/s along the velocity axis. By comparing the time coordinates of this area and the source data (Figure 4.5) we can conclude that the highly correlated signals are the seismic waves induced by an approaching locomotive. They propagate 100-200 m ahead of the train and have relatively low amplitude compared to the train signal. When r.m.s.-smoothed, this emergent precursor vibration forms a quasi-linear trend in the direction of the approaching train. Because this precursor signal has no periodic structure, as opposed to the middle part of the train signal, cross-correlation cannot resolve the train's velocity. As a result, within the train precursor pattern essentially any velocity from $\{v_{min}; v_{max}\}$ range will deliver satisfactory, though inconsistent, results. For example, estimates of the train's velocity obtained at different sensors can vary by 5-10 m/s, which is undesirable if the TDA output is cross-checked to validate the algorithm's real-time performance. More importantly, the mZNCC matrix computed for a rockfall signal displays the same "train precursor" pattern (*e.g.* Figure A.7). In other words, the "train precursor" pattern within the cost function image does not uniquely identify a train signal as one being induced by a train. A negative side effect of this is the necessity for the TDA algorithm to skip the precursor pattern, which delays train (and therefore rockfall) identification by 10-15 s. These weaknesses of the TDA algorithm prompted further experiments with train identification techniques which resulted in two locomotive detection algorithms discussed further in this chapter.

In an attempt to suppress the vehicle precursor pattern within ||mZNCC||, the following modification of the normalized cross-correlation formula was used:

---

[18] The TDA algorithm performs a simple 2D scan by applying a pre-set correlation threshold in order to detect the characteristic train pattern within the mZNCC image. Also, the Hough transform can be used to identify lines in the image (Duda and Hart, 1973).

$$R_i^{N,w}(\boldsymbol{a},\boldsymbol{b}) = \frac{\sqrt{\sum_{j=i-N+1}^{i}(a_j-\bar{a})(b_j-\bar{b})}}{\left(\sqrt{\sum_{j=i-N+1}^{i}(a_j-\bar{a})^2}+w*\sigma_{\bar{n}}\right)\left(\sqrt{\sum_{j=i-N+1}^{i}(b_j-\bar{b})^2}+w*\sigma_{\bar{n}}\right)} \tag{4.2}$$

where $\sigma_{\bar{n}}$ is the r.m.s. of the background noise, $\bar{n}$ (*e.g.* the noise floor of the data acquisition system) within the correlation window, $w^{ZNCC}(v)$;

w is an arbitrary weight of the background noise.

The idea of weighted ZNCC is based on the assumption that rail traffic generates seismic signals with a high signal-to-noise ratio; therefore, adding the weighted energy of the background noise to the normalization coefficients is not expected to significantly reduce the cost function in the middle of the train signal, whereas the correlation coefficients of a train's precursor signal will be reduced. Though in some cases this technique improved the quality of train pattern (Figure 4.7), it did not perform well in general because it was not clear what noise weight *w* should be used. For instance, PGV of high-rails can be of the same scale as the locomotive precursor vibration. This turned *w* into another variable of the trial-and-error pattern identification algorithm, and this research avenue was abandoned.

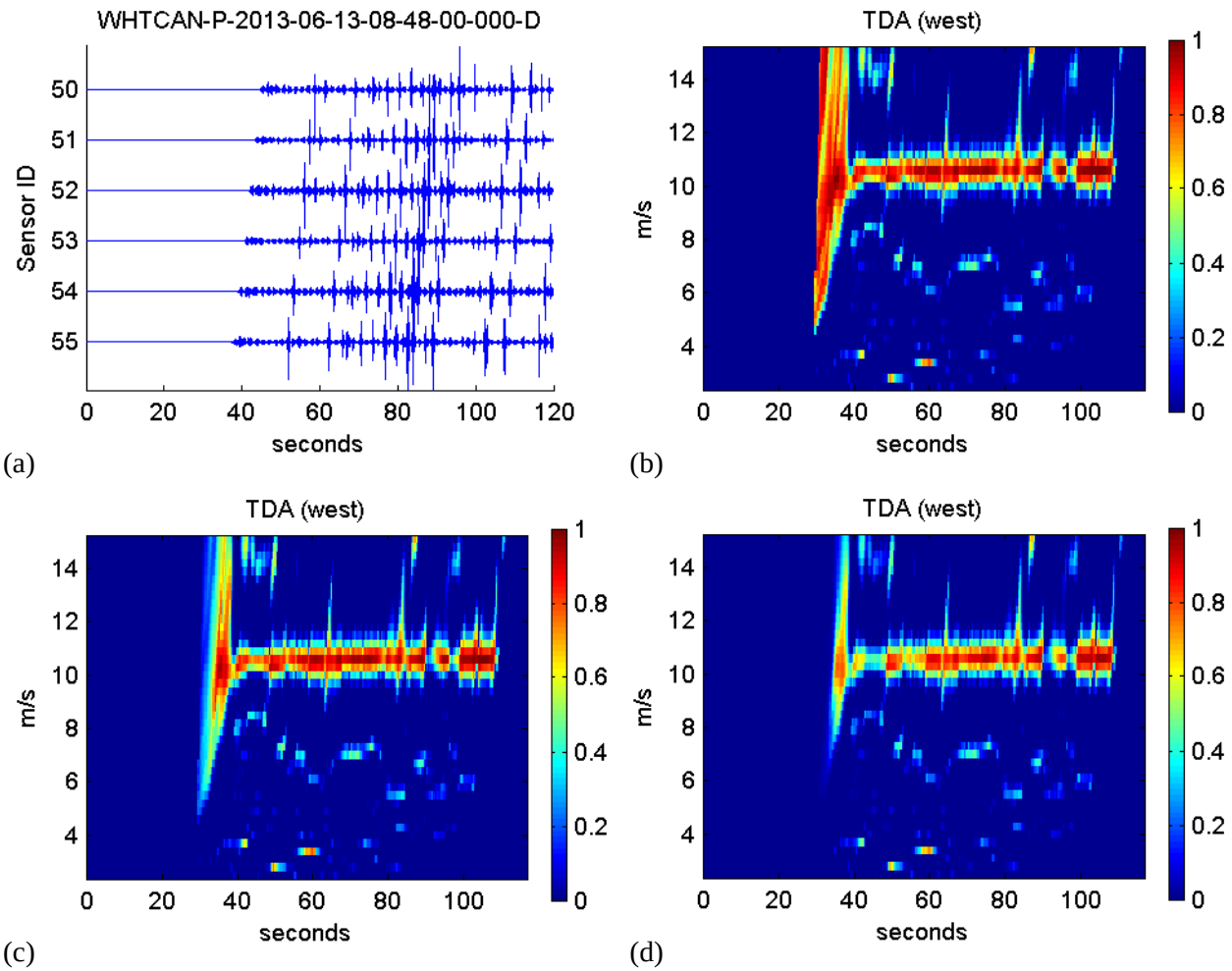

Figure 4.7. Train detection using weighted ZNCC and two reference sensors (the TDA). (a) 120 seconds of seismic data acquired with the reference sensor Z-55 and two comparison sensors, Z-50, Z-51; (b) cost functions (mZNCC) obtained for a westbound train, weight w = 0.0; (c) weighted mZNCC with sensitivity weight w = 1.0; (d) weighted ZNCC with sensitivity weight w = 10.0. With larger sensitivity weights, the vehicle precursor pattern observed at 30 s begins to shrink.

Seismic records of individual railcars often display distinct seismic signatures, apparently caused by the combination of their weight and the imperfections on their wheels (*e.g.* Figure 4.4). Averaging train signals suppresses individual transients and can have an aliasing effect on the cost function which is observed in the middle part of the train signal. In other words, r.m.s.-smoothed envelopes of the seismic signals induced by different railcars may correlate well which leads to uncertainty in the identification of train velocity (Figure 4.2). In Figure 4.8, two cost functions (mZNCC) were computed based on the

hypotheses of westbound and eastbound trains. Both cost function images display patterns indicative of a moving train, while in fact the train is actually westbound.

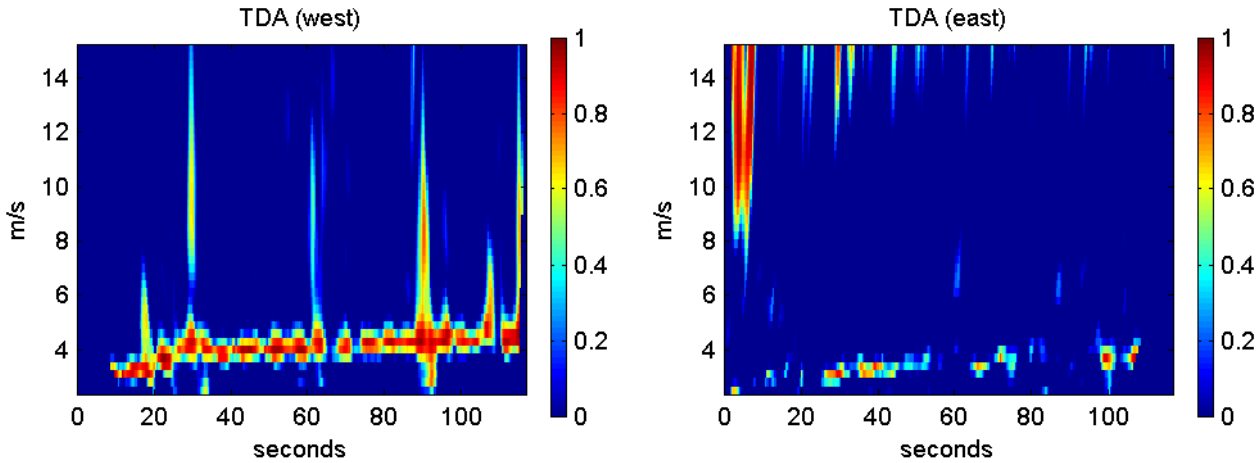

(a) (b)

Figure 4.8. This example demonstrates the negative effect of aliasing of train signals which can result in inconsistent output of the TDA. The cost function mZNCC in plot (a) was computed based on the hypothesis of a westbound train, while the mZNCC in (b) was computed assuming an eastbound train. While the train is actually westbound, at 25-40 s image (b) displays the pattern of a train that is moving east at 3-4 m/s.

4.2.2. Identification of regular trains

The TDA targets the middle section of the train signal which begins after the locomotive and contains periodic signal patterns. The ZNCC-based TDA is not sensitive to transients within this part of the train signal because of higher signal-to-noise ratio compared to locomotive precursor signals. For identification of regular traffic (*i.e.* trains that pass by the sensor array without stopping and whose seismogram contains the locomotive signal), a pattern search algorithm based on STA/LTA technique will be used.

The "short-time-average *versus* long-time-average trigger", STA/LTA, is the most broadly used algorithm in seismology where it is known to be beneficial at seismically quiet sites where earthquake signals are the dominant type of events (Trnkoczy, 2002). The STA/LTA algorithm uses two sliding time windows in order to filter seismic signals, a short-time average window (STA) and a long-time average window

(LTA). The STA measures the "instantaneous" amplitude of the seismic signal while the LTA stores the current background noise amplitude. The STA/LTA algorithm continuously evaluates the changes in the seismic noise amplitude at the geophone and automatically adjusts its sensitivity to the actual level of background noise. Because the STA/LTA algorithm uses averaged signals, it is less sensitive to the transients (spike-type noise) than the preset amplitude threshold.

In the context of rail vehicle detection, there is always a gap of several seconds between high-rails, and a gap of at least a few minutes between trains; thus, the LTA component of the STA/LTA detector has time to adjust to the quiet environment. In order to configure the STA/LTA for locomotive or high-rail detection, one has to select the following:

- STA time window. The SRFDS uses two STA windows: 1 s window for vehicles moving at a regular speed (>12 km/h, or 3.3 m/s); the other, longer window (2 s), is for trains moving at Restricted Speed;

- LTA time window. Similar to the STA configuration, two LTA time windows were used: 5 s window for regular traffic, and 10 s for trains moving at Restricted Speed. The LTA must be long enough to "remember" the relatively weak ground vibration preceding the vehicle arrival ("precursor signal") in order for the STA/LTA ratio to increase. The two STA/LTA configurations are applied in a trial-and-error pattern search procedure;

- STA/LTA trigger threshold. Since a 1:5 time window ratio was used, the trigger ratio cannot exceed 5; an empirically obtained threshold, STA/LTA = 3.5, was utilized for vehicle detection.

Figure 4.9 illustrates locomotive detection using STA/LTA. When a locomotive approaches a sensor, the STA increases much faster than the LTA, and the STA/LTA ratio displays a surge. The STA/LTA exceeds the threshold and then drops to ~1.0 after the LTA catches up with the STA. The STA/LTA surges induced by a steadily moving locomotive result in a characteristic time delay pattern which can be detected automatically. Similar to the TDA, the time-delay between the STA/LTA surges that occur at the reference and the comparison sensors is important for reliable train detection. The fact that the STA/LTA exceeded the threshold does not necessarily mean an arrival of a vehicle; it could be induced by a rockfall. In order to estimate the train velocity, the STA/LTA signals at sensors installed 15-90 m apart are compared, which is similar to cross-correlation of r.m.s. signals within the TDA algorithm. The discrepancy between the reference and the comparison signals (*i.e.* the cost function) can be measured: the STA/LTA of the reference and the comparison sensors are normalized with their peak values within the sliding time window and compared using L^{∞} norm. The discrepancy between the reference $\{\boldsymbol{a}_i\}$ and

comparison $\{\boldsymbol{b}_i\}$ vectors is computed as $\|\boldsymbol{a}_i - \boldsymbol{b}_i\|_\infty = max\{|a_1 - b_1|, \dots, |a_n - b_n|\}$. When L^∞ norm is applied to similar signals, its output is close to zero; whereas when the normalized signals are sufficiently different, the output is close to 1.0. Based on the field tests, $\|\boldsymbol{a}_i - \boldsymbol{b}_i\|_\infty < 0.3$ is indicative of a locomotive arrival. Since there is no ambiguity with respect to the train direction when a locomotive signal is available, only one comparison sensor is needed.

The output of the locomotive detection algorithm which will be referred to as LDA(1), is a matrix of cost functions and it can be visualized as a velocity *vs* time plot, similar to that generated by the TDA algorithm (Figure 4.12 (f)). In order to bring the cost functions computed by the TDA and the LDA(1) into the same frame of reference ("larger cost function means more similarity between the reference and the comparison signals"), the output of the LDA(1) is plotted as (1.0 - $\|\boldsymbol{a}_i - \boldsymbol{b}_i\|_\infty$).

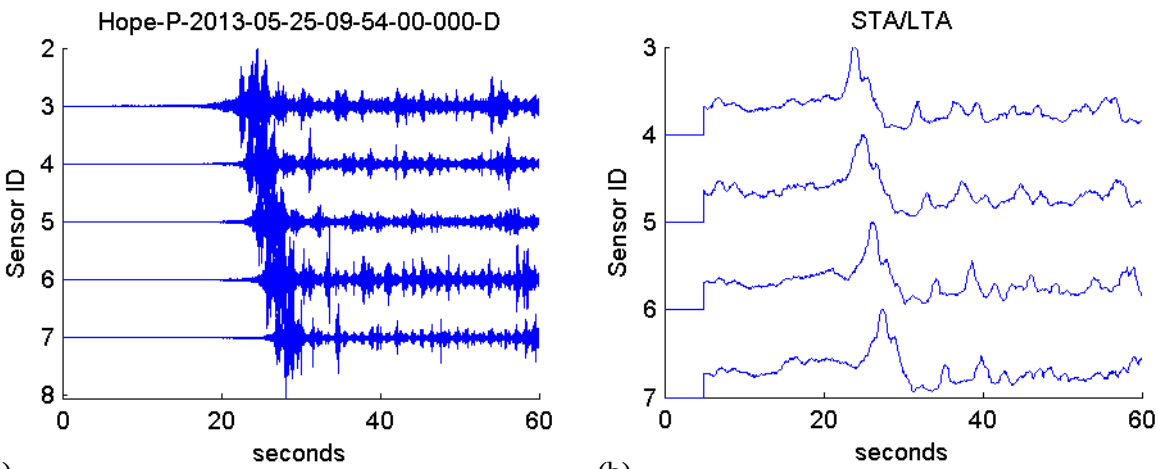

(a) (b)

Figure 4.9. (a) Seismic signals induced by a train; (b) STA/LTA, where $w^{LTA} = 5$ s, $w^{STA} = 1$ s; first 5 seconds of STA/LTA are zeroed because there is not enough data to compute LTA.

The following formulas have been used to compute STA/LTA values, $\gamma^j_{STA/LTA}(t_i)$:

$$\gamma^j_{STA}(t_i) = \frac{1}{N_{STA}} \sum_{m=i}^{m-N_{STA}+1} |x^j_m| \tag{4.3}$$

$$\gamma^j_{LTA}(t_i) = \frac{1}{N_{LTA}} \sum_{m=i}^{m-N_{LTA}+1} |x^j_m| \tag{4.4}$$

$$\gamma^j_{STA/LTA}(t_i) = \frac{\gamma^j_{STA}(t_i)}{\gamma^j_{LTA}(t_i)} \tag{4.5}$$

where $t_i = t_0 + i * \Delta t$; j – sensor index; Δt – sampling interval.

N_{STA} and N_{LTA} are the number of data samples within the STA and LTA windows respectively.

The performance of LDA(1) can degrade in the presence of precursor seismic signals excited by the locomotive wheels hitting the rail expansion joints. This can lead to higher-than-expected discrepancies between STA/LTA signals and a failure of the LDA(1) to identify the locomotive pattern.

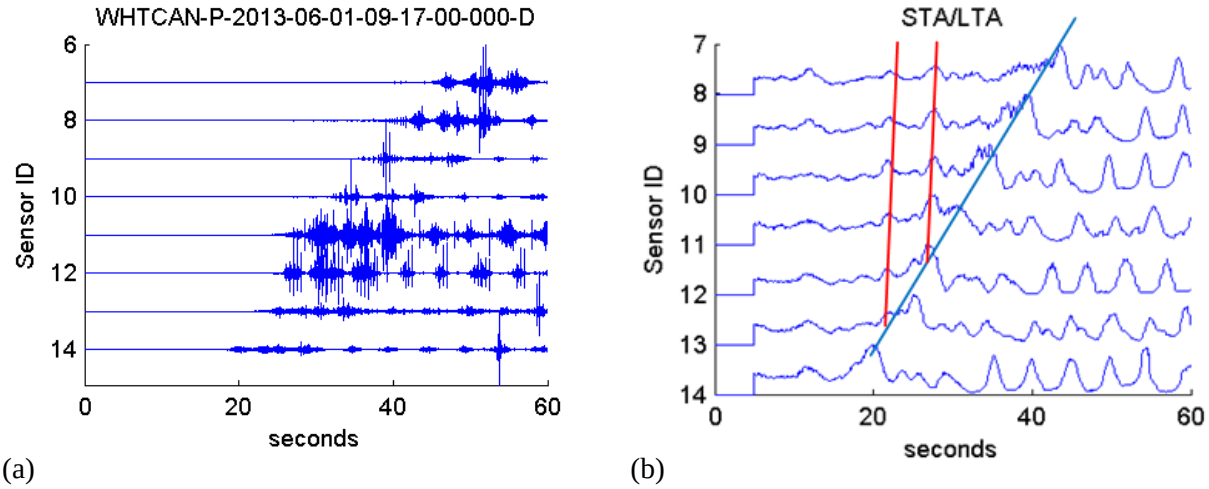

(a) (b)

Figure 4.10. The presence of rail expansion joints results in train precursor vibration and near-simultaneous surges of STA/LTA which is highlighted with the red lines. The move-out pattern of the STA/LTA surges induced by the locomotive arrivals is highlighted with the blue line.

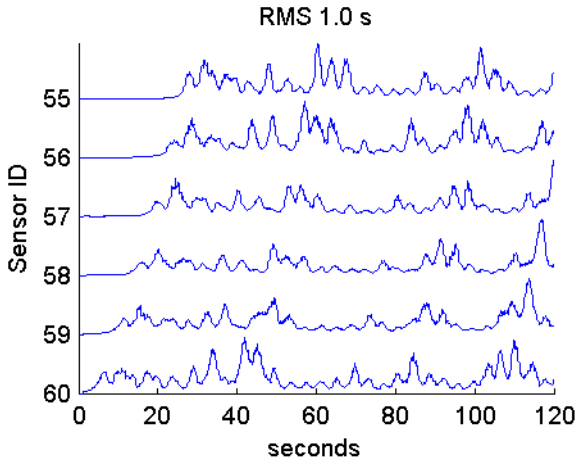

Figure 4.11. Time-adjusted envelope of locomotive signals can be consistent at different sensors; this property is used for train detection in the LDA(2) algorithm.

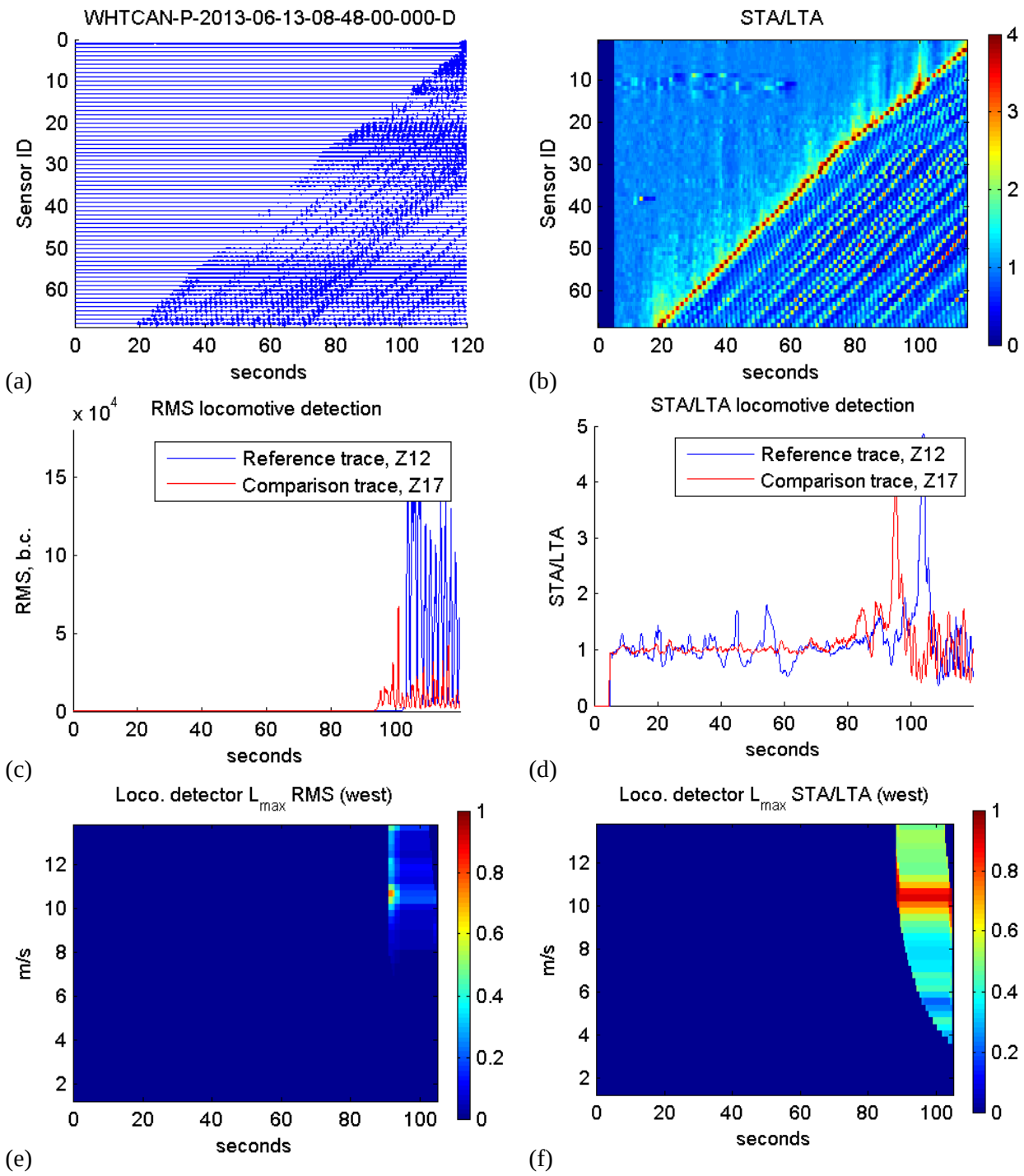

Figure 4.12. Detection of a locomotive using STA/LTA (LDA(1)) and r.m.s. data (LDA(2)). (a) 120 s of seismic data; (b) STA/LTA; (c) r.m.s.-smoothed data at Z-12 (reference sensor) and Z-17 (comparison sensor); (d) STA/LTA at Z-12 (reference sensor) and Z-17 (comparison sensor); (e) LDA(2) detector; (f) LDA(1). Both techniques identified the locomotive at 90 s with 74% and 97% matching level, respectively. The blue area in (e) and (f) means that the reference and comparison signals were not processed because the STA/LTA was too low, *i.e.* not indicative of a vehicle arrival.

The LDA(2) is a modification of the LDA(1) which utilizes r.m.s.-smoothed data, rather than normalized STA/LTA, to compute the cost function. This pattern detection algorithm is less sensitive to the precursor noise near the tunnels and rail joints, because the precursor noise is weaker than the actual locomotive signal in the vicinity of a sensor (Figure 4.11). The cost function of the LDA(2) detector is shown in Figure 4.12 (e)).

LDA(1) and LDA(2) techniques can also be used to identify high-rails. Formal descriptions of the vehicle detection algorithms introduced in this chapter are in Appendix B. Examples of train and high-rail detection with the TDA, LDA(1) and LDA(2) are in Appendix A.

4.2.3. Tracking the rail traffic

Strong ground vibration induced by rail traffic is the only "excuse" for the SRFDS not to report a hazardous rock. Therefore, it is important for the SRFDS, after it has identified a moving rail vehicle, to go back into the rockfall detection mode as soon as the vehicle signal is over. A number of techniques can be used to detect the end of vehicle signal.

The end-of-train detection techniques

In the absence of other sources of seismic signals, the amplitude of ground vibration generated by a departing vehicle drops to the background noise level within 5-20 s, depending on the velocity, which results in a STA/LTA trough because the STA drops faster than the LTA. This effect can be exploited to detect the end-of-train (EoT) by applying a threshold to the STA/LTA trough. In Figure 4.13 we demonstrate how the EoT is detected. Several parameters need to be specified in order to configure the EoT detector: STA window, w_{EoT}^{STA}; LTA window w_{EoT}^{LTA}; the EoT trigger threshold, $R_{EoT}^{STA/LTA}$; and the minimum amount of time , $w_{EoT}^{STA/LTA}$, that the STA/LTA ratio stays below $R_{EoT}^{STA/LTA}$. For high-rails and trains moving at Track Speed the following parameters are used: w_{EoT}^{STA} = 2 s, w_{EoT}^{LTA} = 10 s, $R_{EoT}^{STA/LTA}$ = 0.2, and $w_{EoT}^{STA/LTA}$ = 6 s. For trains moving at Restricted Speed: w_{EoT}^{STA} = 2 s, w_{EoT}^{LTA} = 30 s, $R_{EoT}^{STA/LTA}$ = 0.4, and $w_{EoT}^{STA/LTA}$ = 30 s.

If the train is moving slower than Restricted Speed, STA/LTA is less likely to have a long trough, in which case this technique may fail to identify the end of the train signal and other techniques should be applied:

1. A pre-set threshold can be used to detect the absence of seismic signal. If the peak amplitude of the seismic signal drops below a specific threshold, we can assume that the train is either gone or stopped.

2. Detect the end of the train pattern in the TDA cost function image (Figure A.6). This method's weakness is that sometimes inconsistencies in the train signal result in a gap within the train pattern (Figure 4.6).

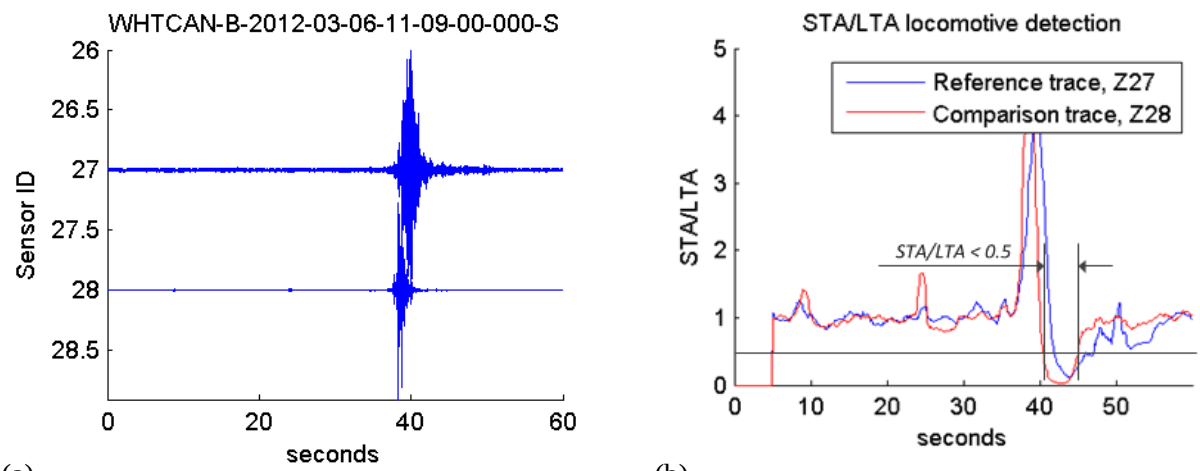

(a) (b)

Figure 4.13. Application of the end-of-train detection technique based on the STA/LTA to high-rail signal (a). Both STA/LTA curves have ~5 s long depression where STA/LTA < 0.5 which indicates that the vehicle signal is over (b).

Traffic tracking

The train velocities and departure times obtained at individual sensors need to be consistent across the seismic array. After a vehicle passage has been identified by the TDA/LDA at the sensor level, individual event records are further analyzed by the Traffic Tracking Algorithm (TTA) at the system level. For example, the TTA can be programmed to check that individual vehicle events have consistent velocities, and that the vehicle was detected at a specific minimum number of sensors, *etc*.

There are a number of reasons for introducing the TTA into the SRFDS data analysis framework. First, in order to minimize the delay in reporting rockfalls, traffic identification is attempted as soon as possible,

without waiting for the complete seismic record of the train to become available (which can take up to several minutes). On the down side, the SRFDS cannot see the big picture at the time when a traffic event is being identified at an individual sensor. The second reason is that sometimes migrating animals induce seismic signals whose patterns look similar to rail traffic (Figure 4.14). Such signals can be misinterpreted by the SRFDS as an indication that there is no obstruction on the track.

In Figure 4.14, the time-delay patterns of seismic signals generated by animal movements display a strong resemblance to the records of a moving vehicle, including the peak amplitudes. If one used only local signals for traffic identification without a follow-up check of the vehicle's full trajectory, this signal would have been identified as non-hazardous by the SRFDS. In order to differentiate high-rail signals from those of migrating animals, a minimum path threshold (*e.g.* 200 meters) can be applied to the vehicle path. In addition, the dominant frequencies of many high-rail and train signals can be used to identify an approaching train (*e.g.* Figure 3.65, Figure 3.67, and Figure 3.76).

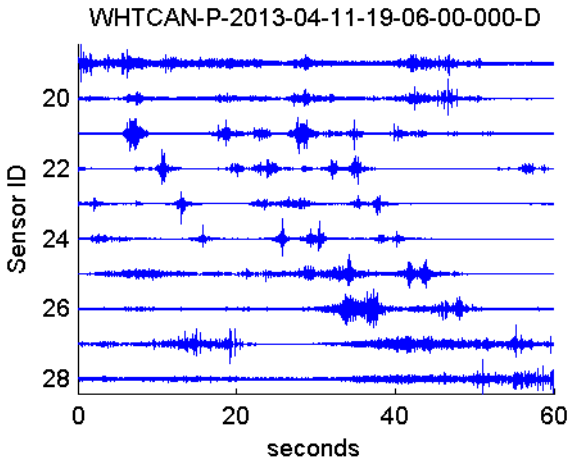

Figure 4.14. In this example, seismic signals induced by animal migration look similar to rail traffic signals.

4.3. Identification of rockfall patterns

The rockfall detection procedure described in Section 4.1.2, relies on negative decision logic. It begins by detecting all signals that deviate from the train patterns, which are then analyzed as potentially hazardous rockfalls. In the presence of frequent and strong anthropogenic signals (trains) this approach incurs undesirable delays in reporting hazardous rockfalls, because ground vibration induced by rocks first needs

to be analyzed by the train detector algorithms. Alternatively, a trigger algorithm based on detection of known rockfall patterns is an example of positive decision logic. If such an algorithm is applied to seismic signals before train identification is complete, this would minimize the system latency in reporting hazardous rocks. The two approaches are not mutually exclusive and can be combined within the SRFDS data processing workflow.

A technique for real-time rockfall recognition will be presented below which is based on a coincidence trigger (also called an array, or network, trigger) and zero-lag cross-correlation (ZLCC) of r.m.s.-averaged data. Generally, the methods based on cross-correlation can be computationally intensive; however, ZLCC will be applied only to pairs of adjacent stations. We will also demonstrate how the STA/LTA trigger can be adapted for rockfall detection in the presence of rail traffic noise. STA/LTA will be combined with zero lag cross-correlation in order to filter out signal patterns associated with rail traffic.

4.3.1. Rockfall detection with zero-lag cross-correlation (ZLCC)

For low latency detection of hazardous rocks a modification of the matched filtering technique that was implemented in the Train Detection Algorithm will be used. The difference is that the sliding time window w^{ZLCC} is the same for both the reference sensor and the comparison sensors, and only one comparison sensor will be used. The time adjustments are not applied to the comparison traces (in other words, the time adjustment is 0.0 seconds), and the seismic data is correlated using a zero time lag. The technique is referred to as the ZLCC algorithm. Similar to the TDA, this algorithm uses signal envelope obtained through r.m.s. smoothing, and it searches for rockfall patterns within a sliding time window advanced in time increments Δt, since the arrival time of the seismic signal induced by rockfall is one of the variables. Because the travel time adjustment is zero seconds for all pairs of sensors, one cross-correlation matrix $\|R_{max}^{N}(t_i)\|$ can be computed for the entire sensor array. $\|R_{max}^{N}(t_i)\|$ is N x T matrix, where N is the number of sensors in the array; T is the number of cross-correlation windows used. Elements of $\|R_{max}^{N}(t_i)\|$ are defined in eq. (4.6) and (4.7). The matrix $\|R_{max}^{N}(t_i)\|$ is then analyzed in order to detect an array trigger (Figure 4.15). Thus, for each input data file:

Step [0]. Compute the envelope signals (r.m.s.);

Step [1]. Within sliding time window w^{ZLCC}, compute normalized ZLCC for each pair of adjacent sensors. For each sensor, except the first and the last one, select the largest of the two cross-correlation values, $R_{max}^{j}(t_i)$:

$$R^{j,k}(t_i) = \frac{\sum_{m=i}^{i-N_w}\left(s_m^j - \bar{s}^j\right)\left(s_m^k - \bar{s}^k\right)}{\sum_{m=i}^{i-N_w}\left(s_m^j - \bar{s}^j\right)^2 \sum_{m=i}^{i-N_w}\left(s_m^k - \bar{s}^k\right)^2} \tag{4.6}$$

$$R_{max}^j(t_i) = max\{R^{j,j-1}(t_i),\ R^{j,j+1}(t_i)\},\ j = 2, N-1 \tag{4.7}$$

$$R_{max}^1(t_i) = R^{1,2}(t_i);$$

$$R_{max}^N(t_i) = R^{N,N-1}(t_i);$$

where $\{s_m^j\}$ – r.m.s.-smoothed data acquired at sensor *j*;

N_w is the number of data samples within w^{ZLCC} time window;

$R^{j,k}(t_i)$ – normalized ZLCC of two data segments which start at time t_i. One data segment is acquired at sensor *j*, the other at sensor *k*;

t_i- beginning of the cross correlation window, $t_i = t_0 + i * \Delta t$;

Step [2]. Apply a pre-set cross-correlation threshold R^{ZLCC} to detect a network trigger. A characteristic pattern of correlated seismic signals induced by rockfall is demonstrated in Figure 4.15. Detection of the rockfall pattern within the matrix $\|R_{max}^N(t_i)\|$ relies on the sensitivity threshold N^{ZLCC}. If the number of highly correlated envelopes, $N^{j,k}(t_i)$, exceeds N^{ZLCC} a network trigger is flagged.

$$f^j(t_i) = \begin{cases} 1, & R_{max}^j(t_i) \geq R^{ZLCC} \\ 0, & R_{max}^j(t_i) < R^{ZLCC} \end{cases} \tag{4.8}$$

$$N^{j,k}(t_i) = \sum_{m=j}^{k} f^m(t_i) \tag{4.9}$$

$$N^{j,k}(t_i) \geq N^{ZLCC} \tag{4.10}$$

where $f^j(t_i)$ – is the flag function which returns "1" if $R_{max}^j(t_i)$ exceeds the cross-correlation threshold R^{ZLCC}, otherwise it returns zero. For example, R^{ZLCC} = 0.8;

$N^{j,k}(t_i)$ - is the number of highly correlated envelope functions between sensors *j* and *k*;

N^{ZLCC}- the critical number of simultaneously triggered sensors used as the algorithm's trigger threshold. In order to filter out signal patterns induced by train precursors and not to raise a false positive (*e.g*. Figure 4.16), this threshold has to exceed the maximum propagation distance of the precursor ground vibration. Near rail expansion joints this distance can be as large as 150-200 m. In the current study this threshold has been obtained empirically based on field observations because it depends on a number of site-specific parameters: the number and location of rail joints, speed of trains, and ground conditions.

Step [3]. If a network trigger was detected in Step [2], apply the PGV *vs* distance threshold to the windowed signals in order to identify hazardous rocks (Section 3.3).

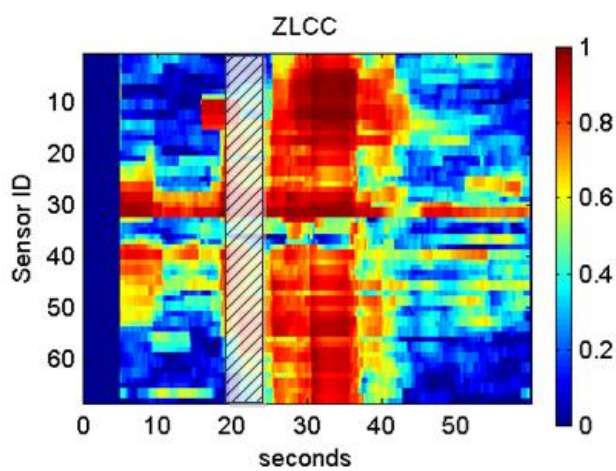

Figure 4.15. Pattern recognition analysis of a seismogram the June 5, 2013 rockfall (White Canyon) using the ZLCC algorithm. *Y*-coordinates are sensor IDs. The rectangle overlaying the ZLCC plot illustrates the network trigger window.

Because the seismic wave velocities are finite, the arrival times of seismic signals induced by rockfalls as they propagate across the seismic array are delayed by a few tens of milliseconds, assuming the sensors are 10-20 m apart. However, since the ZLCC uses r.m.s.-smoothed data, this technique does not appear to be sensitive to: minor travel time delays; amplitude decay due to geometrical spreading; nor frequency-

dependent intrinsic attenuation effects as a seismic wave travels between sensors. For instance, in Figure 4.15 signal envelopes correlate at 0.8-1.0.

Since the source data are r.m.s.-averaged, envelopes can be sub-sampled in Step [1] which reduces the amount of computations and allows for pattern-matching in real-time.

The ZLCC technique has been applied to ground vibration induced by rockfalls (Figure 4.15), a train (Figure 4.16), and a high-rail (Figure 4.18). In all examples, w^{RMS} = 1 s, the correlation window w^{ZLCC} is 5 s and it is advanced in Δt = 0.2 s time increments. Negative ZLCC values within $\|R^N_{max}(t_i)\|$ are replaced with zeros because a negative correlation coefficient means dissimilar waveforms recorded at adjacent velocity transducers, which is not indicative of a rockfall.

The ZLCC technique is sensitive to transients near rail expansion joints (Figure 4.16), and it sometimes produces inconsistent patterns near the rockfall epicenter. Figure 4.15 demonstrates $\|R^N_{max}(t_i)\|$ computed for one of the largest rockfalls recorded in White Canyon during the four years of field tests. Similarity of waveforms resulted in highly-correlated signal envelopes around 20-35 s. However, there is a discontinuity within the seismogram-image in the middle of the highly correlated area (sensors Z-32 to Z-38 at 15-32 seconds, also see Figure 4.21). The rockfall material covered about 100 meters of track; the extent of the area between Z-32 and Z-38 that was buried under debris was several times greater than the distance between sensors. The discontinuity within the $\|R^N_{max}(t_i)\|$ image is due to uncorrelated waveforms induced at the epicenter sensors by strong near-field ground vibration. Such discontinuities result in undesirable fragmentation of rockfall patterns. In order for the array trigger detector (Step [2]) not to miss a hazardous rockfall, such discontinuities can be filled in programmatically with R^{ZLCC} values within Step [1] of the ZLCC algorithm.

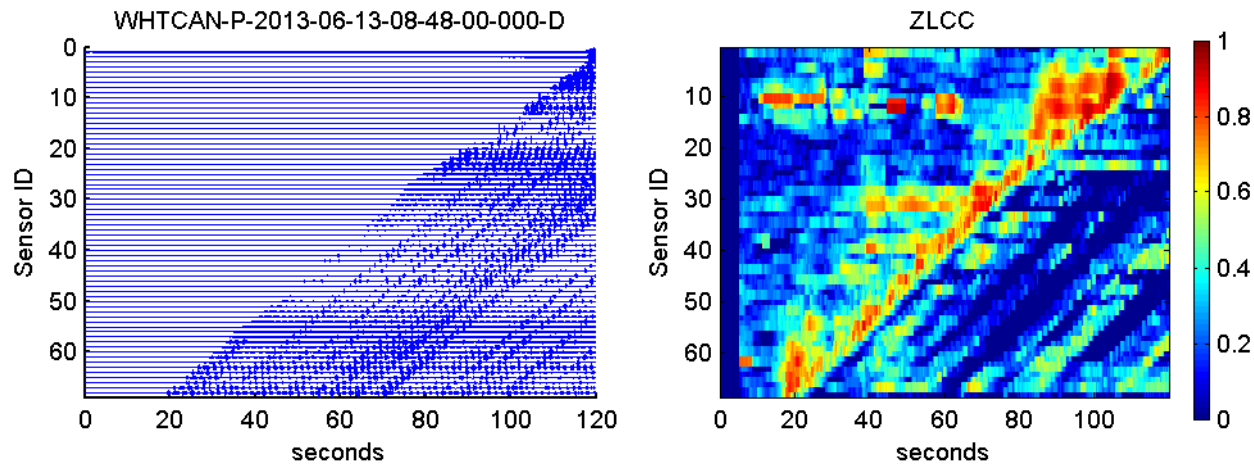

(a) (b)

Figure 4.16. (a) Seismogram of a steadily moving train; and (b) output of the ZLCC algorithm.

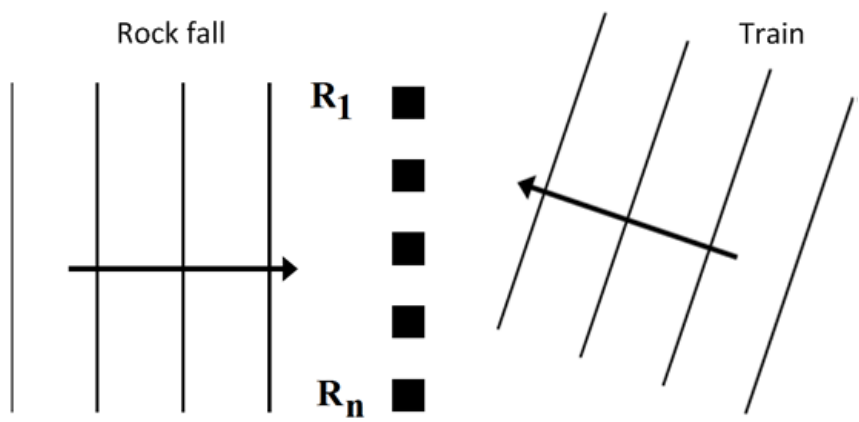

Figure 4.17. Schematic illustration of two wave fronts impinging onto the geophone array: a high-velocity one induced by rockfall and a low velocity train signal.

The $\|R_{max}^{N}(t_i)\|$ plot obtained for a train seismogram (Figure 4.16) demonstrates two important properties of the ZLCC: it cancels out ground vibrations induced by trains and highlights precursor signals. The mechanism of cancellation is explained in Figure 4.17 where the apparent velocity of the wave-front induced by rockfall (200-1,000 m/s) is much higher than the apparent velocity of r.m.s.-smoothed train signal (3-15 m/s). When two windowed train signals acquired at two geophones installed 10-20 m apart are correlated without travel time adjustment (as it is done in the TDA), the result is a low correlation coefficient. In Figure 4.16 most of the ZLCC values obtained in the midst of the train signal are close to zero.

The $\|R_{max}^{N}(t_i)\|$ plot in Figure 4.16 demonstrates that correlation coefficients in $\|R_{max}^{N}(t_i)\|$ can be affected by the presence of tunnels, rock sheds and rail joints. For instance, the train precursor noise near M94.0 tunnel results in highly correlated ground vibration at sensors Z-58 to Z-68 around 20 s. The rail expansion joints near Z-12 caused highly correlated signals at Z-01 to Z-12 around 80-100 s; high correlation coefficients at Z-50 to Z-55 (30 s) and Z-08 to Z-22 (80 s) are probably due to the welded rail joints in these areas. High correlation coefficients at Z-28 to Z-32 (70 s) are related to the 30 m long rock shed in this area.

Application of the ZLCC detector to a seismic record of a rockfall that occurred 200 m away from a moving high-rail is demonstrated in Figure 4.18. The $\|R_{max}^{N}(t_i)\|$ image shows that the ZLCC algorithm highlights the rockfall signal which was detected by 20 sensors that span 300 m, and suppresses the high-rail signal, though incompletely because of the coherent precursor and receding ground vibration induced by the vehicle.

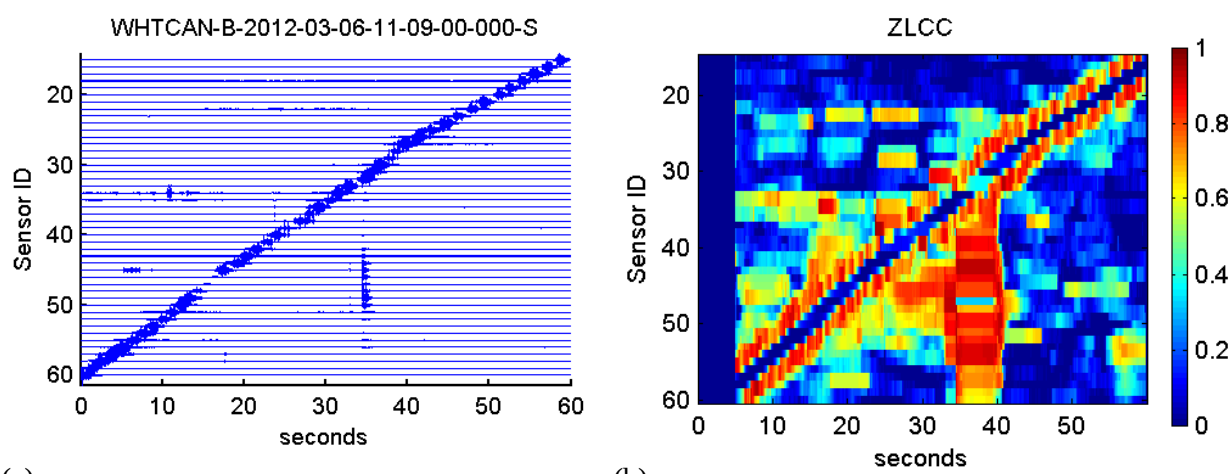

(a) (b)

Figure 4.18. Application of the ZLCC detector (b) to ground vibration induced by a rockfall and a moving high-rail (a). The rockfall occurred at 35 s; the characteristic rockfall signal pattern highlighted by the ZLCC detector begins at 35-37 s. This rockfall can be detected and reported with low 1-2 s latency.

Calibration of the ZLCC rockfall detector

The ZLCC detector has to be calibrated to be able to differentiate between non-hazardous seismic events and hazardous rockfalls. In the image of matrix $\|R_{max}^{N}(t_i)\|$ in Figure 4.16 the train precursor signal decays within 15 sensors, or 300 m, of the locomotive. Compare this to the $\|R_{max}^{N}(t_i)\|$ image of a

rockfall in Figure 4.15 where the pattern of near-simultaneously triggered sensors spans across the 1,100 m long seismic array. For example, if the ZLCC detector is configured to scan $\|R_{max}^{N}(t_i)\|$ using N^{ZLCC} = 20 sensors (approx. 400 m) as an array trigger threshold, then it will detect the rockfall in Figure 4.15, and skip the train precursor signal (Figure 4.16). A more refined approach will use threshold $N^{ZLCC}(d)$ which is dependent on the location *d* along the geophone array. For instance, $N^{ZLCC}(d)$ will be relatively high in proximity of rail joints and tunnels.

Selection of the correlation window

A w^{ZLCC} = 5 s correlation window has been used in this study because at Restricted Speed (3.5-4 m/s), a 5 second window is equivalent to 20 m, which is close to the average length of a railcar. Selecting a shorter time window may result in correlating less than one full period of the signal of interest, which can result in aliasing and failure of the ZLCC to mask the signals induced by rail traffic. Using a significantly wider time window will lower the time resolution of the ZLCC detector and will increase the chances of cross-correlating rockfall signals with ground vibrations of rail traffic, and missing the hazardous event.

4.3.2. Rockfall detection with STA/LTA

Arguably, STA/LTA is the most popular technique for detection of earthquakes and micro-seismic events. It can be used for rockfall detection at individual sensors, and combined with the array trigger criterion. If a critical number of sensors trigger within a narrow time window, this can be indicative of the arrival of seismic waves induced by a rockfall. The examples below illustrate this technique.

Configuration and calibration of the STA/LTA detector

The STA time window must be longer than a few periods of the expected seismic signal; otherwise the STA is no longer a measure of the average signal (signal envelope); instead, it becomes influenced by individual periods of the seismic signal. In the following examples w^{STA} = 0.05 s was used. A short LTA window allows the LTA to adjust to the slowly increasing amplitude of emergent seismic waves. In strong motion seismology, using a short LTA can sometimes mitigate false triggers due to traffic;

examples of such cases could be a single vehicle approaching and passing close to the seismic station on a local road, or trains on a nearby railway (Trnkoczy, 2002). This effectively diminishes trigger sensitivity to such events and the STA/LTA ratio remains low in spite of increasing STA. In the case of the SRFDS, a relatively short LTA will accommodate the detector's sensitivity to gradual changes of continuous anthropogenic seismic noise, *e.g.* approaching high-rails. In the following example, w^{LTA} = 5.0 s was used.

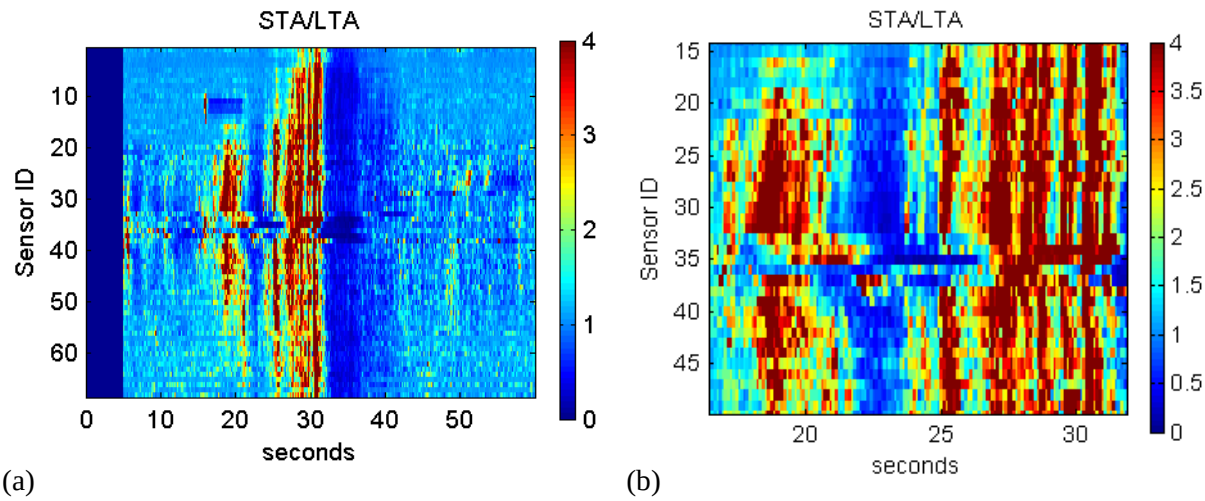

(a) (b)

Figure 4.19. Output of STA/LTA detector computed for the June 5, 2013 rockfall (a); a zoomed-in area of the STA/LTA plot (b).

After the matrix of STA/LTA values, $\left\|\gamma^{j}_{STA/LTA}(t_i)\right\|$, has been computed, a specific threshold $R^{STA/LTA}$ is applied to STA/LTA ratios within the array trigger window $w_{tr}^{STA/LTA}$. If any STA/LTA within $w_{tr}^{STA/LTA}$ exceeds $R^{STA/LTA}$ the sensor is considered triggered. If the total number of triggered sensors exceeds array trigger threshold $N^{STA/LTA}$, this is indicative of a rockfall; the same concept was used in the ZLCC algorithm in order to detect a network trigger. For example, if threshold $N^{STA/LTA}$ = 20 sensors is applied to $\left\|\gamma^{j}_{STA/LTA}(t_i)\right\|$ in Figure 4.20, the high-rail noise will be filtered out, whereas the rockfall signal will cause an array trigger. In Figure 4.19 and Figure 4.20, $\left\|\gamma^{j}_{STA/LTA}(t_i)\right\|$ values larger than $R^{STA/LTA}$ were replaced with $R^{STA/LTA}$ in order to keep the color-coding uniform.

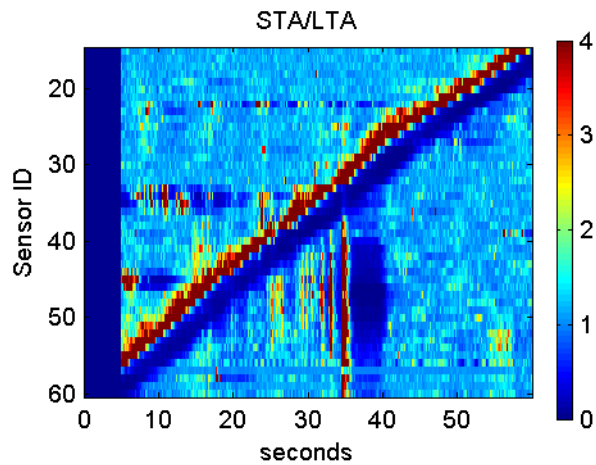

Figure 4.20. Output of STA/LTA detector computed for a high-rail and a rock (also see Figure 4.18).

In the following examples, we used $R^{STA/LTA}$ = 4.0, $w_{tr}^{STA/LTA}$ = 0.7 s. The array trigger window $w_{tr}^{STA/LTA}$ was selected based on the estimated velocity of the Rayleigh wave, 200 m/s. Within 0.7 seconds after a surface impact, seismic waves travel at least 140 m in each direction and trigger geophones within a 280 m section of the seismic array. The wave front of ground vibrations excited by a rock is at least 0.1 s long, and it typically grows with distance. Therefore, a 0.7 s time window will capture array triggers spanning more than 280 m. In addition, impacts of rocks onto the railway ballast tend to excite body waves in the underlying bedrock which propagate much faster than 200 m/s. Selecting $w_{tr}^{STA/LTA}$ larger than 1.0 s may lead to false positives induced by trains (Figure 4.22).

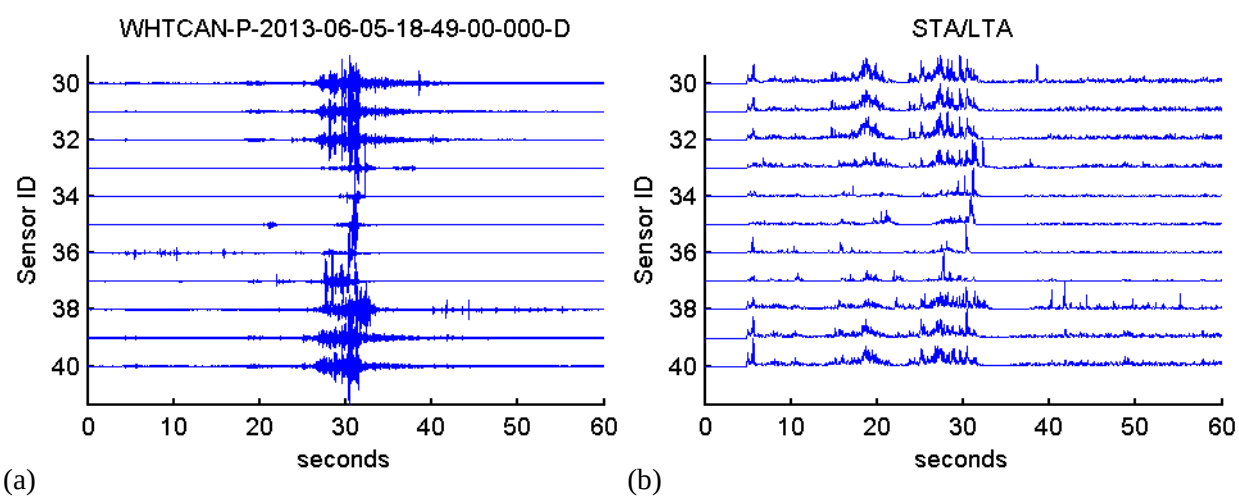

Figure 4.21. Seismograms of the June 5, 2013 rock slide in White Canyon acquired near the epicenter (a), and corresponding STA/LTA (b).

The STA/LTA detector has an advantage over the ZLCC detector in that the rockfall patterns within $\left\|\gamma_{STA/LTA}^{j}(t_i)\right\|$ usually do not have discontinuities near the epicenter. This is demonstrated in Figure 4.21 where seismograms acquired at the sensors located near the epicenter display uncorrelated waveforms, whereas the sensors located in the far field outside the landslide area detected similar waveforms. Regardless of these differences, when the rockfall occurred at 28 s, STA/LTA exceeded the threshold $R^{STA/LTA}$ at all sensors between Z-15 and Z-50 (Figure 4.19 (b)).

If a rockfall is preceded by another one, LTA may become saturated by the precursor signal which will bring down the STA/LTA ratio at the sensors near the epicenter. In Figure 4.19, the discontinuity at 18 s within the $\left\|\gamma_{STA/LTA}^{j}(t_i)\right\|$ image was caused by the precursor rockfall.

Detection of contiguous array triggers. The STA/LTA rockfall detector

The algorithm uses the $\left\|\gamma_{STA/LTA}^{j}(t_i)\right\|$ matrix to detect a contiguous array trigger identified at individual sensors using STA/LTA. This algorithm can be executed before train identification is complete in order to minimize the system response to hazardous rockfalls. The geophone array must be longer than the maximum propagation distance of traffic precursor vibration observed at the site.

Step [0]. Average the data with r.m.s.;

Step [1]. Compute the $\left\|\gamma_{STA/LTA}^{j}(t_i)\right\|$ matrix. Programmatically fill in the discontinuities within $\left\|\gamma_{STA/LTA}^{j}(t_i)\right\|$ near the epicentral area.

Step [2]. Scan the $\left\|\gamma_{STA/LTA}^{j}(t_i)\right\|$ matrix and apply threshold $R^{STA/LTA}$ to detect an array trigger. The spatial extent of the detected array trigger, $D_{STA/LTA}^{j,k}(t_i)$, must exceed a pre-set threshold $D^{STA/LTA}$. $D_{STA/LTA}^{j,k}(t_i)$ is defined as the length of a sub-array that consists of simultaneously triggered sensors *j*, *j+1, …, k*.

Step [3]. If an array trigger was detected in Step [2], apply the PGV *vs* distance threshold to identify hazardous rocks.

The STA/LTA detector is sensitive to the train pre-cursor noise which is relatively strong at tunnel portals and near rail expansion joints. For instance, in Figure 4.22(a) multiple near-simultaneous triggers occur at sensors Z-05 to Z-12 around 100 s when the locomotive wheels hit the rail expansion joints located near Z-12 and Z-13. Thus, in order to prevent rail traffic from raising false positives, the array trigger threshold $D^{STA/LTA}$ of the STA/LTA detector needs to be calibrated in the same manner as it was described for the ZLCC algorithm.

Within the train signal, LTA remains saturated with strong ground vibration induced by a moving train which results in mostly low STA/LTA. In Figure 4.22, the majority of STA/LTA values within the train signal are within the 1.0 to 1.5 range, *i.e*. lower than the sensor's trigger threshold, $R^{STA/LTA}$ = 4.0. In Figure 4.22 (b), high STA/LTA values correspond to surges of signal amplitude when the train wheels approach seismic sensors every 1-2 s. In combination with a narrow trigger window, $w_{tr}^{STA/LTA}$ = 0.7 s, this prevents the STA/LTA detector from false-triggering on train signals.

4.3.3. Combination of ZLCC and STA/LTA

The STA/LTA rockfall detector described in the previous section performs well when a rockfall occurs without a precursor and is large enough to excite a contiguous array trigger (no gaps between triggered sensors) within a narrow time window. An example of such a rockfall is shown in Figure C.1. Based on the field observations in White Canyon, such a scenario is atypical for rockfalls that involve tens and hundreds of cubic meters of material and start with precursor rockfalls. For example, the event illustrated in Figure 4.19(a) began with precursor rockfalls whose signals saturated the LTA and resulted in an inconsistent, patchy pattern of STA/LTA peaks near the epicenter image when the main rockfall occurred at 27-30 s (Figure 4.19(b)).

The STA/LTA rockfall detector will be improved in two ways. The algorithm will be modified to detect an array trigger at time t_i by calculating the percentage (in other words, density) of high STA/LTA values $P_{STA/LTA}^{j,k}(t_i)$ within the array trigger window $(t_i; t_i + w_{tr}^{STA/LTA})$. This algorithm will skip trains because of a low percentage of high STA/LTAs within the train signal (Figure 4.22). In order for this detector to distinguish a rockfall pattern, $P_{STA/LTA}^{j,k}(t_i)$ must exceed a pre-set threshold $P^{STA/LTA}$. In the following examples (also see Appendix C for more examples), thresholds $P^{STA/LTA} = 50\%$, and $D^{STA/LTA}$ = 250 m

will be used to demonstrate this technique. The advantage of this modification is that the array trigger can be detected even if the pattern of STA/LTA peaks induced by a rockfall is inconsistent.

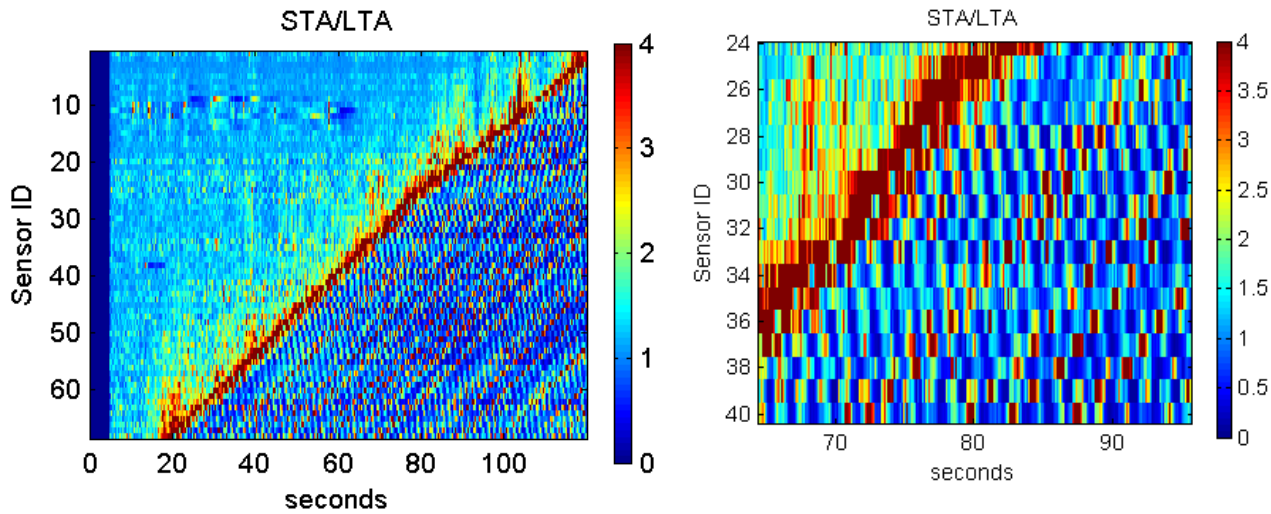

(a) (b)

Figure 4.22. (a) Output of the STA/LTA detector computed for a moving train. A zoomed-in area (b) of the left-hand image demonstrates the relatively low count of high STA/LTA values within the train signal.

Using Figure 4.19 as an illustration, the detector of a contiguous STA/LTA pattern is expected to recognize the network trigger at 31 s and miss the patchy rockfall patterns at 25-29 s; whereas the latter will be identified by the STA/LTA percentage detector. This detector can be further improved by filtering out train signals with the ZLCC using an element-wise product of $\left\|\gamma^{j}_{STA/LTA}(t_i)\right\|$ and $\|R^{N}_{max}(t_i)\|$, $\|R^{N}_{max}(t_i)\| \circ \left\|\gamma^{j}_{STA/LTA}(t_i)\right\|$. From eq. (4.5) and (4.7):

$$H^{j}_{max}(t_i) = \gamma^{j}_{STA/LTA}(t_i) * R^{j}_{max}(t_i) \qquad (4.11)^{19}$$

In this modification of the STA/LTA detector algorithm, the $H^{STA/LTA}$threshold will be applied to $H^{j}_{max}(t_i)$ values in order to detect individual sensor triggers.

[19] This matrix operation is called a Hadamard product.

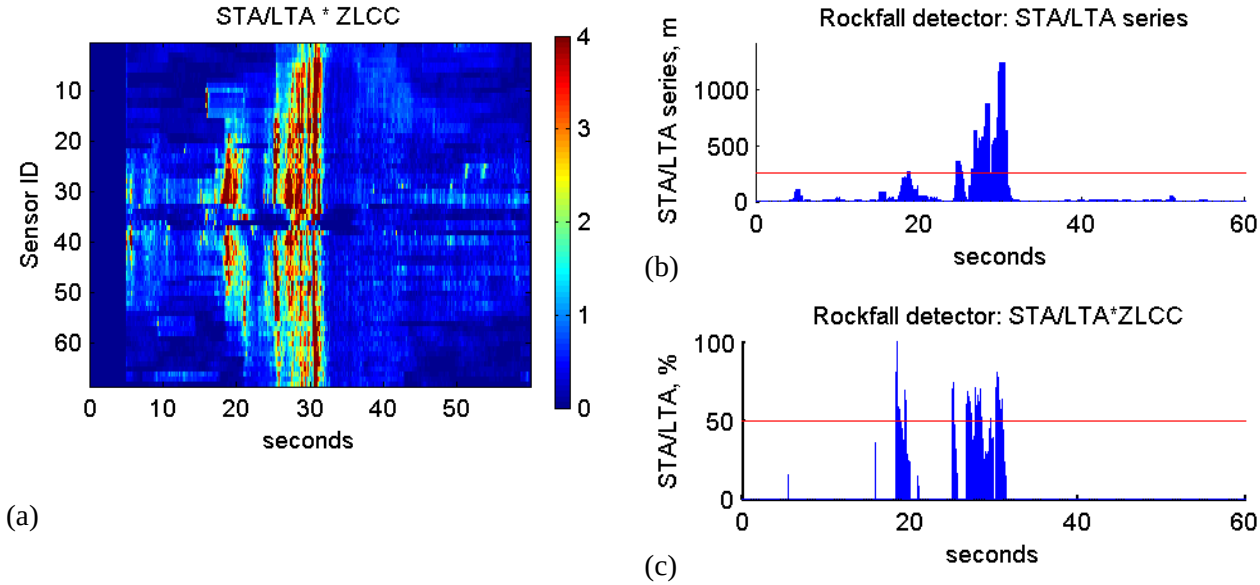

Figure 4.23. Example of pattern recognition analysis of rockfall signals using STA/LTA and ZLCC: detection of the June 5, 2013 rock slide.

Matrix $\left\|H_{max}^{j}(t_i)\right\|$ is displayed in plot (a). Plot (b) displays $D_{STA/LTA}^{j,k}(t_i)$ which is the spatial extent of the array triggers within the sliding time window. Plot (c) displays $P_{STA/LTA}^{j,k}(t_i)$ which is the percentage of $H_{max}^{j}(t_i) \geq H^{STA/LTA}$ within the sliding time window. Both $D_{STA/LTA}^{j,k}(t_i)$ and $P_{STA/LTA}^{j,k}(t_i)$ exceeded the thresholds (red horizontal lines in (b) and (c)) at 25 s, and a rockfall was flagged. The seismogram of this event is in Figure 3.63; zero time lag cross-correlation, $\|R_{max}^{N}(t_i)\|$, is illustrated in Figure 4.15; $\left\|\gamma_{STA/LTA}^{j}(t_i)\right\|$ is illustrated in Figure 4.19.

The rockfall detection algorithm based on the pattern recognition analysis of $\left\|H_{max}^{j}(t_i)\right\|$ will be referred to as the ZLCC*STA/LTA detector. This technique combines the ability of the ZLCC to filter out traffic signals, and the relatively low sensitivity of the STA/LTA to emergent signals; the latter is typical for train precursor vibration. In the following examples, the LTA window, w^{LTA}, was selected to be of the same length as w^{ZLCC} window, or 5.0 s, which removes ambiguity in interpreting the element-wise product of $\|R_{max}^{N}(t_i)\|$ and $\left\|\gamma_{STA/LTA}^{j}(t_i)\right\|$. The STA window is the same as used in the STA/LTA detector, w^{STA} = 0.05 s. Because $\gamma_{STA/LTA}^{j}(t_i)$ are multiplied by $R_{max}^{N}(t_i)$, the trigger threshold for $\left\|H_{max}^{j}(t_i)\right\|$ is computed as a product of $R^{STA/LTA}$ and R^{ZLCC}. For instance, if $R^{STA/LTA}$ = 4.0 and R^{ZLCC} = 0.8, then $H^{STA/LTA}$ = 3.2.

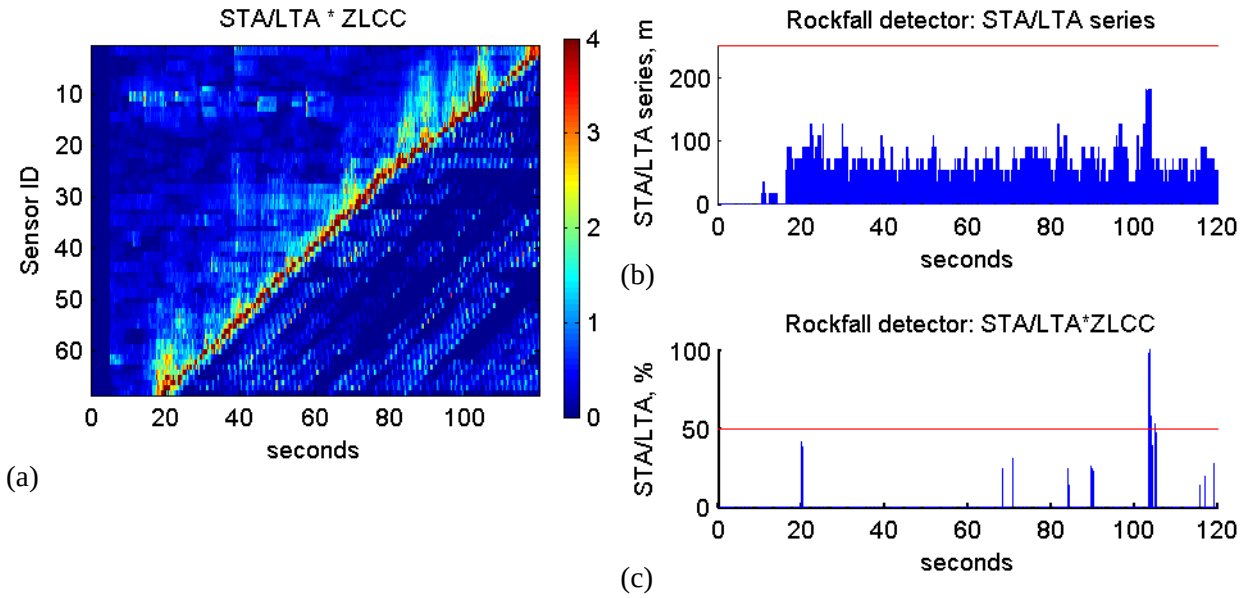

Figure 4.24. Pattern recognition analysis of ground vibration induced by a train using the ZLCC*STA/LTA algorithm.

Matrix $\left\|H_{max}^{j}(t_i)\right\|$ is displayed in plot (a). Plot (b) displays $D_{STA/LTA}^{j,k}(t_i)$; plot (c) displays $P_{STA/LTA}^{j,k}(t_i)$. In this example, the train vibration was ignored by the ZLCC*STA/LTA detector because $D_{STA/LTA}^{j,k}(t_i)$ stayed below 250 m for all t_i. Raw seismic data and $\|R_{max}^{N}(t_i)\|$ are in Figure 4.16; $\left\|\gamma_{STA/LTA}^{j}(t_i)\right\|$ is illustrated in Figure 4.22.

The ZLCC*STA/LTA rockfall detector algorithm

This algorithm uses the product of $\left\|\gamma_{STA/LTA}^{j}(t_i)\right\|$ and $\|R_{max}^{N}(t_i)\|$ matrices to filter out train signals and detect array triggers. This algorithm can be run before train identification is complete. In order to detect an array trigger, this modification of the STA/LTA rockfall detector computes the percentage of high STA/LTA values within the array trigger window.

Step [0]. Average the input seismic data with r.m.s.;

Step [1]. Compute $\left\|\gamma_{STA/LTA}^{j}(t_i)\right\|$ and $\|R_{max}^{N}(t_i)\|$ matrices, and take an element-wise product, $\left\|H_{max}^{j}(t_i)\right\|$.

Step [2]. Scan the $\left\|H_{max}^{j}(t_i)\right\|$ matrix and apply threshold $H^{STA/LTA}$ to detect individual sensor triggers. Count individual triggers within the moving time window and apply $P^{STA/LTA}$ threshold to detect an array trigger.

Step [3]. If an array trigger was detected in Step [2], apply the PGV threshold to identify hazardous rocks.

More examples of the rockfall detection techniques are in Appendix C.

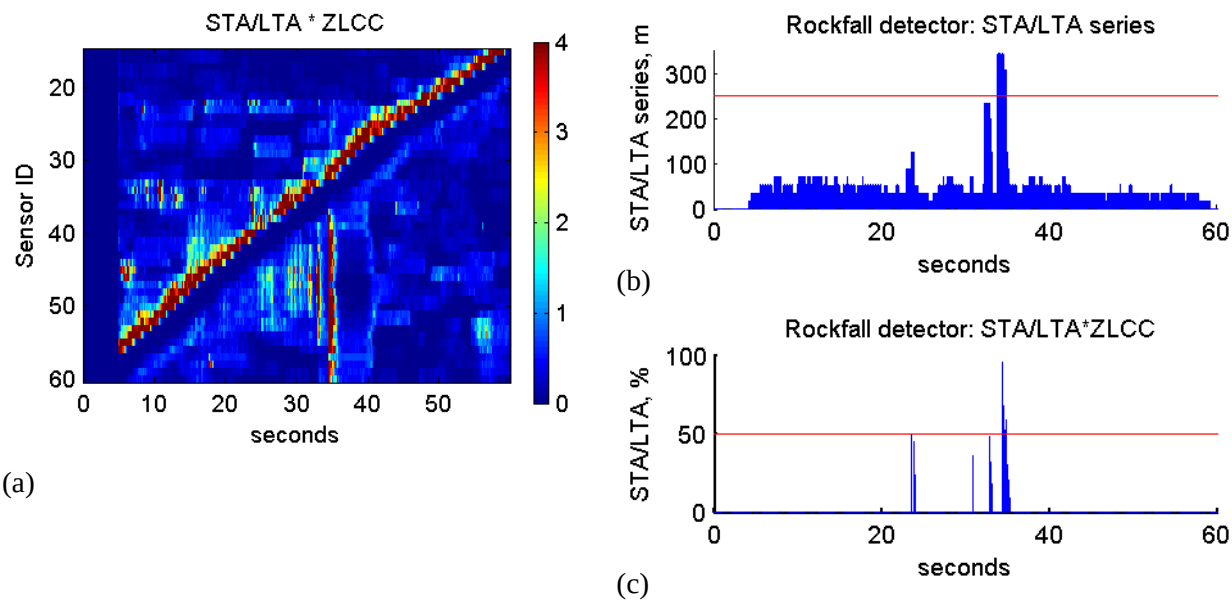

Figure 4.25. Pattern recognition analysis of ground vibration induced by a high-rail and a rockfall. Matrix $\left\|H_{max}^{j}(t_i)\right\|$ is displayed in plot (a). Plot (b) displays $D_{STA/LTA}^{j,k}(t_i)$; plot (c) displays $P_{STA/LTA}^{j,k}(t_i)$. In this example the vehicle vibration was ignored while both $D_{STA/LTA}^{j,k}(t_i)$ and $P_{STA/LTA}^{j,k}(t_i)$ exceeded the thresholds (red horizontal lines in (b) and (c)) at 35 s, and a rockfall was flagged. Raw seismic data and $\|R_{max}^{N}(t_i)\|$ are in Figure 4.18; $\left\|\gamma_{STA/LTA}^{j}(t_i)\right\|$ is illustrated in Figure 4.20.

4.4. Summary

Though it does not seem to be possible to detect hazardous rockfalls in the presence of ground vibration generated by moving trains, this deficiency is not considered critical by the railway operators involved in current research. The reason is that usually it takes a train several hundred meters to stop and, in practice, such rockfall reports will have no practical value. On the other hand, if the SRFDS can be programmed to identify regular (non-stop) passages of trains and high-rails, this information can be used to: ignore the ground vibration and avoid raising a false alarm; and rearm the SRFDS automatically. When a vehicle passes the geophone array without stopping, this means that there is no obstruction on the track. In the following chapter it will be demonstrated that automatic rearming can result in a significant reduction of the average number of slowed-down trains compared to the existing SDF.

Train delays related to activations of the SRFDS due to track maintenance can be avoided by instructing the crews to rearm the monitoring system before leaving the site.

In order to reduce the chances of false alarms by rail traffic, seismic signals are first analyzed by the train identification algorithms before the PGV threshold is applied. The train detection algorithms presented in this chapter identify trains and high-rails by comparing seismic signals recorded at the reference sensor and two or more comparison sensors. In order to identify irregular traffic, the Train Detection Algorithm (TDA) follows a trial-and-error procedure based on match-filtering of r.m.s.-smoothed signals time-adjusted for velocity, train arrival time, and the relative location of the reference and the comparison sensors. The other two algorithms, the Locomotive Detection Algorithm, LDA (1) and the LDA (2), were designed to detect regular rail traffic (high-rails and train locomotives). These algorithms use STA/LTA to average the data and detect vehicle arrivals. The vehicle detector algorithms were supplemented with three techniques for detection of the end of the train signal.

In order to cross-check the results of vehicle detection as it passes along the seismic array, after a vehicle passage has been identified by the TDA/LDA detectors at the sensor level, individual event records must be further analyzed by the Traffic Tracking Algorithm (TTA) at the sensor array level the TTA can be programmed to check that individual vehicle events have consistent velocities, and that the vehicle was detected at a specific minimum number of sensors, *etc*. Sometimes the time-delay patterns of seismic signals generated by animal movements display a strong resemblance to the records of a moving vehicle, including the peak amplitudes. Therefore there is a risk that the SRFDS will be misinterpreted such signals as an indication that there is no obstruction on the track. In order to differentiate high-rail signals

from those of migrating animals, a minimum path threshold (*e.g.* 200 meters) can be applied to the vehicle path computed by the TTA.

It is important for the SRFDS to minimize the lead time for a rockfall warning. In many cases the train detection analysis can be skipped, and hazardous rockfalls can be identified within a few seconds. Two pattern recognition algorithms introduced in this chapter can help identify hazardous rocks before train identification is complete. The algorithms are based on STA/LTA and zero-lag cross-correlation combined with the concept of array triggering widely used in seismic monitoring. If properly calibrated, the algorithms will ignore strong ground vibrations induced by rail traffic and detect array triggers induced by rockfall. Assuming that it takes 2.0 seconds for the data acquisition system to digitize seismic signals and store them in a digital data format, a hazardous rock can be detected and reported within <3 s. This is based on the assumption that it takes less than 1 s for the ground vibration induced by the falling rock to propagate across the seismic array and excite the critical number of sensors.

5. Performance Comparison of the SDF and the SRFDS at the Test Sites

One of the negative effects of prolonged SDF activations on rail traffic is the high number of trains slowed down by false alarms. The two rockfall detection technologies, SDF and SRFDS, will be compared using the ratio of slowed-down trains. Evaluation of other side effects such as safety hazards and cost of maintenance require additional information which is outside the scope of this research. In this chapter we will discuss activations of the SDF observed at the White Canyon and Hope test sites. Performance of the rockfall monitoring systems will be modeled using historical seismic data, and the results will be compared to the actual performance of the SDF. With the SRFDS self-rearming capability in effect, a non-threatening activation causes no more than one train delay. It will be shown that, based on the results of computer modeling, the average number of trains that would have been slowed down if the SFRDS were connected to the signal system is significantly lower than the average number of trains slowed down by SDF activations.

5.1. Collection of SDF data

The rockfall systems installed near Hope and in White Canyon monitored SDF activations from April 2012 and October 2010 respectively until the early 2015. Each SRFDS was equipped with a digital input relay connected to the SDF. On a limited number of occasions, signal maintainers who repaired the broken trip wires provided written reports which were sometimes accompanied by photos of the rocks that likely triggered the slide fence. CN shared reports on the Lasha SDF activations in White Canyon between February 27, 2012 and April 19, 2012. The CP reports cover the majority of the SDF activations between May 4, 2013 and July 24, 2013. These reports, complete with corresponding seismograms are included in Appendix D and Appendix E.

In the absence of consistent feedback from signal maintainers, the SDF activations were interpreted in the following manner. Knowing the accurate timing of SDF activation, one can investigate seismic records obtained at the time of activation and determine the cause. Generally, even under adverse weather conditions, rockfalls are rare, including non-hazardous ones, no more than several rockfall-like seismic

events per day. Therefore, if a slide fence is activated within 2-3 seconds of a seismic event (*e.g.* a rockfall or animal migration), the chances are that these two events occurred not only at the same time, but also at the same place, and that one caused the other. If the location of a wire break, and therefore the nature of the SDF activation, is still questionable, it can be ascertained later, when the SDF is repaired by a signal maintainer. The footsteps of the maintainer and subsequent ground vibration generated by a departing high-rail produce a characteristic seismic signature at the location of the wire break. The location is accurate to the nearest seismic sensor, which is good enough for the purpose of event interpretation. In this way, the majority of slide fence activations were identified and located.

On a number of occasions unambiguous interpretation of slide fence activations was impossible either because a train was on site, or because there was no simultaneous seismic event at the time of SDF activation. Also, sometimes a SDF is broken more than once before it is repaired; in this case the timing, and therefore the cause, of wire breaks other than the first one cannot be established with confidence.

At the Hope site where a web camera was available, more detailed information about the cause of SDF activations could be obtained remotely, *e.g.* a rock, a piece of ice, a fallen tree on the ground, or a working track maintenance crew.

5.2. Analysis of SDF activations

It is important to separate SDF activations by hazardous rocks (*i.e.* true positive events) from nuisance activations by animals and non-hazardous rocks (false postives). Since only few field reports from S&C maintainers are available, the size of the rocks (hazardous *vs* non-hazardous) was estimated based on the seismic records. If the PGV exceeded the system activation threshold described in Chapter 3, the rock was considered hazardous. The same criteria will be used to qualify the SRFDS activations later in this chapter. With regard to the timing of SRFDS and SDF activations, the following scenarios were observed at the two test sites:

- A seismic event whose PGV exceeds the system activation threshold occurs simultaneously with a SDF activation. Such SDF activations were interpreted to have been induced by hazardous rocks. A number of SDF activations occurred while track maintenance crews were at work. In this case it was assumed that wires were broken by excavators (which was usually the case) while they were cleaning up the upslope ditch of the accumulated debris. Sometimes the SDF remains

activated for more than a day; an extreme example of such a prolonged activation took place during the rock scaling program carried out at CP CASC 038.90 (the Hope site) between March 31, 2014 and June 11, 2014. Scaling is a slope stabilization procedure which involves removing large trees and loose rocks from the rock cliff overlooking the rail track in a controlled manner. Usually it results in extensive damage to the existing slide fence, and repairs are postponed until the scaling is complete.

- The PGV of the seismic event that was detected at the time of SDF activation did not exceed the threshold. These scenarios usually occur when a non-hazardous rock or a piece of ice breaks the wire. If the SDF activation coincided in time and space with a pattern of animal migration the wire was considered to have been broken by animal(s).

- No seismic event was detected when the SDF was activated. Between 2010 and 2015 this happened only a couple of times; in one case, according to a signal maintainer, the wire corroded and broke.

- A number of times the slide fences were activated when a train was passing. Thus, weaker seismic events were overshadowed by the traffic noise making analysis of the rockfall signal impossible.

- Intermittent SDF activations that occurred asynchronously with seismic events and were caused by malfunctioning SDF hardware.

- A number of seismic events, apparently rockfalls, occurred while the SDF remained deactivated, *i.e.* rocks either missed the trip wire or stopped in the catchment ditch.

In the summary tables below, the SDF activations are classified as having been caused by one of the following factors:

Rockfall. If a seismic event occurred whose peak ground velocity exceeded the threshold simultaneously with the SDF activation and in the absence of animal or track maintenance activity, it was assumed that the activation was induced by a hazardous rockfall;

Non-hazardous rocks / ice. This category is similar to the previous one, except that the accompanying ground vibration did not exceed the SRFDS activation threshold obtained for the hazardous rock;

Train noise. The SDF activation occurred when a train was passing, *i.e.* it was probably caused by rocks. This usually means that the rock(s) were non-hazardous because no derailment occurred at the test sites between 2010 and 2015.

Animals. The SDF activation was probably caused by animals. Such activations occurred only at the White Canyon site;

Track maintenance. The SDF was activated while a track maintenance crew was on site;

Unknown. Usually this means that at the time of activation both the SDF Activation and Track Occupancy data were available while the corresponding seismic data were not, *e.g.* because of malfunctioning recording equipment. This event category was applied only to the White Canyon SRFDS where Track Occupancy signal is available. In other words, the SRFDS recorded the timing of slide fence activations as well as the number of slowed down trains, but in the absence of accompanying seismic records the cause of activation was impossible to figure out.

Other. One atypical SDF activation occurred when, according to a signal maintainer, the wire rusted out and broke by itself.

The monthly and annual percentages of delayed trains was calculated assuming that 24 trains pass the site per day (*e.g.* Table 5.3 - Table 5.5). Seismic data were used to count trains slowed down by SDF activations. When slide fence activations lasted less than 24 hours, the number of slowed down trains was counted manually, otherwise the number of slowed down trains was estimated using the daily average.

5.2.1. Activations of the SDF at CP Cascade M38.90 (near Hope, BC)

This section contains examples of SDF activations at CP CASC 038.90 (Hope, BC). Two years of continuous seismic data will be used to model the behaviour of the Hope SRFDS, 2013 to 2014 and compare it to the activations of the SDF within the same time frame.

Examples of individual activations are in Table 5.1, Table 5.2. In Table 5.3 and Table 5.4 individual SDF activations are grouped by category. Each column represents a separate event category and contains two

values. The first one shows the number of slide fence activations per month, the second one is the monthly total of slowed-down trains. For example, in June 2013 one SDF activation by a hazardous rock caused two trains to slow down before the wire was repaired.

Table 5.1. Individual SDF activations complete with the number of slowed-down trains (January-December 2013). Qualitative estimates of the rock size are based on the PGV of ground vibration induced by the rock.

SDF alarm was raised on	SDF was repaired on	Train slow-downs	Cause
January 2, 2013	January 2, 2013	0	Hazardous rock (>0.028 m^3)
January 7, 2013	January 7, 2013	5	Non-hazardous rock
January 8, 2013	January 9, 2013	12	Non-hazardous rock
January 11, 2013	January 11, 2013	1	Non-hazardous rock
January 16, 2013	January 16, 2013	2	(train noise)
January 18, 2013	January 18, 2013	11	Non-hazardous rock
January 18, 2013	January 18, 2013	0	Track maintenance
January 19, 2013	January 20, 2013	26	Non-hazardous rock
January 25, 2013	January 25, 2013	3	(train noise)
February 6, 2013	February 6, 2013	9	Non-hazardous rock
February 7, 2013	February 7, 2013	0	Track maintenance
February 19, 2013	February 20, 2013	14	Non-hazardous rock
May 4, 2013	May 5, 2013	13	Non-hazardous rocks
June 16, 2013	June 16, 2013	5	Non-hazardous rocks
June 23, 2013	June 23, 2013	2	Hazardous rocks
July 24, 2013	July 25, 2013	7	Electric wire rusted out
October 17, 2013	October 18, 2013	10	Non-hazardous rock
November 22, 2013	November 24, 2013	36	Hazardous rock
Total		**156**	

Table 5.2. Individual SDF activations complete with the number of slowed-down trains (January-December 2014). Qualitative estimates of the rock size are based on the PGV of ground vibration induced by the rock.

SDF alarm was raised on	SDF was repaired on	Train slow-downs	Cause
February 11, 2014	February 12, 2014	24	Non-hazardous rock(s) (<0.028 m^3)
March 4, 2014	March 4, 2014	5	Non-hazardous rock/ice
March 31, 2014	June 11, 2014	1722	Rock stabilization programme
September 9, 2014	September 9, 2014	5	Hazardous rock
September 14, 2014	September 14, 2014	1	Hazardous rock
October 25, 2014	October 26, 2014	40	Hazardous rock
November 27, 2014	December 15, 2014	432	Non-hazardous rock followed by a large tree
Total		**2,229**	

Table 5.3. Monthly summary of SDF activations at CASC 038.90 (Hope, BC) *versus* the number of train delays (January-December 2013). Each column represents an event category and contains two values. The first one shows the number of slide fence activations per month, the second one is the monthly total of slowed-down trains.

2013	Rock falls		Non-haz. rocks		(train noise)		Track maintenance		Other		Total	
January	1	0	5	55	2	5	1	0			9	60
February			2	23			1	0			3	23
March											0	0
April											0	0
May			1	13							1	13
June	1	2	1	5							2	7
July									1	7	1	7
August											0	0
September											0	0
October			1	10							1	10
November	1	36									1	36
December											0	0
Total											**18**	**156**
Percentage of delayed traffic[†]												**1.8%**

[†] The annual percentage is based on the average of 24 trains per day.

Table 5.4. Monthly summary of SDF activations at CP CASC 038.90 (Hope, BC) versus the number of train delays (January-December 2014).

2014	Rock falls		Non-haz. rocks		(train noise)	Track maintenance		Other	Total		Total[††]	
January									0	0	0	0
February			1	24					1	24	1	24
March			1	5		1	6		2	11	0	5
April							720[†]		0	720	0	0
May							744[†]		0	744	0	0
June							252[†]		0	252	0	0
July									0	0	0	0
August									0	0	0	0
September	2	6							2	6	2	6
October	1	40							1	40[†]	1	40
November	1	432							1	84[†]	1	84
December									0	348	0	348
Total									**7**	**2,229**	**5**	**507**
Percentage of delayed traffic										**25.4%**		**5.8%**

[†] The number of rains slowed down during prolonged SDF activations is estimated based on the average of 24 trains per day.

[††] Not including the train delays during the scaling program in March-June 2014.

Table 5.5. Summary of CP CASC 038.90 SDF activations and train delays by year, 2013-2014.

Year	Total number of activations[†]	Total number of slowed-down trains	Annual percentage of slowed down trains[††]	Data completeness
2013	16	156	1.8%	
2014	6	2,229	25.4%	
2014	5	507	5.8%	Train slow-downs during the scaling procedure undertaken in May-June 2014 are not included

[†] Not including activations by track maintenance crews.

[††] Based on the average of 24 trains per day.

[†††] Not including train delays during the scaling program in March-June 2014.

Interpretation of the SDF activations

At the Hope site, SDF activations have a seasonal trend. For example, in 2013 twelve out of 16 activations, or 75%, happened in January and February, while only four activations occurred between March and September.

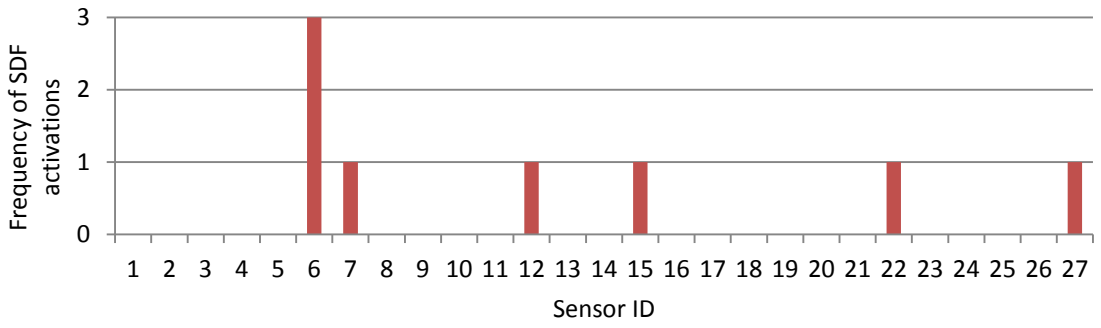

Figure 5.1. Distribution of CASC 038.90 SDF activations in January 2013. The horizontal axis displays sensor indexes.

The SDF activation histogram in Figure 5.1 demonstrates that in the winter time, the most active area is near sensors Z-06 and Z-07. It appears that in this area the trip wire was broken due to ice build-up (Figure 5.2). Given such a strong seasonal bias, which was also observed in 2014, the two rockfall warning technologies, SRFDS and SDF, should be compared only when complete records are available for a specific year. For example, since the statistics of trip wire activations in 2012 is incomplete, this year will be excluded from the comparison analysis below. Another striking anomaly in the recorded trip wire activations is the number of trains slowed down during the three month long scaling program in 2014. Since rock scaling is performed relatively rarely[20], the summary of slowed down trains in Table 5.5 does not include the effects of the scaling program. Field reports from signal maintainers are available for some SDF activations (Appendix D).

[20] Based on the information available about the Hope site, the previous scaling took place in 1999.

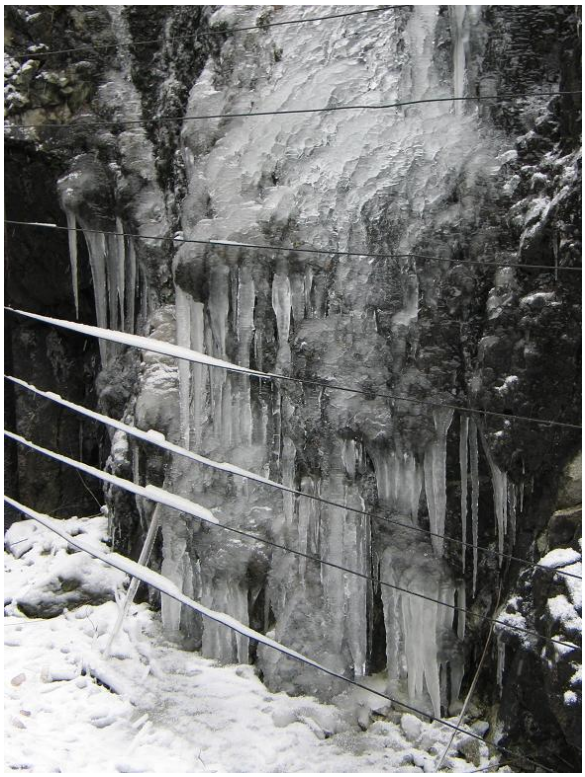

Figure 5.2. Photo of the area approximately 70-90 m east of Mile 039.30 tunnel, near sensor Z-06. Ice and snow buildup on trip wires is clearly visible. The photo was taken in November 2011.

5.2.2. Activations of the SDF at CN Ashcroft M94.50 (near Lytton, BC)

Compared to the Hope site, slide fence activations in White Canyon occur significantly more often. For example, Table 5.6 has a summary of trip wire alarms in June 2013. Considering the incompleteness of the available seismic data (Table 5.9), hypothetical behaviour of the White Canyon SRFDS will be modeled using 2012-2013 data.

Table 5.6. Summary of the Lasha SDF, Fence B activations in June 2013. Estimates of the rock size are based on the PGV of ground vibration induced by the rock.

Activated	Deactivated	Cause	Trains delayed
Jun 2, 2013 4:38 PST	Jun 2, 2013 15:06 PST	Rockfall	9
Jun 4, 2013 6:14 PST	Jun 4, 2013 9:55 PST	Non-hazardous rocks	1
Jun 5, 2013 18:48 PST	Jun 8, 2013 14:06 PST	Rockfall	60
Jun 09, 2013 11:33 PST	Jun 09, 2013 13:08 PST	Non-hazardous rock	0
Jun 13, 2013 12:07 PST	Jun 13, 2013 12:11 PST	Track maintenance	0
Jun 14, 2013 19:47 PST	Jun 15, 2013 19:01 PST	Non-hazardous rock	18
Jun 19, 2013 11:09 PST	Jun 19, 2013 12:08 PST	Rockfall	2
Jun 19, 2013 15:26 PST	Jun 19, 2013 15:30 PST	Track maintenance	0
Jun 20, 2013 05:07 PST	Jun 20, 2013 09:08 PST	Non-hazardous rock	4
Jun 20, 2013 09:56 PST	Jun 20, 2013 15:24 PST	Non-hazardous rock	5
Jun 20, 2013 20:09 PST	Jun 20, 2013 8:53 PST	Rockfall	15
Jun 21, 2013 12:18 PST	Jun 21, 2013 14:01 PST	Non-hazardous rock	0
Jun 24, 2013 08:37 PST	Jun 24, 2013 10:33 PST	Non-hazardous rock	2
Jun 29, 2013 20:08 PST	Jun 30, 2013 8:50 PST	Non-hazardous rocks	13
Total			**129**

Table 5.7. Monthly summary of Lasha SDF, Fence B activations in January-December 2012. Each column represents one event category and contains two values. The first one shows the number of slide fence activations per month, the second one is the monthly total of slowed-down trains.

2012	Rockfall		Non-haz. rocks		(train noise)		Animals		Track maint.		unknown	Total	
January			6	88	1	2			3	11		10	101
February	1	2	4	47	2	26	1	18	1	0		9	93
March	3	70	4	14			1	2	1	0		9	86
April	1	126	3	48					8	0		12	174
May	1	27	2	17					1	0		4	44
June	1	16	7	54					1	0		9	70
July	3	40	7	69	3	23	2	11	2	0		17	143
August	1	2	1	19	2	29	1	0	4	0		9	50
September	2	25	2	15								4	40
October			2	24	1	15			2	0		5	39
November	1	105	2	37			3	40	2	3		8	185
December	1	18	2	23			1	14				4	55
Total	**15**								**25**			**100**	**1080**
Percentage of delayed traffic													**12.3%**

Table 5.8. Monthly summary of Lasha SDF, Fence B activations in January-December 2013.

2013	Rock-fall		Non-haz. rocks		(train noise)		Animals		Track maint.		unknown		Total	
January	1	3	10	195			1	2					12	200
February	1	4	4	66			1	26			1	90	7	186
March	1	4	7	59	2	28	2	28	2	1			14	120
April	1	24	5	60	1	3	2	63					9	150
May	3	87	3	34									6	121
June	4	86	6	43					2	0			12	129
July	3	24	3	20	2	45							8	89
August	1	4			2	9			7	39			10	52
September			1	21	1	19	3	5	3	7			8	52
October	1	9	2	10	1	19	1	4	1	0			6	42
November			5	72	1	30	10	71					16	173
December	1	1	5	50			8	39	1	29			15	119
Total	**17**								**16**				**123**	**1433**
Percentage of delayed traffic														**16.4%**

Table 5.9. Summary of Lasha SDF, Fence B activations by year, 2011-2014.

Year	Total number of activations	Total number of slowed-down trains	Annual percentage of slowed down trains†	Data quality
2011	70	712	8.10%	Low (incomplete SDF and seismic data)
2012	72	986	12.30%	High
2013	105	1387	16.40%	High
2014	85	1102	12.60%	Low (incomplete SDF and seismic data)

† The ratios of slowed down trains were calculated from the available timing of the SDF triggers and seismic data which contained train seismograms.

Interpretation of the Lasha SDF (Fence B) activations (CN Ashcroft Sub M94.50)

The annual percentages of slowed-down trains in Table 5.9 do not show significant year-to-year fluctuations as was the case at the Hope test site. These numbers are close to the historical average, which, according to the railway operator, is 20% of all rail traffic (Table 5.7, Table 5.8). The historical average of SDF activations and train delays provided by CN includes both Fence B (the more active area which is included in this research) and Fence A (the less active area; this part of the slide fence was not

monitored in current research) of Lasha SDF (Carlson, 2010). The relatively low percentage of slowed-down trains in 2011 may have to do with incomplete records of SDF activations.

Assuming that hazardous (>0.028 m^3) and non-hazardous rocks were correctly identified based on their seismic signatures, the total number of SDF activations by hazardous rocks in 2012 was 15 out of 75 (not including 25 activations by track maintenance personnel). This means that only 20% of activations were due to hazardous rocks in 2012 (Table 5.7). For 2013, 17 out of 107 SDF activations (not including 16 SDF activations by track maintenance personnel) were due to hazardous rocks, or 16%. These field observations correlate well with estimates from other sources: Transport Canada (2007) estimated that 40% to 70% of all SDF activations are false alarms; Peckover (1975) reported an 80% false alarm rate.

In the following comparison analysis, seismic records obtained in 2012 and 2013 will be used because of their completeness. Field reports from S&C maintainers are available for some Lasha SDF (Fence B) activations; however, in a number of cases the responsible rocks were not unambiguously identified by the maintainers. Thus the author had to try to interpret the seismic records and field photos (see Appendix E).

5.3. Computer modeling of the Hope SRFDS

Since the SRFDS analytical software was finalized only in 2014, hypothetical performance of the SRFDS installations was modeled by processing historical seismic data. This modeling was used to evaluate the potential benefits of the SRFDS.

Computer modeling of the SRFDS behaviour consisted of two steps. First, continuous seismic data were processed by the SRFDS/Data Analysis software. It was programmed to log a time-stamped record every time its status changed from rearmed to activated and *vice versa* complete with a description of what caused the activation, *e.g.* an abnormal traffic pattern, a rockfall, and so on. Then seismic records corresponding to individual activations were examined and, depending on what caused the system to activate, each SRFDS activation was assigned one of five event categories: regular rail traffic, train stops, track maintenance, animals, or rockfalls (*e.g.* Table 5.10).

SRFDS activations in the **Regular rail traffic** category were caused by unusually strong precursor vibration, for example, near the rail expansion joints or tunnels, which the SRFDS identified as a rockfall. This is a *false positive* activation. In the majority of such cases the SRFDS rearmed itself automatically

within seconds because the strong precursor noise was followed by a train pattern. Table 5.10 and Table 5.11 contain two numbers under this event category: the first one is the number of system activations by regular trains, the other is the number of such activations that left the system activated.

System activations placed in the **Train stop** category mean that the SRFDS was activated by strong ground vibration induced by a stopping train. The majority of such activations were cleared once the train resumed its journey and the SRFDS rearmed automatically. Similar to the **Regular rail traffic** category, in the summary tables activations of this type are represented by two numbers: the number of SRFDS activations by train stops, and the subset of these activations when the system did not rearm automatically. The latter usually happened when the train was moving too slowly, or stopped multiple times.

System activations in the **Track maintenance** category have to do with high-amplitude ground vibrations generated by track maintenance personnel. Though the number of such activations can be significant, such false alarms would not result in train slow-downs if the approach described in Section 4.1 were followed. This is because the railway operators are always aware of the whereabouts of their maintenance personnel who can be instructed to rearm the SRFDS before leaving the site. Thus, the estimates of the percentage of delayed trains do not include SRFDS activations under this category. In Table 5.11, SRFDS activations induced during the scaling program in April – July 2014 are in the "Track maintenance noise" column.

Animals. This category includes seismic signals generated by migrating animals and interpreted by the SRFDS as rockfalls.

Rockfalls. All seismic signals that were not induced by slow trains, track maintenance, or animals and whose amplitudes exceed the trigger threshold were categorized as rockfalls. This category also includes ice falls at the Hope site as well as what appears to be ground vibration generated by thermal expansion (section 5.4.2). All such activations would result in no more than one train slow-down[21]. In the computer model each activation by rockfall was assumed to result in one slowed-down train.

[21] Occasionally the system is rearmed by a passing high-rail vehicle before a train approaches the site.

EMI noise

Spikes in the seismic data induced by electro-magnetic interference have been a source of false positives only in the White Canyon SRFDS installation where a number of sensor cables are unshielded. System activations caused by high-amplitude electric spikes that were misidentified as rockfalls were excluded from the statistical summaries below, except when EMI noise was caused by lightning. The reason is that experience has shown that susceptibility of a seismic monitoring system to EMI can be significantly reduced by proper cable shielding, *i.e.* it is not inherent to the method of seismic rockfall detection implemented in this research.

Data integrity

Several AC-power outages lasting from a few minutes to several hours occurred at the test sites between 2012 and 2015, during which the data acquisition system continued to be powered by the backup batteries. Since the external HDD where the data were stored was powered by the AC line, these power outages resulted in loss of some seismic data. The SRFDS/Data Analysis software is programmed to report an alarm when a discontinuity is detected within the input seismic data. Discontinuities in the input data caused activations of the SRFDS computer model when the historical data were processed. These false alarms were not included in the following analysis because they have to do with the integrity of backup data rather than with the SRFDS model.

The Peak Ground Velocity (PGV) threshold model

The PGV threshold obtained in the Squamish tests (Table 3.1) was used at the Hope and the White Canyon sites for rockfall detection in real time, as well as to model the SRFDS behaviour with historical data. Detailed information about the ground conditions at the Squamish and the White Canyon sites was not available; however, when the geophones were installed the track structure and the depth of bedrock and/or boulders at the Squamish site appeared similar to the other two sites. The assumption about the similarity of ground response to surface impacts at these three locations was later confirmed by the field reports from CN and CP signal maintainers who repaired the electric fences activated by natural rockfalls (Appendix E). The field reports, sometimes accompanied by photos of the rocks, helped to relate the size of the rocks to the peak amplitudes.

In Chapter 3 it was observed that when the geophone array is installed along a curved rail track, the amplitude of seismic waves generated by rockfalls tends to decrease at a higher rate compared to straight alignment. For modeling of the Hope SRFDS, a one-sided PGV threshold model was used which increased the SRFDS sensitivity and may have resulted in overestimation of the number of hazardous rocks. The maximum epicentral distance in the PGV model in Table 3.1 is 45 m. For the White Canyon SRFDS a two-sided PGV model (*i.e.* 90 m) was utilized because this site does not have steep curves.

5.3.1. Summary of the Hope SRFDS activations

Since the SDF activations at the Hope site have a pronounced seasonal trend, two years of continuous seismic data were processed in order to obtain statistical data on the anticipated SRFDS performance. The results of computer modeling of the hypothetical behaviour of the Hope SRFDS are summarized in Table 5.10 and Table 5.11. The tables contain the number of trains that would have been slowed down if the SRFDS were connected to the CP signaling system. A significant reduction in the number of delayed trains (2-3 times) can be achieved by instructing track maintenance crews to rearm the system upon completion of their work. The effect of this procedure on the potential number of delayed trains is demonstrated in columns [8] and [9]. The columns in Table 5.10, Table 5.11, Table 5.13 and Table 5.14 which contain the annual summaries of SRFDS activations are numbered as follows:

[1], [2] The number of SRFDS activations (column [1]) caused by regular trains and high-rails *versus* the number of activations when the SRFDS remained activated after the train left the site (col. [2]).

[3], [4] The number of system activations by train stops (col. [3]) *versus* the number of activations when the SRFDS remained activated after the train left the site (col. [4]). For example, in April, 2013 only 1 out of 5 trains that activated the SRFDS by stopping at the site failed to rearm the system after resuming its journey and leaving the site.

[5] SRFDS activations by track maintenance.

[6] SRFDS activations by animals.

[7] SRFDS activations by rockfall and other natural sources of strong ground vibrations, including wind loads on trees, falling ice, trees, thunder claps *etc*.

[8] Combined number of SRFDS activations from columns [1], [3], [5], [6], [7].

Table 5.10. Computer simulation of the behaviour of the Hope SRFDS using one year of continuous seismic data from January 1, 2013 to December 31, 2013.

2013	Regular rail traffic		Train stops		Track maint.	Animals	Rock-fall	Total activations	Total number of train delays w/o track mtnce
	[1]	[2]	[3]	[4]	[5]	[6]	[7]	[8]	[9]
January	0	0	8	5	11	0	11	30	16
February	0	0	0	0	2	0	0	2	0
March	0	0	2	1	2	0	4	8	5
April	0	0	5	1	2	0	3	10	4
May	0	0	3	0	2	0	3	8	3
June	1	0	3	0	3	0	6	13	6
July	1	0	4	1	4	0	0	9	1
August	1	0	1	0	1	0	0	3	0
September	1	0	5	1	1	0	1	8	2
October	0	0	1	0	3	0	5	9	5
November	0	0	5	0	5	0	2	12	2
December	0	0	6	3	3	0	4	13	7
Total							**39**	**125**	**51**
Percentage of delayed traffic								**1.4%**	**0.6%**

Table 5.11. Computer simulation of the behaviour of the Hope SRFDS using year of continuous seismic data from January 1, 2014 to December 31, 2014.

2014	Regular rail traffic		Train stops		Track maint.	Animals	Rock-fall	Total activations	Total number of train delays w/o track mtnce
	[1]	[2]	[3]	[4]	[5]	[6]	[7]	[8]	[9]
January	0	0	2	2	0	0	2	4	4
February	0	0	4	2	8	1	4	17	7
March	9	4	0	0	11	0	0	20	4
April	0	0	10	1	52	0	4	66	5
May	3	0	14	0	40	0	1	58	1
June	4	0	4	0	55	0	1	64	1
July	0	0	10	1	43	0	3	56	4
August	1	1	15	4	1	0	1	18	6
September	0	0	0	0	0	1	3	4	4
October	1	0	2	1	2	1	3	9	5
November	0	0	8	3	1	0	5	14	8
December	1	0	6	1	9	0	27	43	28
Total							**54**	**373**	**77**
Percentage of delayed traffic								**4.3%**	**0.9%**

[9] Combined number of train slow-downs from columns [2], [4], [6], [7]. This category includes all SRFDS activations, not including the activations when the system rearmed automatically by a train, and the activations caused by track maintenance. In other words, col. [9] contains the number of train slow-downs which would have been caused by SRFDS activations assuming that the system can rearm automatically when it detects a moving vehicle. This assumption means that one SRFDS activation causes no more than one train delay.

5.3.2. Interpretation of the results of computer modeling

The web camera installed at CP CASC 038.90 was instrumental in providing feedback from the site and interpreting the results of seismic monitoring. Computer simulation of the CASC 038.90 SRFDS behaviour using 24 months of continuous seismic data resulted in 498 activations (Table 5.10, Table 5.11). The three most important causes are rockfalls (93 activations), train stops (118), and track maintenance (261). Assuming that the track maintainers are instructed to rearm the monitoring system before leaving the site, only 128 activations would have resulted in train slow-downs, including 51 activations in 2013 and 77 activations in 2014. The estimated number of system activations by supposedly hazardous rocks between 2013 and 2014, 39 and 54 respectively, appears rather high compared to the field observations. None of the CASC 038.90 SDF activations reported by signal maintainers in 2013 involved rock(s) of 0.028 m^3 or larger. Several explanations for this can be offered.

Firstly, 17 out of 39 hazardous rocks reported in 2013, and 40 out of 54 rockfalls reported in 2014 occurred in the cold time of the year, between November and February. Field observations with the web camera combined with the distribution of surface impacts along the site (Figure 5.3-Figure 5.5) suggest that many of these activations were due to ice falls.

Secondly, it is possible that the PGV threshold used to identify hazardous rocks was too conservative. The applicability of the SRFDS trigger threshold obtained at a different site (near Squamish) to the Hope site can be evaluated using the SDF activations by rocks in the summer time. For example, between March, 2013 and September, 2013 the SDF was activated by rocks only once, whereas the SRFDS triggered 17 times. Assuming that the frequency of SDF activations correlates with the frequency of rocks that are cobble-size and larger, the PGV threshold must be lower than what this site's ground conditions suggest. The field records obtained in 2014 cannot be used for the evaluation of the PGV threshold because of the SDF's three month long activation due to the slope stabilization program.

(a) (b)

Figure 5.3. Photos taken with the web camera on December 1, 2014 (a) and December 4, 2014 (b). Photo (a) illustrates the area near sensors Z-17 and Z-18. Photo (b) illustrates the area between Z-19 and Z-20. Chunks of ice up to 0.028 m^3 in diameter are clearly visible on the ground.

(a) (b)

Figure 5.4. (a) Photo taken on December 4, 2014 with the web camera zoomed in on the area between sensors Z-10 and Z-15. (b) The same area on December 8, 2014. Chunks of ice up to 0.028 m^3 in diameter are clearly visible on the ground near the frozen waterfall.

Another possible explanation is that, because of the site topography, the system was activated by high-energy rocks and pieces of ice smaller than 0.028 m^3 which originated from significantly higher elevations than 4 m. Besides, chunks of ice disintegrate upon impact on a hard surface and eventually melt.

In 2014, only five SRFDS activations were caused by regular trains and high-rails out of the 8,760 trains that passed the site; in other words only 0.06% of rail traffic (the high-rails were not counted). Thus, the traffic detection algorithms designed in this research were able to correctly identify practically every train and high-rail.

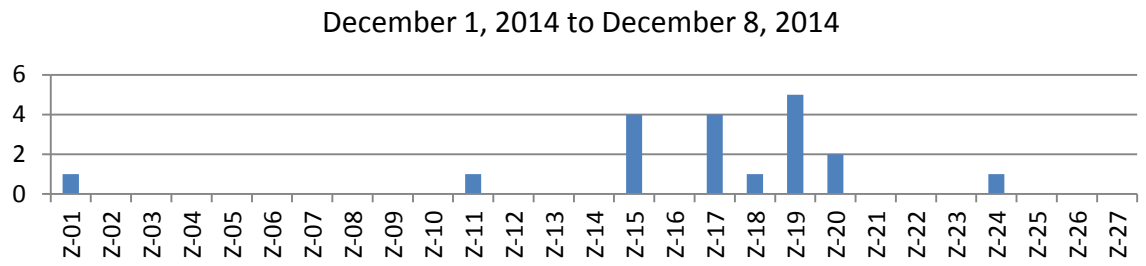

Figure 5.5. Distribution of the surface impacts that caused the Hope SRFDS to activate in November-December 2014, according to the computer model. These results are confirmed by field observations with the web camera (Figure 5.3, Figure 5.4).

5.3.3. Comparison of the SRFDS and SDF activations

Table 5.12 contains annual summaries of the actual CASC 038.90 SDF activations as well as the SRFDS activations generated by the computer model. The SRFDS activations were modeled using historical seismic data, and do not include the false alarms raised by track maintenance activity. Assuming that the maintainers rearm the rockfall monitoring system before leaving the site, only 128 SRFDS activations would have resulted in train slow-downs. This number includes 51 activations in 2013 (0.6% of the annual train traffic) and 77 activations in 2014, or 0.9% of the annual train traffic.

Though the number of SRFDS activations can be up to 15 times greater than the number of SDF activations, it is not the number of activations *per se* that should be used to compare the two systems. Rather, it is the adverse effects of false alarms measured as the number of slowed down trains: the number of trains delayed by SDF activations is 3-6 times greater than the number of delays by the SRFDS activations. This estimate does not include the train slow-downs that resulted from the prolonged SDF activation caused by the scaling program in 2014.

Table 5.12. Annual summaries of CASC 038.90 SDF and SRFDS activations between 2013 and 2014 together with the number of slowed-down trains.

Year	Activations of CP CASC 039.80 SDF			SRFDS activations	
	Total	Number of slowed-down trains	Percentage of annual traffic	Number of slowed-down trains	Percentage of annual traffic
2013	16	156	1.8%	51	0.6%
2014	5	507	5.8%	77	0.9%

5.4. Computer modeling of the White Canyon SRFDS

Because of hardware malfunctions in 2014, several months of seismic data are missing which is why the computer model is based on the 2012-2013 records. Thus, two years of near-complete seismic and SDF data were available for the comparison test. Computer modeling was performed using the PGV threshold obtained at the Squamish test site. The results of computer modeling are in Table 5.13 - Table 5.15.

5.4.1. Summary of the White Canyon SRFDS activations

Summary of the computer simulation of the SRFDS behaviour using historical data between January 1, 2012 and December 31, 2013 is in Table 5.13 and Table 5.14. The data are organized in the same manner as Table 5.10. Similar to the results obtained for the Hope SRFDS, the number of delayed trains can be significantly reduced if the track maintenance crews rearm the system before leaving the site. This effect is demonstrated in column [9] which contains the statistics from column [8] except for the activations caused by track maintenance.

Table 5.13. Summary of the computer simulation of CN ASH 094.50 SRFDS activations using one year of continuous seismic data between January 1, 2012 and December 31, 2012.

2012	**Regular rail traffic**		**Train stops**		**Track maint.**	**Animals**	**Rock-fall**	**Total activations**	**Total activations w/o track mtnce**
	[1]	**[2]**	**[3]**	**[4]**	**[5]**	**[6]**	**[7]**	**[8]**	**[9]**
January	2	2	13	3	35	1	7	48	13
February	2	2	6	5	12	1	1	21	9
March	0	0	15	6	22		6	34	12
April	4	0	11	6	17		11	34	17
May	8	0	10	6	26		36	68	42
June	6	0	1	1	49		21	71	22
July	14	0	8	1	23		23	47	24
August	31	0	6	3	31		9	43	12
September	2	0	6	1	19		31	51	32
October	1	0	10	4	32		6	42	10
November	0	0	14	10	51		11	72	21
December	0	0	26	10	20		1	31	11
Total							**162**	**562**	**225**
Percentage of delayed traffic								**6.4%**	**2.6%**

Table 5.14. Summary of the computer simulation of CN ASH 094.50 SRFDS activations using one year of continuous seismic data between January 1, 2013 and December 31, 2013. Thirteen days of seismic data are missing in September, 2013.

2013	Regular rail traffic		Train stops		Track maint.	Animals	Rock-fall	Total activations	Total activations w/o track mtnce
	[1]	[2]	[3]	[4]	[5]	[6]	[7]	[8]	[9]
January	4	4	13	8	25		10	47	22
February	0	0	11	1	25	1	9	36	11
March	5	3	7	2	13		14	32	19
April	3	1	7	4	10	2	7	24	14
May	2	1	9	3	14		10	28	14
June	0	0	2	0	34		13	47	13
July	3	1	16	13	16		14	44	28
August	6	1	25	12	37		3	53	16
September	3	0	6	4	23		3	30	7
October	3	0	7	4	9		2	15	6
November	2	1	7	3	26		7	37	11
December	1	0	10	4	36		11	51	15
Total							**103**	**444**	**176**
Percentage of delayed traffic								**5.1%**	**2.0%**

Table 5.15. Annual summaries of CN ASC 094.50 SDF and SRFDS activations together with the number of slowed-down trains.

Year	Activations of CN ASH 094.50 SDF			SRFDS activations	
	Total	Number of slowed-down trains	Percentage of annual traffic	Total	Percentage of annual traffic
2012	72	986	12.3%	225	2.6%
2013	105	1387	16.4%	176	2.0%

5.4.2. Interpretation of the results of computer modeling

Unlike the Hope SRFDS, which is equipped with a web camera, it is harder to interpret the results in Table 5.13 and Table 5.14, in particular the relatively high occurrence of what the SRFDS identified as rockfalls. It is possible that many system activations that were reported as rockfalls in May-July 2012 were actually caused by thermal expansion of the rails, or perhaps the rock mass. In a similar research project, Akkerman and Prahl (2013) stated that "thermally induced movement of the track causes 80% of nuisance alarms".

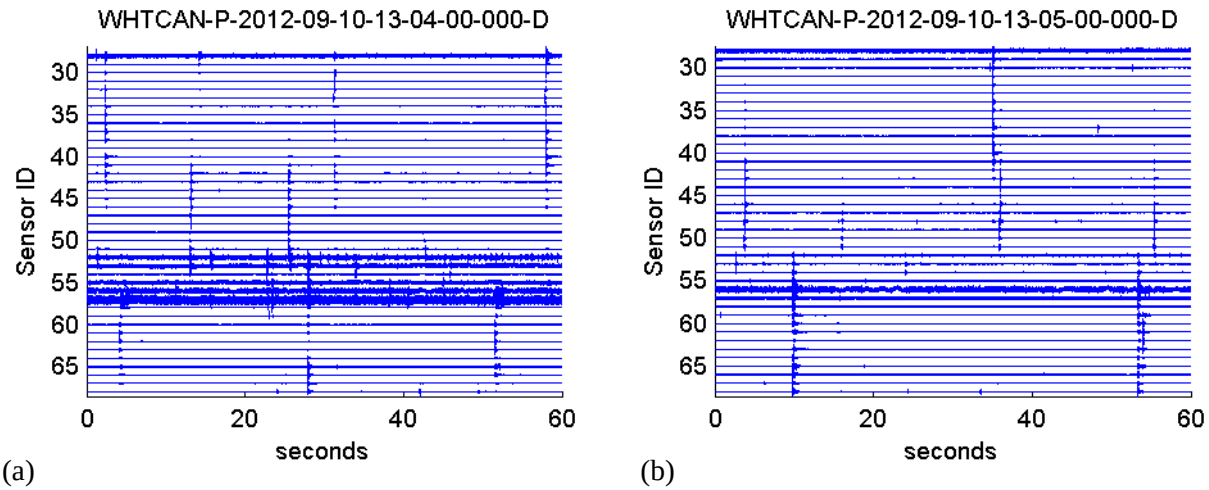

Figure 5.6. Two minutes of continuous seismic data (White Canyon, September 10, 2012). This is an example of what appears to be ground vibration induced by thermal expansion of the rails or the rock: events with similar-looking waveforms occur in the same areas every 20-30 seconds.

Compared to waveforms generated by surface impacts, these events are dominated by high frequencies, and, at 1 kHz sampling rate, appear under-sampled. This situation is similar to the one where rail vibrations are excited by weight impact (Figure 3.4). The amplitude decay *versus* epicentral distance and the arrival times of the thermally induced events are inconsistent with ground vibrations generated by rockfalls. Oftentimes they occur quasi-periodically, *e.g.* every 20-30 s (Figure 5.6) which is not typical for rockfalls. Locations and wave forms of the thermally induced movements are consistent (Figure 5.6,

Figure 5.7); they tend to occur during the hottest time of the day[22], and their occurrence correlates well with the annual and daily temperature fluctuations, peaking around noon but continuing into the late hours. The latter can be attributed to thermal contraction as the ground and the rails are cooling off. It should be noted that no events of this kind were identified within ~200 meters of the rail expansion joints at Z-12; rather, they clustered predominantly between M94.4 rock shed and M94.0 tunnel.

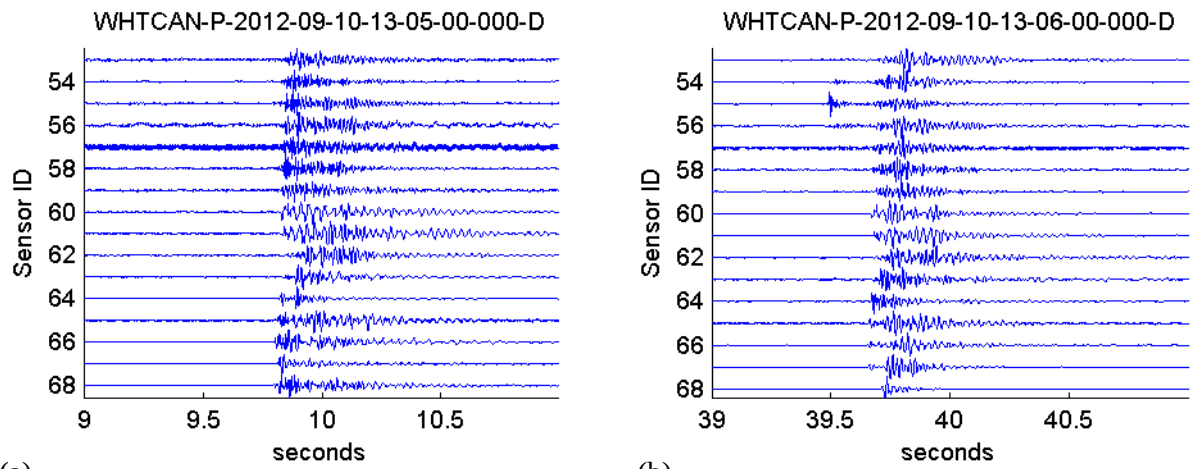

(a) (b)

Figure 5.7. Illustration of similar-looking waveforms of two seismic events that occurred 30 s apart.

Compared to 2012, fewer false positives were induced by thermal movement of the track in 2013 and 2015 (the summer 2014 seismic data were of low quality and were not included in the analysis). Assuming these signals are actually caused by thermal expansion / contraction of the rails, and that the absence of such noise in the area between sensors Z-05 and Z-25 is due to the presence of the rail expansion joints at Z-12, these false alarms can be potentially suppressed by adding more rail expansion joints.

The applicability of the trigger threshold obtained near Squamish to the ground conditions at the White Canyon site can be evaluated using the slide fence activations. In 2012-2013, the Lasha SDF was triggered by rocks on average 1-2 times a month. On the other hand, the monthly average for the computer model was 8-13 triggers. To minimize the bias from what appears to be thermally induced

[22] During the summer heat waves, Lytton is often the hottest spot in Canada: https://en.wikipedia.org/wiki/Lytton,_British_Columbia. Last checked on February 1, 2016.

movement of the track, we will analyze only the cold time of the year, from November to February: unlike the Hope SDF, the slide fence in this part of White Canyon is not subject to ice falls or ice build-up on the wires in the winter time. The SRFDS model triggered between once per month (February 2012 and December 2012) to as many as ten times in January 2013. These numbers are either equal to, or exceed, the average number of Lasha SDF activations for the same time of the year (*i.e.* 1-2 per month). Therefore, we can conclude that the PGV threshold used in the computer modeling experiment is a good approximation for the ground conditions at the White Canyon test site.

5.4.3. Comparison of the SRFDS and SDF activations

The results of computer modeling suggest that introduction of the SRFDS to replace SDF rockfall warnings can potentially reduce the annual rate of delayed trains from between 12% and 16% to between 2.0 % and 2.6 %. These estimates were calculated on the assumption that the number of SDF activations does not change significantly from year to year. This conclusion is based on the facts summarized as follows:

- Computer modeling of the SRFDS activations and delayed trains was carried out using 24 months of continuous seismic data recorded between January 2012 and December 2013. Between January 2012 and December 2013 with the PGV threshold obtained in this research for the hazardous rock ($0.028m^3$), the SRFDS model activated 1,006 times: 562 times in 2012; and 444 times in 2013. This number does not include activations due to EMI noise picked up by the unshielded sensor cables. Assuming that the SRFDS can rearm itself when a train passes, this means 1,006 delayed trains in two years, or 6.4% of the annual traffic in 2012 and 5.1% in 2013. This number includes 266 trains delayed by what was identified as hazardous rockfalls. This conclusion is based on the assumption that the track maintenance crews will leave the system activated, and that every train stop will activate the SRFDS which will remain activated until the next train passes the site. For comparison, in 2012 and 2013 12.3% and 16.4% of trains respectively were required to slow down because of SDF activations;
- Not all trains that stop leave the SRFDS computer model in an activated state after they resume their journey. Out of 246 train stops that caused the SRFDS computer model to activate only in 114 cases (or 46% of train stops) did the system remain activated after the trains left the site;

- The two most significant causes of SRFDS activations other than rockfalls (266) are train stops (246 cases) and track maintenance (605 cases). Combined, the train stops and the track maintenance caused 70% of activations, where activations induced by train stops and starts constitute 20% of the SRFDS activations in 2012-2013. This is why the performance of the autonomous SRFDS is largely determined by how efficiently these signals can be identified;
- The percentage of delayed trains could be further reduced if delays caused by track maintenance were eliminated. This could be achieved by instructing the maintenance crews to rearm the system upon completion of their work. Had this been done, within the two-year period analyzed with the computer model, the SRFDS would have delayed only 401 trains, or 2.3% of trains passing through White Canyon (2.6% in 2012 and 2.0% in 2013);
- Only five SRFDS activations in 24 months were caused by animals compared to 37 SDF activations for the same time period (the number is estimated based on the seismic records).

5.5. Summary

The Hope SDF

Only a small subset of the SDF activations registered by the SRFDS installation during the field tests in 2012-2014 was documented by S&C maintainers. At the Hope site, field reports were provided by CP for 5 months out of approx. 3.5 years of tests, or 12% of the time; at the White Canyon site, CN provided witness reports on SDF activations that cover 3 months out of approx. 4.5 years of tests, or 6% of the time. At the Hope site, the witness reports are in accord with the SRFDS automatic event analysis (Appendix D). All five rockfalls that caused SDF activations were non-hazardous ones. The SRFDS reported a ~0.5 ft^3 / 0.014 m^3 rock as hazardous, and correctly ignored the other four.

The White Canyon SDF

Nine witness event reports are available for the White Canyon site complete with rock photos and seismograms (Appendix E): five non-hazardous rocks (<0.028 m^3); and four hazardous. In one case

which involved a hazardous rock approx. 1 m^3 in volume (Figure E.2) it was impossible to identify the rock's seismic signature within the continuous seismic data, *i.e.* this event report is incomplete.

The four hazardous rocks include the March 11, 2011 rockfall (Figure E.16), the March 25, 2012 rockfall (Figure E.13), and the June 5, 2013 rockfall (Figure 3.61) which were correctly identified by the SRFDS as hazardous. The five non-hazardous rocks that broke the SDF wires were correctly identified and ignored by the SRFDS.

However, the March 24, 2012 event (Figure E.10 in Appendix E) which involved a rock about 0.028 m^3 was identified by the SRFDS as non-hazardous and ignored, probably because the impact energy was partially absorbed by soft talus deposits. This example raises the concern that if a hazardous rock falls onto the track area covered by, for instance, unconsolidated talus deposits, the impact will generate weaker ground vibration than what is expected based on the calibration tests, and the signal amplitude will not exceed the PGV threshold. This possibility needs to be accounted for when evaluating the applicability of the SRFDS, calibrating the system with test impacts, or when planning the site maintenance.

The SRDFS/ Data Analysis software utilized in this experiment implements the approach described in Chapters 3 and 4. With the SRFDS self-rearming capability in effect, a non-threatening activation causes no more than one delay.

Computer modeling of the SRFDS

The behaviour of the SRFDS was modeled with four years of continuous seismic data from the two test sites. For automatic detection of hazardous rocks the PGV model obtained near Squamish was used. The system performance was evaluated based on the percentage of delayed rail traffic and compared to the actual number of train delays caused by the SDF activations.

According to the computer model, for the Hope SRFDS site, the annual number of slowed-down trains was 51 in 2013 (0.6% of the annual train traffic) and 77 in 2014, or 0.9% of the annual train traffic. For comparison, the Hope SDF activations slowed-down 1.8% of trains in 2013, and 5.8% of trains in 2014. At the White Canyon site, the SRFDS activations would have delayed only 225 trains in 2012 (2.6% of the annual train traffic), and 176, or 2.0% of annual traffic, in 2013. The White Canyon SDF activations slowed-down 12.3% of trains in 2012, and 16.4% of trains in 2013.

The introduction of the SRFDS can potentially reduce the average number of trains currently slowed down by SDF activations, most of which are due to non-hazardous causes, *e.g.* animals, cobble-size rocks, and ice. Depending on location, the reduction in the number of slowed-down trains can be between 3 and 8 times. This estimate includes the false positives produced by ice falls (the Hope site) and by what seems to be track movement induced by thermal expansion (the White Canyon site).

This assessment is based on the assumptions that track maintenance crews will rearm the monitoring system upon completion of their work; and that it will take only one train to rearm the SRFDS automatically.

SRFDS activations by wild life depend on the location; at the test sites involved in this research their number has been insignificant.

6. Summary and Conclusions

Transportation routes through mountainous terrain are often susceptible to landslide hazards, particularly rockfalls and rockslides that can cause traffic delays, damage, injury, and death to users of these routes. Dangerous rockfall locations can be addressed by one of the four principal approaches or their combination: (a) relocation of the alignment to avoid or minimize the hazard; (b) slope stabilization, *i.e.* by preventing rocks from detaching, *e.g.* through rock scaling, bolting and shotcreting; (c) protection, *i.e.* keeping rocks that do move out of place from reaching the roadway, *e.g.* with walls, tunnels, rock sheds or catchment ditches; and (d) warning, *i.e.* signaling the rail traffic when rocks fall in the vicinity of the track. Warning systems are installed where occasional falls are expected but the anticipated protection or stabilization measures would be extremely difficult or expensive.

The warning device most widely used by North American railway operators is the electric slide detector fence (SDF) which is composed of multiple wires supported on timber poles. SDF has a number of drawbacks: 40% to 70% of SDF triggers are false alarms caused by animals and non-hazardous rocks; it takes eight hours on average to repair an activated signal fence; and maintenance of the SDF can be expensive. In areas with high rockfall activity, the ratio of slowed down trains can exceed 20% of rail traffic. Since trains can be derailed by rocks as small as 30 cm, this research is concerned with detection of rocks of this size and larger which will be referred to as *hazardous* rocks; by *non-hazardous* rocks we will means rocks smaller than 0.028 m^3.

Seismic monitoring can offer a solution to the problems associated with using SDF in active rockfall areas. The Seismic Rockfall Detection System (SRFDS) uses an array of geophones in order to convert seismic signals to analog outputs which are subsequently digitized and processed by a central computer. When a rock falls (or another event occurs, such as a train or vehicle passing the site, or an animal walking along the track, *etc.*) the analytical software running on the central computer will apply a set of criteria in order to determine whether a rockfall has occurred. Once the rock has been cleared off the track or an inspection reveals the alarm was a false trigger, the system can be reset electronically, without requiring the signal maintainer to be on site to physically repair the system.

Previous attempts to design a seismic monitoring system for automatic warning of hazardous rockfall along transportation corridors were unsuccessful. For instance, researchers have experienced the problem of strong anthropogenic seismic signals in the proximity of highways. The concept of an autonomous SRFDS implemented in this research relies on several unique properties of the railway operating environment.

First, the SRFDS is deployed along railway lines in remote areas where sources of anthropogenic noise are few and can be identified relatively easily. Some of these signals frequently display distinct patterns which can be used for their identification (*e.g.* railway traffic); others are too weak to be confused with a hazardous rockfall (*e.g.* tree roots, aircraft, animal migration).

Second, the SRFDS is allowed to ignore rockfall when a train is passing by because such information would not have practical value. The peak ground velocity (PGV) of the signal generated by a hazardous rockfall is typically smaller than the PGV of ground vibrations induced by rail traffic, which means that the rockfall monitoring system is incapacitated every time a train passes. However, according to the railway operators who supported this research, they are prepared to tolerate this deficiency. The reason is that even if the SRFDS were able to identify a hazardous rockfall within much stronger train noise, this information would be practically useless because it takes a train several hundred meters to stop. On the other hand, if a train continues its journey it means that either there were no hazardous rockfalls before the train entered the block, or that the rocks were not large enough to derail the train.

As a result, the third unique property of the SRFDS is that it can be programmed to interpret a train transit signal as a confirmation that there is no obstruction on the track, and rearm automatically. The advantages of the concept of SRFDS self-rearming are that the system will not require human intervention to become rearmed, and that no more than one train will be delayed by any activation. It should be noted that this concept does not apply to seismic rockfall monitoring of highways (motorists can drive around an obstruction without stopping); nor does it apply to railways with multiple parallel tracks, unless the SRFDS is supplemented with wheel detectors.

Finally, even though track maintenance (*e.g.* ballast cleaning, rail grinding, SDF repairs, debris removal, *etc*.) may be a frequent cause of false positives, there is no need to identify these seismic signals automatically. Seismic signals excited by these activities display unpredictable patterns which are almost impossible to identify automatically. However, the Railway Traffic Control centre is always aware of the whereabouts of the maintenance crews, and measures can be taken to ignore these alarms and/or rearm the system when the crew leaves the site.

Automatic recognition of hazardous rocks

Automatic identification of individual seismic phases induced by surface impacts can be challenging and, if attempted, would be prone to error. This has to do with the presence of multiple propagation media, including rails, and variations in the depth of bedrock as well as an inhomogeneous medium which

consists of gravel, sand, large boulders *etc*. Therefore, it was decided not to calculate rockfall location in real time; instead, an approach with the intention of detecting hazardous rocks has been adapted that is based only on the analysis of peak amplitudes.

Amplitude of the seismic signals induced by rockfall as they propagate away from the source depends on a number of factors which are not always possible to model accurately, including the surface and sub-surface ground conditions. An approach to the identification of hazardous rocks in real time has been developed that includes an empirical PGV threshold model obtained in a series of calibration tests. The trigger threshold is applied in a 2D grid search procedure and, if a location is found at which the recorded PGV exceeds the threshold, the SRFDS reports a hazardous rock.

It is assumed that impacts of hazardous rocks can be modeled in the system calibration tests; and that the consistent ground response to the surface impacts can be ascertained experimentally. In practice, a near-vertical rock face appears to be the only type of geology that meets these expectations. To illustrate the opposite example, a debris flow carrying pebbles can potentially cause a derailment; yet, it does not seem to be possible to model such a scenario. It is also expected that a) the selected calibration rock and the minimum drop elevation are representative of the hazardous conditions that the SRFDS has to report; and that b) larger rocks will induce ground vibrations with larger amplitude. It is further assumed that, once the system trigger threshold has been established experimentally in a series of calibration tests, the geotechnical conditions of the site will not change in such a way as to weaken the ground response to hazardous rocks, *e.g.* due to weather (precipitation, temperature), ballast fouling or accumulation of soft deposits at the bottom of the slope. If the ground response is found to depend on the location, the lowest PGV observed across the test site should be utilized as the empirical PGV threshold. For this purpose, test drops need to be carried out along the entire site. In order to plan the system calibration procedure, trajectory models (*e.g.* free-falling, rolling), minimum elevation, and rockfall volume distribution are required for the instrumented site.

Pattern recognition: train detection

It is desirable for an autonomous SRFDS to be able to identify railway traffic for two reasons: first, not to raise a false alarm (or, to rearm the SRFDS after it was activated by a train that stopped at the site, once the train resumes its journey); and second, to confirm that there is no obstruction on the track. Train seismograms display a characteristic pattern of periodic, spatially correlated signals whose time shift is proportionate to the train speed. This pattern can be used to identify trains and high-rails automatically.

Three train detection algorithms were implemented which combine beam-forming, matched-filtering and STA/LTA techniques to detect patterns of moving rail vehicles within seismic data. The algorithms detect train patterns in the seismic signal generated by an approaching locomotive, as well as the periodic patterns in the middle of the train signal. The vehicle identification techniques were supplemented with the end-of-train detector algorithms.

Pattern recognition: rockfall detection

The rockfall detection procedure described previously relies on negative decision logic: it begins by detecting all signals that deviate from the train patterns, which are then analyzed as potentially hazardous rockfalls. In the presence of frequent and strong anthropogenic signals (trains) this approach incurs undesirable delays in reporting hazardous rockfalls, because ground vibration induced by rocks first needs to be analyzed by the train detector algorithms. Alternatively, a trigger algorithm based on detection of known rockfall patterns is an example of positive decision logic. If such an algorithm is applied to seismic signals before train identification is complete, this would minimize the system latency in reporting hazardous rocks. The two approaches are not mutually exclusive and can be combined within the SRFDS data processing workflow.

A technique for real-time rockfall recognition in the presence of train noise was implemented which is based on a coincidence trigger (also called an array, or network, trigger) and zero-lag cross-correlation (ZLCC) of r.m.s.-averaged data. The algorithm allows the SRFDS to skip the traffic identification which reduces the latency in reporting hazardous rocks to less than 3 seconds on average, assuming 5 s long input data files.

Electric spikes are induced by electromagnetic interference (EMI) of velocity transducers and cables with power lines or lightning strikes. In seismic records EMI spikes appear as outliers whose seismic signature, after r.m.s.-averaging, can look similar to that of a rockfall. In order to reduce the chances of false positives due to EMI spikes, an outlier detection algorithm was implemented for removal of EMI spikes from raw seismic data.

Field tests near Hope (BC, Canada)

The web camera installed at CP CASC 038.90 (near Hope, BC) was instrumental in providing feedback from the site and interpreting the results of seismic monitoring. Computer simulation of the CASC

038.90 SRFDS behaviour using 24 months of continuous seismic data resulted in 498 activations. The three most important causes are rockfalls (93 activations), train stops (118), and track maintenance (261). Only in 27 cases out of 118 did the SRFDS remain activated after the train left the site.

Assuming that the track maintainers are instructed to rearm the monitoring system before leaving the site, only 128 activations would have resulted in train slow-downs, including 51 activations in 2013 (0.6% of the annual train traffic) and 77 activations in 2014, or 0.9% of the annual train traffic. For comparison, the Hope SDF activations slowed-down 1.8% of trains in 2013, and 5.8% of trains in 2014.

At the Hope site, both SRFDS and SDF activations have displayed a seasonal trend. Field observations with the web camera combined with the distribution of surface impacts along the site suggest that many of the SRFDS activations were due to ice falls.

The available witness reports on natural rockfalls from CP signal maintainers are in accord with the SRFDS automatic event analysis. All five rockfalls that caused SDF activations were non-hazardous. The SRFDS reported a ~0.014 m^3 rock as hazardous, and correctly ignored the other four.

Field tests in White Canyon (BC, Canada)

Computer modeling of the SRFDS installed at CN ASH 094.50 in White Canyon (near Lytton, BC, Canada) was carried out using 24 months of continuous seismic data recorded between January, 2012 and December, 2013. The SRFDS model activated 1,006 times. The two most frequent causes of SRFDS activations other than rockfalls (266) are train stops (246 cases) and track maintenance (605 cases). Only in 114 cases out of 246 (46% train stops) did the SRFDS remain activated after the train left the site. It is possible that many of the SRFDS activations that were reported by the computer model as rockfalls in May-July 2012 were actually caused by thermal expansion of the rails.

The percentage of delayed trains could be further reduced if delays caused by track maintenance were eliminated which could be achieved by instructing the maintenance crews to rearm the system upon completion of their work. Had this been done, within the two-year period of time analyzed with the computer model the SRFDS would have delayed only 401 trains, or 2.3% of trains passing through White Canyon (2.6% in 2012 and 2.0% in 2013). For comparison, in 2012 and 2013, 12.3% and 16.4% of trains respectively were required to slow down because of SDF activations.

Nine reports on natural rockfalls are available complete with photos and seismograms. Eight rockfalls were correctly reported by the SRFDS as either hazardous or non-hazardous. One of the documented

events which involved a rock about 0.028 m^3 was identified by the SRFDS as non-hazardous and ignored, probably because the impact energy was largely absorbed by soft talus deposits in this area of White Canyon. One needs to consider the possibility of hazardous rocks falling onto soft talus slopes, rather than impacting rails or ties, when evaluating the applicability of the SRFDS to a specific location, or when planning the system calibration procedure.

Introduction of the SRFDS can potentially reduce the average number of trains slowed down by SDF activations, and eliminate the bottleneck effect currently associated with prolonged SDF activations. The actual reduction of the number of delayed trains is between 3 and 8 times, depending on the location.

Suggestions for Future Research

The comparison between the Slide Detector Fences and the SRFDS presented in this research is based on one parameter: the ratio of slowed down trains. The differences between these two landslide warning technologies should be further explored from the standpoint of their safety and reliability. Probabilistic Quantitative Risk Assessment (QRA) models can be used, for example, to quantify the risks related to a warning system missing a hazardous rock when seismic signals are buried within the ground vibration generated by a moving train (*e.g.* Figure 3.59).

In this study, a number of assumptions about the consistency of ground response to surface impacts were made to develop a methodology of automatic recognition of hazardous rocks. Also, the system calibration procedure involved dropping a weight vertically. In future research, the influence of precipitation, temperature, and other factors that can potentially affect the ground conditions should be investigated with regard to their influence on the sensitivity of the seismic monitoring system. Future efforts should also focus on the applicability of the SRFDS to locations where slope movements are not limited by vertical or near-vertical trajectories, and involve rolling and bouncing rocks.

References

Abott, B., Bruce, I., Savigny, W., Keegan, T., and F. Oboni (1998). A methodology for the assessment of rockfall hazard and risk along linear transportation corridors. *In 8th Internation IAEG Congress*, Balkema, Rotterdam, Vol. 1-5, 1195-1200.

Agioutantis Z., Mertikas, S., Steiakakis, C., Daskalakis, A., Tripolitsiotis, A., Krtitikakis, G., Apostolou, E., and G. Kaplanidis (2014) Rockfall monitoring system for improving road safety, The 2014 ISRM European Rock Mechanics Symposium-EUROCK2014, Vigo, Spain, 27-29 May 2014.

Aki, K. and P.G. Richards (2002). Quantitative Seismology, 2nd Edition. University Science Books.

Akkerman, J., and F. Prahl (2013). Fiber Optic Sensing for Detecting Rock Falls on Rail Rights of Way. *The American Railway Engineering and Maintenance-of-Way Association (AREMA), 2013 Conference*.

Allen, R. (1978). Automatic earthquake recognition and timing from single traces, *Bull. Seism. Soc. Am.* 68, 1521-1532.

Allen, R. (1982). Automatic phase pickers: their present use and future prospects, *Bull. Seism. Soc. Am.* 72, S225-S242.

Allen, R.M., and H.Kanamori (2003). The potential for earthquake early warning system in southern California, *Science* 300, 786-789.

Almendros, J., Ibanez, J. M., Alguacil, G., and E. Del Pezzo (1999). Array analysis using circular-wave-front geometry: An application to locate the nearby seismo-volcanic source, *Geophys. J. Int.* 136, 159–170.

Altmann, J., (2004). Acoustic and seismic signals of heavy military vehicles for co-operative verification, *Journal of Sound and Vibration* 273 (2004) 713–740.

Alves Costa, P., Calcada, R., and A. Silva Cardoso (2012). Track–ground vibrations induced by railway traffic: In-situ measurements and validation of a 2.5D FEM-BEM model, *Soil Dynamics and Earthquake Engineering* 32, 111–128.

Ambuter, B. P., and S.C. Solomon (1974). An event-recording system for monitoring small earthquakes. *Bull. Seismol. Soc. Am.* 64, 1181-1188.

Amitrano, D., Grasso, J.R., and G. Senfaute (2005). Seismic precursory patterns before a cliff collapse and critical point phenomena, *Geophysical Research Letters* 32: L08314.

Amitrano, D., Gaffet, S., Malet, J., and O. Maquaire (2007). Understanding mudslides through micro-seismic monitoring: The Super-Sauze (South French Alps) case study. *Bulletin de la Société Géologique de France*, 178 (2), pp.149-157.

Anderson, K. R. (1982). Syntactic analysis of seismic waveforms using augmented transition network grammars, *Geoexploration*, 20, 161-182.

Anderson, T., Ketcham, S., Moran, M., and R.Greenfield (2001). FDTD Seismic Simulation of Moving Battlefield Targets Unattended Ground Sensor Technologies and Applications III, Edward M. Carapezza, Editor, *Proceedings of SPIE* Vol. 4393.

Andrew, R.D., Arndt, B., and A.K.Turner (2012). Instrumentation and Monitoring Technology, In: Rockfall Characterization and Control, edited by Turner and Schuster, pp. 212–284. Washington, DC, United States of America: Transportation Research Board.

AREMA Practical Guide to Railway Engineering (2003). Published by American Railway Engineering and Maintenance of Way Association (AREMA).

Auersch, L. (2010a). Technically Induced Surface Wave Fields, Part I: Measured Attenuation and Theoretical Amplitude-Distance Laws, *Bull. Seismol. Soc. Am.* Vol. 100, no. 4, 1528–1539, doi: 10.1785/0120090228.

Auersch, L. (2010b). Technically Induced Surface Wave Fields, Part II: Measured and Calculated Admittance Spectra, *Bull. Seismol. Soc. Am.* 100, 1540-1550.

Auersch, L., and S.Said (2010). Attenuation of ground vibrations due to different technical sources, *Earthquake Engineering and Engineering Vibration*, Vol. 9, Issue 3, 337-344.

Baer, M., and U. Kradolfer (1987). An automatic phase picker for local and teleseismic events, *Bull. Seism. Soc. Am.* 77, 1437-1445.

Barnett, V., and T. Lewis (1994). Outliers in Statistical Data. Wiley, New York.

Barsikow, B., King III, W. F., and E. Pfizenmaier (1987). Wheel/rail noise generated by a high-speed train investigated with a line array of microphones, *J. Sound Vib.* 118, 99–122.

Barsikow, B. (1996). Experiences with various configurations of microphone arrays used to locate sound sources on railway trains operated by the DB AG, *Journal of Sound and Vibration*, 193, 283–293.

Bessason, B., Eiríksson, G., Thórarinsson, Ó., Thórarinsson, A., and S.Einarsson (2007). Automatic detection of avalanches and debris flows by seismic methods, *Journal of Glaciology*, Vol. 53, no. 182, 461-472(12).

Bobrowsky, P., Sladen, W., Huntley, D., Qing, Z., Bunce, C., Edwards, T., Hendry, M.T., Martin, C.D. and E. Choi (2014). Multi-parameter monitoring of a slow-moving landslide: Ripley Landslide, British Columbia, Canada. International Association of Engineering Geologists (IAEG) 2014, Turin, Italy, September 15-19.

Bonnefous, O., and P. Pesque (1986). Time domain formulation of pulse-Doppler ultrasound and blood velocity estimation by cross-correlation, *Ultrason. Imaging*, vol. 8, no. 2, 73 -85.

Bonnefoy-Claudet, S., Cotton, F. and P.Bard (2006). The nature of noise wavefield and its applications for site effects studies. A literature review, *Earth Sci. Rev.*, (3–4), 205–227.

Bornitz, G. (1931). Über die Ausbreiting der von Grosskolbenmaschinen erzengten Bondenschwingungen in die Tiefe. Berlin: Springer.

Bose, M., Hauksson, E., Solanki, K., Kanamori, H., Wu, Y.-M., and T. H. Heaton (2009). A new trigger criterion for improved real-time performance of onsite earthquake early warning in southern California, *Bull. Seismol. Soc. Am.* 99, no. 2A, doi: 10.1785/0120080034.

Brackett, P. (2002). Railway Rockfall Electromagnetic Field Disturbance Sensing System Development and Test Results, Transport Canada, TP 13928E.

Brady, B.T., and F.W. Leighton (1977). Seismic anomaly prior to a moderate rock burst: A case study. *International Journal of Rock Mechanics, Mining Science, and Geomechanics Abstracts,* 14, 127-132.

Brawner C. O., and D.C. Wyllie (1976). Rock slope stability on railway projects. American Railway Engineering Association, Bulletin 656. Chicago, IL.

Briechle, K., and U.D. Hanebeck (2001). Template matching using fast normalized cross correlation. In: *Proceedings of SPIE*, V. 4387, Optical Pattern Recognition XII, Orlando, FL. 95–102.

Brink, A.v.Z., Canbulat, I., and S.M.Spottiswoode (2002). Development and evaluation of a warning device for impending rood instability in mines. *Proceedings of the SANIRE 2002 Symposium — 'Re-Defining the Boundaries'.*

Bunce, C., Cruden, D., and N.Morgenstern (1997). Assessment of the hazard from rock fall on a highway. *Can. Geotech. J.* 34 : 344-356.

Bunce C.M. (2008). Risk estimation for railways exposed to landslides. PhD thesis. University of Alberta. Edmonton, Canada.

Bunce, C.M., Martin, C.D., Keegan, T., Hutchinson, D.J., Ruel, M., and P.Lemay (2006). An overview of the Canadian Railway Ground Hazard Research Program. *7th World Congress on Railway Research.* 4 - 8 June 2006, Montreal, Canada. 14 p.

Calvetti, F., Di Prisco, C., and M.Vecchiotti (2005). Experimental and numerical study of rock-fall impacts on granular soils, *Rivista Italiana di Geotecnica*, 4, 95–109.

Carlson, S.J. (2010). Evaluation of a new seismic slide detection system to replace the existing Lasha Slide Detector fences, Near Lytton, BC. University of Alberta, Edmonton, Alberta (not published).

Chen, C.H. (1978). Seismic Pattern Recognition, *Geoexploration*, 16, 133-146.

Chen, G.Q., Zheng L., Zhang, Y.B., and J.Wu (2013). Numerical simulation in rockfall analysis: a close comparison of 2-D and 3-D DDA. Rock Mech Rock Eng 46:527–541.

Cleave, R., Myrvoll, F., and R. Nålsund (2009). Microseismic monitoring and early warning of geohazards along railway lines in Norway. ICSMGE.

Collins, B. D. and N. Sitar (2007). Processes of coastal bluff erosion in weakly lithified sands, Pacifica, California, USA, Geomorphology, 97, 483–501, doi:10.1016/j.geomorph.2007.09.004, 2008.

Collins, D.S., Toya, Y., Hosseini, Z. and C.-I. Trifu (2014). Real time detection of rock fall events using a microseismic railway monitoring system, *Geohazards*, Kingston, Canada.

Connolly, D., Giannopoulos, A., and M.C.Forde (2013). Numerical modelling of ground borne vibrations from high speed rail lines on embankments, *Soil Dynamics and Earthquake Engineering* 46, 13–19.

Cruden, D.M. and D.J. Varnes (1996). Landslide types and processes. In: Turner AK, Schuster RL (eds.) Landslides investigation and mitigation. Transportation research board, US National Research Council. Special Report 247, Washington, DC, Chapter 3, pp. 36–75.

Dammeier, F., Moore, J.R., Haslinger, F., and S.Loew (2011). Characterization of alpine rockslides using statistical analysis of seismic signals. *Journal of Geophysical Research*, doi:10.1029/2011JF002037.

Davies, D., Kelly, E. J., and J.R. Filson (1971). Vespa process for analysis of seismic signals, *Nature Phys. Sci., 232*, 8–13, 1971.

Denholm-Price, J. C.W., and J. M. Rees (1999). Detecting waves using an array of sensors. *Mon. Wea. Rev.*, 127, 57–69.

Deparis, J., Jongmans, D., Cotton, F., Baillet, L., Thouvenot, F., and D.Hantz (2008). Analysis of rock-fall and rock-fall avalanche seismograms in the French Alps. *Bulletin of the Seismological Society of America* 98: 2: 1781-1796.

DeRoin, N. and R.S. McNutt (2012). Rockfalls at Augustine Volcano, Alaska: The influence of eruption precursors and seasonal factors on occurrence patterns 1997-2009, *Journal of Volcanology and Geothermal Research*, 211-212, 61-75

Ditzel, A., Herman, G.C., and G.G.Drijkoningen (2001). Seismograms of moving trains: comparison of theory and measurements, *Journal of Sound and Vibration*, 248 (2001) 635–652.

Dowla, F. U., Taylor, S. R., and R. W. Anderson (1990). Seismic discrimination with artificial neural networks: preliminary results with regional spectral data, *Bull. Seism. Soc. Am*. 80, 1346–1373.

Duda, R., and P.Hart (1973). Pattern classification and scene analysis, New York, Wiley.

Durkin, J., and R.J. Greeenfield (1981). Evaluation of the seismic system for locating trapped miners. Bureau of Mines Report of Investigations RI/8567. 61 pp.

Edmund Nuttall Limited (2007). Report on rockfall detection and protective measures evaluation study, Donaldson Associates Ltd. (Draft; not published).

Eisner, L., Abbott, D., Barker, W. B., Lakings, J., and M. P. Thornton (2008). Noise suppression for detection and location of microseismic events using a matched filter: *78th Annual International Meeting, SEG, Expanded Abstracts*, 1431–1435.

Eshraghian, A., Martin, C.D., and D.M.Cruden (2007). Complex earth slides in the Thompson River Valley, Ashcroft, British Columbia. *Environmental & Engineering Geoscience*, 13(2): 161–181. doi:10.2113/gseegeosci.13.2.161

Eshraghian, A., Martin, C.D., and N.R.Morgenstern (2008). Movement triggers and mechanisms of two earth slides in the Thompson River Valley, British Columbia, Canada. *Canadian Geotechnical Journal*, 45 (9): 1189–1209. doi:10.1139/T08-047.

Esposito, A. M., F. Giudicepietro, S. Scarpetta, L. D'Auria, M. Marinaro, and M. Martini (2006). Automatic discrimination among landslide, explosion-quake and microtremor seismic signals at Stromboli volcano using neural networks, *Bull. Seismol. Soc. Am*. 96, no. 4A, 1230 – 1240, doi 10.1785/0120050097.

Evans, S.G., and O. Hungr (1993). The analysis of rock fall hazard at the base of talus slopes. *Canadian Geotechnical Journal*, 30 : 620–636.

Farin, M., A. Mangeney, R. Toussaint, J. de Rosny, N. Shapiro, T. Dewez, C. Hibert, C. Mathon, O. Sedan, and F. Berger (2015). Characterization of rockfalls from seismic signal: Insights from laboratory experiments, *J. Geophys. Res. Solid Earth*, *120*, 7102–7137, doi:10.1002/2015JB012331.

Foti, S. (2000). Multistation methods for geotechnical characterization using surface waves. *PhD dissertation*, Politecnico di Torino, Italy.

Frankel, A., Hough, S., Friberg, P., and R. Busby (1991). Observations of Loma Prieta aftershocks from a dense array in Sunnyvale, California, *Bull. Seism. Soc. Am*., 80 (1991), 1900–1922.

Fritschen, R. (2010). Mining-induced seismicity in the Saarland, Germany. *Pure and Applied Geophysics* 167, 77–89.

Fryba, L. (1972). Vibration of solids and structures under moving loads. Groningen, The Netherlands: Noordhoff International Publishing.

Gauthier D., Lato M., Edwards T., and D.J.Hutchinson (2012a). Observations of an annual cycle of rock fall, debris flux, and erosion affecting a railway corridor in the White Canyon of the Thompson River, BC, from serial LiDAR scans, Canadian Geotechnical Conference; Montreal, Canada. Sept 29-Oct 3, 2013.

Gauthier D., Lato M., Edwards T., and D.J. Hutchinson (2012b). Rockfall and talus accumulation from serial LiDAR scans: A railway case study from the White Canyon, Thompson River, BC, Canadian Geotechnical Conference; Manatoba.

Gibbons, M. (1978). Low frequency microseisms in relation to mine roof stability. *AE/MS in Geologic Structures and Materials: Proceedings of the 2nd Conference*. 246-257.

Gibbons, S. J. and F.Ringdal (2006). The detection of low magnitude seismic events using array-based waveform correlation. *Geophys. J. Int.* 165, 149–166.

Gibowicz, S.J. (1990). Keynote lecture: The mechanism of seismic events induced by mining. *Rockbursts and Seismicity in Mines: Proceedings of the 2nd International Symposium:* 3-27.

Gibowicz, S.J. and A.Kijko (1994). An Introduction to Mining Seismology, Academic Press, San Diego, CA.

Gischig,V.S., Hungr, O., Mitchell,A., and F.Bourrier (2015). Pierre3D: a 3D stochastic rockfall simulator based on random ground roughness and hyperbolic restitution factors, Can. Geotech. J. 52: 1360–1373.

Gledhill, K.R. (1985). An earthquake detector employing frequency domain techniques, *Bull. Seism. Soc. Am*. 75, 1827-1835.

Got, J.-L., Mourot, P., and J.Grangeon (2010). Pre-failure behaviour of an unstable limestone cliff from displacement and seismic data. *Nat. Hazards Earth Syst. Sci*. 10, 819–829.

Gucunski, N. (1991). Generation of low frequency Rayleigh waves for the spectral analysis of surface waves method, *Ph.D. thesis*, University of Michigan, Ann Arbor, Mich.

Gutowski, T., and C. Dym (1976). Propagation of ground vibration, a review, *J. Sound Vib*. 49, 179–193.

Hardy, H.R., Jr., Belesky, R., Kimble, E.J., Mrugala, M., Hager, M.E. and F. Taioli (1988). A study to investigate the potential of the acoustic emission/microseismic technique as a means of evaluating slope stability, Final Project Report, PennDot and US Department of Transportation.

Hardy, H.R.J., and E.J. Kimble (1991). Application of high frequency AE/MS techniques to rock slope monitoring. Proceedings of the 5th Conference on Acoustic Emission/ Micro- seismic Activity in Geologic Structures and Materials. Pennsylvania State University, Trans Tech Publications, Clausthal, Germany, pp. 457–477.

Hardy, H.R. (1992). Geotechnical field applications of AE / MS techniques at the Pennsylvania State University: a historical review, International Conference on Monitoring and Predictive Maintenance of Plants and Structures, 17-20 May 1992, Firenze, Italy.

Hasegawa, H. S., Basham, P. W. and M. J. Berry (1981). Attenuation Relations for Strong Seismic Ground Motion in Canada. *Bulletin of the Seismological Society of America* 71 (6): 1943 – 1962.

Haskell, N. (1953). The dispersion of surface waves on multilayered media. *Bulletin of the Seismological Society of America* 73, 17-43.

Hatch Mott MacDonald Inc. (2009). Evaluation of the E & N Railway Corridor: Baseline Reference Report, BC Ministry of Transportation and Infrastructure, http://www2.gov.bc.ca/gov/content/transportation/transportation-reports-and-reference/reports-studies/vancouver-island/e-n-rail (last checked on April 20, 2016).

Hatherly, P (2013). Overview on the application of geophysics in coal mining, *International Journal of Coal Geology* 114 , 74–84.

Hawkins, D. (1980). Identification of Outliers, Chapman and Hall.

Helmstetter, A. and S.Garambois (2010). Seismic monitoring of Séchilienne rockslide (French Alps); analysis of seismic signals and their correlation with rainfalls. *Journal of Geophysical Research* 115: F3: F03016. DOI: 10.1029/2009JF001532.

Hibert, C., Mangeney, A., Grandjean, G., and C. Baillard (2014). Automated identification, location, and volume estimation of rockfalls at Piton de la Fournaise volcano, *J. Geophys. Res. Earth Surf.*, 119, 1082–1105, doi:10.1002/2013JF002970.

Higgins, J. D., and R. D. Andrew (2012a). Rockfall Types and Causes. In: Rockfall Characterization and Control, edited by Turner and Schuster, 21–55. Washington, DC, United States of America: Transportation Research Board.

Higgins, J. D., and R. D. Andrew (2012b). Site Characterization. In: Rockfall Characterization and Control, edited by Turner and Schuster, 177–211. Washington, DC, United States of America: Transportation Research Board.

Huang, C.J., Yin, H.Y., and C.Y. Chen (2007). Ground vibration produced by rock motions and debris flows, *J. Geophys. Res.*, 112, F02014.

Hutchinson, D.J., Lato, M., Gauthier, D., Kromer, R., Ondercin, M., MacGowan, T., and T. Edwards (2015). Rock Slope Monitoring and Risk Management for Railway Infrastructure in the White

Canyon, British Columbia, Canada. *Engineering Geology for Society and Territory*, Vol. 2, Landslide Processes, doi: 10.1007/978-3-319-09057-3_70.

Hungr, O., and S.G. Evans (1988). Engineering evaluation of fragmental rockfall hazards, Proc. 5th international Symposium on Landslides, July 10-15, 1988, Lausanne, Switzerland (C.Bonnard, ed.) Vol.1, A.A.Balkema, Leiden, Netherlands, pp.685-680.

Hungr, O., Evans, S.G., and J. Hazzard (1999). Magnitude and Frequency of Rock Falls and Rock Slides Along the Main Transportation Corridors of Southwestern British Columbia. *Canadian Geotechnical Journal* 36: 224–238.

Hungr O., Leroueil S., and L.Picarelli (2012). Varnes classification of landslide types, an update. In: Eberhardt E., Froeses C., Keith Turner A., Leroueil S. (eds.) Landslides and engineered slopes. Protecting society through improved understanding, vol 1. CRC Press, London, pp 47–58.

Hwang, J. H., and T.Y. Tu (2006). Ground Vibration Due to Dynamic Compaction, *Soil. Dyn. Earthquake Eng.*, Vol. 26, 337–346.

Jaboyedoff, M., Oppikofer, T., Abellàn, A., Derron, M.H., Loye, A., Metzger, R., and A. Pedrazzini (2010). Use of LIDAR in landslide investigations: a review, Natural Hazards 61, 5-28.

Jedele, L. (2005). Energy-Attenuation Relationships from Vibrations Revisited. Soil Dynamics Symposium in Honor of Professor Richard D. Woods: pp. 1-14. doi: 10.1061/40780(159)6.

Joswig, M. (1990). Pattern recognition for earthquake detection, *Bull. Seism. Soc. Am.* 80, 170-186.

Joswig, M. (1993). Single-trace detection and array-wide coincidence association of local earthquakes and explosions, *Comput. Geosci*. 19, 207–221.

Joswig, M. (1995). Automated classification of local earthquake data in the BUG small array, *Geophys. J. Int.* 120, 262–286.

Ju, S.-H., Lin, H.-T., and J.-Y. Huang (2009). Dominant frequencies of train-induced vibrations. *Journal of Sound and Vibration*, Vol. 319, No. 1-2, 2009, 247–259.

Jurkevics, A. (1988). Polarization analysis of three-component array data, *Bull. Seism. Soc. Am*. 78, 1725-1743.

Kanamori, H. (2007). Real-time Earthquake Damage Mitigation Measures. In: Earthquake Early Warning Systems. Editors: Prof. P.Gasparini, Prof. G. Manfredi, Prof. Dr. J. Zschau, ISBN: 978-3-540-72240-3.

Kausel, E., and J.M. Roesset (1981). Stiffness matrices for layered soils, *Bull. Seism. Soc. Am*. vol. 71 (6), 1743-1761.

Kenny, J. (1954). Steady-state vibrations of beam on elastic foundation for moving load. *Journal of Applied Mechanics*, 76: 359–64.

Kennett, B.L.N. (1974). Reflections, rays and reverberations, *Bull. Seism. Soc. Am*. vol. 64 (6), pp. 1685-1696.

Kennett, B.L.N. (1979). Seismic waves in stratified half space, *Geophysical J. Royal Astron. Soc.*, vol. 57, pp. 557-583.

Kim, D.-S., and J.S. Lee (2000). Propagation and attenuation characteristics of various ground vibrations. *Soil Dyn. Earthquake Eng.*;19:115–26.

Knapp, C., and G. Carter (1976). The generalized correlation method for estimation of time delay, *IEEE Transaction on Acoustics, Speech, Signal Processing*, 24 (4), 320-327.

Knorr, E., Ng, R., V.Tucakov (2000). Distance-based outliers: Algorithms and applications, *VLDB Journal: Very Large Data Bases*, 8(3-4):237-253.

Köhler, A., Ohrnberger, M., and F.Scherbaum (2010). Unsupervised pattern recognition in continuous seismic wavefield records using self-organizing maps, *Geophys. J. Int.*, 182, 1619–1630, doi:10.1111/j.1365-246x.2010.04709.x.

Kouroussis, G, Verlinden, O., and C.Conti (2009). Ground propagation of vibrations from railway vehicles using a finite/infinite-element model of the soil. Proceedings of the Institution of Mechanical Engineers, Part F: *Journal of Rail and Rapid Transit* 2009; 223(4): 405–13.

Kouroussis, G., Verlinden, O. and C. Conti (2012). Influence of some vehicle and track parameters on the environmental vibrations induced by railway traffic. *Vehicle System Dynamics*, Vol. 50, No. 4, 2012, 619–639.

Kouroussis, G., Conti, C., and O. Verlinden (2013). Investigating the influence of soil properties on railway traffic vibration using a numerical model. *Vehicle System Dynamics*, Vol. 51, No. 3, 2013, 421–442.

Kouroussis, G., Verlinden, O., Connolly, D., and M.Forde (2014). Estimating Railway Rolling Stock Speed from Free Field Ground Vibrations Measurement, Transportation Research Board Annual Meeting 2014 Paper #14-0814.

Kromer, R., Hutchinson, D., Lato, M., Gauthier, D., and T. Edwards (2015). Identifying rock slope failure precursors using LiDAR for transportation corridor hazard management, *Engineering Geology*, Vol. 195, 93–103.

Krylov, V. V. (1996). Vibrational impact of high-speed trains. I. Effect of track dynamics, *Journal of the Acoustical Society of America* 100, 3121-3134.

Kuyuk, H. S., Allen, R.M., Brown, H., Hellweg, M., Henson, I., and D. Neuhauser (2013). Designing a Network-Based Earthquake Early Warning Algorithm for California: ElarmS-2, *Bull. Seism. Soc. Am*., published ahead of print, December 24.

Lacroix, P., and A.Helmstetter (2011). Location of seismic signals associated with microearthquakes and rockfalls on the Sechilienne Landslide, French Alps. *Bull. Seism. Soc. Am*. 101: 341-353.

Lai, C.G. (1998). Simultaneous inversion of Rayleigh phase velocity and attenuation for near-surface site characterization, *Ph.D. Dissertation*., Georgia Inst. of Techn., Atlanta (Georgia, USA).

Lamb, H. (1904). On the propagation of tremors over the surface of an elastic solid, *Phil. Trans. Royal Soc*. London A203, 1–42.

Lambert S., and F. Nicot (2011) Rockfall engineering. Wiley/ISTE Ltd., New York/London.

Lan, H., Martin, C.D. and C.H.Lim (2007). Rock fall analyst: A GIS extension for three-dimensional and spatially distributed rock fall hazard modeling, *Computers and Geosciences*, Vol. 33, pp. 262–279.

Lato, M., Hutchinson, J., Diederichs, M., Ball, D. and R. Harrap (2009) Engineering monitoring of rockfall hazards along transportation corridors: using mobile terrestrial LiDAR, *Nat. Hazards Earth Syst. Sci.*, 9, 935–946.

Lato, M.J., Diederichs, M.S., Hutchinson, D.J., and R. Harrap (2012). Evaluating roadside rockmasses for rockfall hazards using LiDAR data: optimizing data collection and processing protocols, Nat. Hazards 60:831–864, DOI 10.1007/s11069-011-9872-y

Lato, M., Hutchinson, D.J., Gauthier, D., Edwards, T., and M. Ondercin (2015). Comparison of airborne laser scanning, terrestrial laser scanning, and terrestrial photogrammetry for mapping differential slope change in mountainous terrain. *Canadian Geotechnical Journal*, 2015, Volume 52, Issue 2.

Lee, W.H.K., and J.C. Lahr (1972). HYPO71: A computer program for determining hypocenter, magnitude, and first motion pattern of local earthquakes. *U.S. Geological Society Open File Report* 72-0224.

Lee, P.A., and T.Anderson (1981). Fault Tolerance. Principles and practice. Prentice-Hall.

Lee, E. M., and D.K.C. Jones (2004). Landslide Risk Assessment. Thomas Telford Limited.

Li, L., and H.Lan (2015). Probabilistic modeling of rockfall trajectories: a review, *Bulletin of Engineering Geology and the Environment*, November 2015, Volume 74, Issue 4, pp 1163-1176

Liu, H.-H., and K.-S. Fu (1983). An application of syntactic pattern recognition to seismic discrimination, *IEEE Trans. Geosc. Rem. Sens*. GE-21 (2), 125-132.

Luo, J. and E.E.A. Konofagou (2010). Fast normalized cross-correlation method for motion estimation, *IEEE Trans Ultrason Ferroelectr Control*, 57 (7) (2010), 1347–1357.

Maimon, O. and L. Rockach (Eds.) (2005). Data Mining and Knowledge Discovery Handbook: A Complete Guide for Practitioners and Researchers, Kluwer Academic Publishers, ISBN 0-387-2443.

Macciotta R., Cruden D.M., Martin C.D., and N.R. Morgenstern (2011). Combining geology, morphology and 3D modelling to understand the rock fall distribution along the railways in the Fraser River Valley, between Hope and Boston Bar. In: Eberhardt E, Stead D (eds) Slope stability 2011. Proceedings of the 2011 international symposium on rock slope stability in open pit mining and civil engineering. 18–21 September 2011. Canadian Rock Mechanics Association, Vancouver.

Macciotta R., Martin C.D., and D.M.Cruden (2014a). Probabilistic estimation of rockfall height and kinetic energy based on a three-dimensional trajectory model and Monte Carlo simulation. Landslides. 2014. doi:10.1007/s10346-014- 0503-z.

Macciotta, R., Hendry, M., Martin, C.D., Elwood, D., Lan, H., Huntley, D., Bobrowsky, P., Sladen, W., Bunce, C., Choi, E. and T.Edwards (2014b). Montoring of the Ripley Landslide in the Thompson

River Valley, BC. 6th Canadian Geohazards Conference, Kingston ON, 15-18 June. DOI: 10.13140/2.1.2811.7125

Macciotta, R., Martin, C.D., Edwards, T., Cruden D.M., and T. Keegan (2015a). Quantifying weather conditions for rock fall hazard management, Georisk: Assessment and Management of Risk for Engineered Systems and Geohazards, 9:3, 171-186.

Macciotta R., Martin C.D., N. R. Morgenstern, and D. M. Cruden. (2015b). Quantitative Risk Assessment of Slope Hazards Along a Section of Railway in the Canadian Cordillera—a Methodology Considering the Uncertainty in the Results. *Landslides*, January. doi:10.1007/s10346-014-0551-4.

Maloney, S. and N. Miller (2004). Natural Rail Hazards - Detection Technology Evaluation. Prepared for Railway Ground Hazard Research Program by Geomechanics Research Centre, MIRARCO. Transport Canada 14537E, File No 2450-GP12, Cont. No T8200-033519/001/MTB.

Mayne, P.W., Jones, J.S. and J.C. Dumas (1984). Ground response to dynamic compaction, *J. Geotech. Engng*. 110 (6), 757–774.

McEvilly, T. V. and E. L. Majer (1982). ASP: An automated seismic processor for microearthquake networks, *Bull. Seism. Soc. Am.* 72, 303-325.

McGarr, A., and D. Simson (1997). Keynote lecture: a broad look at induced and triggered seismicity. Rockbursts and Seismicity in Mines. Balkema, Rotterdam.

Moran, M., and R.Greenfield (1997). Seismic Detection of Military Operations, 97-CEP-511-1, U.S. Army Maneuver Support Battle Laboratory, Ft. Leonard Wood, MO.

Moran, M., Boulanger, P., Greenfield, R., and T. Gilligan (1998). Range Estimation with Seismic Sensors for Early Detection, Final report 98-CEP-0505, Maneuver Support Battle Lab, U.S. Army Engineer School, Ft. Leonard Wood, MO.

Murdoch, J. and C. Hutt (1983). A new event detector designed for the seismic research observatories, U.S. Geol. Surv. Open-File Rep. 83-785, 37 pp.

Ni, S.-H., Huang, Y.-H., and K.-F. Lo (2011). An automatic procedure for train speed evaluation by the dominant frequency method. Computers and Geotechnics, Vol. 38, No. 4, 416–422.

Norris, R. D. (1994). Seismicity of rockfalls and avalanches at three Cascade Range volcanoes: implications for seismic detection of hazardous mass movements, *Bull. Seis. Soc. Am.*, 84, 1925-1939.

Peckover, F. L. (1975). Treatment of rock falls on railway lines. American Railway Engineering Association, Bulletin 653. Chicago, IL.

Peckover, F L, and J. W. G. Kerr (1977). Treatment and Maintenance of Rock Slopes on Transportation Routes. *Canadian Geotechnical Journal* 14 (4): 487–507. doi:10.1139/t77- 051.

Piteau, D.R., and F.L. Peckover (1978). Engineering of Rock Slopes. In Landslides Analysis and Control. Special Report 176. Edited by R. L. Schuster and R.J. Krizek, Transportation research board, National Academy of Sciences, Washington, DC., pp. 192–228

Plouffe, M., Côté, M., and D. Lebel (2007). Test and Evaluation of a Seismic Approach to Monitor Rock Falls on the Railway Right-of-Way. CANMET Mining and Mineral Sciences Laboratories Client Report MMSL07-004(CR).

Prochaska, A. B., Santi, P. M., and J. D.Higgins (2008). Relationships between Size and Velocity for Particles within Debris Flows. Canadian Geotechnical Journal, 45: 1778–1783, doi:10.1139/T08-088

Remington, P. J. (1987). Wheel/rail rolling noise. I. Theoretical analysis, *J. Acoust. Soc. Am.* 81, 1805–1823.

Richart, F.E., Jr., Hall, J.R., Jr. and R.D.Woods (1970). Vibrations of Soils and Foundations , Prentice - Hall, Englewood Cliffs, N.J., 414 pp.

Ritchie A.M.(1963) Evaluation of rockfall and its control. In: Highway research record, no. 17, pp 13-28

Robb, D. (1971). Report on rock slide detector fence installations of the B.C. South Line. Office of the Regional Engineer, Edmonton, Alberta.

Roesset, J.H., Kausel, E., Cuellar, V., Monte, J.L., and J. Valerio (1993). Impact of weight falling onto the ground, *J. Geotech. Eng.*, 120 (8) (1993), 1394–1412.

Rosser, N., Lim, M., Petley, D., Dunning, S., and R.Allison (2007). Patterns of precursory rockfall prior to slope failure. *Journal of Geophysical Research* 112: F04014, doi: 10.1029/2006/JF000642.

Rost, S., and C. Thomas (2002). Array seismology: Methods and applications, *Rev. Geophys.*, 40(3), 1008, doi:10.1029/2000RG000100.

Roth, M., and L.H. Blikra (2009). Seismic monitoring of an unstable rock slope at Aaknes, Norway. *Geophysical Research Abstracts* 11: EGU2009-3680: EGU General Assembly.

Rudd, B. O. and E. S. Husebye (1992). A new three-component detector and automatic single-station bulletin production, *Bull Seism. Soc. Am*. 82, no. 1,221-237.

Savard, G. and M.Bostock (2015). Detection and Location of Low-Frequency Earthquakes Using Cross-Station Correlation, *Bull. Seism. Soc. Am*., Vol. 105, No. 4, pp. 2128–2142.

Schweigl, J. (2015). Monitoring and Risk Management of the Rockfall in Spitz (Austria), Engineering Geology for Society and Territory - Volume 2 Landslide Processes, G.Lollino (ed.), Springer International Publishing, ISBN: 3-319-09056-9, 978-3-319-09056-6.

Senfaute, G., Duperret, A., and J.A. Lawrence (2009). Micro-seismic precursory cracks prior to rock-fall on coastal chalk cliffs: a case study at Mesnil-Val, Normandie, NW France. Natural Hazards and Earth System Science 9 (5): 1625-1641.

Severin, J., Eberhardt, E., Leoni, L., and S. Fortin (2014). Development and application of a pseudo-3D pit slope displacement map derived from ground-based radar, *Engineering Geology* 181, 202–211.

Sharpe, C.F.S. (1938) .Landslides and Related Phenomena, a Study of Mass Movements of Soil and Rock. Columbia Univ. Press, New York. (137 p., reprinted 1960 by Pageant Books Inc., Paterson, N.J.).

Shearer, P. (2009). Introduction to seismology, Cambridge University Press.

Sheng, X. , Jones, C.J.C. and M. Petyt (1999). Ground vibration generated by a load moving along a railway track. *Journal of Sound and* V*ibration* 228, 129-156.

Sheriff, R. E., and L. P. Geldart (1995). Exploration Seismology, Cambridge Univ. Press, New York.

Shiotani, T., and M.Ohtsu (1998). Evaluation of progressive slope failure by acoustic emission. *Progress in Acoustic Emissions IX,* II-70-II-79.

Sklaroff, J. R. (1976). Redundancy Management Technique for Space Shuttle Computers, *IBM Journal of Research and Development* 20 (1), 20-28.

Stevenson, R. (1976). Microearthquakes at Flathead Lake, Montana: A study using automatic earthquake processing, *Bulletin of the Seismological Society of America* 66, 61-79.

Stewart, S. S. (1977). Real-time detection and location of local seismic events in central California, *Bull. Seism. Soc. Am.* 67, 433-452.

Succi, G., Prado, G., Gampert, R., Pedersen, T. and H. Dhalival (2000). Problems in Seismic Detection and Tracking, *Unattended Ground Sensor Technologies and Applications, Proc. SPIE* Vol. 4040, p. 165-173, E. Carapezza, T. Hintz, Ed.

Thompson, D.J. (1993). Wheel-rail noise generation, Part I: Introduction and interaction model, *Journal of Sound and Vibration* 161(3), 387-400.

Thompson, D.J. (1996). On the relationship between wheel and rail surface roughness and rolling noise, *Journal of Sound and Vibration,* 193(1), 149-160.

Thomson, W. T. (1950). Transmission of elastic waves through a stratified soil medium. *Journal of Applied Physics* 21, 89-93.

Tonnellier, A., Helmstetter, A., Malet, J., Schmittbuhl, J., Corsini, A., and J.Manfred (2013). Seismic monitoring of soft-rock landslides: the Super-Sauze and Valoria case studies, *Geophysical Journal International*, Vol. 193, Issue 3, pp.1515-1536.

Transport Canada (2007). Call for Expressions of Interest Development and Deployment of a seismic rock fall detection and monitoring system. Ref. no. 129324, Source ID FD.DP.ON.10891.C47748.

Trnkoczy, A. (2002). Understanding and parameter settings of STA/LTA trigger algorithm, in: P. Bormann (Ed.), *IASPEI New Manual of Seismological Observatory Practice*, vol. 2, GeoForschungsZentrum Potsdam, Ch. IS 8.1, 1–19.

Tselentis, G., Martakis, N., Paraskevopoulos, P., Lois, A., and E. Sokos (2012). Strategy for automated analysis of passive microseismic data based on S-transform, Otsu's thresholding, and higher order statistics, *Geophysics* 77, no. 6, KS43 –KS54.

Turner A.K. and J.D. Duffy (2012). Modeling and Prediction of Rockfall. In: Rockfall Characterization and Control, edited by Turner and Schuster, pp. 334-406. Washington, DC, United States of America: Transportation Research Board.

Turner, R.J.W., Clague, J.J., Groulx, B.J., and J.M. Journeay (1998). GeoMap Vancouver, geological map of the Vancouver Metropolitan area.

http://ftp2.cits.rncan.gc.ca/pub/geott/ess_pubs/209/209909/of_3511_e.pdf (last checked on February 1, 2016).

Vandewater, C.J., Dunne, W.M., Mauldon M., Drumm E.C., and V. Bateman (2005). Classifying and assessing the geologic contribution to rockfall hazard. *Journal of Environmental & Engineering Geosciences* 11 (2):141–154.

Varnes, D.J. (1978). Slope movement types and processes. In: Schuster RL, Krizek RJ (eds) Landslides, analysis and control, special report 176: Transportation research board, National Academy of Sciences, Washington, DC., pp. 11–33.

Vilajosana, I., Surinach E., Abellán A., Khazaradze G., Garcia D., and J. Llosa (2008). Rockfall induced seismic signals: case study in Montserrat, Catalonia. *Natural Hazards and Earth System Sciences* 8: 805-812.

Viola, F. and W. F. Walker (2003). A comparison of the performance of time-delay estimators in medical ultrasound, *IEEE Trans. Ultrason. Ferroelectr. Freq. Control*, vol. 50, no. 4, 392–401.

Wagner, G., and T. Owens (1996). Signal detection using multi-channel seismic data, *Bull. Seism. Soc. Am*. 86, 221–231.

Walker, W.F. and G.E.Trahey (1995). A fundamental limit on delay estimation using partially correlated speckle signals, *IEEE Trans. Ultrason., Ferroelect., Freq. Contr.* , vol. 42, no. 2, 301–308.

Whittow, J. (1984). Dictionary of Physical Geography. London, 1984.

Wieczorek, G.F. (1996). Landslide triggering mechanisms. In: Turner, A.K., Schuster, R.L. (Eds.), Landslides—Investigation and Mitigation. : Special Report 247, Transport. Res. Board, National Res. Council. National Academic Press, Washington, D.C, pp. 76–90

Wiss, J.F. (1981). Construction Vibrations: State–of–the-Art, *Journal of the Geotechnical Engineering Division*, ASCE, Vol. 107, GT2, Feb., 167-181.

Withers, M., Aster, R., Young, C., Beiriger, J., Harris, M., Moore, S., and J.Trujillo (1998). A Comparison of Select Trigger Algorithms for Automated Global Seismic Phase and Event Detection. *Bull. Seism. Soc. Am.*, Vol. 88, No. 1, 95-106.

Woods, R.D. and L.P. Jedele (1985). Energy-Attenuation Relationships from Construction Vibrations, *Proceedings of a Symposium sponsored by the Geotechnical Engineering Division in conjunction with the ASCE Convention in Detroit*, Michigan, p. 229-246.

Wyllie, D. (2015). Rock fall engineering, CRC Press.

Zaicenco, A., Huffman, S., and I. Weir-Jones (2010). Seismic P-wave Polarization in the Context of On-site Early Warning System, *5th International Conference on Recent Advances in Geotechnical Earthquake Engineering and Soil Dynamics*, San Diego, May 24-29.

Zimmer, V.L. (2011). Seismic and Acoustic Investigations of Rock Fall Initiation, Processes, and Mechanics. *Ph.D. Dissertation.* University of California, Berkeley.

Zimmer, V., Collins, B.D., Stock, G.M., and N.Sitar (2012). Rock fall dynamics and deposition: an integrated analysis of the 2009 Ahwiyah Point rock fall, Yosemite National Park, USA. *Earth Surface Processes and Landforms* 37, 680–691.

Zimmer, V., and N. Sitar (2015). Detection and Location of Rock Falls Using Seismic and Infrasound Sensors. *Engineering Geology* 193 (July): 49–60. doi:10.1016/j.enggeo.2015.04.007.

Zollo,A., Amoroso, O., Lancieri, M., Wu, Y.M., and H.Kanamori (2010). A Threshold-Based Earthquake Early Warning Using Dense Accelerometer Networks. *Geophys. J. Int.* Vol. 183, 2, 963-974.

Appendices

Some of the data samples and Matlab scripts included in the Appendices can be downloaded from the Supplementary Thesis Materials and Errata Collection in the UBC cIRcle: http://hdl.handle.net/2429/58080.

Appendix A.Pattern recognition analysis of rail traffic

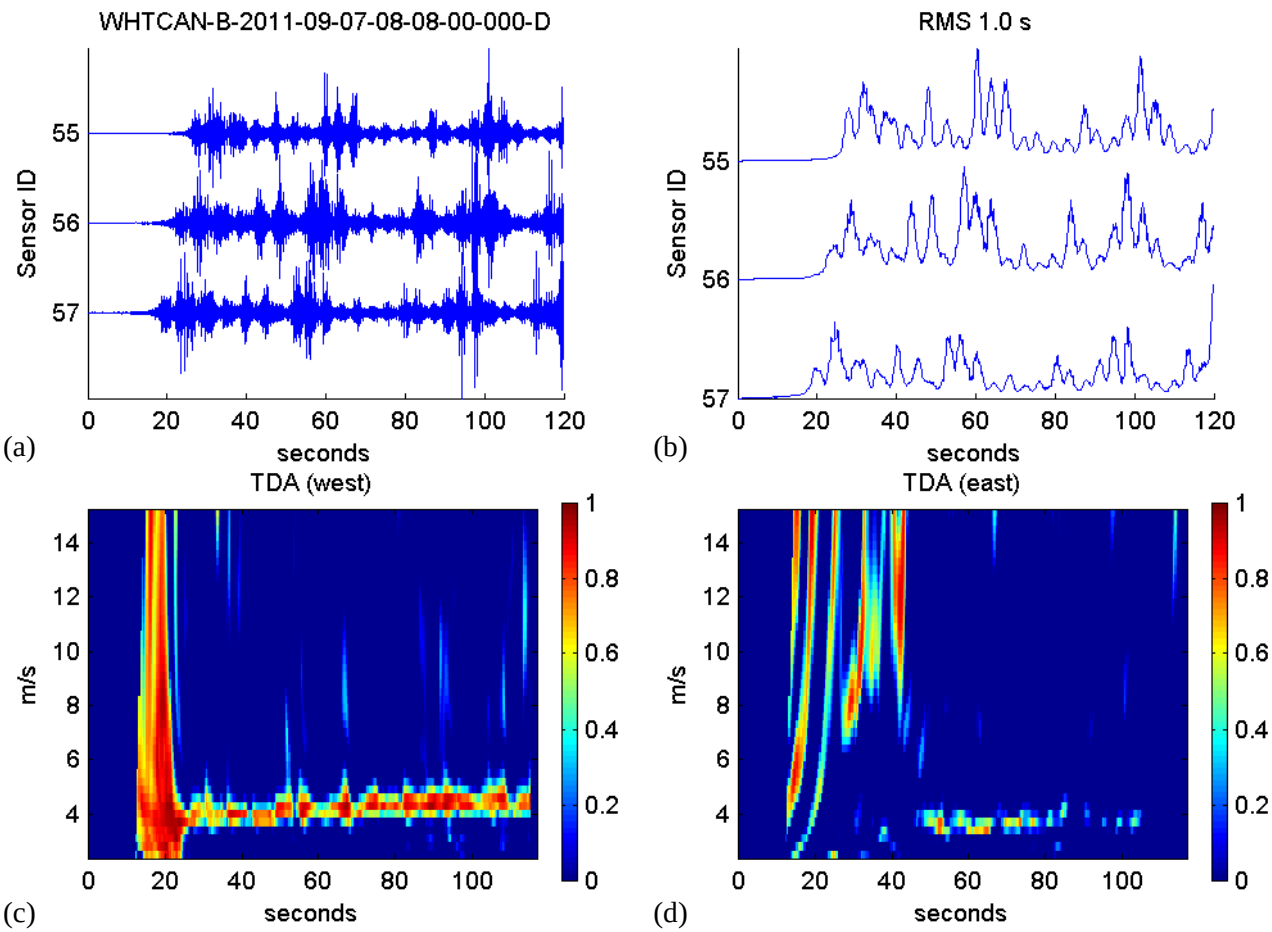

Figure A.1. Detection of a slow train with the TDA.

(a) 120 s of seismic data; (b) R.m.s.-smoothed signals (w^{RMS} = 1.0 s) of the reference sensor Z-55 and two comparison sensors, Z-56, Z-57, which are adjacent to the reference one. The cost functions (mZNCC) obtained for westbound (c) and eastbound (d) trains. Plot (c) displays a consistent pattern of a train transit which is slowly accelerating from 4 m/s to about 4.5 m/s over 100 seconds. In Figure A.2 the same train signal will be processed using a larger distance between the reference and the comparison sensors.

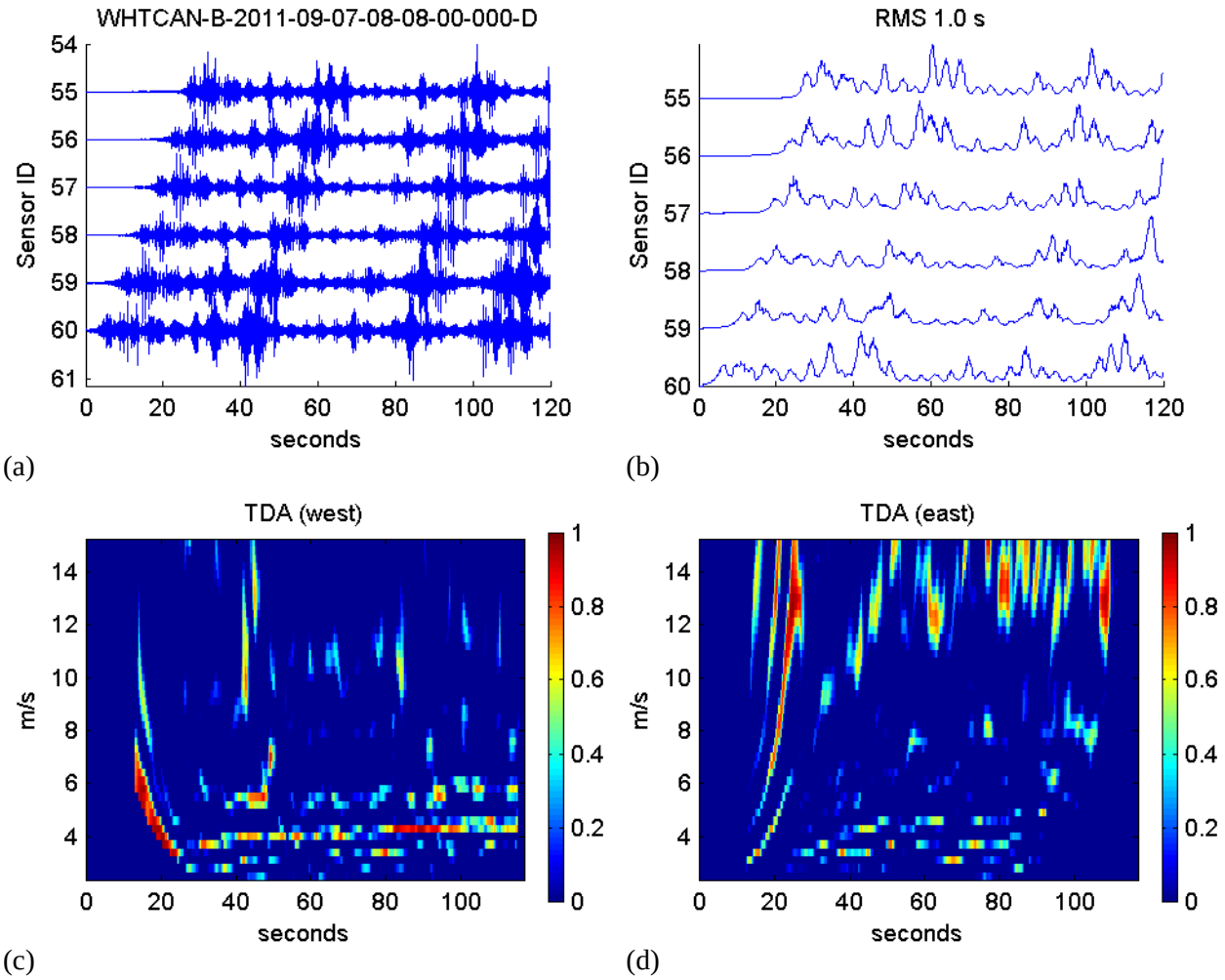

Figure A.2. Detection of an accelerating train using the TDA.

(a) 120 s of seismc data; (b) R.m.s.-smoothed signals of the reference sensor Z-55 and comparison sensors, Z-59, Z-60 (w^{RMS} = 1.0 s). The cost functions (mZNCC) obtained for westbound (c) and eastbound (d) trains. This example demonstrates that not all combinations of reference and comparison sensors produce consistent train patterns. Here, an attempt to identify a slowly accelerating train is made with two comparison sensors, Z-59 and Z-60, located more than 50 meters away from the reference sensor Z-55. The maximum distance between the reference sensor and the comparison sensor is 75 m. Neither the westbound (c) nor the eastbound (d) plots of the cost function display consistent train patterns because the train signal changes as it moves from the reference sensor to the comparison ones. The comparison sensors were selected using the minimum distance of 50 meters.

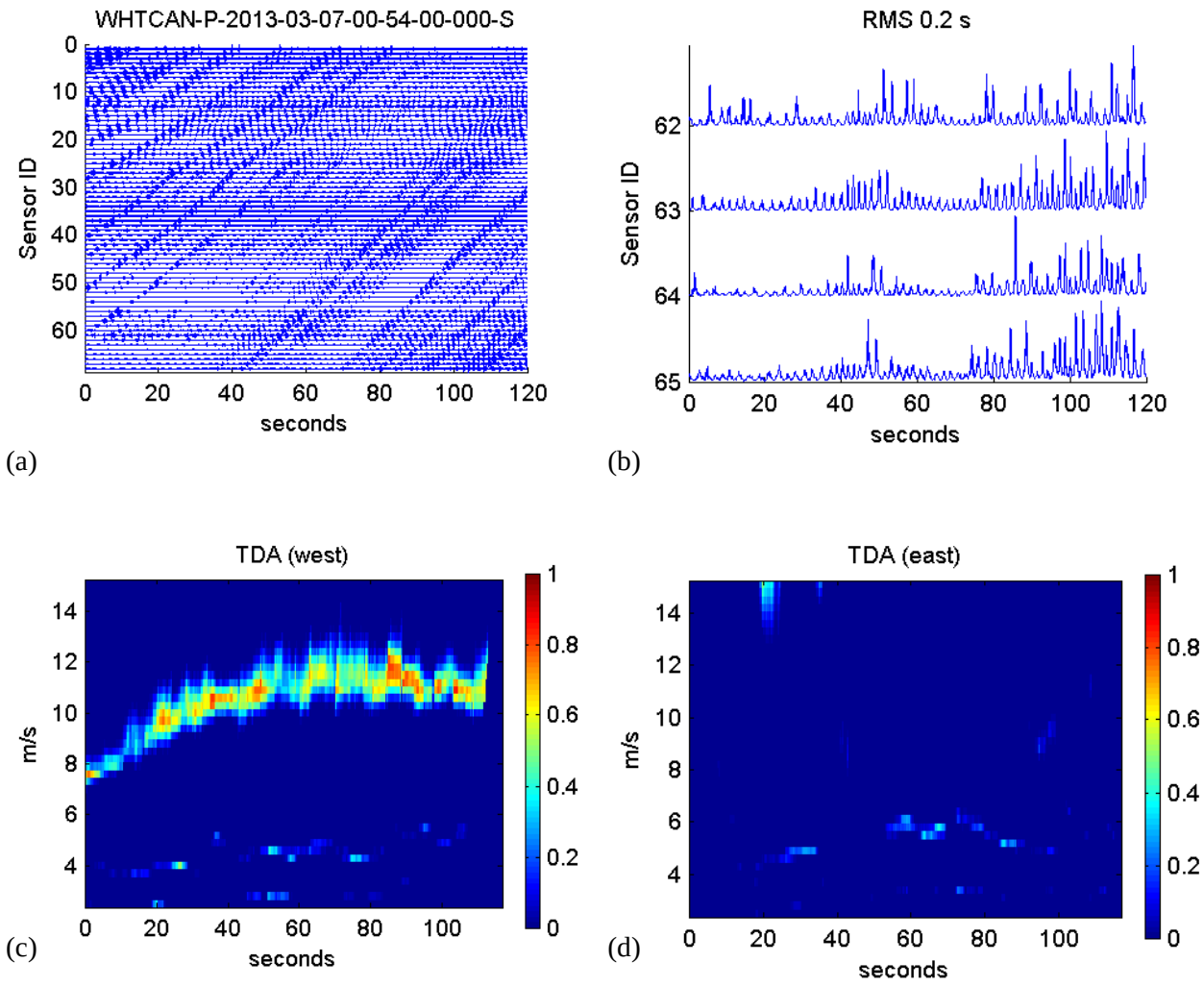

Figure A.3. Detection of a train using the TDA.

(a) 120 s of seismic data; (b) R.m.s.-smoothed signals of the reference sensor Z-65 and comparison sensors, Z-62, Z-63 and Z-64 (w^{RMS} = 0.2 s). The cost functions (mZNCC) obtained for westbound (c) and eastbound (d) trains. The train accelerated from 8 m/s to 12 m/s in one minute. Plot (c) displays a typical pattern of an accelerating train. Compared to the previous example, a small aperture sub-array produced a much more consistent train pattern in (c). The maximum distance between the reference sensor and the comparison sensors is 45 m.

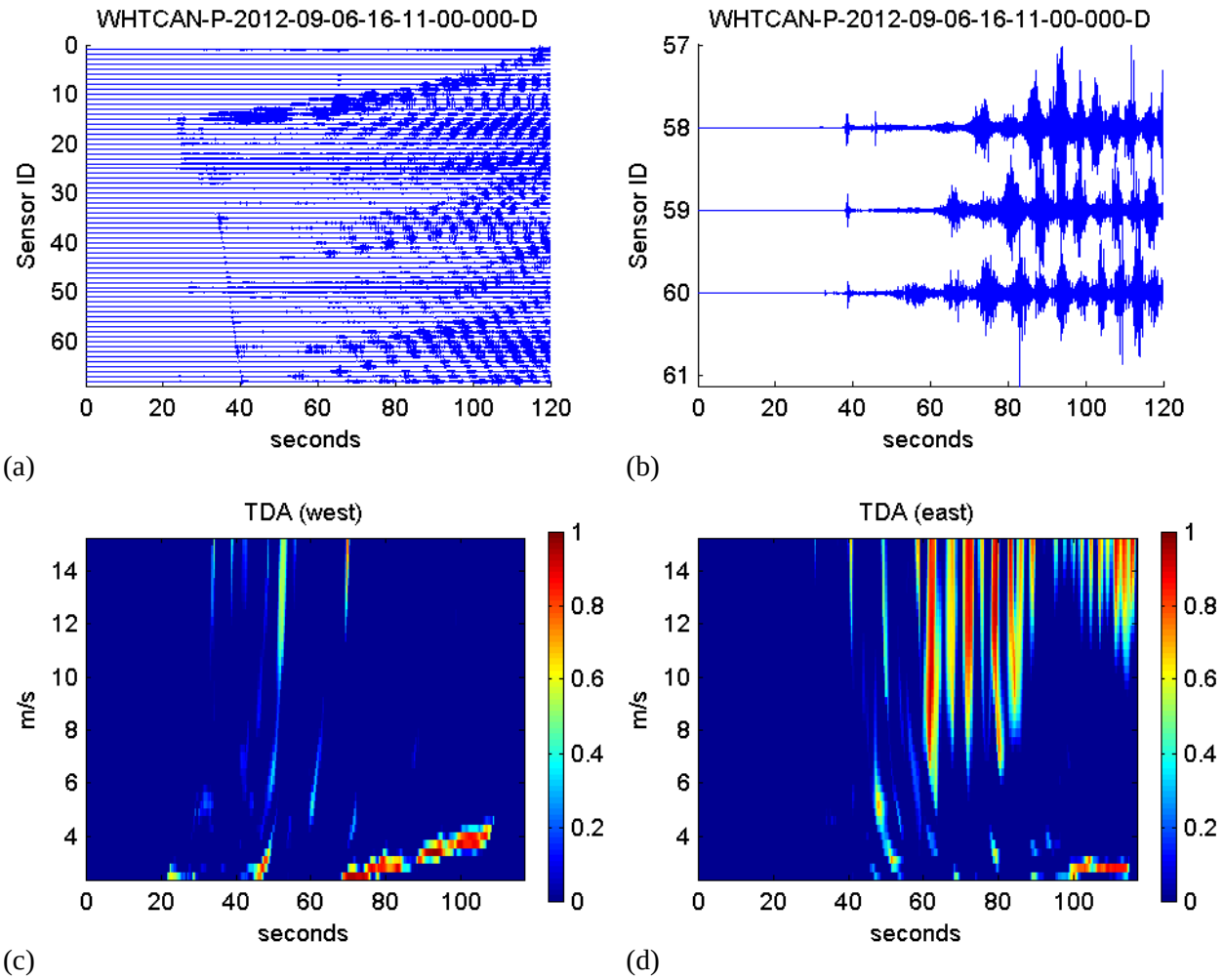

Figure A.4. Detection of a starting train using the TDA.

(a) 120 s of seismic data; (b) R.m.s.-smoothed signals of the reference sensor Z-60 and comparison sensors, Z-58 and Z-59. The cost functions (mZNCC) obtained for westbound (c) and eastbound (d) trains. Plot (c) begins to show the pattern of an accelerating train about 60 s after the train start.

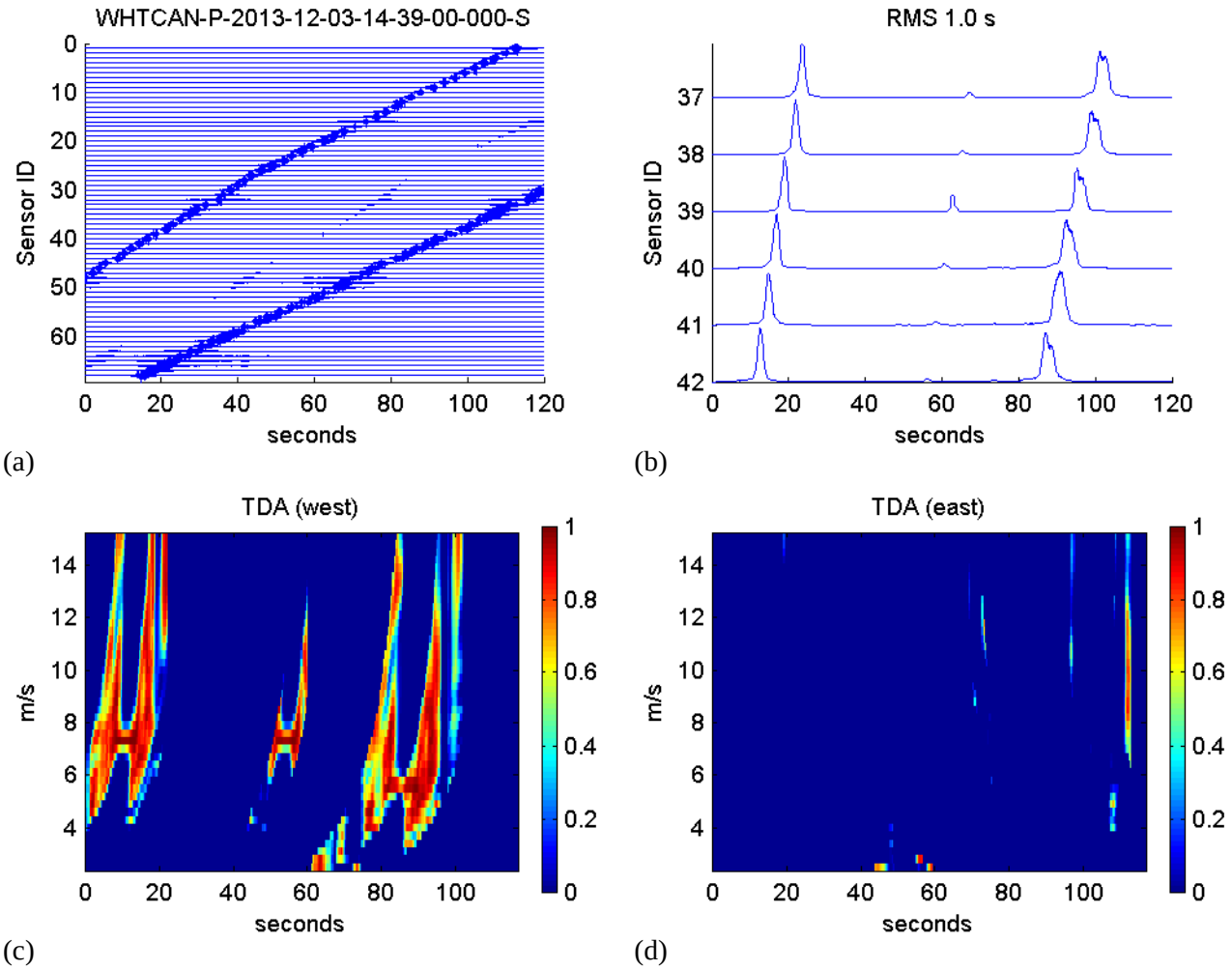

Figure A.5. Detection of high-rails using the TDA.

(a) 120 s of seismic data; (b) R.m.s.-smoothed signals of the reference sensor Z-42 and comparison sensors, Z-37 and Z-38. The cost functions (mZNCC) obtained for westbound (c) and eastbound (d) vehicles. The distance between the reference sensor and the comparison sensors is 45 meters. Plot (c) displays patterns of high-rail signals contaminated by the vehicles' precursor and receding ground vibration.

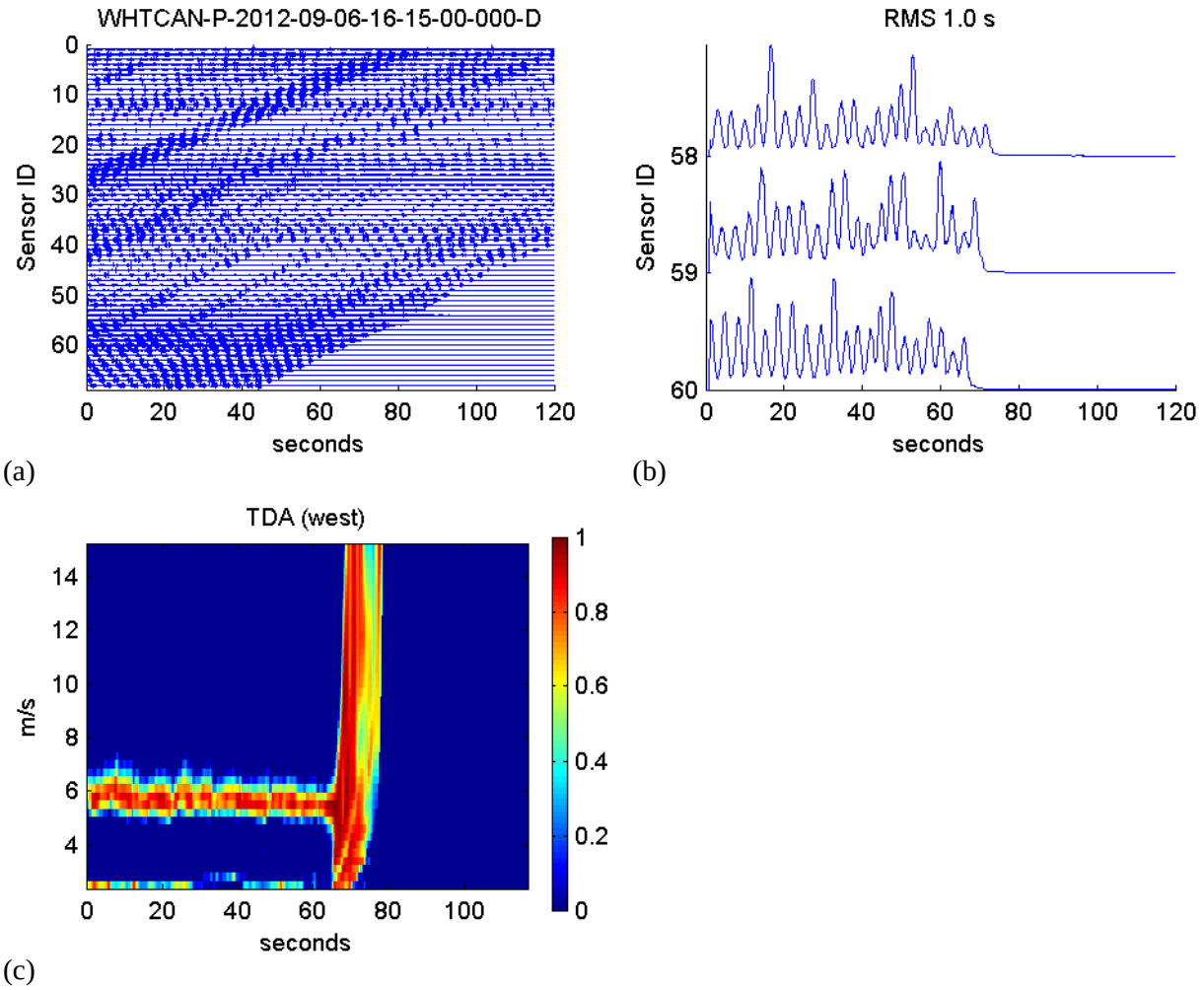

Figure A.6. Detection of the end-of-train using the TDA.

(a) 120 s of raw data; (b) R.m.s.-smoothed signals of the reference sensor Z-60 and comparison sensors, Z-58 and Z-59. The cost function (mZNCC) obtained for the westbound train is in plot (c) which displays the pattern of a steadily moving train. The receding noise at the end of the train signal results in a pattern similar to that of the locomotive precursor vibration, *e.g.* Figure 4.6 and Figure 4.7. This property can be used to detect the end of the train signal which occurs around 65-70 s.

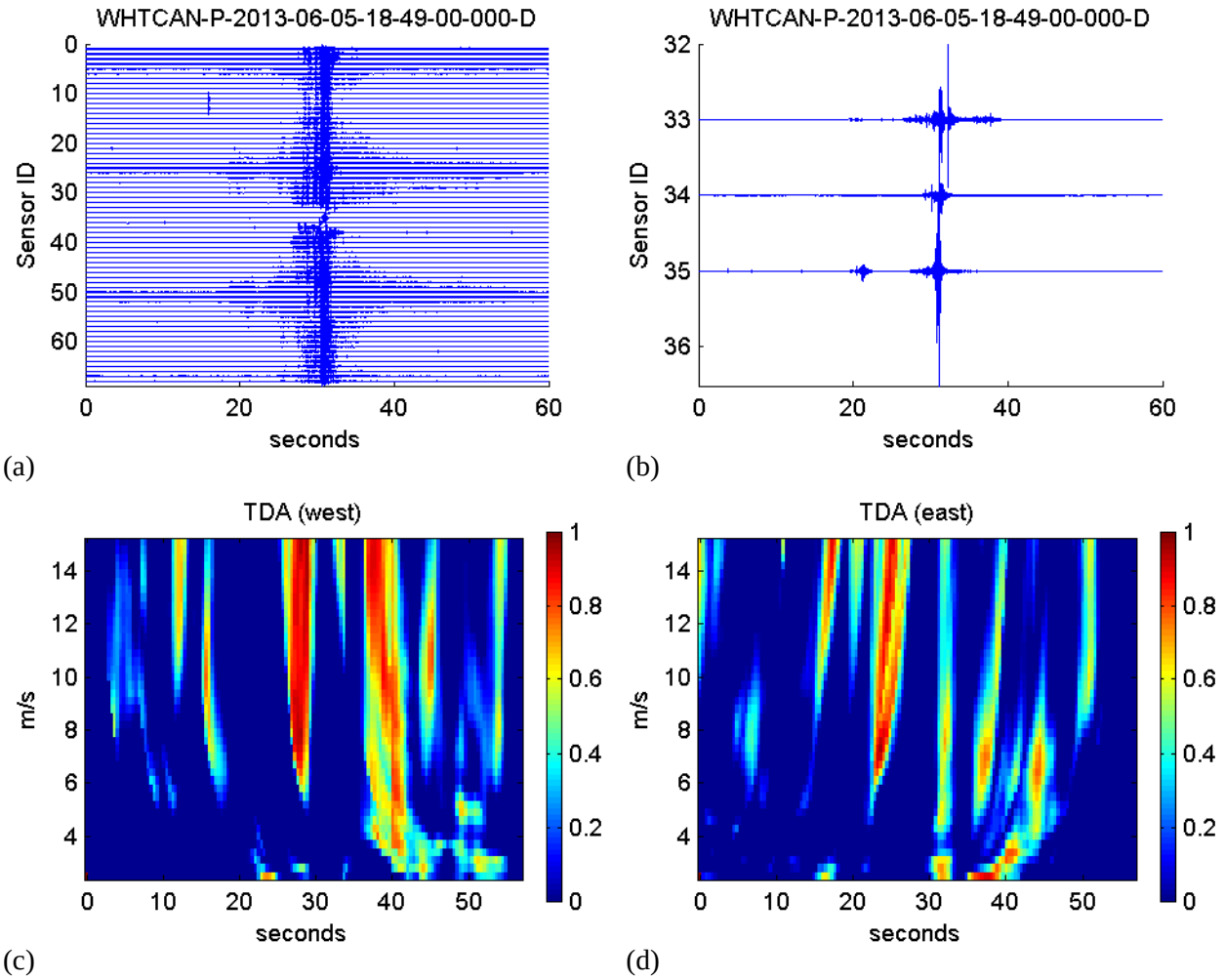

Figure A.7. Cost functions produced by the Train Detection Algorithm for the seismic signals generated by the June 5, 2013 rockfall.

(a) 60 s of seismic data (68 channels); (b) 60 s of seismic data recorded at the three sensors closest to the rockfall epicenter. The cost functions (mZNCC) computed for westbound (c) and eastbound (d) vehicles using Z-33 as the reference sensor, and Z-34 and Z-35 as the comparison sensors. This example demonstrates that if the TDA is applied to a rockfall signal, its output will be inconsistent with the train pattern (*e.g.* Figure 4.6, Figure A.3), and that the TDA is unlikely to misidentify a rockfall as a train.

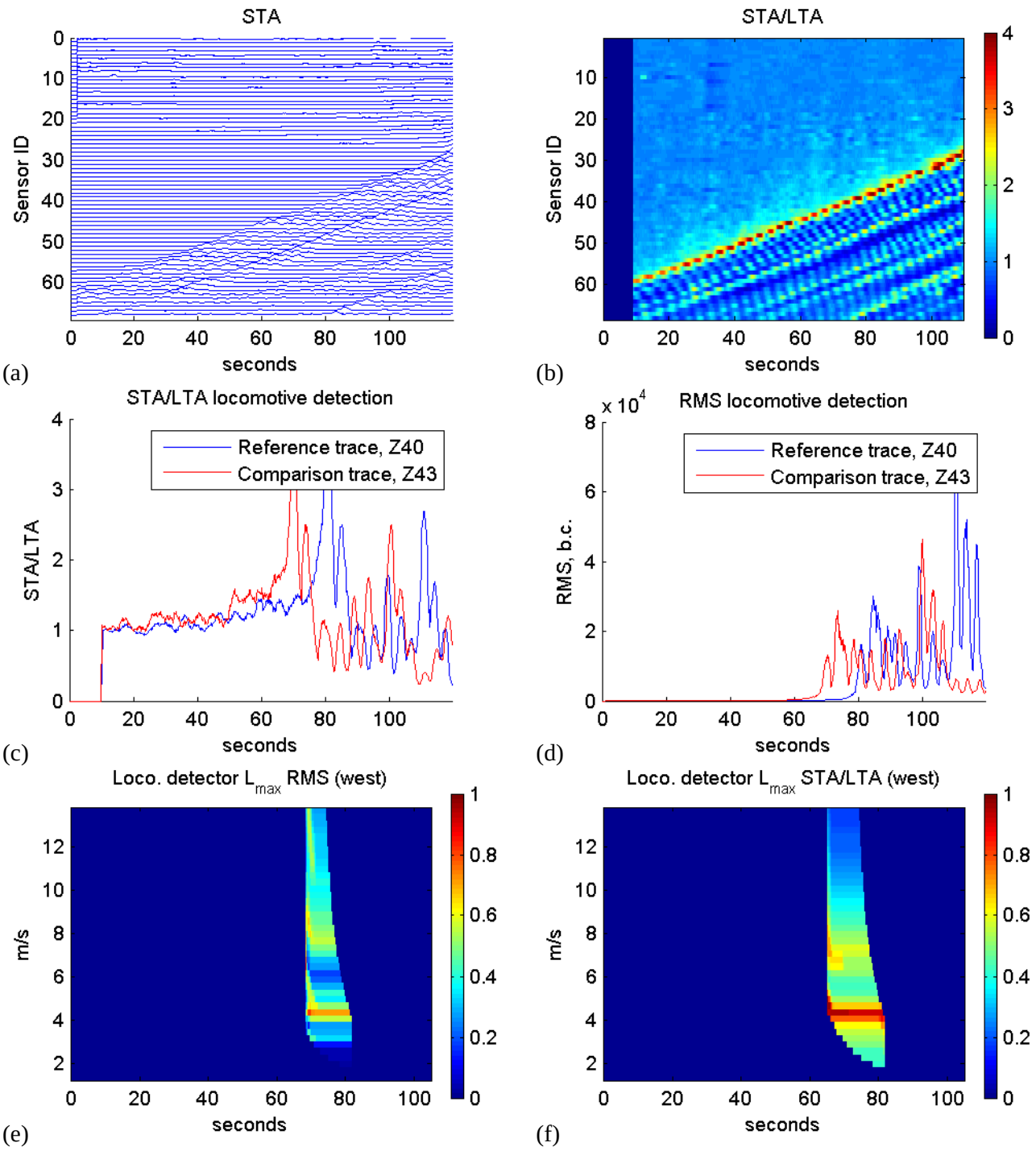

Figure A.8. Detection of a slow-moving locomotive using STA/LTA and r.m.s.-smoothed data. (a) 120 s of r.m.s.-smoothed data; (b) STA/LTA of Z-43 (reference sensor) and Z-40 (comparison sensor); (c) r.m.s.-smoothed data of Z-12 (reference sensor) and Z-17 (comparison sensor), w^{RMS} = 1 s; (d) STA/LTA, w^{STA} = 2.0 s; w^{LTA} = 10 s; cost functions produced by (e) the LTA(2) detector and (f) the LTA(1) detector. Both techniques identified the locomotive at 70 s with an 83% and 98% matching level respectively.

Appendix B.Traffic identification algorithms

B.1. The Train Detection Algorithm (TDA)

Train Detection Algorithm (TDA).
Identification of the middle part of the train signal pattern at a sensor Z^R (called *reference* sensor) within time window $t \in (t_1;\ t_N)$. The algorithm uses r.m.s.-smoothed signal and Pearson's correlation coefficients.

Algorithm description:
For a given range of velocities, a product of correlation coefficients is computed for each pair { *reference* sensor; *comparison* sensor} within a sliding time window. If the product exceeds the threshold, a combination of {time t^R; velocity v^R} is stored as a potential solution.

Input:	2D data slice $D = \{x_i^j : i = 1, \dots, N; j = 1, .., S\}$, where N is the number of data samples; S is the number of data traces acquired with uniaxial sensors; Sensor coordinates $\overline{Z^J}$;	
Output:	t^R- the arrival time of a vehicle at sensor Z^R; v^R- the velocity of the identified vehicle;	
Parameters:	w^{RMS}	*RMS* time window $w^{RMS} =$ 0.2 seconds for detecting trains with velocities $v \geq 5\ ms$; $w^{RMS} = 1.0\ s$ for detecting trains with velocities $v < 5\ ms$;
	w_{max}, w_{min}	the maximum and minimum lengths of the time window used to compute the correlation coefficient, *e.g.* $w_{max} =$ 5 s, $w_{min} = 3$ s;
	$\boldsymbol{V} = \{v_p : p = 1, .., P\}$	a discrete set of P velocities used to detect a vehicle; $v_{max} = \max\{\lvert v_p \rvert\}, v_{min} = \min\{\lvert v_p \rvert\}$;
	N^{CS}	the number of the comparison sensors Z^c, $c = \overline{1, N^{CS}}$. Reference sensors are selected arbitrarily, for instance by using specific minimum distance between the main sensors and a reference sensor;
	C^T	threshold for Pearson's correlation coefficient, *e.g.* $C^T =$ 0.75;
	Δt^{test}	solution verification window, *e.g.* Δt^{test}= 2 s;
	Δv	velocity tolerance, Δv = 5 ms;

/* compute r.m.s.-smoothed signal */

for each sensor trace $D(j)$

Use w^{RMS} to compute RMS_i^j, $i = \overline{1,N}$; $j = \overline{1,S}$;

end for

for each data sample t_i^R, $i = \overline{1, N - w_{min}}$

for each velocity $v_p \in \boldsymbol{V}$

/* compute the current time window length */

$w(v_p) = w_{min} + \frac{w_{max} - w_{min}}{v_{max} - v_{min}}(v_p - v_{min})$;

/* use $w(v_p)$ to obtain a time window for the reference sensor */

$w_i^R(v_p) = (t_i^R;\ t_i^R + w(v_p))$;

for each reference sensor Z^c, $c = \overline{1, N^{CS}}$

/* compute the travel time delay */

$\Delta t^{R,c}(v_p) = \frac{|\overline{Z^R} - \overline{Z^c}|}{v_p}$;

/* compute the comparison time window */

$w_i^c(v_p) = (t_i^R + \Delta t^{R,c}(v_p);\ t_i^R + \Delta t^{R,c}(v_p) + w(v_p))$;

/* compute the correlation coefficient for each pair of sensors Z^R and Z^c */

$C_i^{R,c}(v_p) = corr\left(RMS^R(w_i^R(v_p)), RMS^c(w_i^c(v_p))\right)$;

/* if the correlation coefficient is negative, move on to the next velocity */

if $C_i^{R,c}(v_p) < 0$

goto next v_p**;**

end if

end for each reference sensor

/* compute the product of the correlation coefficients */

$$C_i^{R,N^{RS}}(v_p) = \prod_c^{N^{CS}} C_i^{R,c}(v_p)$$

/* if $C_i^{R,N^{CS}}(v_p)$ is too low, move on to the next data sample */

if $C_i^{R,N^{RS}}(v_p) < (C^T)^{N^{CS}}$

goto next t_i^R**;**

else

/* we found a potential solution; store the identified arrival time and velocity */

$t^R = t_i^R$;

$v^R = v_p$;

end if

/* verify the solution within time interval $\left(t_i^R;\ t_i^R + \Delta t^{test}\right)$ */

for each data sample $t_j^R \in \left(t_i^R;\ t_i^R + \Delta t^{test}\right)$

for each velocity $v_n \in \boldsymbol{V}$

1. compute the current time window length $w(v_n)$;
2. obtain time window $w_j^R(v_n) = \left(t_j^R;\ t_j^R + w(v_n)\right)$;

for each reference sensor $Z^c,\ c = \overline{1, N^{CS}}$

1. compute the travel time delay $\Delta t^{R,c}(v_n)$;
2. compute the reference time window $w_j^c(v_n)$;
3. compute the correlation coefficients $C_j^{R,c}(v_n)$;

if $C_j^{R,c}(v_n) < 0$

goto next v_p**;**

end if

4. compute the product $C_j^{R,N^{CS}}(v_n)$;

/* if for some v_n outside the velocity tolerance interval */
/* the correlation product is high, discard the current */
/* solution $\left\{t_i^R;\ v_n\right\}$ */

if $\left|v_n - v_p\right| > \Delta v$ **and** $C_j^{R,N^{CS}}(v_n) \geq (C^T)^{N^{CS}}$

$t^R = 0$;

$v^R = 0$;

goto next t_i^R**;**

end if

end for each reference sensor

end for each velocity v_n

end for each data sample;

return TRUE;

end for each velocity v_p

end for each data sample

return FALSE.

B.2. Matlab implementation of the TDA

```
% ************************************************************************
% NAME:     tda_train_detection
%
% PURPOSE:  Demonstration of the Train Detection Algorithm (TDA).  Train
%           pattern is detected by cross-correlating r.m.s'd traces at the
%           reference and each of the comparison sensors, and taking a
%           product of correlation coefficients obtained for each pair of
%           sensors.
%
% INPUT:    IN_site_ID - alphanumeric ID of a test site, e.g.
%               'white_canyon' which is needed to find sensor coordinates,
%               etc.
%
%           IN_FILE_name1,  IN_FILE_name2 - names of data files in *.csv
%               format. The first column contains the timing in
%               seconds, e.g. 0.0, 0.001; the rest of the columns
%               contain traces stored in  binary counts of A/D board
%
%           IN_DIR_name - directory where IN_FILE_name1 & IN_FILE_name2 are
%
%           IN_destination_folder - the directory where output *.jpeg,
%               *.png etc images should be stored. It does not have to
%               exist
%
%           IN_destination_subfolder - a subdirectory under
%               IN_destination_folder
%
%           IN_concatenate_traces - TRUE if the traces in IN_FILE_name1,
%               IN_FILE_name2 must be concatenated
%
%           IN_reference_sns_idx - index of the reference sensor used in
%               the TDA;
%
%           IN_number_of_comparison_sns - the number of comparison sensors;
%           must be >= 1 (2-3 is recommended).
%
%           IN_minimum_distance_to_comparison_sns_meters- the minimum
%                distance between the reference sensor and the comparison
%                sensors whose indexes will be computed within the
%                algorithm. This parameter defined the aperture of the
%                train detection sub-array used within the TDA. E.g. for
%                slow trains (< 15 kph), this parameter can be zero. For
%                trains traveling at 45-60 kph, it can be 40-50 meters. The
%                algorithm will abort if it is unable to find
%                <IN_number_of_comparison_sns> sensors at the specified
%                distance.
%
%           IN_use_WEST_reference_sensors - defines the direction with
%               respect to the reference sensor in which the comparison
%               sensors should be searched.
%
%           IN_RMS_length_seconds - r.m.s.- window for averaging the data
%
%           IN_detrend_RMS - true if r.m.s. signals have to be de-trended
```

```
%           (DC-corrected) before they are cross-correlated.
%
% OUTPUT:   A text file with the algorithm output and lots of .png and
%           .fig figures stored under  IN_destination_subfolder
%
% AUTHOR:   Bohdan Nedilko <bohdan.nedilko@alumni.ubc.ca>
%
% DATE:     February 2016
%           This code was tested under Matlab R2008b
% ************************************************************************
function tda_train_detection( IN_site_ID, ...
                    IN_FILE_name1,  IN_FILE_name2, ...
                    IN_DIR_name, ...
                    IN_concatenate_traces, ...
                    IN_destination_folder, IN_destination_subfolder, ...
                    IN_reference_sns_idx, IN_number_of_comparison_sns, ...
                    IN_minimum_distance_to_comparison_sns_meters, ...
                    IN_use_WEST_reference_sensors, ...
                    IN_RMS_length_seconds, ...
                    IN_detrend_RMS )

close all

train_search_direction = [ 'WEST'; 'EAST' ];
train_search_dir_cells = cellstr( train_search_direction );

white_canyon_BC2EU = 0.0000000151281;
hope_BC2EU = white_canyon_BC2EU;
DATA_UNITS_STR = 'm/s';

white_canyon_channel_permutation = [ ...
  12 11 10 9 8 7 6 5 4 3 2 1 32 31 30 29 28 27 26 25 24 23 22 21 20 ...
  19 18 17 16 15 14 13 33 45 34 46 35 47 36 48 37 49 38 50 39 51 40 ...
  52 41 53 42 54 43 55 44 56 57 63 58 64 59 65 60 66 61 67 62 68 ...
];

% Initialize
site_ID                     = IN_site_ID;
FILE_name1                  = IN_FILE_name1;
FILE_name2                  = IN_FILE_name2;
DIR_name                    = IN_DIR_name;
concatenate_traces          = IN_concatenate_traces;

destination_folder          = IN_destination_folder;
destination_subfolder       = IN_destination_subfolder;

reference_sns_idx           = IN_reference_sns_idx;
use_WEST_reference_sensors  = IN_use_WEST_reference_sensors;
number_of_comparison_sns    = IN_number_of_comparison_sns;
minimum_distance_to_comparison_sns_meters = ...
    IN_minimum_distance_to_comparison_sns_meters;
RMS_length_seconds          = IN_RMS_length_seconds;
detrend_RMS                 = IN_detrend_RMS;

% output images
graphic_format_ext              = '.tiff';
MATLAB_format_ext               = '.fig';
```

```
DataProcessingParametersFile    = 'dsp_parameters.txt';

raw_data_file_name              = 'raw_data';
raw_subdata_file_name           = 'raw_data_subwindow';
RMS_subdata_file_name           = 'rms_data_subwindow';
rms_smoothed_data_file_name     = 'rms_smoothed_data';

TDA_west_data_file_name         = 'tda_west_test';
TDA_east_data_file_name         = 'tda_east_test';

% Open a data file as a *.csv  file
csv_01 = csvread( [ DIR_name, FILE_name1 ]);
csv_02 = csvread( [ DIR_name, FILE_name2 ]);

% compute sampling rate
sampling_rate_seconds = csv_01(2,1) - csv_01(1,1);

csv_01 = csv_01(:,2:end);
csv_02 = csv_02(:,2:end);
if( strcmp( IN_site_ID, 'white_canyon' ) == 1 )
    csv_01 = csv_01(:,white_canyon_channel_permutation)';
    csv_02 = csv_02(:,white_canyon_channel_permutation)';
else
    if( strcmp( IN_site_ID, 'hope' ) == 1 )
        csv_01 = csv_01';
        csv_02 = csv_02';
    end
end

if concatenate_traces
   src_traces = [ white_canyon_BC2EU*csv_01 white_canyon_BC2EU*csv_02 ];
else
   src_traces = white_canyon_BC2EU*csv_01;
end

sampling_rate_Hz = 1.0 / sampling_rate_seconds;

[ m,n ] = size( src_traces );
Last_sample_Idx  = n;
num_channels     = m;

% Notch Filter frequencies, Hertz
Apply_x60Hz              = true;
Notch_Hz                 = [ 60 ];
% remove DC and 60 Hz
for idx=1:num_channels
    src_traces(idx, :) = src_traces(idx, :) - mean(src_traces(idx, :));

    % notch-filter the data
    if Apply_x60Hz
        src_traces(idx, :) = notch_filter( src_traces(idx, :), ...
            sampling_rate_Hz, Notch_Hz );
    end
end

% Read sensors' coordinates
sensor_xy = [];
```

```
% populate the array of sensor coodinates
for sns = 1:num_channels
    sns_name  = sprintf( 'Z%02d', sns );
    [ sns_x, sns_y ] = get_site_sensor_xy( site_ID, sns_name );

    sensor_xy(sns).x = sns_x;
    sensor_xy(sns).y = sns_y;
end

%    Color bar options
normalize_color_bar        = true;
maximum_xcorr_value        = 1.0;

% RMS parameters
RMS_length_samples          = RMS_length_seconds * sampling_rate_Hz;

%  Sub-sampling
RMS_subsampling_factor = 20;
RMS_Trigger_Level_ms   = 200 * white_canyon_BC2EU;

%  Speed/ arrival time identification parameters
Max_train_speed_kmHr    = 70;
Min_train_speed_kmHr    = 9;

Max_train_speed_mpsec    = Max_train_speed_kmHr / 3.6;
Min_train_speed_mpsec    = Min_train_speed_kmHr / 3.6;

Min_speed_xcorr_window_sec     = 5.0;
Max_speed_xcorr_window_sec     = 3.0;

% time increment
arrival_time_step_sec   = 0.4;
arrival_time_step_samples = arrival_time_step_sec / sampling_rate_seconds;
% speed increment
speed_step_mpsec        = 0.3;

speed_range = [ Min_train_speed_mpsec : speed_step_mpsec : ...
    Max_train_speed_mpsec ];

% Train detection parameters
tda_threshold = power( 0.8, IN_number_of_comparison_sns );
max_tda_speed_tolerance_ms = 2.5;
min_tda_time_tolerance_s   = 4;
time_step_sec = arrival_time_step_samples/ sampling_rate_Hz;

train_start_seconds = 0;
best_velocity_ms    = 0;

% Correlation window
TDA_min_window_length_sec  = ...
    get_xcorr_window_seconds( Min_train_speed_mpsec, ...
        Max_train_speed_mpsec, Min_speed_xcorr_window_sec, ...
        Max_speed_xcorr_window_sec, Max_train_speed_mpsec);

TDA_min_window_length_millisec = ...
    TDA_min_window_length_sec * sampling_rate_Hz;
```

```
[file_pathstr, file_name, file_ext] = fileparts(IN_FILE_name1);

% Figures
fh_FilteredData = figure( 'Name', 'Raw data' );
xlabel('seconds');
set(gca,'YDir', 'reverse');
ylabel('Sensor ID');
title( [  strrep(file_name, '_', '-') ] );

fh_FilteredData_WorkSensors = figure( 'Name', 'Raw data' );
xlabel('seconds');
set(gca,'YDir', 'reverse');
ylabel('Sensor ID');
title( [ strrep(file_name, '_', '-') ] );
set(gca,'ytick',0:100);


fh_RMS_Data_WorkSensors = figure( 'Name', 'RMS' );
xlabel('seconds');
set(gca,'YDir', 'reverse');
ylabel('Sensor ID');
rms_sec_str = sprintf( '%3.1f s', RMS_length_seconds );
title( [ 'RMS ' rms_sec_str  ] );
set(gca,'ytick',0:100);

raw_data_max = -realmax;
raw_data_min = realmax;

work_sensors_raw_data_max = -realmax;
work_sensors_raw_data_min = realmax;

work_sensors_RMS_data_max = -realmax;
work_sensors_RMS_data_min = realmax;

%     1. select the main sensor index
%
%     2. select the minimum distance to the reference sensor(s) and their
%     total number (if adjacent sensors are used, specify dist= 0.0 meters)
%
%     3. specify the direction in which the reference sensors are WRT the
%     main one
%
%     4. specify the RMS-window, in seconds
%
%     Loop #1
%     5. scan the data file; obtain RMS-smoothed data for the main sensor
%     and all traces in - between it and the ref. sensors
%
%     Loop #2
%     6. assuming eastward and west-ward trains, cross-correlate the main
%     and the reference data and plot 2D graphs

% Steps ## 1..3
reference_sns_name  = sprintf( 'Z%02d', reference_sns_idx );
fprintf( '\t\nMain sensor ID: %s\t\n', reference_sns_name );

x1 = sensor_xy(reference_sns_idx).x;
```

```
y1 = sensor_xy(reference_sns_idx).y;

if use_WEST_reference_sensors
    % if there's not enough reference sensors in the requested direction,
    % report an ERROR
    if reference_sns_idx - number_of_comparison_sns < 1
        fprintf( 'SRFDS logical ERROR: bad WEST reference sensors!');
        return;
    end

    % if there's not enough distance to the reference sensors in the
    % requested direction, report an error
    if minimum_distance_to_comparison_sns_meters > 0
        x2 = sensor_xy(1).x;
        y2 = sensor_xy(1).y;
        dist_meters = sqrt(sum(( [ x1, y1 ] - [ x2, y2 ] ) .^ 2));

        if dist_meters < minimum_distance_to_comparison_sns_meters
            fprintf( 'SRFDS logical ERROR: bad WEST reference sensors!');
            return;
        end
    end
else % use EAST sensors

    % if there's not enough reference sensors in the requested direction,
    % report an ERROR
    if reference_sns_idx + number_of_comparison_sns > num_channels
        fprintf( 'SRFDS logical ERROR: bad EAST reference sensors!');
        return;
    end

    % if there's not enough distance to the reference sensors in the
    % requested direction, report an error
    if minimum_distance_to_comparison_sns_meters > 0

        x2 = sensor_xy(num_channels).x;
        y2 = sensor_xy(num_channels).y;
        dist_meters = sqrt(sum(( [ x1, y1 ] - [ x2, y2 ] ) .^ 2));

        if dist_meters < minimum_distance_to_comparison_sns_meters
            fprintf( 'SRFDS logical ERROR: bad EAST reference sensors!');
            return;
        end
    end
end

% Obtain comparison sensors
comparison_sns_names = cell(number_of_comparison_sns, 1);
comparison_sns_idxs = zeros(number_of_comparison_sns, 1);

current_sns_idx = reference_sns_idx;
total_comparison_sensors = 0;

while true
    if total_comparison_sensors >= number_of_comparison_sns
        break;
    end
```

```
if use_WEST_reference_sensors

    % if there's no minimum distance, add a refernce sensor
    if minimum_distance_to_comparison_sns_meters == 0
        comparison_sns_names{total_comparison_sensors+1} = ...
            sprintf( 'Z%02d', current_sns_idx - 1 );
        comparison_sns_idxs(total_comparison_sensors+1) = ...
            current_sns_idx - 1;

        current_sns_idx = current_sns_idx - 1;
        total_comparison_sensors = total_comparison_sensors + 1;

    else
        % if the minimum distance has been observed, add a refernce
        % sensor
        sns_name  = sprintf( 'Z%02d', current_sns_idx - 1 );
        x2 = sensor_xy(current_sns_idx).x;
        y2 = sensor_xy(current_sns_idx).y;
        dist_meters = sqrt(sum(( [ x1, y1 ] - [ x2, y2 ] ) .^ 2));

        if dist_meters >= minimum_distance_to_comparison_sns_meters
            comparison_sns_names{total_comparison_sensors+1}= sns_name;
            comparison_sns_idxs(total_comparison_sensors+1) = ...
                current_sns_idx - 1;

            total_comparison_sensors = total_comparison_sensors + 1;

            % Disaply the added sensor IDs
            fprintf( 'Added a reference sensor: %s\t\n', sns_name );
        end

        current_sns_idx = current_sns_idx - 1;
        continue;
    end
else % east
    % if there's no minimum distance, add a  sensor
    if minimum_distance_to_comparison_sns_meters == 0
        comparison_sns_names{ total_comparison_sensors+1 } = ...
            sprintf( 'Z%02d', current_sns_idx + 1 );
        comparison_sns_idxs(total_comparison_sensors+1) = ...
            current_sns_idx + 1;

        current_sns_idx = current_sns_idx + 1;
        total_comparison_sensors = total_comparison_sensors + 1;
    else
        % if the minimum distance has been observed, add a refernce
        % sensor
        sns_name  = sprintf( 'Z%02d', current_sns_idx + 1 );
        x2 = sensor_xy(current_sns_idx).x;
        y2 = sensor_xy(current_sns_idx).y;
        dist_meters = sqrt(sum(( [ x1, y1 ] - [ x2, y2 ] ) .^ 2));

        if dist_meters >= minimum_distance_to_comparison_sns_meters
            comparison_sns_names{ total_comparison_sensors+1 } = ...
                sns_name;
            comparison_sns_idxs(total_comparison_sensors+1) = ...
```

```
                    current_sns_idx + 1;

                total_comparison_sensors = total_comparison_sensors + 1;

                % Disaply the added sensor IDs
                fprintf( 'Added a reference sensor: %s\t\n', sns_name );
            end

            current_sns_idx = current_sns_idx + 1;
            continue;
        end
    end
end

sensor_index_low = 1;
sensor_index_high = num_channels;

%   Init this variable only once
tmp_x = [ 0:1:Last_sample_Idx - 1 ] ./ sampling_rate_Hz;
RMS_2D = zeros( Last_sample_Idx, num_channels );

for sns = sensor_index_high:-1:sensor_index_low
    % get trace #1
    trace_current = src_traces( sns, :);

    % Plot the source data ( filtered and DC-corrected )
    figure( fh_FilteredData );
    hold on
    % we need to multiply by -1 because the Y-axis is upside down
    tmp_y = trace_current / ( 1.05*max( abs(trace_current) )) + sns;
    plot( tmp_x, tmp_y, 'b' );

    max_tmp_y = max( tmp_y );
    min_tmp_y = min( tmp_y );

    if raw_data_max < max_tmp_y
        raw_data_max = max_tmp_y;
    end;

    if raw_data_max < max_tmp_y
        raw_data_max = max_tmp_y;
    end;

    if raw_data_min > min_tmp_y
        raw_data_min = min_tmp_y;
    end;
    hold off

    % Show Work Sensors ( Raw data )
    if ((sns >= reference_sns_idx) && (sns <= max(comparison_sns_idxs)))...
            || ...
        ((sns <= reference_sns_idx) && ( sns >= min( comparison_sns_idxs)))
        figure( fh_FilteredData_WorkSensors );
        hold on
        % we need to multiply by -1 because the Y-axis is upside down
        tmp_y = trace_current / ( 1.05*max( abs( trace_current ) )) + sns;
        plot( tmp_x, tmp_y, 'b' );
```

```
    max_tmp_y = max( tmp_y );
    min_tmp_y = min( tmp_y );

    if work_sensors_raw_data_max < max_tmp_y
        work_sensors_raw_data_max = max_tmp_y;
    end;

    if work_sensors_raw_data_max < max_tmp_y
        work_sensors_raw_data_max = max_tmp_y;
    end;

    if work_sensors_raw_data_min > min_tmp_y
        work_sensors_raw_data_min = min_tmp_y;
    end;
    hold off
end

% Allocate memory buffers & Initialize RMS
current_RMS = zeros( 1, length( trace_current ) );

% RMS
current_RMS( RMS_length_samples ) = ...
    sum( trace_current( 1:RMS_length_samples ).^2 );

% Compute RMS
for i = RMS_length_samples + 1:length( trace_current )
     current_RMS(i) = current_RMS(i-1) + trace_current(i).^2 - ...
         trace_current(i - RMS_length_samples).^2;
end

% Normalize RMSs by the RMS length
current_RMS = current_RMS / RMS_length_samples;

% Square-root
for i = 1:length( trace_current )
     current_RMS(i) = sqrt( current_RMS(i) );
end

% Show Work Sensors ( RMS data )
if ((sns >= reference_sns_idx) && (sns <= max(comparison_sns_idxs)))...
        || ...
    ((sns <= reference_sns_idx) && (sns >= min(comparison_sns_idxs)))
    figure( fh_RMS_Data_WorkSensors );
    hold on
    tmp_y = current_RMS / ( -1.05*max( current_RMS )) + sns;
    plot( tmp_x, tmp_y, 'b' );

    max_tmp_y = max( tmp_y );
    min_tmp_y = min( tmp_y );

    if work_sensors_RMS_data_max < max_tmp_y
        work_sensors_RMS_data_max = max_tmp_y;
    end;

    if work_sensors_RMS_data_max < max_tmp_y
        work_sensors_RMS_data_max = max_tmp_y;
```

```
        end;

        if work_sensors_RMS_data_min > min_tmp_y
            work_sensors_RMS_data_min = min_tmp_y;
        end;
        hold off
    end

    % RMS
    RMS_2D(:, sns )     = current_RMS;
end


% -------------------------------------------------------
% Train signal detection using RMS data and L2 norm
% NOTE: good for the middle part of the train signal
% -------------------------------------------------------
start_time_samples = 1;

L2_time_line_samples = start_time_samples : arrival_time_step_samples : ...
    ( Last_sample_Idx - TDA_min_window_length_millisec );
L2_RMS_west = zeros( length( L2_time_line_samples ), length(speed_range ));
L2_RMS_east = zeros( length( L2_time_line_samples ), length(speed_range ));
time_range = L2_time_line_samples .* sampling_rate_seconds;

% east-west loop
for train_direction_idx = 1:2
     % loop over the speeds
     speed_idx = 1;

     for speed_msec = speed_range
        % Main TDA train detector loop
        time_idx     = 1;
        % time
        for tm = L2_time_line_samples
            xcorr_window_seconds = get_xcorr_window_seconds( ...
                Min_train_speed_mpsec, Max_train_speed_mpsec, ...
                Min_speed_xcorr_window_sec, Max_speed_xcorr_window_sec, ...
                speed_msec );

            L2_window_length_samples=xcorr_window_seconds*sampling_rate_Hz;

            window_end_time_samples = tm + L2_window_length_samples;

            % if we are out of data on the main sensor, exit
            if window_end_time_samples > Last_sample_Idx
                time_idx = time_idx + 1;
                continue;
            end

            main_data_segment = RMS_2D( tm: RMS_subsampling_factor : ...
                    window_end_time_samples, reference_sns_idx );

            % check min/max
            max_main_data_segment = max( main_data_segment );

            if max_main_data_segment < RMS_Trigger_Level_ms
```

```
     time_idx = time_idx + 1;
     continue;
end

% init. the product of cross-correlations
xcorr = 1.0;

% remove the mean value
if detrend_RMS
    main_data_segment = main_data_segment - ...
        mean( main_data_segment );
end

% scan the comparison sensors
for cmp_sns_idx = 1:total_comparison_sensors
    % compute the time delay for a train to move from one
    % sensor to the other
    time_shift_samples = ...
     get_train_delay_samples( sampling_rate_Hz, speed_msec, ...
               train_search_dir_cells(train_direction_idx), ...
       reference_sns_idx, comparison_sns_idxs(cmp_sns_idx), ...
               sensor_xy);

    time_shift_samples = int32( time_shift_samples );

    reference_time_window_out_of_scope = false;

    if tm + time_shift_samples > Last_sample_Idx
        reference_time_window_out_of_scope = true;
    end


    if tm + time_shift_samples < 1
        reference_time_window_out_of_scope = true;
    end


    if window_end_time_samples + time_shift_samples > ...
                    Last_sample_Idx
        reference_time_window_out_of_scope = true;
    end


    % if the time window exceed the available data, break the
    % sensor loop. Assign '0' to the TDA x/corr matrix and quit
    if reference_time_window_out_of_scope
        xcorr = 0.0;
        break; % break the ref. sensor loop
    end

    % get the comparison data segment
    reference_data_segment = RMS_2D((tm+time_shift_samples):...
            RMS_subsampling_factor:(window_end_time_samples+...
            time_shift_samples), ...
            comparison_sns_idxs( cmp_sns_idx ) );

    % check max
```

```
            max_reference_data_segment = max(reference_data_segment );

            if max_reference_data_segment < RMS_Trigger_Level_ms
                xcorr = 0.0;
                break; % break the ref. sensor loop
            end

            % remove the mean
            if detrend_RMS
                reference_data_segment = reference_data_segment - ...
                    mean( reference_data_segment );
            end

            xc = 0;

            if length( reference_data_segment ) > ...
                        length( main_data_segment )
         reference_data_segment(length( main_data_segment )+1:end)= [];
                xc = sum( main_data_segment .*reference_data_segment);
            else
                if length( main_data_segment ) > ...
                        length( reference_data_segment )
                    temp_main_data_segment = main_data_segment( 1 : ...
                        length( reference_data_segment ) );

                    xc = sum( temp_main_data_segment .* ...
                        reference_data_segment );
                else
                    % length #1 == length #2
                    xc = sum( main_data_segment .* ...
                        reference_data_segment );
                end
            end

            % negative correlation == no train
            if xc <= 0
                xcorr = 0.0;
                break; % break the ref. sensor loop
            end

            xcorr = xcorr * xc / ( norm( reference_data_segment ) * ...
                norm( main_data_segment ) );
        end % reference sensors

        % assign the product
       if strncmp('WEST',train_search_dir_cells(train_direction_idx),4)
            L2_RMS_west( time_idx, speed_idx ) = xcorr;
        else
            L2_RMS_east( time_idx, speed_idx ) = xcorr;
        end

        time_idx = time_idx + 1;

    end % for time

    speed_idx = speed_idx + 1;
end % for speeds
```

```
end


% detect westward trains
[train_start_w, train_velocity_west_ms ] = detect_train( ...
            L2_RMS_west, speed_range, time_range, tda_threshold, ...
               max_tda_speed_tolerance_ms, min_tda_time_tolerance_s, ...
               time_step_sec, speed_step_mpsec );

% detect eastward trains
[train_start_e, train_velocity_east_ms ] = detect_train( ...
            L2_RMS_east, speed_range, time_range, tda_threshold, ...
               max_tda_speed_tolerance_ms, min_tda_time_tolerance_s, ...
               time_step_sec, speed_step_mpsec );

if train_velocity_west_ms > 0
   best_velocity_ms = -train_velocity_west_ms;
   train_start_seconds = train_start_w;
else
    if train_velocity_east_ms > 0
        best_velocity_ms = train_velocity_east_ms;
        train_start_seconds = train_start_e;
    end
end

if normalize_color_bar
    L2_RMS_west( 1, 1 ) = maximum_xcorr_value;
    L2_RMS_east( 1, 1 ) = maximum_xcorr_value;
end

fh_figure_TDA_west = figure( 'Name', 'Train detector: westbound train' );
imagesc( time_range, speed_range, L2_RMS_west' );
title( [ 'TDA (west)' ] );
set(gca,'YDir','normal');
ylabel('m/s');
xlabel('seconds');
cb = colorbar('location','EastOutside') ;
thin_colorbar( fh_figure_TDA_west, cb );

% fh_figure_TDA_east
fh_figure_TDA_east = figure( 'Name', 'Train detector: eastbound train' );
imagesc( time_range, speed_range, L2_RMS_east' );
title( [ 'TDA (east)' ] );
set(gca,'YDir','normal');
ylabel('m/s');
xlabel('seconds');
cb = colorbar('location','EastOutside') ;
thin_colorbar( fh_figure_TDA_east, cb );


%-----------------------------------------------------------------
% Save the figures here
[pathstr,name,ext] = fileparts(FILE_name1);
subfolder_full_name = [ destination_folder, destination_subfolder, ...
    name, '_', reference_sns_name '\' ];
mkdir( subfolder_full_name );
```

```
% Raw data
figure( fh_FilteredData );
xLimits = get( gca, 'XLim' );
axis( [ xLimits(1) xLimits(2) raw_data_min raw_data_max ] );

saveas( fh_FilteredData, [ subfolder_full_name, raw_data_file_name, ...
    graphic_format_ext ] );
saveas( fh_FilteredData, [ subfolder_full_name, raw_data_file_name, ...
    MATLAB_format_ext ] );
print_two_column_fig_png( fh_FilteredData, subfolder_full_name, ...
    raw_data_file_name );
clear fh_FilteredData;

% sub-window
figure( fh_FilteredData_WorkSensors );
xLimits = get( gca, 'XLim' );
axis( [ xLimits(1) xLimits(2) work_sensors_raw_data_min  ...
    work_sensors_raw_data_max ] );
saveas( fh_FilteredData_WorkSensors, [ subfolder_full_name, ...
    raw_subdata_file_name, graphic_format_ext ] );
saveas( fh_FilteredData_WorkSensors, [ subfolder_full_name, ...
    raw_subdata_file_name, MATLAB_format_ext ] );
print_two_column_fig_png( fh_FilteredData_WorkSensors, ...
    subfolder_full_name, raw_subdata_file_name );
clear fh_FilteredData_WorkSensors;


figure( fh_RMS_Data_WorkSensors );
xLimits = get( gca, 'XLim' );
axis( [ xLimits(1) xLimits(2) work_sensors_RMS_data_min  ...
    work_sensors_RMS_data_max ] );
saveas( fh_RMS_Data_WorkSensors, [ subfolder_full_name, ...
    RMS_subdata_file_name, graphic_format_ext ] );
saveas( fh_RMS_Data_WorkSensors, [ subfolder_full_name, ...
    RMS_subdata_file_name, MATLAB_format_ext ] );
print_two_column_fig_png( fh_RMS_Data_WorkSensors, ...
    subfolder_full_name, RMS_subdata_file_name );

% fh_figure_TDA_west
saveas( fh_figure_TDA_west, [ subfolder_full_name, ...
    TDA_west_data_file_name, graphic_format_ext ] );
saveas( fh_figure_TDA_west, [ subfolder_full_name, ...
    TDA_west_data_file_name, MATLAB_format_ext ] );
print_two_column_fig_png( fh_figure_TDA_west, subfolder_full_name, ...
    TDA_west_data_file_name );
clear  fh_figure_TDA_west;

% fh_figure_TDA_east
saveas( fh_figure_TDA_east, [ subfolder_full_name, ...
    TDA_east_data_file_name, graphic_format_ext ] );
saveas( fh_figure_TDA_east, [ subfolder_full_name, ...
    TDA_east_data_file_name, MATLAB_format_ext ] );
print_two_column_fig_png( fh_figure_TDA_east, subfolder_full_name, ...
    TDA_east_data_file_name );
clear  fh_figure_TDA_east;
```

```
%  Save the data procesing parameters
fileID = fopen( [ subfolder_full_name, DataProcessingParametersFile ],'w');

% Source data
fprintf( fileID, 'Source folder   = %s\r\n', DIR_name );
fprintf( fileID, 'Source file #1  = %s\r\n\r\n', FILE_name1 );

% Dump the TDA parameters
fprintf( fileID, 'RMS_length_seconds         = %3.1f\r\n', ...
    RMS_length_seconds );
fprintf( fileID, 'Cross-corr. window, seconds = %3.1f to %3.1f\r\n', ...
 get_xcorr_window_seconds(Min_train_speed_mpsec, Max_train_speed_mpsec, ...
                    Min_speed_xcorr_window_sec, ...
                    Max_speed_xcorr_window_sec, Max_train_speed_mpsec), ...
 get_xcorr_window_seconds(Min_train_speed_mpsec, Max_train_speed_mpsec, ...
                    Min_speed_xcorr_window_sec, ...
                    Max_speed_xcorr_window_sec, Min_train_speed_mpsec));

fprintf( fileID, 'Cross-corr. speeds min/max = %3.1f to %3.1f\r\n', ...
         Min_train_speed_mpsec , ...
         Max_train_speed_mpsec );

if detrend_RMS
    fprintf( fileID, ...
    '\r\nDetrend the RMS data before cross-correlation = ENABLED\r\n' );
else
    fprintf( fileID, ...
    '\r\nDetrend the RMS data before cross-correlation = DISABLED\r\n' );
end

fprintf( fileID, '\r\nMain sensor          = %s\r\n', reference_sns_name );
fprintf( fileID, ...
    'Minimum distance to reference sensors, meters = %3.1f\r\n', ...
    minimum_distance_to_comparison_sns_meters );
fprintf( fileID, 'Reference sensors:\r\n' );

for cmp_sns_idx = 1:total_comparison_sensors
    fprintf( fileID, '  Sns %d = %s\r\n', cmp_sns_idx, ...
        comparison_sns_names{cmp_sns_idx} );
end

if best_velocity_ms ~= 0
    fprintf( fileID, ...
       'TDA: train detected at %3.1fs; velocity = %3.1f m/s\r\n', ...
        train_start_seconds, best_velocity_ms);
end

fclose(fileID);


% ************************************************************************
% NAME:     detect_train
% PURPOSE:  Returns train's arrival time and speed based on the
%           cross-correlation matrix
%
% INPUT:    L2_RMS  - MxN matrix of cross-correlations, where M= number of
%           time increments; N=number of speed increments
```

```
%           speed_range    - range of speeds for which L2_RMS was computed
%           time_range     - time steps for which L2_RMS was computed
%           tda_threshold  - train patte threshold
%           max_tda_speed_tolerance_ms  - tolerance for the width of the
%                       train pattern in L2_RMS along the speed axis;
%           min_tda_time_tolerance_s    - threshold for the min. length of
%                       the train pattern in L2_RMS
%           time_step_sec  - time increment used in <time_range>;
%           speed_step_mpsec - speed inrement (m/s) used in speed_range;
%
% OUTPUT:   train_start  - if a train is detected, this is its timing WRT
%           the beginning of L2_RMS;
%           train_velocity_ms  - train speed (always a positive value)
% ************************************************************************
function [train_start, train_velocity_ms ] = ...
 detect_train( L2_RMS, speed_range, time_range, tda_threshold, ...
               max_tda_speed_tolerance_ms, min_tda_time_tolerance_s, ...
               time_step_sec, speed_step_mpsec )
% search for a train pattern
[m, n] = size( L2_RMS );

min_tda_time_tolerance_steps = min_tda_time_tolerance_s/time_step_sec;

train_start = 0;
train_velocity_ms = 0;

pattern_length = 0;
current_best_train_velocity_ms = 0;
current_best_corelation = 0;

for t=1:m
   high_xcorr = find( L2_RMS(t,:) >= tda_threshold );

   if( isempty(high_xcorr) )
      train_start = 0;
      pattern_length = 0;
      current_best_train_velocity_ms = 0;
      current_best_corelation = 0;
      continue;
   end

   tda_speed_tolerance= speed_step_mpsec*(max(high_xcorr)-min(high_xcorr));

   if( tda_speed_tolerance <= max_tda_speed_tolerance_ms )
       if( 0 == train_start )
         train_start = time_range(t);
         pattern_length = 1;
       else
         pattern_length = pattern_length + 1;

         % keep track of the best matching pattern
         [M,I] = max(L2_RMS(t,high_xcorr));

         if M > current_best_corelation
            current_best_corelation = M;
            current_best_train_velocity_ms = speed_range(high_xcorr(I));
         end
```

```
        if( pattern_length >= min_tda_time_tolerance_steps )
            train_velocity_ms = current_best_train_velocity_ms;
            return;
        end
      end
   else
     pattern_length=0;
     train_start=0;
   end;
end



% ************************************************************************
% NAME:     get_train_delay_samples
% PURPOSE:  Returns sensor-to-sensor travel time
%
% INPUT:    sampling_rate  - in seconds
%           cur_speed      - m/s
%           direction      - 'WEST' | 'EAST'
%           compar_sns_idx - comparison sns index
%           refer_sns_idx  - reference sensor index
%           sensors_xy     - array of sensor coordinates
% OUTPUT:   delay_samples  - delay btw compar_sns_idx and refer_sns_idx
% ************************************************************************
function [ delay_samples ] = ...
       get_train_delay_samples( sampling_rate, cur_speed, ...
          train_search_dir, refer_sns_idx, compar_sns_idx, sensor_xy )
x1 = sensor_xy(compar_sns_idx).x;
y1 = sensor_xy(compar_sns_idx).y;
x2 = sensor_xy(refer_sns_idx).x;
y2 = sensor_xy(refer_sns_idx).y;

delay_samples = sqrt((x1-x2)*(x1-x2) + (y1-y2)*(y1-y2)) ...
    / cur_speed * sampling_rate;

if( compar_sns_idx > refer_sns_idx )
    if ( strcmp( train_search_dir, 'WEST' ) == 1 )
        delay_samples = - delay_samples;
    end
end

if( compar_sns_idx < refer_sns_idx )
    if( strcmp( train_search_dir, 'EAST' ) == 1 )
        delay_samples = - delay_samples;
    end
end



% ************************************************************************
% NAME:     get_xcorr_window_seconds
% PURPOSE:  Returns the length, in seconds, of a cross-correlation window
%           depending on the train speed
% ************************************************************************
function [ x ] = get_xcorr_window_seconds( ...
```

```
        min_speed_msec, max_speed_msec, min_speed_window_sec, ...
            max_speed_window_sec, speed_meters_per_sec )

frac = ( speed_meters_per_sec - min_speed_msec) / ...
    ( max_speed_msec - min_speed_msec );

x = min_speed_window_sec + frac * ...
    ( max_speed_window_sec - min_speed_window_sec ) ;


% ************************************************************************
% NAME:     get_site_sensor_xy
% PURPOSE:  Return (X;Y) coordinates of a sensor
% INPUT:    site_ID - unique site name, e.g. 'white_canyon', 'hope'
%           sns_name - sensor ID, e.g. 'Z01', 'Z02'
% OUTPUT:   sensor coordinates
% ************************************************************************
function [ x, y ] = get_site_sensor_xy( site_ID, sns_name )

if( strcmpi( site_ID, 'white_canyon' ) )
switch upper( sns_name )
    case 'Z01'
        x = 12.80;    y = 197.36;
        return
    case 'Z02'
        x = 18.60;    y = 178.59;
        return
    case 'Z03'
        x = 22.91;    y = 159.12;
        return
    case 'Z04'
        x = 25.71;    y = 138.79;
        return
    case 'Z05'
        x = 26.98;    y = 121.40;
        return
    case 'Z06'
        x = 27.35;    y = 104.25;
        return
    case 'Z07'
        x = 26.86;    y = 87.17;
        return
    case 'Z08'
        x = 26.29;    y = 70.54;
        return
    case 'Z09'
        x = 24.77;    y = 53.90;
        return
    case 'Z10'
        x = 22.50;    y = 34.17;
        return
     case 'Z11'
         x = 19.81;    y = 17.65;
        return
     case 'Z12'
         x = 16.90;    y = 1.88;
        return
```

```
case 'Z13'
    x = 15.56;    y = -5.83;
   return
case 'Z14'
    x = 10.06;    y = -27.69;
   return
case 'Z15'
    x = 5.07;    y = -44.97;
   return
case 'Z16'
    x = -1.78;    y = -64.98;
   return
case 'Z17'
    x = -10.06;    y = -83.95;
   return
case 'Z18'
    x = -17.21;    y = -100.04;
   return
case 'Z19'
    x = -25.77;    y = -116.79;
   return
case 'Z20'
    x = -34.21;    y = -131.13;
   return
case 'Z21'
    x = -46.21;    y = -149.29;
   return
case 'Z22'
    x = -57.81;    y = -164.79;
   return
case 'Z23'
    x = -70.27;    y = -180.32;
   return
case 'Z24'
    x = -81.70;    y = -193.23;
   return
case 'Z25'
    x = -97.37;    y = -208.39;
   return
case 'Z26'
    x = -111.45;    y = -221.53;
   return
case 'Z27'
    x = -126.14;    y = -234.30;
   return
case 'Z28'
    x = -134.97;    y = -242.07;
   return
case 'Z29'
    x = -144.46;    y = -249.89;
   return
case 'Z30'
    x = -154.11;    y = -258.21;
   return
case 'Z31'
    x = -161.45;    y = -264.10;
   return
```

```
case 'Z32'
    x = -168.08;    y = -269.40;
   return
case 'Z33'
    x = -192.58;    y = -284.20;
   return
case 'Z34'
    x = -205.44;    y = -293.68;
   return
case 'Z35'
    x = -215.16;    y = -300.54;
   return
case 'Z36'
    x = -227.82;    y = -308.91;
   return
case 'Z37'
    x = -239.05;    y = -316.71;
   return
case 'Z38'
    x = -249.72;    y = -323.45;
   return
case 'Z39'
    x = -267.17;    y = -334.33;
   return
case 'Z40'
    x = -280.59;    y = -342.13;
   return
case 'Z41'
    x = -294.26;    y = -349.77;
   return
case 'Z42'
    x = -308.24;    y = -356.69;
   return
case 'Z43'
    x = -322.57;    y = -363.35;
   return
case 'Z44'
    x = -333.84;    y = -368.59;
   return
case 'Z45'
    x = -354.92;    y = -378.39;
   return
case 'Z46'
    x = -365.18;    y = -383.16;
   return
case 'Z47'
    x = -377.06;    y = -387.93;
   return
case 'Z48'
    x = -390.67;    y = -393.41;
   return
case 'Z49'
    x = -403.30;    y = -398.29;
   return
case 'Z50'
    x = -412.78;    y = -401.60;
   return
```

```
 case 'Z51'
     x = -426.01;    y = -406.41;
    return
 case 'Z52'
     x = -439.58;    y = -411.11;
    return
 case 'Z53'
     x = -452.82;    y = -415.10;
    return
 case 'Z54'
     x = -466.51;    y = -418.82;
    return
 case 'Z55'
     x = -481.04;    y = -422.50;
    return
 case 'Z56'
     x = -495.44;    y = -426.00;
    return
 case 'Z57'
     x = -510.50;    y = -428.95;
    return
 case 'Z58'
     x = -525.23;    y = -431.34;
    return
 case 'Z59'
     x = -540.03;    y = -433.50;
    return
 case 'Z60'
     x = -554.83;    y = -435.69;
    return
 case 'Z61'
     x = -570.00;    y = -437.42;
    return
 case 'Z62'
     x = -585.05;    y = -439.03;
    return
 case 'Z63'
     x = -599.45;    y = -441.57;
    return
 case 'Z64'
     x = -614.13;    y = -444.82;
    return
 case 'Z65'
     x = -628.28;    y = -449.07;
    return
 case 'Z66'
     x = -642.26;    y = -453.62;
    return
 case 'Z67'
     x = -656.80;    y = -458.88;
    return
 case 'Z68'
     x = -669.47;    y = -465.75;
    return

otherwise
    disp(['***ERROR::get_sensor_XY(). Bad sensor name!' ]);
```

```
end; % switch
end; % if

if( strcmpi( site_ID, 'hope' ) )
switch upper( sns_name )
    case 'Z01'
        x = 12.20;    y = 322.5;
        return
    case 'Z02'
        x = 8.60;    y = 308;
        return
    case 'Z03'
        x = 3.2;    y = 294.3;
        return
    case 'Z04'
        x = 0.2;    y = 280.0;
        return
    case 'Z05'
        x = -1.9;    y = 265.4;
        return
    case 'Z06'
        x = -1.6;    y = 250.6;
        return
    case 'Z07'
        x = -1.6;    y = 235.9;
        return
    case 'Z08'
        x = -1.0;    y = 221.3;
        return
    case 'Z09'
        x = -1.1;    y = 206.5;
        return
    case 'Z10'
        x = -0.7;    y = 192.0;
        return
     case 'Z11'
         x = -0.2;    y = 177.4;
        return
     case 'Z12'
         x = 0.5;    y = 162.9;
        return
     case 'Z13'
         x = 0.7;    y = 148.4;
        return
     case 'Z14'
         x = -0.6;    y = 133.8;
        return
     case 'Z15'
         x = -1.1;    y = 118.7;
        return
     case 'Z16'
         x = -2.1;    y = 104.7;
        return
     case 'Z17'
         x = -3.4;    y = 90.2;
        return
     case 'Z18'
```

```
        x = -4.3;    y = 75.7;
       return
    case 'Z19'
        x = -4.7;    y = 61.0;
       return
    case 'Z20'
        x = -4.8;    y = 46.4;
       return
    case 'Z21'
        x = -3.5;    y = 31.8;
       return
    case 'Z22'
        x = -1.5;    y = 17.1;
       return
    case 'Z23'
        x = 1.3;    y = 2.9;
       return
    case 'Z24'
        x = 4.8;    y = -11.2;
       return
    case 'Z25'
        x = 9.3;    y = -25.0;
       return
    case 'Z26'
        x = 14.0;    y = -39.0;
       return
    case 'Z27'
        x = 19.0;    y = -52.7;
       return

   otherwise
       disp(['***ERROR::get_site_sensor_xy(). Bad sensor name!' ]);
end; % switch
end; % if


%-----------------------------------------------------------------
% NAME: notch_filter
%-----------------------------------------------------------------
function [ y ] = notch_filter( x, sampling_rate, Notch_Hz )
trace_in = x;

for i = 1:length( Notch_Hz )
   w0_60 = Notch_Hz(i) / ( sampling_rate / 2 );

   bw_60 = w0_60/35;       % set the Q factor for the filter to 35

   [num,den] = iirnotch( w0_60, bw_60 );
   y = filter( num, den, trace_in);

   if( i < length( Notch_Hz ) )
      trace_in = y;
   end
end

%-----------------------------------------------------------------
% NAME: thin_colorbar
```

```
%-----------------------------------------------------------------
function thin_colorbar( fig_handle, colorbar_handle )
ColorBarLeft = 0.90;
left_margin_image          = 0.08;
right_margin_image         = 0.14;

pf=get( fig_handle,'position');
pcb = get( colorbar_handle ,'position');
pcb(1) = ColorBarLeft;
pcb(3) = 0.5*pcb(3);
set( colorbar_handle, 'position', pcb);
set( fig_handle,'position', pf);
marg = get(gca,'LooseInset');
set(gca, 'LooseInset', [ left_margin_image, marg(2), ...
    right_margin_image, marg(4) ]);

%-----------------------------------------------------------------
function print_two_column_fig_png( fig_handle, ...
                        subfolder_full_name, data_file_name )

width_in  = 3.2;
height_in = 2.4;

set( fig_handle, 'PaperUnits', 'inches' );
set( fig_handle, 'PaperPosition', [0 0 width_in height_in ] );
set( fig_handle, 'PaperPositionMode', 'manual' );

print( fig_handle, [ subfolder_full_name, data_file_name ],'-dpng');
```

B.3. The Locomotive Detection Algorithm #1 (LDA-1)

Locomotive Detection Algorithm #1 (LDA-1).
Detection of the arrival of a locomotive or a high-rail at a sensor Z^R (called *reference* sensor) within time window $t \in (t_1;\ t_N)$. The algorithm uses the uniform norm $l(x)^\infty = \max_i |x_i|$ to compare *STA/LTA* signals at the main and the reference sensor(s). The current version uses one *comparison* sensor, Z^C.

Algorithm description
For a given range of train velocities, discrepancy between windowed *STA/LTA* signals at the reference and the comparison sensor is computed. If the discrepancy is below the threshold, combination of {time t^R; velocity v^R} is stored as a potential solution.
To verify the solution, the $l(x)^\infty$ test is performed for the rest of the train velocities.

Input:	2D data slice $D = \{x_i^j : i = 1, \dots, N; j = 1, .., S\}$, where *N* is the number of data samples; *S* is the number of data traces acquired with uniaxial sensors; Sensor coordinates $\overline{Z^J}$;	
Output:	t^R – the arrival time of a vehicle at sensor Z^R; v^R- the velocity of the identified vehicle;	
Parameters:	w^{STA}	the length of the *STA* time window, *e.g.* $w^{STA} = 1$ second;
	w^{LTA}	the length of the *LTA* time window, *e.g.* $w^{LTA} = 5$ s;
	w_{l^∞}	the length of the time window used to compute l^∞ - norm, *e.g.* 15 s;
	$\boldsymbol{V} = \{v_p : p = 1, .., P\}$	a discrete set of *P* velocities used to detect a vehicle; $v_{max} = \max\{\lvert v_p \rvert\}, v_{min} = \min\{\lvert v_p \rvert\}$;
	$\boldsymbol{StaLta}_{MIN}$	the threshold for the STA/LTA surge induced by arriving locomotive, *e.g.* $StaLta_{MIN}$ = 3.2;
	$\boldsymbol{R}_{min/max}^{STA/LTA}$	the ratio of *min(STA/LTA)* and *max(STA/LTA)* within the sliding time window w_{l^∞}, *e.g.* $R_{min/max}^{STA/LTA}$ = 0.5;
	$\Delta \boldsymbol{t}_{min}^{R,C}$	travel time of the train as it passes from sensor Z^R to a comparison sensor Z^C. This parameter is used to select a comparison sensor adaptively, depending on the train's velocity. *E.g.* $\Delta t_{min}^{R,C}$ = 3 s;
	$\boldsymbol{d}_{max}^{R,C}$	the threshold for the l^∞ discrepancy test. *E.g.* $d_{max}^{R,C}$= 0.25;
	Δv	the velocity tolerance, Δv = 5 ms;

/* compute STA/LTA */
for each sensor trace $D(j)$

Use w^{STA} and w^{LTA} to compute $StaLta_i^j,\ i = \overline{1,N};\ j = \overline{1,S}$

end for

for each sliding time window $w_i^R = \left(t_i^R;\ t_i^R + w_{l^\infty}\right),\ i = \overline{1, N - w_{l^\infty}}$

/* detect a STA/LTA surge induced by a locomotive on the main sensor Z^R */

if $max\left\{StaLta^R(w_i^R)\right\} < \boldsymbol{StaLta}_{MIN}$ **then**

/* skip the rest of the time window loop */

continue;

end if

if $min\left\{StaLta^R\left(w_i^R\right)\right\}/max\left\{StaLta^R\left(w_i^R\right)\right\} < \boldsymbol{R}_{min/max}^{STA/LTA}$ **then**

continue;

end if

for each velocity $v_p \in \boldsymbol{V}$

/* ensure there is enough distance between the reference and the comparison sensor */

1. find a closest *comparison* sensor, Z^C, for which the travel time delay $\Delta t^{R,C}\left(v_p\right)$ is at least $\Delta \boldsymbol{t}_{min}^{R,C}$ seconds long:

$$\Delta t^{R,C}\left(v_p\right) = \frac{\left|\overline{Z^R} - \overline{Z^C}\right|}{v_p};$$

2. compute the reference time window

$$w_i^R(v_p) = \left(t_i^M + \Delta t^{M,R}\left(v_p\right);\ t_i^M + \Delta t^{M,R}\left(v_p\right) + w_{l^\infty}\right);$$

/* detect a STA/LTA surge induced by the locomotive in the comparison signal */

if $max\left\{StaLta^C\left(w_i^C(v_p)\right)\right\} < \boldsymbol{StaLta}_{MIN}$ **then**

continue;

end if

if $min\left\{StaLta^C\left(w_i^C(v_p)\right)\right\}/max\left\{StaLta^C\left(w_i^C(v_p)\right)\right\} < \boldsymbol{R}_{min/max}^{STA/LTA}$ **then**

continue;

end if

/* calculate discrepancy between the two normalized STA/LTA vectors */

$$d_i^{R,C}(v_p) = max\left\{\frac{StaLta^R\left(w_i^R\right)}{max\ \left(StaLta^R\left(w_i^R\right)\right)} - \frac{StaLta^C\left(w_i^C(v_p)\right)}{max\left(StaLta^C\left(w_i^C(v_p)\right)\right)}\right\}$$

if $d_i^{R,C}(v_p) > \boldsymbol{d}_{\max}^{R,C}$ **then**

continue;

else

/* we found a potential solution; store the identified arrival time and velocity */

$t^R = t_i^R$;

$v^R = v_p$;

end if

/* use comparison sensor Z^C to verify the consistency of the solution */

for each velocity $v_n \in \boldsymbol{V}$

1. compute delay time $\Delta t^{R,C}(v_n)$;
2. compute reference time window $w_i^C(v_n)$;
3. compute l^∞ - discrepancy $d_i^{R,C}(v_n)$ between the main and the reference signals;

/* if for some v_n outside the velocity tolerance interval */

/* the discrepancy is small, discard the current solution $\{t_i^R;\ v_p\}$ */

if $|v_n - v_p| > \Delta v$ **and** $d_i^{R,C}(v_n) < \boldsymbol{d}_{max}^{R,C}$ **then**

$t^R = 0$;

$v^R = 0$;

goto next v_p**;**

end if

return TRUE;

end for each velocity v_n

end for each velocity v_p

end for time window

return FALSE.

B.4. The Locomotive Detection Algorithm #2 (LDA-2)

Locomotive Detection Algorithm #2 (LDA-2).
Detection of the arrival of a locomotive or a high-rail at a sensor Z^R (called *reference* sensor) within time window $t \in (t_1;\ t_N)$. The algorithm uses the uniform norm $l(x)^\infty = \max_i |x_i|$ to compare *RMS* and *STA/LTA* signals at the reference and the comparison sensor(s).
The current version uses one *comparison* sensor, Z^C.

Algorithm description:
For a given range of train velocities, discrepancy between the windowed *r.m.s.* signals at the reference and comparison sensors is computed. If the discrepancy is below the threshold, combination of {time t^R; velocity v^R} is stored as a potential solution.
To verify the solution, the $l(x)^\infty$ test is performed for the rest of the train velocities.

Input: 2D data slice $D = \{x_i^j : i = 1, \dots, N; j = 1, .., S\}$,
where *N* is the number of data samples;
S is the number of data traces acquired with uniaxial sensors;

Sensor coordinates $\overline{Z^J}$;

Output: t^R- the arrival time of a vehicle at sensor Z^R;
v^R- the velocity of the identified vehicle;

Parameters:

w^{RMS}	the r.m.s. time window $w^{RMS} =$ 0.2 s for detecting trains with velocities $v \geq 5$ ms; $w^{RMS} = 1.0$ s for detecting trains with velocities $v < 5$ ms;
w^{STA}	the length of the *STA* time window. *E.g.* $w^{STA} = 1.0$ s if $v \geq 5$ ms; $w^{STA} = 2.0$ s if $v < 5$ ms;
w^{LTA}	length of the *LTA* time window, *e.g.* $w^{LTA} = 5.0$ s if $v \geq 5$ ms; $w^{STA} = 10.0$ s if $v < 5$ ms;
w_{l^∞}	the length of the time window used to compute l^∞ - norm, *e.g.* 15 s;
$\boldsymbol{V} = \{v_p : p = 1, .., P\}$	a discrete set of *P* velocities used to detect a vehicle; $v_{max} = \max\{\lvert v_p \rvert\}, v_{min} = \min\{\lvert v_p \rvert\}$;
$\boldsymbol{StaLta}_{MIN}$	the threshold for the STA/LTA surge induced by arriving locomotive, *e.g.* $StaLta_{MIN}$ = 3.2;
$\boldsymbol{R}_{min/max}^{RMS}$	the minimum ratio of *min(RMS)* and *max(RMS)* within the sliding time window w_{l^∞}, *e.g.* $R_{min/max}^{RMS}$ = 0.2;
$\Delta \boldsymbol{t}_{min}^{R,C}$	travel time of the train as it passes from sensor Z^R to a comparison sensor Z^C. This parameter is used to select a comparison sensor adaptively, depending on train velocity.

	E.g. $\Delta t_{min}^{R,C}$ = 3 s;
$\boldsymbol{d}_{max}^{R,C}$	the threshold for the l^{∞} discrepancy test. *E.g.* $d_{max}^{R,C}$= 0.35;
Δv	the velocity test tolerance, Δv = 5 ms;

/* compute STA/LTA and r.m.s. */
for each sensor trace $D(j)$
Use w^{STA} and w^{LTA} to compute $StaLta_i^j$, $i = \overline{1,N}$; $j = \overline{1,S}$;
Use w^{RMS} to compute RMS_i^j, $i = \overline{1,N}$; $j = \overline{1,S}$;
end for

for each sliding time window $w_i^R = \left(t_i^R;\ t_i^R + w_{l^{\infty}}\right),\ i = \overline{1, N - w_{l^{\infty}}}$

/* detect a STA/LTA surge induced by a locomotive at the reference sensor Z^R */
if $max\left\{StaLta^R(w_i^R)\right\} < \boldsymbol{StaLta}_{MIN}$ **then**
/* skip the rest of the time window loop */
continue;
end if

check that the $max\left\{StaLta^M(w_i^M)\right\}$ occurs at least 2 seconds after t_i^R, *i.e.* that the STA/LTA peak is not near the edge of the current time window;

/* detect a significant r.m.s. change within the time window which can be indicative of */
/* a vehicle arrival */
if $min\left\{RMS^R(w_i^R)\right\}/max\left\{RMS^R(w_i^R)\right\} > \boldsymbol{R}_{min/max}^{RMS}$ **then**
continue;
end if

/* ensure the minimum distance between the reference and the comparison sensors */
for each velocity $v_p \in \boldsymbol{V}$

1. find a closest *comparison* sensor, Z^C, for which the travel time delay $\Delta t^{R,C}(v_p)$ is at least $\Delta \boldsymbol{t}_{min}^{R,C}$ seconds long:

$$\Delta t^{R,C}(v_p) = \frac{\left|\overline{Z^R} - \overline{Z^C}\right|}{v_p};$$

2. compute the comparison time window

$$w_i^C(v_p) = \left(t_i^R + \Delta t^{R,C}(v_p);\ t_i^R + \Delta t^{R,C}(v_p) + w_{l^{\infty}}\right);$$

/* detect a STA/LTA surge induced by a locomotive at the comparison sensor Z^C */
if $max\left\{StaLta^C(w_i^C(v_p))\right\} < \boldsymbol{StaLta}_{MIN}$**then**
continue;

end if

if $min\{RMS^C(w_i^C(v_p))\}/max\{RMS^C(w_i^C(v_p))\} > \boldsymbol{R}_{min/max}^{RMS}$ **then**

continue;

end if

/* for the current velocity v_p compute peak *RMS* values for the reference */
/* and the comparison sensors */

$MAX\_RMS_i^R(v_p) = max\left(RMS^R(w_i^R(v_p))\right);$

$MAX\_RMS_i^C(v_p) = max\left(RMS^C(w_i^C(v_p))\right)$

/* calculate discrepancy between the two normalized r.m.s. vectors */

$$d_i^{R,C}(v_p) = max\left\{\frac{RMS^R(w_i^R)}{MAX\_RMS_i^R(v_p)} - \frac{RMS^C(w_i^C(v_p))}{MAX\_RMS_i^C(v_p)}\right\}$$

if $d_i^{R,C}(v_p) > \boldsymbol{d}_{max}^{R,C}$ **then**

continue;

else

/* we found a potential solution; store the identified arrival time and velocity */

$t^R = t_i^R;$

$v^R = v_p;$

end if

/* use comparison sensor Z^C to scan the rest of velocities and verify the solution */

for each velocity $v_n \in \boldsymbol{V}$

1. compute delay time $\Delta t^{R,C}(v_n)$;
2. compute reference time window $w_i^C(v_n)$;
3. use $MAX\_RMS_i^R(v_p)$ and $MAX\_RMS_i^C(v_p)$ to compute l^∞- discrepancy $d_i^{R,C}(v_n)$ between the reference and the comparison *r.m.s.* signals;

/* if for some v_n outside the velocity tolerance interval */

/* the discrepancy is small, discard the current solution $\{t_i^R;\ v_p\}$ */

if $|v_n - v_p| > \Delta v$ **and** $d_i^{R,C}(v_n) < \boldsymbol{d}_{max}^{R,C}$ **then**

$t^R = 0;$

$v^R = 0;$

goto next v_p**;**

end if

return TRUE;

end for each velocity v_n

end for each velocity v_p

end for time window

return FALSE.

B.5. Matlab implementations of the LDA-1 and the LDA-2

```
% ************************************************************************
% NAME:     stalta_loco_detector
%
% PURPOSE:  Demonstration of two algorithms for detection of teh locomotive
%           signal patterns within a seismogram acquired with a geophone
%           array.
%
%           1) The first one detects a time shift between STA/LTA at
%                 two sensors using max|a(i)-b(i)| norm; this is the
%                 Locomotive Detection Algorithm #1, LDA-1
%
%           2) The second one is similar, however, it compares
%                 R.M.S.-smoothed signals (LDA-2)
%
% INPUT:    IN_site_ID - alphanumeric ID of a test site, e.g.
%               'white_canyon' which is needed to find sensor coordinates,
%               etc.
%
%           IN_FILE_name1,  IN_FILE_name2 - names of data files in *.csv
%               format. The first column contains the timing in
%               seconds, e.g. 0.0, 0.001; the rest of the columns
%               contain traces stored in  binary counts of A/D board
%
%           IN_DIR_name - directory where IN_FILE_name1 & IN_FILE_name2 are
%
%           IN_sensor_index_low, IN_sensor_index_high - upper and lower
%               indexes of the seismic array to be processed;
%
%           IN_destination_folder - the directory where output *.jpeg,
%               *.png etc images should be stored. It does not have to
%               exist
%
%           IN_destination_subfolder - a subdirectory under
%               IN_destination_folder
%
%           IN_concatenate_traces - TRUE if the traces in IN_FILE_name1,
%               IN_FILE_name2 must be concatenated
%
%           IN_reference_sns_idx, IN_comparison_sns_idx - indexes of the
%           reference and comparision sensors
%
%           IN_RMS_length_seconds - r.m.s.- window, in seconds, used in
%               LDA-1
%
%           IN_STA_length_millisec, IN_LTA_length_millisec - time windows
%           for the STA/LTA-based detector, LDA-1
%
% OUTPUT:   A text file with the algorithms' output and lots of .png and
%           .fig figures stored under  IN_destination_subfolder
%
% AUTHOR:   Bohdan Nedilko <bohdan.nedilko@alumni.ubc.ca>
%
% DATE:     February 2016
%           This code was tested under Matlab R2008b
```

```
% ************************************************************************
function stalta_loco_detector( IN_site_ID, ...
                    IN_FILE_name1,  IN_FILE_name2, ...
                    IN_DIR_name, ...
                    IN_sensor_index_low, IN_sensor_index_high,  ...
                    IN_destination_folder, IN_destination_subfolder, ...
                    IN_concatenate_traces, ...
                    IN_reference_sns_idx, IN_comparison_sns_idx, ...
                    IN_RMS_length_seconds, IN_STA_length_millisec, ...
                    IN_LTA_length_millisec )

close all

train_search_direction = [ 'WEST'; 'EAST' ];
train_search_dir_cells = cellstr( train_search_direction );

white_canyon_BC2EU = 0.0000000151281;
hope_BC2EU = white_canyon_BC2EU;
DATA_UNITS_STR = 'm/s';

white_canyon_channel_permutation = [ ...
  12 11 10 9 8 7 6 5 4 3 2 1 32 31 30 29 28 27 26 25 24 23 22 21 20 ...
  19 18 17 16 15 14 13 33 45 34 46 35 47 36 48 37 49 38 50 39 51 40 ...
  52 41 53 42 54 43 55 44 56 57 63 58 64 59 65 60 66 61 67 62 68 ...
];


% SAVE FIGS
save_figures_automatically = true;


graphic_format_ext              = '.tiff';
MATLAB_format_ext               = '.fig';
DataProcessingParametersFile    = 'dsp_parameters.txt';

raw_data_file_name              = 'raw_data';
sta_smoothed_data_file_name     = 'sta_smoothed_data';

full_stalta_data_file_name      = 'full_stalta_plot';
sns_stalta_data_file_name       = 'sns_stalta_plot';
sns_rms_data_file_name          = 'sns_rms_plot';

stalta_Lmax_file_name           = 'stalta_Lmax';
rms_Lmax_file_name              = 'rms_Lmax';


% Copy input parameters

site_ID = IN_site_ID;

FILE_name1          = IN_FILE_name1;
FILE_name2          = IN_FILE_name2;
DIR_name            = IN_DIR_name;

sensor_index_low        = IN_sensor_index_low;
sensor_index_high       = IN_sensor_index_high;
destination_subfolder   = IN_destination_subfolder;
```

```
destination_folder      = IN_destination_folder;
concatenate_traces      = IN_concatenate_traces;

% INIT
reference_sns_idx = IN_reference_sns_idx;
comparison_sns_idx = IN_comparison_sns_idx;

reference_sns_name = sprintf( 'Z%02d', reference_sns_idx );
comparison_sns_name = sprintf( 'Z%02d', comparison_sns_idx );


RMS_length_seconds     = IN_RMS_length_seconds;
STA_length_millisec    = IN_STA_length_millisec;
LTA_length_millisec    = IN_LTA_length_millisec;

% Notch Filter frequencies, Hertz
Apply_x60Hz              = true;
Notch_Hz                 = [ 60 ];

% Color bar options
normalize_color_bar     = true;
maximum_xcorr_value     = 1.0;

% STA/LTA parameters
STALTA_subsampling_factor          = 5;
STALTA_display_threshold           = 4.001;

%  Speed/ arrival time identification parameters
Max_train_speed_kmHr    = 50;
Min_train_speed_kmHr    = 5;
Max_train_speed_mpsec   = Max_train_speed_kmHr / 3.6;
Min_train_speed_mpsec   = Min_train_speed_kmHr / 3.6;
arrival_time_step_sec   = 0.4;
speed_step_mpsec        = 0.3;
speed_range = [ Min_train_speed_mpsec : speed_step_mpsec : ...
    Max_train_speed_mpsec ];

% Open a data file as a *.csv  file
csv_01 = csvread( [ DIR_name, FILE_name1 ]);
csv_02 = csvread( [ DIR_name, FILE_name2 ]);

% compute sampling rate
sampling_rate_seconds = csv_01(2,1) - csv_01(1,1);

csv_01 = csv_01(:,2:end);
csv_02 = csv_02(:,2:end);
if( strcmp( IN_site_ID, 'white_canyon' ) == 1 )
    csv_01 = csv_01(:,white_canyon_channel_permutation)';
    csv_02 = csv_02(:,white_canyon_channel_permutation)';
else
    if( strcmp( IN_site_ID, 'hope' ) == 1 )
        csv_01 = csv_01';
        csv_02 = csv_02';
    end
end

if concatenate_traces
```

```
   src_traces = [ white_canyon_BC2EU*csv_01 white_canyon_BC2EU*csv_02 ];
else
   src_traces = white_canyon_BC2EU*csv_01;
end

sampling_rate_Hz = 1.0 / sampling_rate_seconds;

[ m,n ] = size( src_traces );
Last_sample_Idx  = n;
num_channels     = m;

% remove DC and 60 Hz
for idx=1:num_channels
    src_traces(idx, :) = src_traces(idx, :) - mean(src_traces(idx, :));

    % notch-filter the data
    if Apply_x60Hz
        src_traces(idx, :) = notch_filter( src_traces(idx, :), ...
            sampling_rate_Hz, Notch_Hz );
    end
end


% Read sensors' coordinates
sensor_xy = [];
% populate the array of sensor coodinates
for sns = 1:num_channels
    sns_name  = sprintf( 'Z%02d', sns );
    [ sns_x, sns_y ] = get_site_sensor_xy( site_ID, sns_name );

    sensor_xy(sns).x = sns_x;
    sensor_xy(sns).y = sns_y;
end


% Train detection parameters
arrival_time_step_samples = arrival_time_step_sec / sampling_rate_seconds;

% STA/LTA parameters
% use STALTA_time_step_sec to subsample STA/LTA trace
STALTA_time_step_sec            = 0.1;
STALTA_loco_time_step_millisec  = STALTA_time_step_sec * sampling_rate_Hz;

% Loco Detection
Lmax_window_length_sec      = 15.0;
Lmax_window_length_samples  = Lmax_window_length_sec * sampling_rate_Hz;
LTA_length_samples = LTA_length_millisec / 1000 * sampling_rate_Hz;

% Loco STA/LTA Magic Numbers
THRESHOLD_STALTA                = 3.2;
Min_STALTA_Max_STALTA           = 0.5;
MAX_MainStaLta_to_MAX_RefStaLta = 0.7;
RMS_length_samples              = RMS_length_seconds * sampling_rate_Hz;
Min_RMS_Max_RMS                 = 0.2;
Min_STALTA_peak_age_seconds     = 2.0;

% Figures
```

```
fh_FilteredData = figure( 'Name', 'Filtered data' );
title( [ 'Raw data ' strrep(FILE_name1, '_', '-') ] );
set(gca,'YDir', 'reverse');
ylabel('Sensor ID')
xlabel('time, seconds');

% Can't find Y-axis actual min/max values to make it look tight
% will be done manually...
raw_data_max = -realmax;
raw_data_min = realmax;

fh_STALTA_STA = figure( 'Name', 'STA/LTA:  STA' );
title( 'STA/LTA:  STA' );
set(gca,'YDir', 'reverse');
ylabel('Sensor ID')
xlabel('time, seconds');

%-------------------------------------------------------------
% Scan sensors sensor_index_high to sensor_index_low
%-------------------------------------------------------------
for sns = sensor_index_high:-1:sensor_index_low

    %  Correlate the current trace with the west neighbour
    sns_next_idx = sns - 1;
    next_trace_available = ( sns_next_idx > 0 );

    % get the trace
    trace_current = src_traces( sns, :);

    if next_trace_available
        trace_next = src_traces( sns_next_idx, :);
    end

    % Plot the source data
    figure( fh_FilteredData );
    hold on
    tmp_x = [ 0:1:length( trace_current ) - 1 ] ./ sampling_rate_Hz;
    tmp_y = trace_current / ( -max( trace_current )) + sns;
    plot( tmp_x, tmp_y, 'b' );
    hold off

    % store max/min for plot scaling
    max_tmp_y = max( tmp_y );
    min_tmp_y = min( tmp_y );

    if raw_data_max < max_tmp_y
        raw_data_max = max_tmp_y;
    end;

    if raw_data_max < max_tmp_y
        raw_data_max = max_tmp_y;
    end;

    if raw_data_min > min_tmp_y
        raw_data_min = min_tmp_y;
    end;
```

```
% Allocate memory buffers
current_STA   = zeros( 1, length( trace_current ) );
current_LTA   = zeros( 1, length( trace_current ) );
current_STALTA = zeros( 1, length( trace_current ) );
current_RMS = zeros( 1, length( trace_current ) );

% Initialize STAs and LTAs: STA/LTA
current_STA( STA_length_millisec ) = ...
    sum( abs( trace_current( 1:STA_length_millisec ) ) );
current_LTA( LTA_length_millisec ) = ...
    sum( abs( trace_current( 1:LTA_length_millisec ) ) );

current_STALTA( LTA_length_millisec ) = ...
    ( current_STA( STA_length_millisec )/ STA_length_millisec ) / ...
    ( current_LTA( LTA_length_millisec ) / LTA_length_millisec );

% RMS
current_RMS( RMS_length_samples ) = ...
    sum( trace_current( 1:RMS_length_samples ).^2 );

% Compute STA, LTA
for i = STA_length_millisec + 1:length( trace_current )
     current_STA(i) = current_STA(i-1) + abs( trace_current(i) ) - ...
         abs( trace_current(i - STA_length_millisec) );
end;
current_STA = current_STA / STA_length_millisec;

for i = LTA_length_millisec + 1:length( trace_current )
     current_LTA(i) = current_LTA(i-1) + abs( trace_current(i) ) - ...
         abs( trace_current(i - LTA_length_millisec) );
end;
current_LTA = current_LTA / LTA_length_millisec;

for i = LTA_length_millisec : length( trace_current )
     current_STALTA(i) = current_STA(i) / current_LTA(i);
end;

% Compute RMS
for i = RMS_length_samples + 1:length( trace_current )
     current_RMS(i) = current_RMS(i-1) + trace_current(i).^2 - ...
         trace_current(i - RMS_length_samples).^2;
end

% Normalize RMSs by the RMS length
current_RMS = current_RMS / RMS_length_samples;

% Square-root
for i = 1:length( trace_current )
     current_RMS(i) = sqrt( current_RMS(i) );
end

figure( fh_STALTA_STA );
hold on
tmp_x = [0:1:length( current_STA )-1 ] ./ sampling_rate_Hz;
plot( tmp_x, current_STA / ( -max( current_STA ) ) + sns, 'b' );
hold off
```

```
    %   Init this variable only once
    if sns == sensor_index_high
        STA_2D = zeros( length( trace_current ), num_channels );
        LTA_2D = zeros( length( trace_current ), num_channels );
        STALTA_2D = zeros( length( trace_current ), num_channels );
        RMS_2D = zeros( length( trace_current ), num_channels );
    end

    % save STA/ LTA
    STA_2D(:, sns )     = current_STA;
    LTA_2D(:, sns )     = current_LTA;
    STALTA_2D(:, sns ) = current_STALTA;
    RMS_2D(:, sns )     = current_RMS;
end

xcorr_window_range = 0 : STALTA_loco_time_step_millisec : ...
    length( trace_current ) - 1 - LTA_length_millisec;

%   STA/LTA matrix
fh_figure_STALTA_raw = figure( 'Name', 'STA/LTA raw' );
STALTA_2D_clipped = STALTA_2D;
high_stalta_idx = find( STALTA_2D >= STALTA_display_threshold );
STALTA_2D_clipped( high_stalta_idx ) = STALTA_display_threshold;
imagesc( xcorr_window_range *sampling_rate_seconds, [ ...
    sensor_index_low:1:sensor_index_high ], STALTA_2D_clipped' );
title( [ 'STA/LTA' ] );
xlabel('seconds');
ylabel('Sensor ID');
colorbar('location','EastOutside') ;

%-----------------------------------------------------------------------
% Train detection
%
% ASSUMPTIONS:
% use a constant-length comparison time window
% use a constant comparison sensor
% INIT:
% init  reference_sns_idx;
% init  comparison_sns_idx;
% init sns2sns_meters = get_sns_distance_meters( reference_sns_idx,
%               comparison_sns_idx );

% 2D correlation matrix
% Lmax_TDA = zeros( time_scale, speed_scale);
% loop over the time
% for time= start_time: end_time
%     % if we are out of data on the reference sensor, exit
%     if time + window_length_sec > end_of_time
%         break;
%     end
%
%     % get the data segment
%     reference_data_segment = ...
%     get_windowed_trace( reference_sns_idx, time, time+window_length_sec)
%
%     % loop over the speeds
%     for speed_msec = speeds
```

```
%         % compute the sensor-to-sensor travel time
%         % if the time window exceed the available data, continue
%         % get the comparison data segment
%         % compute and store the L(max)
%     end speeds
% end time
%-----------------------------------------------------------------------

reference_trace_stalta = STALTA_2D( 1:STALTA_loco_time_step_millisec : ...
    end, reference_sns_idx );
comparison_trace_stalta = STALTA_2D( 1:STALTA_loco_time_step_millisec: ...
    end, comparison_sns_idx );

fig_STALTA_Loco = figure( 'Name', 'STA/LTA Locomotive Detection' );
hold on
plot( [ 1 : STALTA_loco_time_step_millisec : Last_sample_Idx ] * ...
    sampling_rate_seconds, reference_trace_stalta, 'b' );
plot( [ 1 : STALTA_loco_time_step_millisec : Last_sample_Idx ] * ...
    sampling_rate_seconds, comparison_trace_stalta, 'r' );
legend( ['Reference trace, ' reference_sns_name ], ...
    [ 'Comparison trace, ', comparison_sns_name ] );
xlabel('seconds');
ylabel('STA/LTA');
title('STA/LTA Locomotive Detection');
hold off

fig_RMS_STALTA_Loco = figure( 'Name', 'RMS Locomotive Detection' );
hold on
plot( [ 1 : STALTA_loco_time_step_millisec : Last_sample_Idx ] * ...
    sampling_rate_seconds, RMS_2D( 1: STALTA_loco_time_step_millisec : ...
    end, reference_sns_idx ), 'b' );

plot( [ 1 : STALTA_loco_time_step_millisec : Last_sample_Idx ] * ...
    sampling_rate_seconds, RMS_2D( 1: STALTA_loco_time_step_millisec : ...
    end, comparison_sns_idx ), 'r' );

legend( ['Reference trace, ' reference_sns_name ], [ ...
    'Comparison trace, ', comparison_sns_name ] );
xlabel('time, seconds');
ylabel( ['RMS, ', DATA_UNITS_STR ] );
title('RMS Locomotive Detection');
hold off

reversed_speed_range = [ Max_train_speed_mpsec : -speed_step_mpsec : ...
    Min_train_speed_mpsec ];

% ----------------------------------------------
% Locomotive noise detection using STA/LTA data
% NOTE: good for noiseless, consistent loco signal
% ----------------------------------------------
% Lmax_TIME_WINDOW = 15 seconds
%
% STA     = 1.0 sec
% LTA     = 5.0 sec
%
% For each time window, as it slides on in time
%
```

```
% Do the basic STA/LTA presence test on the Main trace:
%
%     - Max{STA/LTA} >= 3.2
%
%     - Min{STA/LTA} / Max{STA/LTA} < 0.5;
%
% For each speed value
%
%     - Select one comparison sensor: delta(T)(speed) > 3.0 seconds;
%
%     - Compute a comparison data segment
%
%     - Check that both the reference and the comparison segments:
%         = have STA/LTA > 3.2
%         = have Min{STA/LTA} / Max{STA/LTA} < 0.5;
%         = Max{ reference STA/LTA } / Max{ refer. STA/LTA} > 0.7 &&
%           Max{ refer. STA/LTA} / Max{ reference STA/LTA } > 0.7
%
%     - Compute Lmax{Main; Ref.} > 0.75;
%
%     - VERIFY THE SOLUITON
%
%         For speeds
%
%             = For the candidate speed, scan all sns in-between and
%                 ensure Lmax{ Main; Ref." } > 0.75;
%
%             = For the current speed, obtain one ref. sensor;
%
%             = Calculate max / min speeds for which the L(max) > 0.75;
%               their difference should not exceed ~ 3.0 meters/sec;
%
%     - CHECK PEAK PGV and Energy values

start_time_samples =  1;

Lmax_time_line_samples = start_time_samples : arrival_time_step_samples:...
    ( Last_sample_Idx - Lmax_window_length_samples );

Lmax_STALTA_west = ...
    zeros( length( Lmax_time_line_samples ), length( speed_range ) );
Lmax_STALTA_east = ...
    zeros( length( Lmax_time_line_samples ), length( speed_range ) );

min_LMax                = 1.0;
best_time_sec           = 0;
best_STALTA_speed_msec  = 0;

for train_direction_idx = 1:2
    start_time_idx     = 1;

    % MAIN STA/LTA LOCO DETECTION LOOP
    % loop over the time
    for tm = Lmax_time_line_samples
        window_end_time_samples = tm + Lmax_window_length_samples;

        % if we are out of data on the reference sensor, exit
```

```
if window_end_time_samples > Last_sample_Idx
    break;
end

reference_data_segment = STALTA_2D( tm: ...
    STALTA_subsampling_factor : window_end_time_samples, ...
    reference_sns_idx );

% Skip the zeroed precursor
min_reference_data_segment  = min( reference_data_segment );

if min_reference_data_segment == 0
     start_time_idx = start_time_idx + 1;
     continue;
end

% check min/max
max_reference_data_segment = max( reference_data_segment );

if min_reference_data_segment / max_reference_data_segment > ...
        Min_STALTA_Max_STALTA
     start_time_idx = start_time_idx + 1;
     continue;
end

if max_reference_data_segment < THRESHOLD_STALTA
     start_time_idx = start_time_idx + 1;
     continue;
end

% loop over the speeds
speed_idx = 1;

for speed_msec = speed_range
    % compute the time delay for a train to move from one sensor
    % to the other
    time_shift_samples = ...
       get_train_delay_samples( sampling_rate_Hz, speed_msec, ...
            train_search_dir_cells(train_direction_idx), ...
            reference_sns_idx, comparison_sns_idx, sensor_xy );

    time_shift_samples = int32( time_shift_samples );

    % if the time window exceed the available data, continue
    if tm + time_shift_samples > Last_sample_Idx
        speed_idx = speed_idx + 1;
        continue;
    end
    if tm + time_shift_samples < 1
        speed_idx = speed_idx + 1;
        continue;
    end
    if window_end_time_samples+time_shift_samples >Last_sample_Idx
        speed_idx = speed_idx + 1;
        continue;
    end
```

```
% get the comparison data segment
comparison_data_segment = ...
    STALTA_2D( (tm + time_shift_samples) : ...
    STALTA_subsampling_factor : (window_end_time_samples + ...
    time_shift_samples), comparison_sns_idx );


min_comparison_data_segment = min( comparison_data_segment );

if min_comparison_data_segment == 0
    speed_idx = speed_idx + 1;
    continue;
end

% check min/max
max_comparison_data_segment = max( comparison_data_segment );

if min_comparison_data_segment/max_comparison_data_segment>...
        Min_STALTA_Max_STALTA
     speed_idx = speed_idx + 1;
     continue;
end

if max_comparison_data_segment < THRESHOLD_STALTA
     speed_idx = speed_idx + 1;
     continue;
end

if max_comparison_data_segment/max_reference_data_segment < ...
        MAX_MainStaLta_to_MAX_RefStaLta
    speed_idx = speed_idx + 1;
    continue;
end

if max_reference_data_segment/max_comparison_data_segment < ...
        MAX_MainStaLta_to_MAX_RefStaLta
    speed_idx = speed_idx + 1;
    continue;
end

% truncate
if length( comparison_data_segment ) > ...
        length( reference_data_segment )
    comparison_data_segment(length(reference_data_segment )+...
        1:end) = [];
end
if length( reference_data_segment ) > ...
        length( comparison_data_segment )
    reference_data_segment(length(comparison_data_segment)+...
        1:end) = [];
end

% compute and store the L(max)
diff = max( reference_data_segment ./ ...
    max_reference_data_segment - comparison_data_segment ./ ...
    max_comparison_data_segment );
```

```
            diff = abs( diff );
            if diff > 1.0
                diff = 1.0;
            end

            if strncmp( 'WEST', ...
                    train_search_dir_cells(train_direction_idx), 4 )
                Lmax_STALTA_west( start_time_idx, speed_idx ) = 1.0 - diff;
            else
                Lmax_STALTA_east( start_time_idx, speed_idx ) = 1.0 - diff;
            end

            speed_idx = speed_idx + 1;

            if min_LMax > diff
                best_time_sec= tm * sampling_rate_seconds;
                best_STALTA_speed_msec = speed_msec;
                min_LMax = diff;
            end
        end % speeds
        start_time_idx = start_time_idx + 1;
    end % for time

    if normalize_color_bar
        if strncmp( 'WEST', train_search_dir_cells(train_direction_idx), 4 )
            Best_Lmax_STALTA_west = max( max( Lmax_STALTA_west, [], 2 ) );
            Lmax_STALTA_west( 1, 1 ) = maximum_xcorr_value;
        else
            Best_Lmax_STALTA_east = max( max( Lmax_STALTA_east, [], 2 ) );
            Lmax_STALTA_east( 1, 1 ) = maximum_xcorr_value;
        end
    end

    if strncmp( 'WEST', train_search_dir_cells(train_direction_idx), 4 )
        fh_figure_Lmax_STALTA_west = figure( 'Name', ...
            'L_m_a_x STA/LTA: westbound train' );
        imagesc( Lmax_time_line_samples .* sampling_rate_seconds, ...
            speed_range, Lmax_STALTA_west' );
        title([ 'Locomotive Detector: L_m_a_x STA/LTA (westbound train)']);
    else
        fh_figure_Lmax_STALTA_east = figure( 'Name', ...
            'L_m_a_x STA/LTA: eastbound train' );
        imagesc( Lmax_time_line_samples .* sampling_rate_seconds, ...
            speed_range, Lmax_STALTA_east' );
        title(['Locomotive Detector: L_m_a_x STA/LTA (eastbound train)']);
    end

    set(gca,'YDir','normal');
    ylabel('speed, meters/sec');
    xlabel('time, seconds');
    colorbar('location','EastOutside') ;
end % hypothetical train direction


%  Locomotive signal detection using RMS series with additional checks of
%  STA/LTA data
%  NOTE: good for noisy (e.g. rail joints) data
```

```
%
% Lmax_TIME_WINDOW = 15 seconds
%
% Test speed > 5 m/sec:
% STA     = 1.0 sec
% LTA     = 5.0 sec
% RMS     = 0.2 sec
%
% Test speed < 5 m/sec:
% STA     = 2.0 sec
% LTA     = 10.0 sec
% RMS     = 1.0 sec
%
% For each time window, as it slides on in time
% Do the basic STA/LTA presence test on the Main trace:
%     - Max{STA/LTA} >= 3.2
%     - the STA/LTA peak is > 2.0 sec old
%     - Min RMS/Max RMS > 0.2 (there's significant signal change)
%
% For each speed value
%     - Select one comparison sensor: delta(T)(speed) > 3.0 seconds;
%     - Compute a comparison data segment
%     - Check that both the reference and the comparison segments:
%         = Have STA/LTA > 3.2
%         != the STA/LTA peak is > 2.0 sec old
%         = Min RMS/Max RMS > 0.2 (there's significant signal change)
%
%     - Compute Lmax{Main RMS; Ref. RMS} > 0.65;
%     - VERIFY THE SOLUITON
%
%         = For the candidate speed, calculate Max RMS for all
%           comparison sensors, as well as for the Main Sensor;
%
%         = For speeds
%
%             == For the candidate speed, scan all sns in-between and
%                ensure Lmax{ Main; Ref." } > 0.65;
%
%             == For the current speed, obtain one ref. sensor;
%
%             == Make sure L(max){RMS} test passes for all comparison
%             sensors IN-BETWEEN
%
%             == L(max)-compare the signals; the signals must be normalized
%                using the prev. calculated Max{RMS}
%
%             == Calculate max / min speeds for which the L(max) > 0.75;
%                their difference should not exceed ~ 5.0 meters/sec;
%
%     - CHECK PEAK PGV and Energy values
Lmax_RMS_west = zeros(length(Lmax_time_line_samples),length( speed_range));
Lmax_RMS_east = zeros(length(Lmax_time_line_samples),length( speed_range));

best_rms_norm = 0;
for train_direction_idx = 1:2
    start_time_idx     = 1;
```

```
%    MAIN RMS LOCO DETECTION LOOP
% loop over the time
for tm = Lmax_time_line_samples

    window_end_time_samples = tm + Lmax_window_length_samples;

    % if we are out of data on the reference sensor, exit
    if window_end_time_samples > Last_sample_Idx
        break;
    end

    % Get STA/LTA
    reference_STALTA_data_segment = STALTA_2D( tm: ...
        STALTA_subsampling_factor : window_end_time_samples, ...
        reference_sns_idx );

    % Get RMS
    reference_RMS_data_segment = RMS_2D( tm: ...
        STALTA_subsampling_factor : window_end_time_samples, ...
        reference_sns_idx );

    % Skip the zeroed precursor
    min_reference_STALTA_data_segment  = ...
        min( reference_STALTA_data_segment );

    if min_reference_STALTA_data_segment == 0
         start_time_idx = start_time_idx + 1;
         continue;
    end

    % check min/max STA/LTA
    max_reference_STALTA_data_segment = ...
            max( reference_STALTA_data_segment );

    if max_reference_STALTA_data_segment < THRESHOLD_STALTA
         start_time_idx = start_time_idx + 1;
         continue;
    end

    % make sure the STA/LTA peak is 2 sec old
    high_stalta_idx = find( reference_STALTA_data_segment >= ...
        max_reference_STALTA_data_segment );
    stalta_peak_seconds = sampling_rate_seconds * ...
        STALTA_subsampling_factor * ...
                ( length( reference_STALTA_data_segment ) - ...
                max( high_stalta_idx ) + 1 );

    if stalta_peak_seconds < Min_STALTA_peak_age_seconds
         start_time_idx = start_time_idx + 1;
         continue;
    end

    % Check min/max RMS
    max_reference_RMS_data_segment = max( reference_RMS_data_segment);
    min_reference_RMS_data_segment = min( reference_RMS_data_segment);

    if min_reference_RMS_data_segment/ ...
```

```
        max_reference_RMS_data_segment > Min_RMS_Max_RMS
     start_time_idx = start_time_idx + 1;
     continue;
end

%  Obtain Max RMS for  the best speed  best_STALTA_speed_msec
%  compute the time delay for a train to move from one sensor to
%  the other
time_shift_samples = get_train_delay_samples( ...
        sampling_rate_Hz, best_STALTA_speed_msec, ...
        train_search_dir_cells(train_direction_idx), ...
        reference_sns_idx, comparison_sns_idx, sensor_xy );

time_shift_samples = int32( time_shift_samples );

% if the time window exceed the available data, stop the test
if tm + time_shift_samples > Last_sample_Idx
    break;
end
if tm + time_shift_samples < 1
    start_time_idx = start_time_idx + 1;
    continue;
end
if window_end_time_samples + time_shift_samples > Last_sample_Idx
    break;
end

% make sure the STA/LTA peak is 2 sec old on the comparison sns
comparison_STALTA_data_segment = ...
    STALTA_2D((tm+time_shift_samples):STALTA_subsampling_factor ...
        : (window_end_time_samples + time_shift_samples), ...
        comparison_sns_idx );

high_stalta_idx = find(comparison_STALTA_data_segment == ...
    max( comparison_STALTA_data_segment ) );

stalta_peak_seconds = sampling_rate_seconds * ...
    STALTA_subsampling_factor * ...
    ( length( comparison_STALTA_data_segment ) - ...
    max( high_stalta_idx ) + 1 );

if stalta_peak_seconds < Min_STALTA_peak_age_seconds
     start_time_idx = start_time_idx + 1;
     continue;
end

comparison_RMS_data_segment = ...
    RMS_2D( (tm + time_shift_samples) : ...
        STALTA_subsampling_factor : (window_end_time_samples + ...
        time_shift_samples), comparison_sns_idx );

BestSpeed_MaxRMS_comparison = max( comparison_RMS_data_segment );

% loop over the speeds
speed_idx = 1;

for speed_msec = speed_range
```

```
% compute the time delay for a train to move from one
% sensor to the other
time_shift_samples = ...
   get_train_delay_samples( sampling_rate_Hz, speed_msec, ...
        train_search_dir_cells(train_direction_idx), ...
        reference_sns_idx, comparison_sns_idx, sensor_xy );

time_shift_samples = int32( time_shift_samples );

% if the time window exceed the available data, continue
if tm + time_shift_samples > Last_sample_Idx
    speed_idx = speed_idx + 1;
    continue;
end
if tm + time_shift_samples < 1
    speed_idx = speed_idx + 1;
    continue;
end
if window_end_time_samples + time_shift_samples>Last_sample_Idx
    speed_idx = speed_idx + 1;
    continue;
end

% get the comparison data segment
comparison_RMS_data_segment = ...
    RMS_2D( (tm + time_shift_samples) : ...
    STALTA_subsampling_factor : (window_end_time_samples + ...
        time_shift_samples), comparison_sns_idx );

comparison_STALTA_data_segment = ...
    STALTA_2D( (tm + time_shift_samples) : ...
    STALTA_subsampling_factor : (window_end_time_samples + ...
    time_shift_samples), comparison_sns_idx );


% check min/max STA/LTA
max_comparison_STALTA_data_segment = ...
    max( comparison_STALTA_data_segment );
min_comparison_STALTA_data_segment = ...
    min( comparison_STALTA_data_segment );

if max_comparison_STALTA_data_segment < THRESHOLD_STALTA
     speed_idx = speed_idx + 1;
     continue;
end

% check RMS
max_comparison_RMS_data_segment = ...
    max( comparison_RMS_data_segment );
min_comparison_RMS_data_segment = ...
    min( comparison_RMS_data_segment );

if min_comparison_RMS_data_segment/ ...
        max_comparison_RMS_data_segment > Min_RMS_Max_RMS
     speed_idx = speed_idx + 1;
     continue;
end
```

```
            % truncate
            if length( comparison_RMS_data_segment ) > ...
                    length( reference_RMS_data_segment )
                comparison_RMS_data_segment(length( ...
                    reference_RMS_data_segment ) + 1:end) = [];
            end
            if length( reference_RMS_data_segment ) > ...
                    length( comparison_RMS_data_segment )
                reference_RMS_data_segment(length( ...
                    comparison_RMS_data_segment ) + 1:end) = [];
            end

            diff = ...
    max( reference_RMS_data_segment ./ max_reference_RMS_data_segment - ...
             comparison_RMS_data_segment ./ BestSpeed_MaxRMS_comparison );

            diff = abs( diff );
            if diff > 1.0
                diff = 1.0;
            end

            if strncmp( 'WEST', ...
                    train_search_dir_cells(train_direction_idx), 4 )
                Lmax_RMS_west( start_time_idx, speed_idx ) = 1.0 - diff;
            else
                Lmax_RMS_east( start_time_idx, speed_idx ) = 1.0 - diff;
            end

            if best_rms_norm < 1.0 - diff
                best_rms_norm = 1.0 - diff;
                best_rms_speed = speed_msec;
            end

            speed_idx = speed_idx + 1;
        end % for speed

        start_time_idx = start_time_idx + 1;
    end % for time

    if normalize_color_bar
        if strncmp( 'WEST', train_search_dir_cells(train_direction_idx), 4)
            Best_Lmax_RMS_west = max( max( Lmax_RMS_west, [],2 ) );
            Lmax_RMS_west( 1, 1 ) = maximum_xcorr_value;
        else
            Best_Lmax_RMS_east = max( max( Lmax_RMS_east, [],2 ) );
            Lmax_RMS_east( 1, 1 ) = maximum_xcorr_value;
        end
    end

    if strncmp( 'WEST', train_search_dir_cells(train_direction_idx), 4 )
fh_figure_Lmax_RMS_west = figure( 'Name', 'L_m_a_x RMS (westbound train)');
imagesc( Lmax_time_line_samples .* sampling_rate_seconds, speed_range, ...
            Lmax_RMS_west');
title( [ 'Locomotive Detector: L_m_a_x RMS (westbound train)' ] );
    else
fh_figure_Lmax_RMS_east = figure( 'Name', 'L_m_a_x RMS (eastbound train)');
```

```
imagesc( Lmax_time_line_samples .* sampling_rate_seconds, speed_range, ...
            Lmax_RMS_east' );
title( [ 'Locomotive Detector: L_m_a_x RMS (eastbound train)' ] );
    end

    set(gca,'YDir','normal');
    ylabel('speed, meters/sec');
    xlabel('time, seconds');
    colorbar('location','EastOutside') ;
end % train direction


%
% save the figures here
%
if save_figures_automatically
    [pathstr,name,ext] = fileparts(FILE_name1);

    subfolder_full_name = [ destination_folder, destination_subfolder, ...
        name, '_', reference_sns_name, comparison_sns_name, '\' ];
    mkdir( subfolder_full_name );

    % RAW data
    figure( fh_FilteredData );
    xLimits = get( gca, 'XLim' );
    axis( [ xLimits(1) xLimits(2) raw_data_min raw_data_max ] );
    saveas( fh_FilteredData, [ subfolder_full_name, raw_data_file_name, ...
        graphic_format_ext ] );

    clear fh_FilteredData;

    figure( fh_STALTA_STA );
    xLimits = get( gca, 'XLim' );
    axis( [ xLimits(1) xLimits(2) raw_data_min raw_data_max ] );
    saveas( fh_STALTA_STA, [ subfolder_full_name, ...
        sta_smoothed_data_file_name, graphic_format_ext ] );

    clear fh_STALTA_STA;

    saveas( fh_figure_STALTA_raw, [ subfolder_full_name, ...
        full_stalta_data_file_name, graphic_format_ext ] );
    saveas( fh_figure_STALTA_raw, [ subfolder_full_name, ...
        full_stalta_data_file_name, MATLAB_format_ext ] );
    clear  fh_figure_STALTA_raw;

    saveas( fig_STALTA_Loco, [ subfolder_full_name, ...
        sns_stalta_data_file_name, graphic_format_ext ] );
    clear  fh_figure_STALTA_raw;

    saveas( fig_RMS_STALTA_Loco, [ subfolder_full_name, ...
        sns_rms_data_file_name, graphic_format_ext ] );
    clear  fig_RMS_STALTA_Loco;

    saveas( fh_figure_Lmax_STALTA_west, [ subfolder_full_name, ...
        stalta_Lmax_file_name, '_WEST', graphic_format_ext ] );
    clear  fh_figure_Lmax_STALTA_west;
```

```
    saveas( fh_figure_Lmax_STALTA_east, [ subfolder_full_name, ...
        stalta_Lmax_file_name, '_EAST', graphic_format_ext ] );
    clear  fh_figure_Lmax_STALTA_east;


    saveas( fh_figure_Lmax_RMS_west, [ subfolder_full_name, ...
        rms_Lmax_file_name, '_WEST', graphic_format_ext ] );
    clear  fh_figure_Lmax_RMS_west;

    saveas( fh_figure_Lmax_RMS_east, [ subfolder_full_name, ...
        rms_Lmax_file_name, '_EAST', graphic_format_ext ] );
    clear  fh_figure_Lmax_RMS_east;

    %  Save the data procesing parameters
    fileID=fopen([subfolder_full_name, DataProcessingParametersFile ],'w');

    % Source data
    fprintf( fileID, 'Source folder   = %s\r\n', DIR_name );
    fprintf( fileID, 'Source file #1  = %s\r\n\r\n', FILE_name1 );

    % Dump the STA/LTA parameters
    fprintf( fileID, 'RMS_length_seconds             = %3.1f\r\n', ...
        RMS_length_seconds );
    fprintf( fileID, 'STA/LTA: STA_length_millisec   = %3d\r\n', ...
        STA_length_millisec );
    fprintf( fileID, 'STA/LTA: LTA_length_millisec   = %3d\r\n', ...
        LTA_length_millisec );
    fprintf( fileID, 'Lmax_window_length_sec         = %3.1f\r\n', ...
        Lmax_window_length_sec );
    fprintf( fileID, 'Reference sensor               = %s\r\n', ...
        reference_sns_name );
    fprintf( fileID, 'Comparison sensor              = %s\r\n', ...
        comparison_sns_name );
    fprintf( fileID, 'Best STALTA speed, m/s         = %3.1f\r\n', ...
        best_STALTA_speed_msec );
    fprintf( fileID, 'Best RMS speed, m/s            = %3.1f\r\n', ...
        best_rms_speed );
    fprintf( fileID, 'Best L(max) STALTA, percent    = %3.1f\r\n', ...
        100*max(Best_Lmax_STALTA_west, Best_Lmax_STALTA_east) );
    fprintf( fileID, 'Best L(max) RMS, percent       = %3.1f\r\n', ...
        100*max(Best_Lmax_RMS_west, Best_Lmax_RMS_east) );
    fclose(fileID);
end


% ************************************************************************
% NAME:     get_train_delay_samples
% PURPOSE:  Returns sensor-to-sensor travel time
%
% INPUT:    sampling_rate  - in seconds
%           cur_speed      - m/s
%           direction      - 'WEST' | 'EAST'
%           compar_sns_idx - comparison sns index
%           refer_sns_idx  - reference sensor index
%           sensors_xy     - array of sensor coordinates
% OUTPUT:   delay_samples  - delay btw compar_sns_idx and refer_sns_idx
% ************************************************************************
```

```
function [ delay_samples ] = ...
       get_train_delay_samples( sampling_rate, cur_speed, ...
          train_search_dir, refer_sns_idx, compar_sns_idx, sensors_xy )
x1 = sensors_xy(compar_sns_idx).x;
y1 = sensors_xy(compar_sns_idx).y;
x2 = sensors_xy(refer_sns_idx).x;
y2 = sensors_xy(refer_sns_idx).y;

delay_samples = sqrt((x1-x2)*(x1-x2) + (y1-y2)*(y1-y2)) ...
    / cur_speed * sampling_rate;

if( compar_sns_idx > refer_sns_idx )
    if ( strcmp( train_search_dir, 'WEST' ) == 1 )
        delay_samples = - delay_samples;
    end
end

if( compar_sns_idx < refer_sns_idx )
    if( strcmp( train_search_dir, 'EAST' ) == 1 )
        delay_samples = - delay_samples;
    end
end


% ************************************************************************
% NAME:      get_site_sensor_xy
% PURPOSE:   Return (X;Y) coordinates of a sensor
% INPUT:     site_ID - unique site name, e.g. 'white_canyon', 'hope'
%            sns_name - sensor ID, e.g. 'Z01', 'Z02'
% OUTPUT:    sensor coordinates
% ************************************************************************
function [ x, y ] = get_site_sensor_xy( site_ID, sns_name )

if( strcmpi( site_ID, 'white_canyon' ) )
switch upper( sns_name )
    case 'Z01'
        x = 12.80;    y = 197.36;
        return
    case 'Z02'
        x = 18.60;    y = 178.59;
        return
    case 'Z03'
        x = 22.91;    y = 159.12;
        return
    case 'Z04'
        x = 25.71;    y = 138.79;
        return
    case 'Z05'
        x = 26.98;    y = 121.40;
        return
    case 'Z06'
        x = 27.35;    y = 104.25;
        return
    case 'Z07'
        x = 26.86;    y = 87.17;
        return
    case 'Z08'
```

```
    x = 26.29;    y = 70.54;
    return
case 'Z09'
    x = 24.77;    y = 53.90;
    return
case 'Z10'
    x = 22.50;    y = 34.17;
    return
 case 'Z11'
     x = 19.81;    y = 17.65;
    return
 case 'Z12'
     x = 16.90;    y = 1.88;
    return
 case 'Z13'
     x = 15.56;    y = -5.83;
    return
 case 'Z14'
     x = 10.06;    y = -27.69;
    return
 case 'Z15'
     x = 5.07;    y = -44.97;
    return
 case 'Z16'
     x = -1.78;    y = -64.98;
    return
 case 'Z17'
     x = -10.06;    y = -83.95;
    return
 case 'Z18'
     x = -17.21;    y = -100.04;
    return
 case 'Z19'
     x = -25.77;    y = -116.79;
    return
 case 'Z20'
     x = -34.21;    y = -131.13;
    return
 case 'Z21'
     x = -46.21;    y = -149.29;
    return
 case 'Z22'
     x = -57.81;    y = -164.79;
    return
 case 'Z23'
     x = -70.27;    y = -180.32;
    return
 case 'Z24'
     x = -81.70;    y = -193.23;
    return
 case 'Z25'
     x = -97.37;    y = -208.39;
    return
 case 'Z26'
     x = -111.45;    y = -221.53;
    return
 case 'Z27'
```

```
    x = -126.14;    y = -234.30;
   return
case 'Z28'
    x = -134.97;    y = -242.07;
   return
case 'Z29'
    x = -144.46;    y = -249.89;
   return
case 'Z30'
    x = -154.11;    y = -258.21;
   return
case 'Z31'
    x = -161.45;    y = -264.10;
   return
case 'Z32'
    x = -168.08;    y = -269.40;
   return
case 'Z33'
    x = -192.58;    y = -284.20;
   return
case 'Z34'
    x = -205.44;    y = -293.68;
   return
case 'Z35'
    x = -215.16;    y = -300.54;
   return
case 'Z36'
    x = -227.82;    y = -308.91;
   return
case 'Z37'
    x = -239.05;    y = -316.71;
   return
case 'Z38'
    x = -249.72;    y = -323.45;
   return
case 'Z39'
    x = -267.17;    y = -334.33;
   return
case 'Z40'
    x = -280.59;    y = -342.13;
   return
case 'Z41'
    x = -294.26;    y = -349.77;
   return
case 'Z42'
    x = -308.24;    y = -356.69;
   return
case 'Z43'
    x = -322.57;    y = -363.35;
   return
case 'Z44'
    x = -333.84;    y = -368.59;
   return
case 'Z45'
    x = -354.92;    y = -378.39;
   return
case 'Z46'
```

```
    x = -365.18;    y = -383.16;
   return
case 'Z47'
    x = -377.06;    y = -387.93;
   return
case 'Z48'
    x = -390.67;    y = -393.41;
   return
case 'Z49'
    x = -403.30;    y = -398.29;
   return
case 'Z50'
    x = -412.78;    y = -401.60;
   return
case 'Z51'
    x = -426.01;    y = -406.41;
   return
case 'Z52'
    x = -439.58;    y = -411.11;
   return
case 'Z53'
    x = -452.82;    y = -415.10;
   return
case 'Z54'
    x = -466.51;    y = -418.82;
   return
case 'Z55'
    x = -481.04;    y = -422.50;
   return
case 'Z56'
    x = -495.44;    y = -426.00;
   return
case 'Z57'
    x = -510.50;    y = -428.95;
   return
case 'Z58'
    x = -525.23;    y = -431.34;
   return
case 'Z59'
    x = -540.03;    y = -433.50;
   return
case 'Z60'
    x = -554.83;    y = -435.69;
   return
case 'Z61'
    x = -570.00;    y = -437.42;
   return
case 'Z62'
    x = -585.05;    y = -439.03;
   return
case 'Z63'
    x = -599.45;    y = -441.57;
   return
case 'Z64'
    x = -614.13;    y = -444.82;
   return
case 'Z65'
```

```
        x = -628.28;    y = -449.07;
       return
     case 'Z66'
        x = -642.26;    y = -453.62;
       return
     case 'Z67'
        x = -656.80;    y = -458.88;
       return
     case 'Z68'
        x = -669.47;    y = -465.75;
       return

    otherwise
       disp(['***ERROR::get_sensor_XY(). Bad sensor name!' ]);
end; % switch
end; % if


if( strcmpi( site_ID, 'hope' ) )
switch upper( sns_name )
    case 'Z01'
       x = 12.20;    y = 322.5;
       return
    case 'Z02'
       x = 8.60;    y = 308;
       return
    case 'Z03'
       x = 3.2;    y = 294.3;
       return
    case 'Z04'
       x = 0.2;    y = 280.0;
       return
    case 'Z05'
       x = -1.9;    y = 265.4;
       return
    case 'Z06'
       x = -1.6;    y = 250.6;
       return
    case 'Z07'
       x = -1.6;    y = 235.9;
       return
    case 'Z08'
       x = -1.0;    y = 221.3;
       return
    case 'Z09'
       x = -1.1;    y = 206.5;
       return
    case 'Z10'
       x = -0.7;    y = 192.0;
       return
     case 'Z11'
        x = -0.2;    y = 177.4;
       return
     case 'Z12'
        x = 0.5;    y = 162.9;
       return
     case 'Z13'
```

```
        x = 0.7;    y = 148.4;
       return
    case 'Z14'
        x = -0.6;    y = 133.8;
       return
    case 'Z15'
        x = -1.1;    y = 118.7;
       return
    case 'Z16'
        x = -2.1;    y = 104.7;
       return
    case 'Z17'
        x = -3.4;    y = 90.2;
       return
    case 'Z18'
        x = -4.3;    y = 75.7;
       return
    case 'Z19'
        x = -4.7;    y = 61.0;
       return
    case 'Z20'
        x = -4.8;    y = 46.4;
       return
    case 'Z21'
        x = -3.5;    y = 31.8;
       return
    case 'Z22'
        x = -1.5;    y = 17.1;
       return
    case 'Z23'
        x = 1.3;    y = 2.9;
       return
    case 'Z24'
        x = 4.8;    y = -11.2;
       return
    case 'Z25'
        x = 9.3;    y = -25.0;
       return
    case 'Z26'
        x = 14.0;    y = -39.0;
       return
    case 'Z27'
        x = 19.0;    y = -52.7;
       return

   otherwise
       disp(['***ERROR::get_site_sensor_xy(). Bad sensor name!' ]);
end; % switch
end; % if

%-----------------------------------------------------------------
% NAME: notch_filter
%-----------------------------------------------------------------
function [ y ] = notch_filter( x, sampling_rate, Notch_Hz )
trace_in = x;

for i = 1:length( Notch_Hz )
```

```
    w0_60 = Notch_Hz(i) / ( sampling_rate / 2 );

    bw_60 = w0_60/35;       % set the Q factor for the filter to 35

    [num,den] = iirnotch( w0_60, bw_60 );
    y = filter( num, den, trace_in);

    if( i < length( Notch_Hz ) )
       trace_in = y;
    end
end
```

B.6. Matlab implementation of the rockfall detector algorithms

```
% ************************************************************************
% NAME:     stalta_zlcc_rockfall_detectors
%
% PURPOSE:  Demonstration of two algorithms which detect rockfall
%           patterns within a seismic array data:
%
%           1) The first one is based on estimation of the density of
%                 high short term/ long term average (STA/LTA) within a
%                 time window; and
%           2) The second one computes the array trigger based on
%               by-element product of STA/LTA and Zero Lag
%               Cross-Correlation (ZLCC);
%
%           After a rockfall pattern has been detected, a Peak Ground
%           Velocity (PGV) threshold model is applied witin the array
%           trigger in order to differentiate hazardous rocks from false
%           alarms
%
% INPUT:    IN_site_ID - alphanumeric ID of a test site, e.g.
%               'white_canyon' which is needed to find sensor coordinates,
%               etc.
%
%           IN_FILE_name1,  IN_FILE_name2 - names of data files in *.csv
%               format. The first column contains the timing in
%               seconds, e.g. 0.0, 0.001; the rest of the columns
%               contain traces stored in  binary counts of A/D board
%
%           IN_DIR_name - directory where IN_FILE_name1 & IN_FILE_name2 are
%
%           IN_sensor_index_low, IN_sensor_index_high - upper and lower
%               indexes of the seismic array to be processed;
%
%           IN_destination_folder - the directory where output *.jpeg,
%               *.png etc images should be stored. It does not have to
%               exist
%
%           IN_destination_subfolder - a subdirectory under
%               IN_destination_folder
%
%           IN_concatenate_traces - TRUE if the traces in IN_FILE_name1,
%               IN_FILE_name2 must be concatenated
%
% OUTPUT:   rockfall_locations_xy - vector of (X;Y) locations that
%                          match the amplitude model
%           rockfall_detected     - TRUE is a rockfall has been detected
%
% AUTHOR:   Bohdan Nedilko <bohdan.nedilko@alumni.ubc.ca>
%
% DATE:     February 2016
%           This code was tested under Matlab R2008b
% ************************************************************************
function stalta_zlcc_rockfall_detectors_disser( IN_site_ID, ...
                   IN_FILE_name1,  IN_FILE_name2, ...
                   IN_DIR_name, ...
```

```
                    IN_sensor_index_low, IN_sensor_index_high,  ...
                    IN_destination_folder, ...
                    IN_destination_subfolder, IN_concatenate_traces )
close all

% Zero Lag Cross Correlation

FontSizeTitle  = 9;
FontSizeYLabel = 9;
FontSizeXLabel = 9;
FontSizeAxes   = 9;
LineWidthAxes  = 1;
ColorBarLeft = 0.90;

white_canyon_BC2EU = 0.0000000151281;
hope_BC2EU = white_canyon_BC2EU;

white_canyon_channel_permutation = [ ...
  12 11 10 9 8 7 6 5 4 3 2 1 32 31 30 29 28 27 26 25 24 23 22 21 20 ...
  19 18 17 16 15 14 13 33 45 34 46 35 47 36 48 37 49 38 50 39 51 40 ...
  52 41 53 42 54 43 55 44 56 57 63 58 64 59 65 60 66 61 67 62 68 ...
];

% PGV model, peak velocity vs distance (Squamish site)
pgv_threshold(1).d   = 5.0;
pgv_threshold(1).pgv = 0.00021179;

pgv_threshold(2).d   = 18.3;
pgv_threshold(2).pgv = 0.00004841;

pgv_threshold(3).d   = 31.6;
pgv_threshold(3).pgv = 0.00003479;

pgv_threshold(4).d   = 45;
pgv_threshold(4).pgv = 0.00000575;

site_ID = IN_site_ID;

% Uncomment this in order to
% fix the default colrmap issue: MatLab 2008b vs 2014
% set( groot, 'DefaultFigureColormap', jet(64));

% reduce the plot margin
reduce_the_plot_margin     = true;
left_margin_image          = 0.08;
right_margin_image         = 0.14;
left_margin_trace          = 0.08;
right_margin_trace         = 0.03;


FILE_name1          = IN_FILE_name1;
FILE_name2          = IN_FILE_name2;
DIR_name            = IN_DIR_name;

sensor_index_low      = IN_sensor_index_low;
sensor_index_high     = IN_sensor_index_high;
destination_subfolder = IN_destination_subfolder;
```

```
destination_folder    = IN_destination_folder;
concatenate_traces    = IN_concatenate_traces;

[pathstr,file_name,file_ext] = fileparts(FILE_name1);

show_EastWest_ZLCC                = false;
show_ZLCC_smoothed_source_data    = true;
show_ZLCC_correlated_pairs        = false;

% Notch Filter frequencies, Hertz
Apply_x60Hz               = true;
Notch_Hz                  = [ 60 ];

%    Color bar options
normalize_color_bar     = true;
maximum_xcorr_value     = 1.0;

replace_negative_xcorr_with_zero = true;

%-------------------------------------------
% ZLCC parameters
%-------------------------------------------
ZLCC_smoothing_length_samples  = 50;
ZLCC_subsampling_factor        = 5;
ZLCC_time_step_millisec        = 100;
ZLCC_time_step_sec             = ZLCC_time_step_millisec / 1000;
ZLCC_window_length_millisec    = 5000;
ZLCC_min_number_xcorr_samples  = ZLCC_window_length_millisec * 0.5;

% ZLCC weights
ZLCC_num_comparison_sensors = 1;

% STA/LTA parameters
STA_length_millisec    = 50;
LTA_length_millisec    = 5000;
STALTA_display_threshold  = 4.001;

STALTA_strong_threshold  = 4.0;
STALTA_weak_threshold    = 3.0;

rail_joint_precursor_meters        = 250.0;
average_sensor_distance_meters     = 18.0;
stalta_trigger_series_window_cells = 7;

% define the window using an integer number of <ZLCC_window_length_sec>
STALTA_percent_fill_window_sec    = 5 * ZLCC_time_step_sec;
STALTA_percent_fill_window_cells  = STALTA_percent_fill_window_sec / ...
    ZLCC_time_step_sec;

STALTA_percentage_fill_threshold = 50;

% open data file as a *.csv  file
csv_01 = csvread( [ DIR_name, FILE_name1 ]);
csv_02 = csvread( [ DIR_name, FILE_name2 ]);

% compute sampling rate
sampling_rate_seconds = csv_01(2,1) - csv_01(1,1);
```

```
csv_01 = csv_01(:,2:end);
csv_02 = csv_02(:,2:end);
if( strcmp( IN_site_ID, 'white_canyon' ) == 1 )
    csv_01 = csv_01(:,white_canyon_channel_permutation)';
    csv_02 = csv_02(:,white_canyon_channel_permutation)';
else
    if( strcmp( IN_site_ID, 'hope' ) == 1 )
        csv_01 = csv_01';
        csv_02 = csv_02';
    end
end

if concatenate_traces
   src_traces = [ white_canyon_BC2EU*csv_01 white_canyon_BC2EU*csv_02 ];
else
   src_traces = white_canyon_BC2EU*csv_01;
end

sampling_rate_Hz = 1.0 / sampling_rate_seconds;
time_idx2sample_idx = ZLCC_time_step_millisec*0.001*sampling_rate_Hz;

[ m,n ] = size( src_traces );
Last_sample  = n;
num_channels = m;
max_time_sec = (Last_sample - 1)*sampling_rate_seconds;


% remove DC and 60 Hz
for idx=1:num_channels
    src_traces(idx, :) = src_traces(idx, :) - mean(src_traces(idx, :));

    % notch-filter the data
    if Apply_x60Hz
        src_traces(idx, :) = notch_filter( src_traces(idx, :), ...
            sampling_rate_Hz, Notch_Hz );
    end
end

% compute rockfall detection parameters
time_window_seconds = 2.0;
time_window_samples = time_window_seconds * sampling_rate_Hz;


% Read in sensors' coordinates
sensor_xy = [];
% populate the array of sensor coodinates
for sns = 1:num_channels
    sns_name  = sprintf( 'Z%02d', sns );
    [ sns_x, sns_y ] = get_site_sensor_xy( site_ID, sns_name );

    if( strcmp( IN_site_ID, 'hope' ) == 1 )
        % swap x and y fore better looks
        sensor_xy(sns).x = sns_y;
        sensor_xy(sns).y = sns_x;
    else
        sensor_xy(sns).x = sns_x;
```

```
        sensor_xy(sns).y = sns_y;
    end
end


f_sns = figure('Name', 'Sensors (E,N)');
hold on
for sns_idx=1:num_channels
    scatter( sensor_xy(sns_idx).x, sensor_xy(sns_idx).y, 'o', ...
              'MarkerEdgeColor', [ 0, 0, 1.0 ],...
              'MarkerFaceColor', [ 0, 0, 1.0 ] );
end
hold off
title({'Detected rockfall locations (if any):', ...
        'Red dots (STA/LTA*ZLCC algorithm)', ...
        'Green dots (STA/LTA density count)'});
ylabel('Y, meters')
xlabel('X, meters');

% init. figures
fh_FilteredData = figure( 'Name', 'Filtered data' );
set(gca,'FontSize',FontSizeAxes,'LineWidth', LineWidthAxes);
title( [ strrep(file_name, '_', '-') ], 'FontSize', FontSizeTitle );
set(gca,'YDir', 'reverse');
ylabel('Sensor ID', 'FontSize', FontSizeYLabel)
xlabel('seconds', 'FontSize', FontSizeXLabel);

raw_data_max = -realmax;
raw_data_min = realmax;

if show_ZLCC_smoothed_source_data
    fh_ZLCC_source_data = figure( 'Name', 'RMS' );
    set(gca,'FontSize',FontSizeAxes,'LineWidth', LineWidthAxes);
    title( 'RMS-smoothed seismic data', 'FontSize', FontSizeTitle );
    set(gca,'YDir', 'reverse');
    ylabel('Sensor ID', 'FontSize', FontSizeYLabel);
    xlabel('seconds', 'FontSize', FontSizeXLabel);
end

fh_STALTA_STA = figure( 'Name', 'STA/LTA:  STA' );
set(gca,'FontSize',FontSizeAxes,'LineWidth', LineWidthAxes);
title( 'STA/LTA:  STA', 'FontSize', FontSizeTitle );
set(gca,'YDir', 'reverse');
ylabel('Sensor ID', 'FontSize', FontSizeYLabel);
xlabel('seconds', 'FontSize', FontSizeXLabel);

% normal STA/LTA view (not color-coded)
fh_STALTA_STALTA = figure( 'Name', 'STA/LTA' );
set(gca,'FontSize',FontSizeAxes,'LineWidth', LineWidthAxes);
title( 'STA/LTA', 'FontSize', FontSizeTitle );
set(gca,'YDir', 'reverse');
ylabel('Sensor ID', 'FontSize', FontSizeYLabel);
xlabel('seconds', 'FontSize', FontSizeXLabel);

%-------------------------------------------------------------------------
% Scan sensors sensor_index_high to sensor_index_low
%
```

```
% Compute STA/LTA, and zero-lag cross-correlate pairs of r.m.s.-averaged
%    signals acquired ad adjacent sensors (ZLCC)
for sns = sensor_index_high:-1:sensor_index_low

    %  Correlate the current trace with the west neighbour
    sns_next_idx = sns - 1;
    next_trace_available = ( sns_next_idx > 0 );

    % get trace #1 and #2
    trace_current = src_traces( sns, :);

    if next_trace_available
        trace_next = src_traces( sns_next_idx, :);
    end

    % Plot the source data ( filtered and DC-corrected )
    figure( fh_FilteredData );
    hold on
    tmp_x = [ 0:1:length( trace_current ) - 1 ] ./ sampling_rate_Hz;
    tmp_y = trace_current / ( -max( trace_current )) + sns;
    plot( tmp_x, tmp_y, 'b' );
    hold off

    % store max/min for plot scaling
    max_tmp_y = max( tmp_y );
    min_tmp_y = min( tmp_y );
    if raw_data_max < max_tmp_y
        raw_data_max = max_tmp_y;
    end;
    if raw_data_min > min_tmp_y
        raw_data_min = min_tmp_y;
    end;

    % allocate memory buffers for ZLCC analyzis
    trace_current_ZLCC_STA = zeros( 1, length( trace_current ) );

    if next_trace_available
        trace_next_ZLCC_STA  = zeros( 1, length( trace_current ) );
    end

    % allocate memory: STA/LTA
    current_STA   = zeros( 1, length( trace_current ) );
    current_LTA   = zeros( 1, length( trace_current ) );
    current_STALTA = zeros( 1, length( trace_current ) );

    % Initialize STAs and LTAs
    trace_current_ZLCC_STA( ZLCC_smoothing_length_samples ) = ...
        sum( trace_current( 1:ZLCC_smoothing_length_samples ).^2 );

    if next_trace_available
        trace_next_ZLCC_STA( ZLCC_smoothing_length_samples ) = ...
            sum( trace_next( 1:ZLCC_smoothing_length_samples ).^2 );
    end

    % compute STA/LTA: initialisation
    current_STA( STA_length_millisec ) = ...
        sum( abs( trace_current( 1:STA_length_millisec ) ) );
```

```
    current_LTA( LTA_length_millisec ) = ...
        sum( abs( trace_current( 1:LTA_length_millisec ) ) );

    current_STALTA( LTA_length_millisec ) = ...
        ( current_STA( STA_length_millisec )/ STA_length_millisec ) / ...
        ( current_LTA( LTA_length_millisec ) / LTA_length_millisec );

    % Compute recursive STAs and LTAs
    for i = ZLCC_smoothing_length_samples + 1:length( trace_current )
        trace_current_ZLCC_STA(i) = trace_current_ZLCC_STA(i-1) + ...
trace_current(i).^2 -trace_current(i-ZLCC_smoothing_length_samples).^2;

        if next_trace_available
            trace_next_ZLCC_STA(i)= trace_next_ZLCC_STA(i-1)+ ...
        trace_next(i).^2 - trace_next(i-ZLCC_smoothing_length_samples).^2;
        end
    end;

    % STA, LTA: recursion
    for i = STA_length_millisec + 1:length( trace_current )
         current_STA(i) = current_STA(i-1) + abs( trace_current(i) ) - ...
             abs( trace_current(i - STA_length_millisec) );
    end;
    current_STA = current_STA / STA_length_millisec;

    for i = LTA_length_millisec + 1:length( trace_current )
         current_LTA(i) = current_LTA(i-1) + abs( trace_current(i) ) - ...
             abs( trace_current(i - LTA_length_millisec) );
    end;
    current_LTA = current_LTA / LTA_length_millisec;

    % STA/LTA
    for i = LTA_length_millisec : length( trace_current )
         current_STALTA(i) = current_STA(i) / current_LTA(i);
    end;
    trace_current_ZLCC_STA = trace_current_ZLCC_STA / ...
        ZLCC_smoothing_length_samples;

    if next_trace_available
        trace_next_ZLCC_STA = trace_next_ZLCC_STA / ...
            ZLCC_smoothing_length_samples;
    end

    % r.m.s. computation: take a square root
    for i = 1:length( trace_current )
        trace_current_ZLCC_STA(i) = sqrt( trace_current_ZLCC_STA(i) );
        if next_trace_available
            trace_next_ZLCC_STA(i)  = sqrt( trace_next_ZLCC_STA(i) );
        end
    end;

    % plot LTAs
    if show_ZLCC_smoothed_source_data
        figure( fh_ZLCC_source_data );
        hold on
        tmp_x = [0:1:length( trace_current_ZLCC_STA )-1]./sampling_rate_Hz;
        plot( tmp_x, trace_current_ZLCC_STA / ...
```

```
            ( -max( trace_current_ZLCC_STA ) ) + sns, 'b' );
    hold off
end

figure( fh_STALTA_STA );
hold on
tmp_x = [0:1:length( current_STA )-1 ] ./ sampling_rate_Hz(1);
plot( tmp_x, current_STA / ( -max( current_STA ) ) + sns, 'b' );
hold off

figure( fh_STALTA_STALTA );
hold on
tmp_x = [0:1:length( current_STALTA )-1 ] ./ sampling_rate_Hz(1);
plot( tmp_x, current_STALTA / ( -max( current_STALTA ) ) + sns, 'b' );
hold off

% Loop over the arrival times
if next_trace_available
    xcorr_window_range = [ 0 : ZLCC_time_step_millisec : ...
        length(trace_current_ZLCC_STA)-1-ZLCC_window_length_millisec];
    rockfall_detection = zeros( length( xcorr_window_range ), 1 );
end

% allocate memory for STA-2D plot, LTA-2D plot
if sns == sensor_index_high
    ZLCC_timeline = 1 : ZLCC_time_step_millisec : ...
        length( trace_current_ZLCC_STA );
    ZLCC_xcorr_pair_2D = zeros(size(ZLCC_timeline, 2), num_channels );
    STA_2D = zeros( length( trace_current ), num_channels );
    LTA_2D = zeros( length( trace_current ), num_channels );
    STALTA_2D = zeros( length( trace_current ), num_channels );
end

% save computed STA/ LTA
STA_2D(:, sns ) = current_STA;
LTA_2D(:, sns ) = current_LTA;
STALTA_2D(:, sns ) = current_STALTA;

if ~next_trace_available
    continue;
end

xcorr_arrival_index = 0;

for arrival_time = ZLCC_timeline
    xcorr_arrival_index = xcorr_arrival_index + 1;

    %  Skip the zero-filled part in the beginning of the LTA trace
    if arrival_time <= ZLCC_smoothing_length_samples
        continue
    end

    % copy subarrays to compute cross-correlation
    ZLCC_segment_current = get_subarray( arrival_time, ...
            ZLCC_window_length_millisec, 0, trace_current_ZLCC_STA, ...
            ZLCC_subsampling_factor );
```

```
        ZLCC_segment_next = get_subarray( arrival_time, ...
                ZLCC_window_length_millisec, 0, trace_next_ZLCC_STA, ...
                ZLCC_subsampling_factor );

        %   Check if there's enough data
        min_trace_length = min( [ length( ZLCC_segment_current ) ...
                        length(ZLCC_segment_next) ] );

        trace_length_samples = ZLCC_subsampling_factor * min_trace_length;

        if( trace_length_samples < ZLCC_min_number_xcorr_samples )
            rockfall_detection( xcorr_arrival_index ) = 0;
            continue;
        end

        rockfall_detection( xcorr_arrival_index ) = ...
            sum( ZLCC_segment_current .* ZLCC_segment_next );

        current_norm = norm(ZLCC_segment_current )*norm(ZLCC_segment_next);

        rockfall_detection( xcorr_arrival_index ) = ...
                rockfall_detection( xcorr_arrival_index ) / current_norm;

        ZLCC_xcorr_pair_2D( xcorr_arrival_index, sns ) = ...
            rockfall_detection( xcorr_arrival_index );
    end
end % for sns = sensor_index_high:-1:sensor_index_low

% fix the ZLCC: make it right-justified, not left
ZLCC_shift_step = ZLCC_window_length_millisec/ ZLCC_time_step_millisec-1;

ZLCC_xcorr_pair_2D = circshift( ZLCC_xcorr_pair_2D, [ZLCC_shift_step 0 ]);


%  Show zero-lag cross-corr. plot
%  Assign "maximum_xcorr_value" in order to bring all color-coded 2D ...
%  xcorr charts into the same color-coding frame of reference
if normalize_color_bar
    ZLCC_xcorr_pair_2D( 1, sensor_index_low ) = maximum_xcorr_value;
end

if show_ZLCC_correlated_pairs
    figure( 'Name', 'ZLCC (pairs)' );
    ZLCC_xcorr_pair_2D_copy = ZLCC_xcorr_pair_2D;

    if replace_negative_xcorr_with_zero
        negative_xcorr_idx = find( ZLCC_xcorr_pair_2D_copy < 0 );
        ZLCC_xcorr_pair_2D_copy( negative_xcorr_idx ) = 0;
    end

    imagesc( ZLCC_xcorr_pair_2D_copy' );

    title( [ 'ZLCC (pairs)' ] , 'FontSize', FontSizeTitle );
    set(gca,'FontSize',FontSizeAxes,'LineWidth', LineWidthAxes);
    xlabel('seconds', 'FontSize', FontSizeXLabel);
    ylabel('Sensor ID', 'FontSize', FontSizeYLabel);
    colorbar('location','EastOutside') ;
```

```
end

%  STALTA_max contains max STA/LTA coefficients within incremental time
%  window
STALTA_max = zeros( size( ZLCC_timeline, 2 ), num_channels );

for sns = sensor_index_high:-1:sensor_index_low
    STALTA_idx = 0;

    for arrival_time = ZLCC_timeline
        STALTA_idx = STALTA_idx + 1;
        % Use MAX{ windowed ( STA/LTA ) }
        STALTA_max( STALTA_idx, sns ) = max( STALTA_2D( arrival_time : ...
            arrival_time + ZLCC_time_step_millisec -1, sns ) );
    end
end

% Compute clipped STA/LTA to achieve uniform color-coding of sta/lta peaks
STALTA_max_clipped = STALTA_max;
high_stalta_idx = find( STALTA_max_clipped >= STALTA_display_threshold );
STALTA_max_clipped( high_stalta_idx ) = STALTA_display_threshold;

% Show STA/LTA
fh_figure_STALTA = figure( 'Name', 'STA/LTA' );
pf=get(fh_figure_STALTA,'position');
set(gca,'FontSize',FontSizeAxes,'LineWidth', LineWidthAxes);
imagesc( ZLCC_timeline / 1000, [ sensor_index_low:1:sensor_index_high ],...
         STALTA_max_clipped( :, sensor_index_low:1:sensor_index_high )' );

title( 'STA/LTA' , 'FontSize', FontSizeTitle );
xlabel('seconds', 'FontSize', FontSizeXLabel);
ylabel('Sensor ID', 'FontSize', FontSizeYLabel);
cb = colorbar('location','EastOutside') ;
pcb = get(cb,'position');
pcb(1) = ColorBarLeft;
pcb(3) = 0.5*pcb(3);
set(cb, 'position', pcb);
set(fh_figure_STALTA,'position', pf);
marg = get(gca,'LooseInset');
set(gca, 'LooseInset', [ left_margin_image, marg(2), ...
    right_margin_image, marg(4) ]);

% Bridge the gaps within STA/LTA
STALTA_bridged = bridge_rockfall_detector_matrix( STALTA_max, ...
                    true, 2, 10, 5, STALTA_display_threshold );

% save the bridged STA/LTA for further analysis:
STALTA_max = STALTA_bridged;

% Clip STA/LTA outliers it before displaying
STALTA_bridged( high_stalta_idx ) = STALTA_display_threshold;

figure( 'Name', 'STA/LTA (bridged)' );
pf=get(fh_figure_STALTA,'position');
set(gca,'FontSize',FontSizeAxes,'LineWidth', LineWidthAxes);
imagesc( ZLCC_timeline / 1000, [sensor_index_low:1:sensor_index_high], ...
             STALTA_bridged( :, sensor_index_low:1:sensor_index_high )' );
```

```
title( 'STA/LTA (bridged)' , 'FontSize', FontSizeTitle );
xlabel('seconds', 'FontSize', FontSizeXLabel);
ylabel('Sensor ID', 'FontSize', FontSizeYLabel);
cb = colorbar('location','EastOutside') ;
pcb = get(cb,'position');
pcb(1) = ColorBarLeft;
pcb(3) = 0.5*pcb(3);
set(cb, 'position', pcb);
set(fh_figure_STALTA,'position', pf);
marg = get(gca,'LooseInset');
set(gca, 'LooseInset', [ left_margin_image, marg(2), ...
    right_margin_image, marg(4) ]);


% Optional: we can use more than one comparison sensor to obtain ZLCC
% Here, multiply ZLCC_num_comparison_sensors cross-corr. coefficients
% moving west.
xcorr_2D_west = zeros( size( ZLCC_timeline, 2 ), num_channels );

for sns = sensor_index_high: -1 : sensor_index_low
    if sns <= ZLCC_num_comparison_sensors
        continue;
    end

    xcorr_arrival_index = 0;

    for arrival_time = ZLCC_timeline
        xcorr_arrival_index = xcorr_arrival_index + 1;

        if arrival_time <= ZLCC_smoothing_length_samples
             continue;
        end

        if xcorr_arrival_index >= size( ZLCC_xcorr_pair_2D, 1 )
             continue;
        end

        xcorr_2D_west( xcorr_arrival_index, sns ) = ...
                    ZLCC_xcorr_pair_2D( xcorr_arrival_index, sns );

        for i = 1 : ZLCC_num_comparison_sensors - 1
                xcorr_2D_west( xcorr_arrival_index, sns ) = ...
                    xcorr_2D_west( xcorr_arrival_index, sns ) *...
                        ZLCC_xcorr_pair_2D( xcorr_arrival_index, sns - i);
        end
    end
end

% Optional: we can use more than one comparison sensor to obtain ZLCC
% Here, multiply ZLCC_num_comparison_sensors cross-corr. coefficients
% moving east.
xcorr_2D_east = zeros( size( ZLCC_timeline, 2 ), num_channels );

for sns = sensor_index_high: -1 : sensor_index_low
    if sns >= num_channels - ZLCC_num_comparison_sensors + 1
        continue;
    end
```

```
    xcorr_arrival_index = 0;

    for arrival_time = ZLCC_timeline % xcorr_window_range
        xcorr_arrival_index = xcorr_arrival_index + 1;

        if arrival_time <= ZLCC_smoothing_length_samples
             continue;
        end

        if xcorr_arrival_index >= size( ZLCC_xcorr_pair_2D, 1 )
             continue;
        end

        % NOTE: ZLCC_xcorr_pair_2D contains correlations with
        % the west neighbour
        xcorr_2D_east( xcorr_arrival_index, sns ) = ...
            ZLCC_xcorr_pair_2D( xcorr_arrival_index, sns + 1 );

        for i = 1 : ZLCC_num_comparison_sensors - 1
             xcorr_2D_east( xcorr_arrival_index, sns ) = ...
                    xcorr_2D_east( xcorr_arrival_index, sns ) *...
                   ZLCC_xcorr_pair_2D( xcorr_arrival_index, sns + 1 + i);
        end
    end
end


if normalize_color_bar
    xcorr_2D_west( 1, sensor_index_low ) = maximum_xcorr_value;
    xcorr_2D_east( 1, sensor_index_low ) = maximum_xcorr_value;
end

if show_EastWest_ZLCC
    figure( 'Name', 'Vertical xcorr stack: West' );
    set(gca,'FontSize', FontSizeAxes, 'LineWidth', LineWidthAxes);
    imagesc( ZLCC_timeline / 1000, ...
        [ sensor_index_low:1:sensor_index_high ], ...
             xcorr_2D_west( :, sensor_index_low:1:sensor_index_high )' );
    title( [ 'Vertical xcorr stack: West' ] , 'FontSize', FontSizeTitle );
    xlabel('seconds', 'FontSize', FontSizeXLabel);
    ylabel('Sensor ID', 'FontSize', FontSizeYLabel);
    colorbar('location','EastOutside') ;
end

if show_EastWest_ZLCC
    figure( 'Name', 'Vertical xcorr stack: East' );
    set(gca,'FontSize',FontSizeAxes,'LineWidth', LineWidthAxes);
    imagesc( ZLCC_timeline / 1000, ...
        [ sensor_index_low:1:sensor_index_high ], ...
             xcorr_2D_east( :, sensor_index_low:1:sensor_index_high )' );
    title( [ 'Vertical xcorr stack:  East' ] , 'FontSize', FontSizeTitle );
    xlabel('seconds', 'FontSize', FontSizeXLabel);
    ylabel('Sensor ID', 'FontSize', FontSizeYLabel);
    colorbar('location','EastOutside') ;
end
```

```
% fill in the gaps
xcorr_2D_west( :, sensor_index_low:ZLCC_num_comparison_sensors ) = ...
    xcorr_2D_east( :, sensor_index_low:ZLCC_num_comparison_sensors );

xcorr_2D_east( :, sensor_index_high - ZLCC_num_comparison_sensors + 1: ...
    sensor_index_high )= ...
    xcorr_2D_west( :, ...
    sensor_index_high - ZLCC_num_comparison_sensors + 1:sensor_index_high);

%  Compute max {east_ZLCC; west_ZLCC}
xcorr_2D_max = max( xcorr_2D_east, xcorr_2D_west );
xcorr_2D_min = min( xcorr_2D_east, xcorr_2D_west );


if replace_negative_xcorr_with_zero
    negative_xcorr_idx = find( xcorr_2D_max < 0 );
    xcorr_2D_max( negative_xcorr_idx ) = 0;

    negative_xcorr_idx = find( xcorr_2D_min < 0 );
    xcorr_2D_min( negative_xcorr_idx ) = 0;
end

%   multiply STA/LTA matrix by ZLCC and display
fh_max_ZLCC = figure( 'Name', 'Vertical xcorr stack: pairs (Shifted)' );
pf=get(fh_figure_STALTA,'position');
set(gca,'FontSize', FontSizeAxes, 'LineWidth', LineWidthAxes);
imagesc( ZLCC_timeline / 1000, sensor_index_low:1:sensor_index_high, ...
             xcorr_2D_max( :, sensor_index_low:1:sensor_index_high )' );
title( 'ZLCC', 'FontSize', FontSizeTitle );
xlabel('seconds', 'FontSize', FontSizeXLabel);
ylabel('Sensor ID', 'FontSize', FontSizeYLabel);
cb = colorbar('location','EastOutside') ;
pcb = get(cb,'position');
pcb(1) = ColorBarLeft;
pcb(3) = 0.5*pcb(3);
set(cb, 'position', pcb);
set(fh_figure_STALTA,'position', pf);
marg = get(gca,'LooseInset');
set(gca, 'LooseInset', [ left_margin_image, marg(2), ...
    right_margin_image, marg(4) ]);


StaLTA_ZLCC = STALTA_max .* xcorr_2D_max;

% show clipped STA/LTA * ZLCC
high_stalta_idx = find( StaLTA_ZLCC >= STALTA_display_threshold );
StaLTA_ZLCC( high_stalta_idx ) = STALTA_display_threshold;


fh_figure_STALTA_x_ZLCC = figure( 'Name', 'STA/LTA x ZLCC' );
pf=get(fh_figure_STALTA,'position');
set(gca,'FontSize',FontSizeAxes,'LineWidth', LineWidthAxes);
imagesc( ZLCC_timeline / 1000, sensor_index_low:1:sensor_index_high, ...
               StaLTA_ZLCC( :, sensor_index_low:1:sensor_index_high )' );
title( 'STA/LTA * ZLCC' , 'FontSize', FontSizeTitle );
xlabel('seconds', 'FontSize', FontSizeXLabel);
```

```
ylabel('Sensor ID', 'FontSize', FontSizeYLabel);
cb = colorbar('location','EastOutside') ;
pcb = get(cb,'position');
pcb(1) = ColorBarLeft;
pcb(3) = 0.5*pcb(3);
set(cb, 'position', pcb);
set(fh_figure_STALTA,'position', pf);
marg = get(gca,'LooseInset');
set(gca, 'LooseInset', [ left_margin_image, marg(2), ...
    right_margin_image, marg(4) ]);

% ----------------------------------------------------------------------
% Rockfall detection
% Scan STA/LTA*ZLCC for percentage fill trigger (i.e. do "pixel counting")
% ----------------------------------------------------------------------
[time_max, sns_max] = size(StaLTA_ZLCC);
stalta_percent_fill = zeros( time_max );

max_array_trigger_idx = -1;
max_array_trigger = 0;

for time_idx = 1:time_max
    start_sns = -1;
    end_sns = -1;

    low_sta_lta_count = 0;

    % find a long sequence
    for sns_idx = 1:sns_max

        high_stalta_found = ...
            ( StaLTA_ZLCC(time_idx, sns_idx) >= STALTA_weak_threshold );

        if high_stalta_found

            if start_sns == -1
                start_sns = sns_idx;
            end

            end_sns = sns_idx;
            low_sta_lta_count = 0;
        else
            % add blob separation code here, if necessary
            low_sta_lta_count = low_sta_lta_count + 1;

            if low_sta_lta_count > 5
                if start_sns > -1
                    triggered_percent = analyze_stalta_density(  ...
                      StaLTA_ZLCC, start_sns, end_sns, time_idx, ...
                STALTA_percent_fill_window_cells, STALTA_weak_threshold );

                stalta_percent_fill( time_idx ) = ...
                    max( stalta_percent_fill(time_idx), triggered_percent);
                end

                start_sns = -1;
                end_sns = -1;
```

```
            end;
        end
    end

    triggered_percent = analyze_stalta_density( StaLTA_ZLCC, ...
                start_sns, end_sns, ...
                time_idx, STALTA_percent_fill_window_cells, ...
                STALTA_weak_threshold );

    stalta_percent_fill( time_idx ) = ...
        max( stalta_percent_fill( time_idx ), triggered_percent );

    % is it a rockfall ?
    if triggered_percent >= STALTA_percentage_fill_threshold
        array_trig = (end_sns - start_sns)* average_sensor_distance_meters;
        % check the spatial extent of the array trigger
        if array_trig >= rail_joint_precursor_meters
           if( max_array_trigger < array_trig );
                max_array_trigger_idx = time_idx;
                max_array_trigger = array_trig;
           end
        end
    end
end


% If a rockfall was detected, plot it it on the site's plan view
if( max_array_trigger >= rail_joint_precursor_meters )

   rf_idx_start = max( max_array_trigger_idx*time_idx2sample_idx - ...
       time_window_samples, 1);
   rf_idx_end   = min( max_array_trigger_idx*time_idx2sample_idx + ...
       time_window_samples, time_max*time_idx2sample_idx);

   sensor_pgv = zeros( 1, num_channels );

   % compute PPV within the current time window
   for sns_idx=1:num_channels
       win_subtrace = src_traces( sns_idx, rf_idx_start : rf_idx_end );
       sensor_pgv(sns_idx) = max( abs( win_subtrace) );
   end

    [ rockfall_detected, rockfall_locations_xy ] = ...
       rockfall_detector( pgv_threshold, sensor_xy, sensor_pgv );

    if rockfall_detected
        figure( f_sns )
        hold on
        for idx=1:length( rockfall_locations_xy )
            scatter( rockfall_locations_xy(idx).x, ...
                rockfall_locations_xy(idx).y, '*', ...
                'MarkerEdgeColor', [ 0.0, 1.0, 0.0 ],...
                'MarkerFaceColor', [ 0.0, 1.0, 0.0 ] );
        end
        hold off
    end
end % if max_array_trigger_idx > 0
```

```
% ----------------------------------------------------------------------
% Rockfall detection
% Find the longest windowed trigger series of STA/LTA
% ----------------------------------------------------------------------
longest_stalta_trigger = zeros( 1, time_max );

max_array_trigger_idx = -1;
max_array_trigger = 0;

for time_idx = 1 : time_max
    current_longest_trigger = 0;
    longest_stalta_trigger( time_idx ) = 0.1;

    % find a long sequence
    for sns_idx = 1:sns_max

        high_stalta_found = false;

        % for the curent sensor, scan a time window
        max_time_window_idx = min( time_max, time_idx + ...
            stalta_trigger_series_window_cells );

        for i=time_idx: max_time_window_idx
            if ( STALTA_max(i, sns_idx) >= STALTA_strong_threshold )
               high_stalta_found = true;
               break;
            end
        end

        if high_stalta_found
            current_longest_trigger = current_longest_trigger + 1;
        else
            if longest_stalta_trigger( time_idx ) < ...
                  current_longest_trigger * average_sensor_distance_meters
             longest_stalta_trigger( time_idx ) = ...
                  current_longest_trigger * average_sensor_distance_meters;
            end

            current_longest_trigger = 0;
        end
    end

    if longest_stalta_trigger( time_idx ) < ...
            current_longest_trigger * average_sensor_distance_meters
        longest_stalta_trigger( time_idx ) = ...
            current_longest_trigger * average_sensor_distance_meters;
    end

    if max_array_trigger < longest_stalta_trigger( time_idx )
        max_array_trigger = longest_stalta_trigger( time_idx );
        max_array_trigger_idx = time_idx;
    end
end
```

```
% If a rockfall was detected, plot it it on the site's plan view
if( max_array_trigger >= rail_joint_precursor_meters )

   rf_idx_start = max( max_array_trigger_idx*time_idx2sample_idx - ...
       time_window_samples, 1);
   rf_idx_end   = min( max_array_trigger_idx*time_idx2sample_idx + ...
       time_window_samples, time_max*time_idx2sample_idx);

   sensor_pgv = zeros( 1, num_channels );

   % compute PPV within the current time window
   for sns_idx=1:num_channels
       win_subtrace = src_traces( sns_idx, rf_idx_start : rf_idx_end );
       sensor_pgv(sns_idx) = max( abs( win_subtrace) );
   end

    [ rockfall_detected, rockfall_locations_xy ] = ...
       rockfall_detector( pgv_threshold, sensor_xy, sensor_pgv );

    if rockfall_detected
        figure( f_sns )
        hold on
        for idx=1:length( rockfall_locations_xy )
            scatter( rockfall_locations_xy(idx).x, ...
                rockfall_locations_xy(idx).y, '.', ...
                'MarkerEdgeColor', [ 1.0, 0, 0.0 ],...
                'MarkerFaceColor', [ 1.0, 0, 0.0 ] );
        end
        hold off
    end
end % if max_array_trigger_idx > 0


% Show the rockfall detector based on the array trigger: max %% fill
fh_figure_STALTA_x_ZLCC_PercentageFill = ...
    figure( 'Name', 'Rockfall detection: STA/LTA x ZLCC ' );
set(gca,'FontSize',FontSizeAxes,'LineWidth', LineWidthAxes);
hold on
temp_bar_x = [ 0:1:time_max-1 ] .* ZLCC_time_step_sec;
bar(temp_bar_x, stalta_percent_fill,'FaceColor','blue','EdgeColor','blue');
title( 'Rockfall detector: STA/LTA*ZLCC' , 'FontSize', FontSizeTitle );
xlabel('seconds', 'FontSize', FontSizeXLabel);
ylabel('STA/LTA, %', 'FontSize', FontSizeYLabel);
xLimits = get( gca, 'XLim' );
pct_x =[ xLimits(1) xLimits(2) ];
pct_y =[STALTA_percentage_fill_threshold STALTA_percentage_fill_threshold];
plot( pct_x, pct_y, 'red');
axis( [ 0 xLimits(2) 0 100 ] );
hold off

% Show the rockfall detector based on the array trigger: max distance
fh_figure_STALTA_x_ZLCC_TriggerDistance = ...
    figure( 'Name', 'Rockfall detector: STA/LTA series' );
hold on
bar(temp_bar_x,longest_stalta_trigger,'FaceColor','blue',...
```

```
    'EdgeColor','blue');
xLimits = get( gca, 'XLim' );
pct_x = [ xLimits(1) xLimits(2) ];
pct_y = [rail_joint_precursor_meters rail_joint_precursor_meters];
plot( pct_x, pct_y, 'red');

xLimits = get( gca, 'XLim' );
yLimits = get( gca, 'YLim' );
axis( [ 0 xLimits(2) yLimits(1) yLimits(2) ] );
title( 'Rockfall detector: STA/LTA series', 'FontSize', FontSizeTitle );
xlabel('seconds', 'FontSize', FontSizeXLabel);
ylabel('STA/LTA series, m', 'FontSize', FontSizeYLabel);
hold off

% ************************************************************************
% NAME:     rockfall_detector
% PURPOSE:  Given a Peak Ground Velocity (PGV) threshold model, sensor
%           coordinates, and PGVs observed at each sensor, detect
%           a rockfall and return all locations within the seismic array
%           that match the amplitude model.
% INPUT:    pgv_threshold - a polyline (X;Y) which describes PGV
%                           (PGV) threshold in
%                           meters-per-second vs distance in meters
%           sensor_xy     - array of N sensor coordinates (X;Y)
%           sensor_pgv    - Vector of observed PGV(sensor(i)), i=1,N
% E.g.
% pgv_threshold(1).d   = 5.0;
% pgv_threshold(1).pgv = 0.00021179;
% pgv_threshold(2).d   = 18.3;
% pgv_threshold(2).pgv = 0.00004841;
% ...
% sensor_xy(1).x = 123.0;
% sensor_xy(1).y = 12.4;
% ...
% OUTPUT:   rockfall_locations_xy - vector of (X;Y) locations that
%                           match the amplitude model
%           rockfall_detected     - TRUE is a rockfall has been detected
% AUTHOR:   Bohdan Nedilko <bohdan.nedilko@alumni.ubc.ca>
% DATE:     February 2016
%           This code was tested under Matlab 2008b
% ************************************************************************
function [ rockfall_detected, rockfall_locations_xy ] = ...
    rockfall_detector( pgv_threshold, sensor_xy, sensor_pgv )

rockfall_detected = false;
num_sensors = length( sensor_xy );

% assume that 0x is directed along the sensor array
% 0y is perpendicular the sensor array
% the sensors are downhill;
% 0y positive direction  is into the slope
% 0x positive direction is along the track
% Orthonormal vectors:
x_ortho = struct;
x_ortho.x  = 0;
x_ortho.y  = 0;
```

```
y_ortho = struct;
y_ortho.x  = 0;
y_ortho.y  = 0;

% scan steps
delta_x = 1;    % 1 meter
delta_y = 1;    % 1 meter

scan_distance_y = 3; % scan three meters in the up-slope direction
% compute the number of scan steps along 0y-axis
num_scan_steps_y = (scan_distance_y / delta_y ) + 1;

rock_xy = struct;
rock_xy.x  = 0;
rock_xy.y  = 0;

% reset the potential locations of rockfalls
rockfall_locations_xy = [];

% Loop over the array sensors
for sns_idx=1:num_sensors-1
    % For each pair of sensors, compute two orthonotmal vectors.
    % 0x vector
    x_ortho.x  = sensor_xy(sns_idx+1).x - sensor_xy(sns_idx).x;
    x_ortho.y  = sensor_xy(sns_idx+1).y - sensor_xy(sns_idx).y;
    sns2sns_distance = sqrt(x_ortho.x*x_ortho.x + x_ortho.y*x_ortho.y);
    % normalize the vectors
    x_ortho.x = x_ortho.x/ sns2sns_distance;
    x_ortho.y = x_ortho.y/ sns2sns_distance;

    % Copmute perpendicular orthonormal vector, 0y
    y_ortho.x  = -x_ortho.y;
    y_ortho.y  = x_ortho.x;

    % compute the number of scan steps along 0x-axis
    num_scan_steps_x = (sns2sns_distance / delta_x) + 1;

    % scan X0Y plane in 0x direction
    for steps_x=1:num_scan_steps_x
        % scan X0Y plane in 0y direction
        for steps_y=1:num_scan_steps_y
            % current distance along 0x
            cur_x = (steps_x-1)*delta_x;

            % current distance along 0y
            cur_y = (steps_y-1)*delta_y;

            % compute current candidate location
            rock_xy.x = sensor_xy(sns_idx).x + ...
                                    x_ortho.x*cur_x + y_ortho.x*cur_y;
            rock_xy.y = sensor_xy(sns_idx).y + ...
                                    x_ortho.y*cur_x + y_ortho.y*cur_y;

            % calculate the rockfall PGV threshold
            sns_threshold_pgv = sns_array_pgv_threshold(pgv_threshold, ...
                    sensor_xy, rock_xy);
```

```
            % if the threshold is exeeded, save the rockfall location
            if( all( sns_threshold_pgv < sensor_pgv ) )
                if( ~rockfall_detected )
                    rockfall_locations_xy(1).x = 0;
                    rockfall_locations_xy(1).y = 0;
                    rockfall_locations_xy(1) = rock_xy;
                else
                    rf_length = length( rockfall_locations_xy );
                    rockfall_locations_xy(rf_length+1).x = 0;
                    rockfall_locations_xy(rf_length+1).y = 0;
                    rockfall_locations_xy(rf_length+1) = rock_xy;
                end
                % report a rockfall
                rockfall_detected = true;
            end
        end % steps_y=1:num_scan_steps_y
    end % steps_x=1:num_scan_steps_x
end % for i=1:num_sensors-1

% ************************************************************************
% NAME:     sns_array_pgv_threshold
% PURPOSE:  Given a PGV threshold model and a hypothetical rockfall
%           compute PGV(epicenter_dist) for each array sensor.
% INPUT:    pgv_threshold - a polyline (X;Y) which describes Peak Ground
%                           Velocity (PGV) threshold
%           sensor_xy     - array of N sensor coordinates (X;Y)
%           rockfall_location_xy  - hypothetical rockfall location (X;Y)
%
% OUTPUT:   sns_threshold_pgv     - vector of N PGV values computed at
%                           {sensor_xy} points using pgv_threshold-polyline
% ************************************************************************
function [ sns_threshold_pgv ] = sns_array_pgv_threshold( pgv_threshold,...
                    sensor_xy, rockfall_location_xy )
% preallocate moemory for speed
sns_threshold_pgv = zeros( 1, length( sensor_xy ) );
% loop over the array sensors
for sns_idx=1:length(sensor_xy)
    dx = sensor_xy(sns_idx).x - rockfall_location_xy.x;
    dy = sensor_xy(sns_idx).y - rockfall_location_xy.y;
    % compute the epicentral distance
    epicenter_dist = sqrt( dx*dx + dy*dy );

    % Compute PGV(epicenter_dist).
    % If epicenter_dist is between  zero and the first point within the
    % plyline threshold model, use the first point's PGV
    if( epicenter_dist > pgv_threshold(length(pgv_threshold)).d )
        sns_threshold_pgv(sns_idx) = 0;
    else
        % if epicenter_dist beyond the model scope, use the polyline's
        % last point's PGV
        if( epicenter_dist <= pgv_threshold(1).d )
            sns_threshold_pgv(sns_idx) = pgv_threshold(1).pgv;
        else
            % ... otherwise use a linea approximation to compute
            % the PGV(epicenter_dist )
            for i=2:length(pgv_threshold)-1;
                if( epicenter_dist <= pgv_threshold(i).d )
```

```
                    sns_threshold_pgv(sns_idx) = pgv_threshold(i-1).pgv + ...
                        ( epicenter_dist - pgv_threshold(i-1).d)* ...
                        (pgv_threshold(i).pgv - pgv_threshold(i-1).pgv) / ...
                            (pgv_threshold(i).d - pgv_threshold(i-1).d);
                end
            end
        end
    end
end


% ************************************************************************
% NAME:     analyze_stalta_density
% PURPOSE:  Computes the percentage of high STA/LTA values within
%           a specific time window
% INPUT:    STALTA_matrix - NxM matrix of STA/LTA values, where
%                 N = number of sensors; M = number of time increments;
%
%           start_sns_idx, end_sns_idx - first and last sensors within the
%                 array trigger;
%           start_time_idx    - index of the time window;
%           time_window_cells - width of the time window;
%           STALTA_threshold  - STA/LTA trigger threshold
% OUTPUT:   triggered_percent - percentage of STA/LTA values that exceed
%                 STALTA_threshold within the spatio-temporal window
% AUTHOR:   Bohdan Nedilko <bohdan.nedilko@alumni.ubc.ca>
% DATE:     February 2016
%           This code was tested under Matlab 2008b
% ************************************************************************
function [ triggered_percent ] = analyze_stalta_density( STALTA_matrix, ...
                    start_sns_idx, end_sns_idx, ...
                    start_time_idx, time_window_cells, ...
                    STALTA_threshold )

triggered_percent = 0;

if start_sns_idx == -1
   return;
end

% ignore nuisance activations
if start_sns_idx + 4 >= end_sns_idx
   return;
end

time_max = size(STALTA_matrix, 1);
time_idx_end = min( time_max, start_time_idx + time_window_cells );
num_scanned_cells = ( end_sns_idx - start_sns_idx + 1 ) * ...
    ( time_idx_end - start_time_idx + 1);
sum_triggered = 0;

for t = start_time_idx:time_idx_end
    for sns = start_sns_idx: end_sns_idx
        if STALTA_matrix(t, sns) >= STALTA_threshold
            sum_triggered = sum_triggered + 1;
        end
    end
```

```
end

triggered_percent = 100 * sum_triggered / num_scanned_cells;

% ************************************************************************
% NAME:     bridge_rockfall_detector_matrix
% PURPOSE:  Fills in a gap, if found, within a sensor array trigger pattern
%           Triggers are computed with STA/LTA; gaps are assumed to be a
%           result of pre-cursor rockfalls  near the epicentre that
%           saturate LTA and result in low STA/LTA.
%
% INPUT:    raw_matrix - NxM matrix of STA/LTA values, where
%                 N = number of sensors; M = number of time increments;
%           bridge_edge_gaps - TRUE if gaps at the edges of the sensor
%                 array must be also filled in;
%           max_gap_edge_sns - max. length of the gap
%           min_gap_prefix_postix_sensors - the minimum number of triggered
%           sensors preceding the gap (e.g. west of the gap), and east of
%           it;
%
%           max_bridged_gap_sensors - maximum size of the gap to be filled
%           in, measured as a number of sensors.  Longer gaps are assumed
%           to be a result of two rockfalls that occured
%           near-simultaneously but separate in space.
%
%           pass_threshold - STA/LTA filler value
%
% OUTPUT:   bridged_matrix - a NxM STA/LTA matrix without gaps inside the
%               array trigger patterns;
% AUTHOR:   Bohdan Nedilko <bohdan.nedilko@alumni.ubc.ca>
% DATE:     February 2016
%           This code was tested under Matlab 2008b
% ************************************************************************
function [ bridged_matrix ] = ...
            bridge_rockfall_detector_matrix( raw_matrix, ...
            bridge_edge_gaps, max_gap_edge_sns,...
            min_gap_prefix_postix_sensors, max_bridged_gap_sensors, ...
            pass_threshold )

bridged_matrix = raw_matrix;

[time_max, sns_max] = size( raw_matrix );

for time_idx = 1: time_max
    %  if bridging border gaps is disabled, skip this step
    if bridge_edge_gaps

        %   A. Bridge the gap between the top edge of the matrix and
        %      the first high xcorr
        if raw_matrix( time_idx, max_gap_edge_sns ) >= pass_threshold
            for  i = 1 : max_gap_edge_sns - 1
                if raw_matrix( time_idx, i ) < pass_threshold
                    bridged_matrix( time_idx, i ) = pass_threshold;
                end
            end
        end
```

```
    %   B. Bridge the gap between the bottom edge of the matrix and
    %      the last high xcorr
    if raw_matrix(time_idx, sns_max-max_gap_edge_sns) >= pass_threshold

        for i = sns_max - max_gap_edge_sns + 1 : sns_max

            if raw_matrix( time_idx, i ) < pass_threshold
                bridged_matrix( time_idx, i ) = pass_threshold;
            end
        end
    end

end % bridge_border_gaps

%   C. Scan and bridge the middle part of the matrix
gap_prefix_sns_count    = 0;
gap_postfix_sns_count   = 0;
gap_sns_count           = 0;

gap_start_sns = 0;
gap_end_sns = 0;

for sns_idx = max_gap_edge_sns+1 : sns_max-max_bridged_gap_sensors - 1

    % if the threshold is high, update the prefix/ post-fix count
    if raw_matrix( time_idx, sns_idx ) >= pass_threshold

        % if gap_sns_count == 0 ,this must be prefix
        if gap_sns_count == 0
            gap_prefix_sns_count = gap_prefix_sns_count + 1;
        else
            % .. otherwise, this is postfix.  if the gap_sns_count is
            % larger than the max allowed gap, reset everything
            if gap_sns_count > max_bridged_gap_sensors
                % the postfix becomes a new prefix
                gap_prefix_sns_count    = 1;
                gap_postfix_sns_count   = 0;
                gap_sns_count           = 0;
            else
                % if the gap is not too wide, keep counting the postfix
                % sensors
                gap_postfix_sns_count = gap_postfix_sns_count + 1;

                % if the postifx is long enough, bridge the gap
                if gap_postfix_sns_count>=min_gap_prefix_postix_sensors

                    for i = gap_start_sns: gap_end_sns
                        bridged_matrix( time_idx, i ) = pass_threshold;
                    end
                    % the postfix becomes a new prefix
                    gap_prefix_sns_count = gap_postfix_sns_count;
                    gap_sns_count = 0;
                    gap_postfix_sns_count = 0;

                    continue;
                end;
            end
```

```
            end
        else % low threshold

            % if this is not a gap between two triggered series,
            % continue
            if ( gap_sns_count == 0 ) && ( gap_prefix_sns_count == 0 )
                continue;
            end

            % if the prefix is  too long, reset all counters
            if gap_sns_count > max_bridged_gap_sensors
                gap_prefix_sns_count    = 0;
                gap_postfix_sns_count   = 0;
                gap_sns_count           = 0;

                continue;
            end

            % if the prefix is too short, reset and continue
            if gap_prefix_sns_count < min_gap_prefix_postix_sensors
                gap_prefix_sns_count    = 0;
                gap_postfix_sns_count   = 0;
                gap_sns_count           = 0;

                continue;
            end

            % count the gap sensors
            gap_sns_count = gap_sns_count + 1;

            % if this is the first sensor of the gap, mark the sns
            % index
            if gap_sns_count == 1
                gap_start_sns = sns_idx;
                gap_end_sns = sns_idx;
            %... otherwise, mark the current last sns idx
            else
                gap_end_sns = sns_idx;
            end
        end
    end
end

% ************************************************************************
% NAME:     get_site_sensor_xy
% PURPOSE:  Return (X;Y) coordinates of a sensor
% INPUT:    site_ID - unique site name, e.g. 'white_canyon', 'hope'
%           sns_name - sensor ID, e.g. 'Z01', 'Z02'
% OUTPUT:   sensor coordinates
% ************************************************************************
function [ x, y ] = get_site_sensor_xy( site_ID, sns_name )

if( strcmpi( site_ID, 'white_canyon' ) )
switch upper( sns_name )
    case 'Z01'
        x = 12.80;    y = 197.36;
        return
```

```
case 'Z02'
    x = 18.60;    y = 178.59;
    return
case 'Z03'
    x = 22.91;    y = 159.12;
    return
case 'Z04'
    x = 25.71;    y = 138.79;
    return
case 'Z05'
    x = 26.98;    y = 121.40;
    return
case 'Z06'
    x = 27.35;    y = 104.25;
    return
case 'Z07'
    x = 26.86;    y = 87.17;
    return
case 'Z08'
    x = 26.29;    y = 70.54;
    return
case 'Z09'
    x = 24.77;    y = 53.90;
    return
case 'Z10'
    x = 22.50;    y = 34.17;
    return
 case 'Z11'
     x = 19.81;    y = 17.65;
    return
 case 'Z12'
     x = 16.90;    y = 1.88;
    return
 case 'Z13'
     x = 15.56;    y = -5.83;
    return
 case 'Z14'
     x = 10.06;    y = -27.69;
    return
 case 'Z15'
     x = 5.07;    y = -44.97;
    return
 case 'Z16'
     x = -1.78;    y = -64.98;
    return
 case 'Z17'
     x = -10.06;    y = -83.95;
    return
 case 'Z18'
     x = -17.21;    y = -100.04;
    return
 case 'Z19'
     x = -25.77;    y = -116.79;
    return
 case 'Z20'
     x = -34.21;    y = -131.13;
    return
```

```
case 'Z21'
    x = -46.21;    y = -149.29;
   return
case 'Z22'
    x = -57.81;    y = -164.79;
   return
case 'Z23'
    x = -70.27;    y = -180.32;
   return
case 'Z24'
    x = -81.70;    y = -193.23;
   return
case 'Z25'
    x = -97.37;    y = -208.39;
   return
case 'Z26'
    x = -111.45;    y = -221.53;
   return
case 'Z27'
    x = -126.14;    y = -234.30;
   return
case 'Z28'
    x = -134.97;    y = -242.07;
   return
case 'Z29'
    x = -144.46;    y = -249.89;
   return
case 'Z30'
    x = -154.11;    y = -258.21;
   return
case 'Z31'
    x = -161.45;    y = -264.10;
   return
case 'Z32'
    x = -168.08;    y = -269.40;
   return
case 'Z33'
    x = -192.58;    y = -284.20;
   return
case 'Z34'
    x = -205.44;    y = -293.68;
   return
case 'Z35'
    x = -215.16;    y = -300.54;
   return
case 'Z36'
    x = -227.82;    y = -308.91;
   return
case 'Z37'
    x = -239.05;    y = -316.71;
   return
case 'Z38'
    x = -249.72;    y = -323.45;
   return
case 'Z39'
    x = -267.17;    y = -334.33;
   return
```

```
case 'Z40'
    x = -280.59;    y = -342.13;
   return
case 'Z41'
    x = -294.26;    y = -349.77;
   return
case 'Z42'
    x = -308.24;    y = -356.69;
   return
case 'Z43'
    x = -322.57;    y = -363.35;
   return
case 'Z44'
    x = -333.84;    y = -368.59;
   return
case 'Z45'
    x = -354.92;    y = -378.39;
   return
case 'Z46'
    x = -365.18;    y = -383.16;
   return
case 'Z47'
    x = -377.06;    y = -387.93;
   return
case 'Z48'
    x = -390.67;    y = -393.41;
   return
case 'Z49'
    x = -403.30;    y = -398.29;
   return
case 'Z50'
    x = -412.78;    y = -401.60;
   return
case 'Z51'
    x = -426.01;    y = -406.41;
   return
case 'Z52'
    x = -439.58;    y = -411.11;
   return
case 'Z53'
    x = -452.82;    y = -415.10;
   return
case 'Z54'
    x = -466.51;    y = -418.82;
   return
case 'Z55'
    x = -481.04;    y = -422.50;
   return
case 'Z56'
    x = -495.44;    y = -426.00;
   return
case 'Z57'
    x = -510.50;    y = -428.95;
   return
case 'Z58'
    x = -525.23;    y = -431.34;
   return
```

```
     case 'Z59'
         x = -540.03;    y = -433.50;
        return
     case 'Z60'
         x = -554.83;    y = -435.69;
        return
     case 'Z61'
         x = -570.00;    y = -437.42;
        return
     case 'Z62'
         x = -585.05;    y = -439.03;
        return
     case 'Z63'
         x = -599.45;    y = -441.57;
        return
     case 'Z64'
         x = -614.13;    y = -444.82;
        return
     case 'Z65'
         x = -628.28;    y = -449.07;
        return
     case 'Z66'
         x = -642.26;    y = -453.62;
        return
     case 'Z67'
         x = -656.80;    y = -458.88;
        return
     case 'Z68'
         x = -669.47;    y = -465.75;
        return

    otherwise
        disp(['***ERROR::get_sensor_XY(). Bad sensor name!' ]);
end; % switch
end; % if


if( strcmpi( site_ID, 'hope' ) )
switch upper( sns_name )
    case 'Z01'
        x = 12.20;    y = 322.5;
        return
    case 'Z02'
        x = 8.60;    y = 308;
        return
    case 'Z03'
        x = 3.2;    y = 294.3;
        return
    case 'Z04'
        x = 0.2;    y = 280.0;
        return
    case 'Z05'
        x = -1.9;    y = 265.4;
        return
    case 'Z06'
        x = -1.6;    y = 250.6;
        return
```

```
case 'Z07'
    x = -1.6;    y = 235.9;
    return
case 'Z08'
    x = -1.0;    y = 221.3;
    return
case 'Z09'
    x = -1.1;    y = 206.5;
    return
case 'Z10'
    x = -0.7;    y = 192.0;
    return
 case 'Z11'
     x = -0.2;    y = 177.4;
    return
 case 'Z12'
     x = 0.5;    y = 162.9;
    return
 case 'Z13'
     x = 0.7;    y = 148.4;
    return
 case 'Z14'
     x = -0.6;    y = 133.8;
    return
 case 'Z15'
     x = -1.1;    y = 118.7;
    return
 case 'Z16'
     x = -2.1;    y = 104.7;
    return
 case 'Z17'
     x = -3.4;    y = 90.2;
    return
 case 'Z18'
     x = -4.3;    y = 75.7;
    return
 case 'Z19'
     x = -4.7;    y = 61.0;
    return
 case 'Z20'
     x = -4.8;    y = 46.4;
    return
 case 'Z21'
     x = -3.5;    y = 31.8;
    return
 case 'Z22'
     x = -1.5;    y = 17.1;
    return
 case 'Z23'
     x = 1.3;    y = 2.9;
    return
 case 'Z24'
     x = 4.8;    y = -11.2;
    return
 case 'Z25'
     x = 9.3;    y = -25.0;
    return
```

```
     case 'Z26'
         x = 14.0;    y = -39.0;
        return
     case 'Z27'
         x = 19.0;    y = -52.7;
        return

    otherwise
        disp(['***ERROR::get_site_sensor_xy(). Bad sensor name!' ]);
end; % switch
end; % if

% ************************************************************************
% NAME:     get_subarray
% PURPOSE:  Returns a segment of a time series
%
% INPUT:    arrival_time      - beginning index of the segment
%           window_length     - length of the segment
%           timeshift_samples - time adjustment (can be zero samples);
%           input_trace       - input time series;
%           subsample_n       - subsampling factor
% OUTPUT:   x                 - a segment of a time series
% ************************************************************************
function [ x ] = ...
    get_subarray( arrival_time, window_length, ...
              timeshift_samples, input_trace, subsample_n )

x = zeros(1);

%   Fool proofing
if ( arrival_time < 1 ) || ...
    ( arrival_time + timeshift_samples < 1 ) || ...
      ( length( input_trace ) < arrival_time + ...
        window_length + timeshift_samples )
    return;
end;

%    Copy subarrays
x = input_trace( arrival_time + timeshift_samples : ...
    arrival_time + window_length + timeshift_samples );

%    Subsample
if ( subsample_n > 1 )
     x  = x( 1: subsample_n : end );
end

%    Normalize
x  = x - mean( x );

%-----------------------------------------------------------------
function [ y ] = notch_filter( x, sampling_rate, Notch_Hz )
trace_in = x;

for i = 1:length( Notch_Hz )
   w0_60 = Notch_Hz(i) / ( sampling_rate / 2 );

   bw_60 = w0_60/35;       % set the Q factor for the filter to 35
```

```
   [num,den] = iirnotch( w0_60, bw_60 );
   y = filter( num, den, trace_in);

   if( i < length( Notch_Hz ) )
      trace_in = y;
   end
end
```

Appendix C. Pattern recognition analysis of rockfalls

In the examples below, the STA/LTA and ZLCC*STA/LTA detectors are applied to the most frequently occurring event categories: rockfalls, regular and irregular rail traffic. The examples demonstrate that signal patterns produced by hazardous rockfalls can be identified with minimum (< 3 s) delay, and before the train identification is complete.

Thresholds $P^{STA/LTA} = 50\%$, and $D^{STA/LTA} = 250$ m will be used; see section 4.3 for detailed explanation of these algorithm parameters.

Some of the data samples and Matlab scripts included in the Appendices can be downloaded from the Supplementary Thesis Materials and Errata Collection in cIRcle, the University of British Columbia digital repository: http://hdl.handle.net/2429/58080.

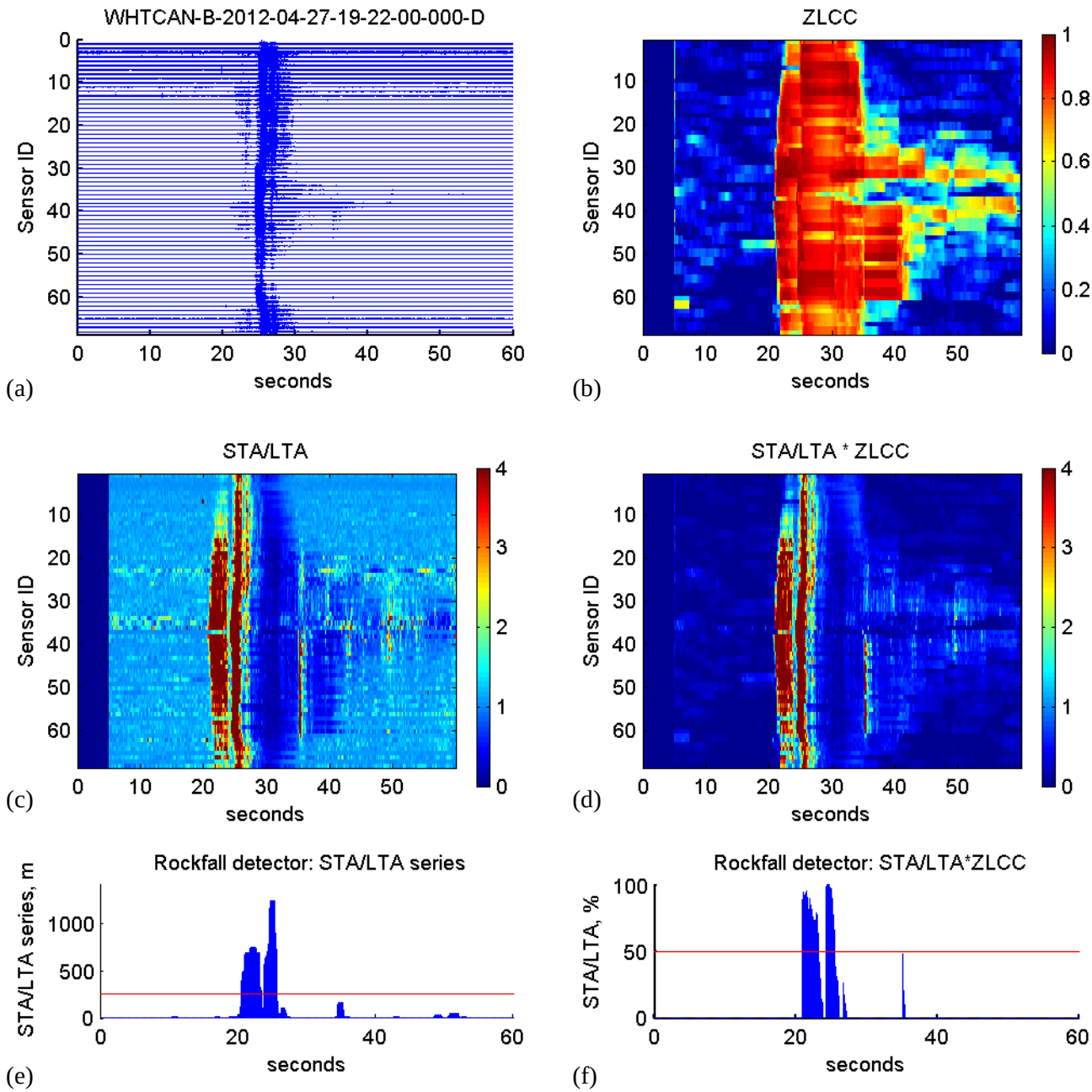

Figure C.1. Pattern recognition analysis of the April 27, 2012 rockfall in White Canyon. (a) Seismogram of the rockfall; (b) $\|R_{max}^{N}(t_i)\|$ matrix; (c) $\left\|\gamma_{STA/LTA}^{j}(t_i)\right\|$ matrix; (d) $\|H_{max}^{j}(t_i)\|$ matrix. Plot (b) displays $D_{STA/LTA}^{j,k}(t_i)$, *i.e.* the spatial extent of the array trigger within the sliding time window. Plot (c) displays $P_{STA/LTA}^{j,k}(t_i)$, *i.e.* the percentage of $H_{max}^{j}(t_i) \geq H^{STA/LTA}$ within the sliding time window. Both $D_{STA/LTA}^{j,k}(t_i)$ and $P_{STA/LTA}^{j,k}(t_i)$ exceeded the thresholds at 20-25 s, and an array trigger was flagged.

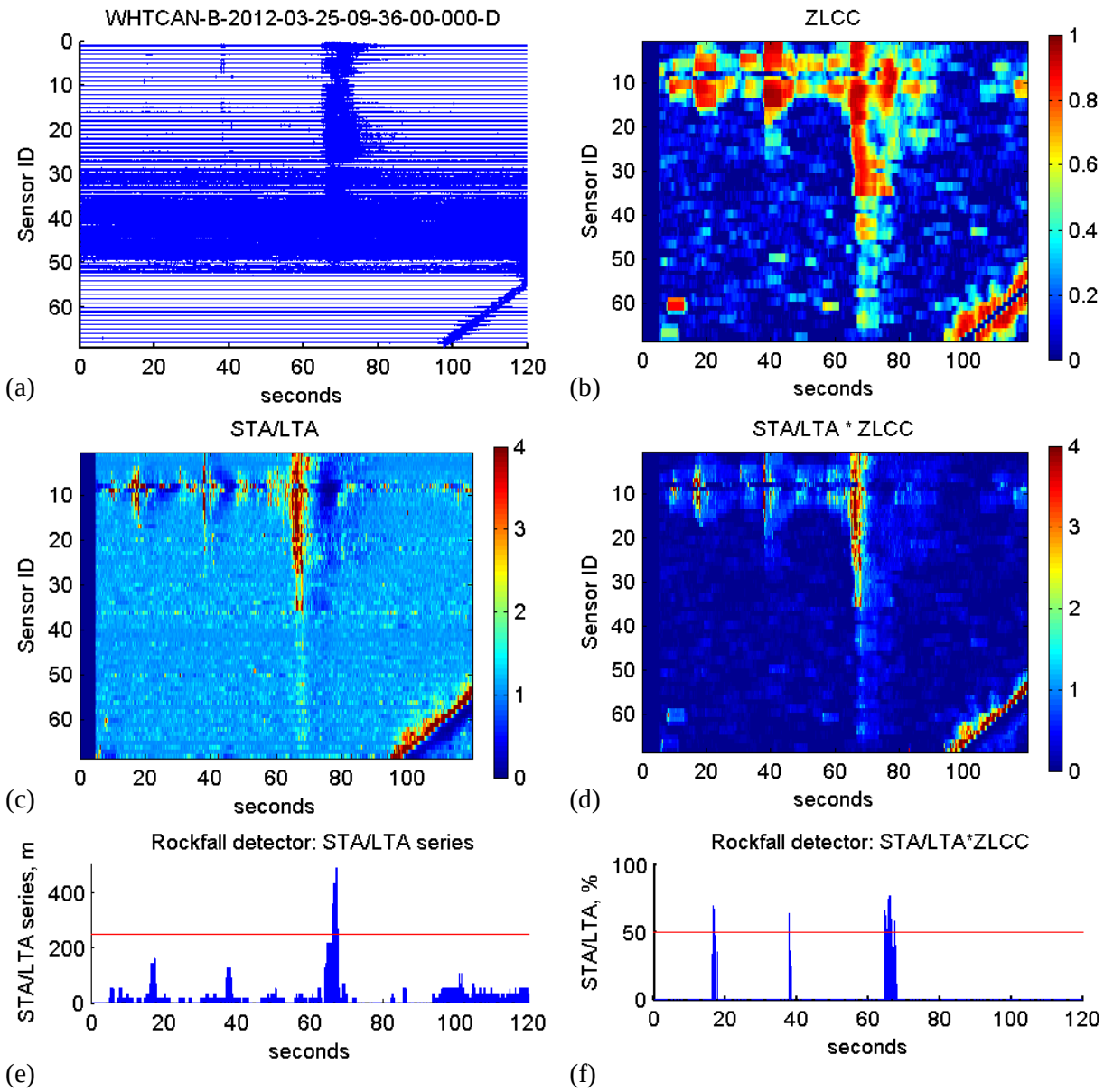

Figure C.2. Pattern recognition analysis of the March 25, 2012 rockfall in White Canyon. (a) Seismogram of the March 25, 2012 rockfall (Figure E.11) and a high-rail; (b) $\|R_{max}^{N}(t_i)\|$ matrix; (c) $\left\|\gamma_{STA/LTA}^{j}(t_i)\right\|$ matrix; (d) $\|H_{max}^{j}(t_i)\|$ matrix. Plot (e) displays $D_{STA/LTA}^{j,k}(t_i)$; plot (f) displays $P_{STA/LTA}^{j,k}(t_i)$. Both $D_{STA/LTA}^{j,k}(t_i)$ and $P_{STA/LTA}^{j,k}(t_i)$ exceeded the thresholds at 65-70 s, and an array trigger was detected. The ground vibration generated by a high-rail at 95-120 s did not pass the array trigger threshold.

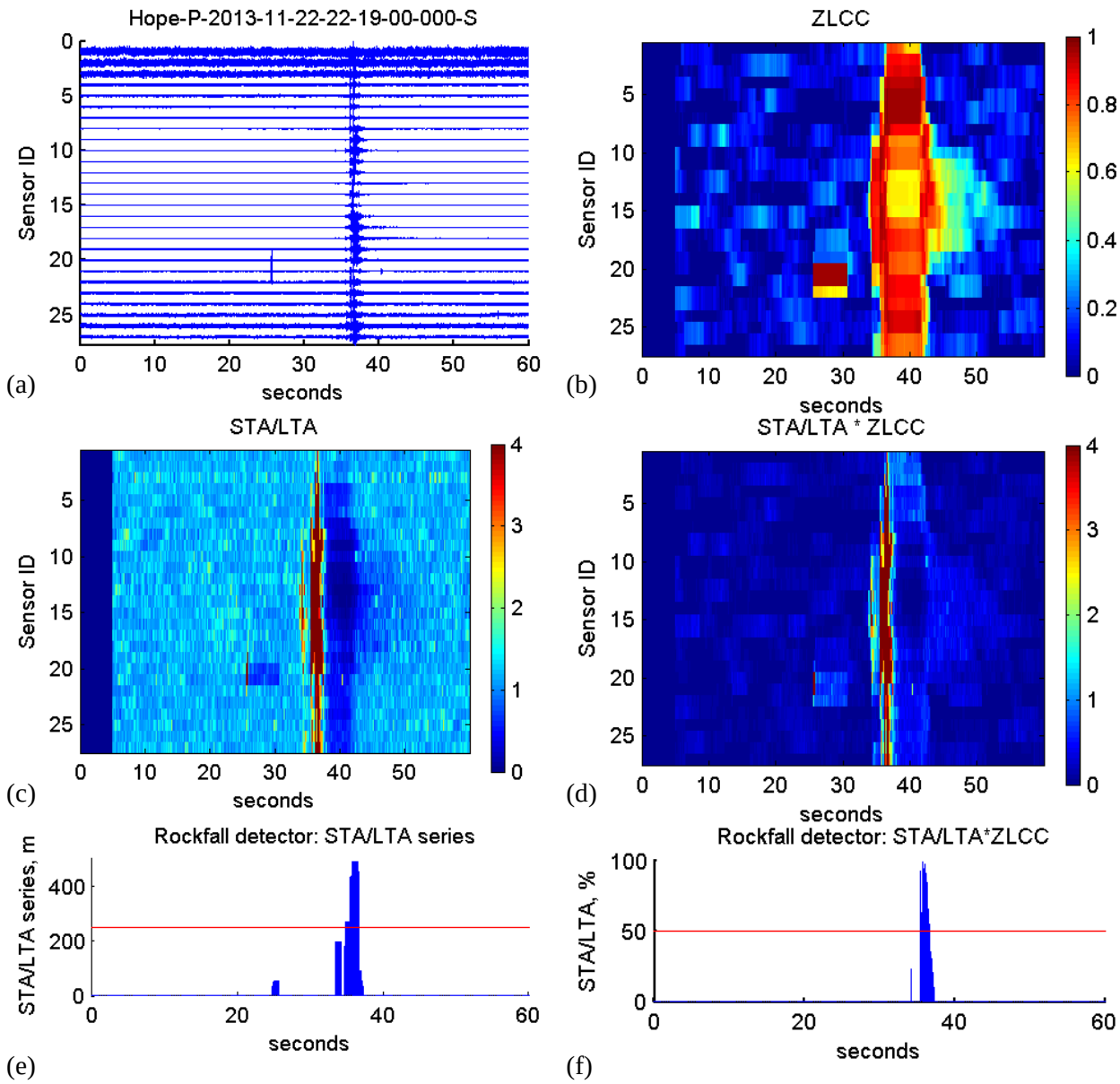

Figure C.3. Pattern recognition analysis of a non-hazardous rockfall.

(a) Seismogram of the rockfall; (b) $\|R_{max}^{N}(t_i)\|$ matrix; (c) $\left\|\gamma_{STA/LTA}^{j}(t_i)\right\|$ matrix; (d) $\|H_{max}^{j}(t_i)\|$ matrix. Plot (e) displays $D_{STA/LTA}^{j,k}(t_i)$; plot (f) displays $P_{STA/LTA}^{j,k}(t_i)$. Both $D_{STA/LTA}^{j,k}(t_i)$ and $P_{STA/LTA}^{j,k}(t_i)$ exceeded both thresholds at 37 s, and an array trigger was detected.

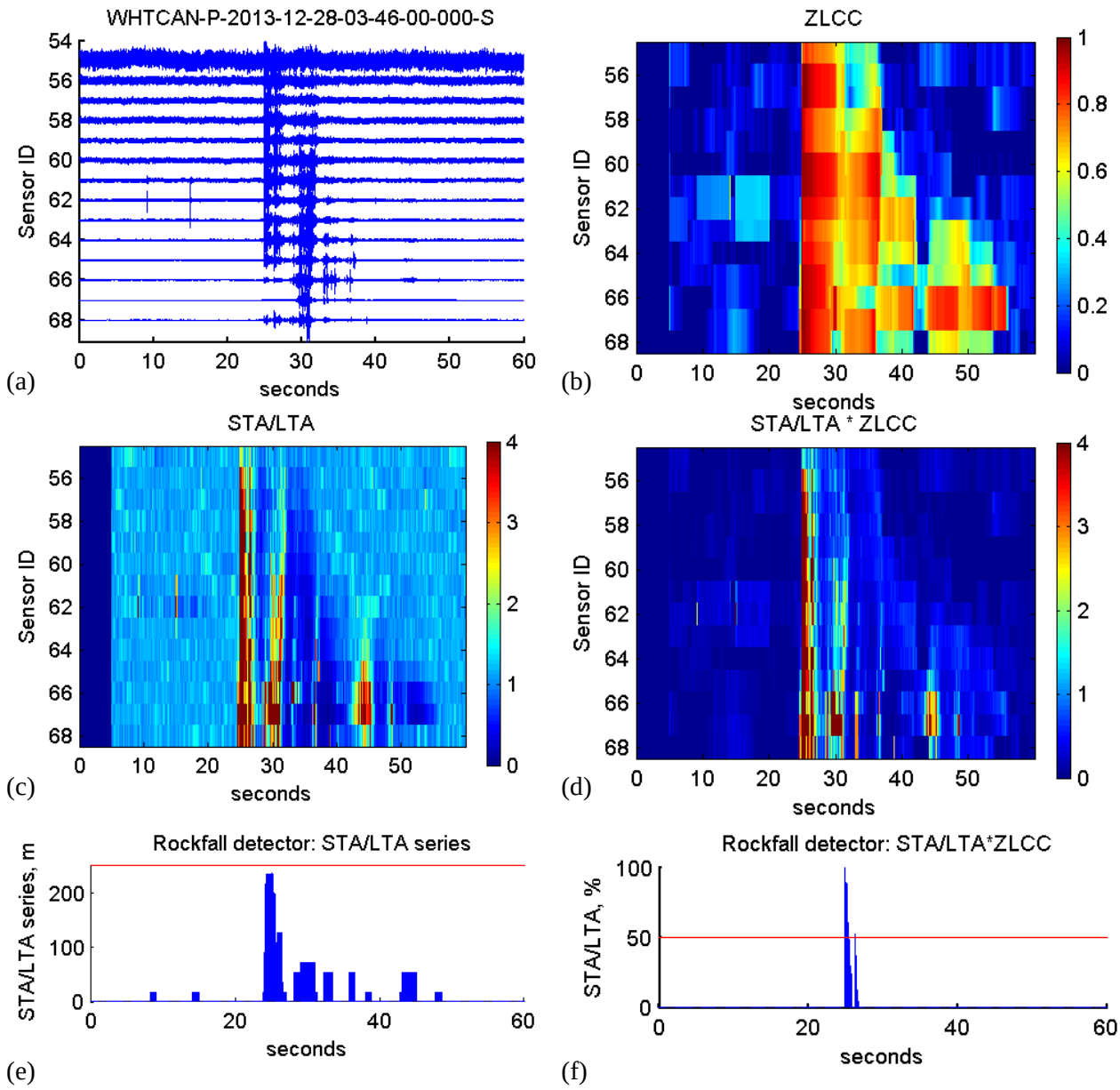

Figure C.4. Pattern recognition analysis of a rockfall at the edge of a geophone array.

(a) Seismogram of the rockfall; (b) $\|R^N_{max}(t_i)\|$ matrix; (c) $\left\|\gamma^j_{STA/LTA}(t_i)\right\|$ matrix; (d) $\|H^j_{max}(t_i)\|$ matrix. Plot (e) displays $D^{j,k}_{STA/LTA}(t_i)$; plot (f) displays $P^{j,k}_{STA/LTA}(t_i)$. Parameter $D^{j,k}_{STA/LTA}(t_i)$ remained below the threshold, which is why the STA/LTA detector missed the (relatively small) rock.

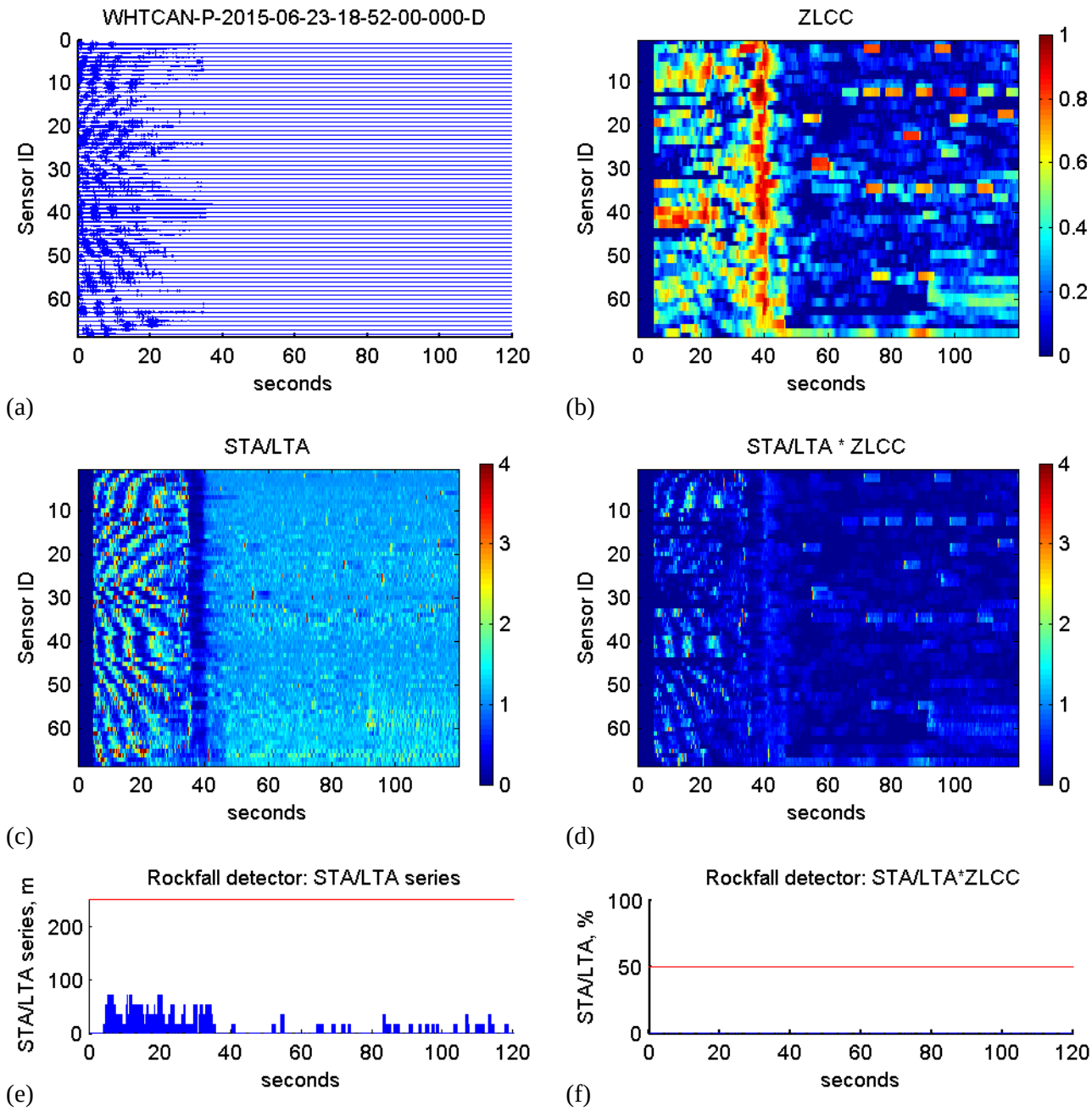

Figure C.5. Pattern recognition analysis of a stopping train (the White Canyon SRFDS). (a) Seismogram of the stopping train; (b) $\|R_{max}^{N}(t_i)\|$ matrix; (c) $\left\|\gamma_{STA/LTA}^{j}(t_i)\right\|$ matrix; (d) $\|H_{max}^{j}(t_i)\|$ matrix. Plot (e) displays $D_{STA/LTA}^{j,k}(t_i)$; plot (f) displays $P_{STA/LTA}^{j,k}(t_i)$. Both $D_{STA/LTA}^{j,k}(t_i)$ and $P_{STA/LTA}^{j,k}(t_i)$ remained below the thresholds, and no array trigger was detected.

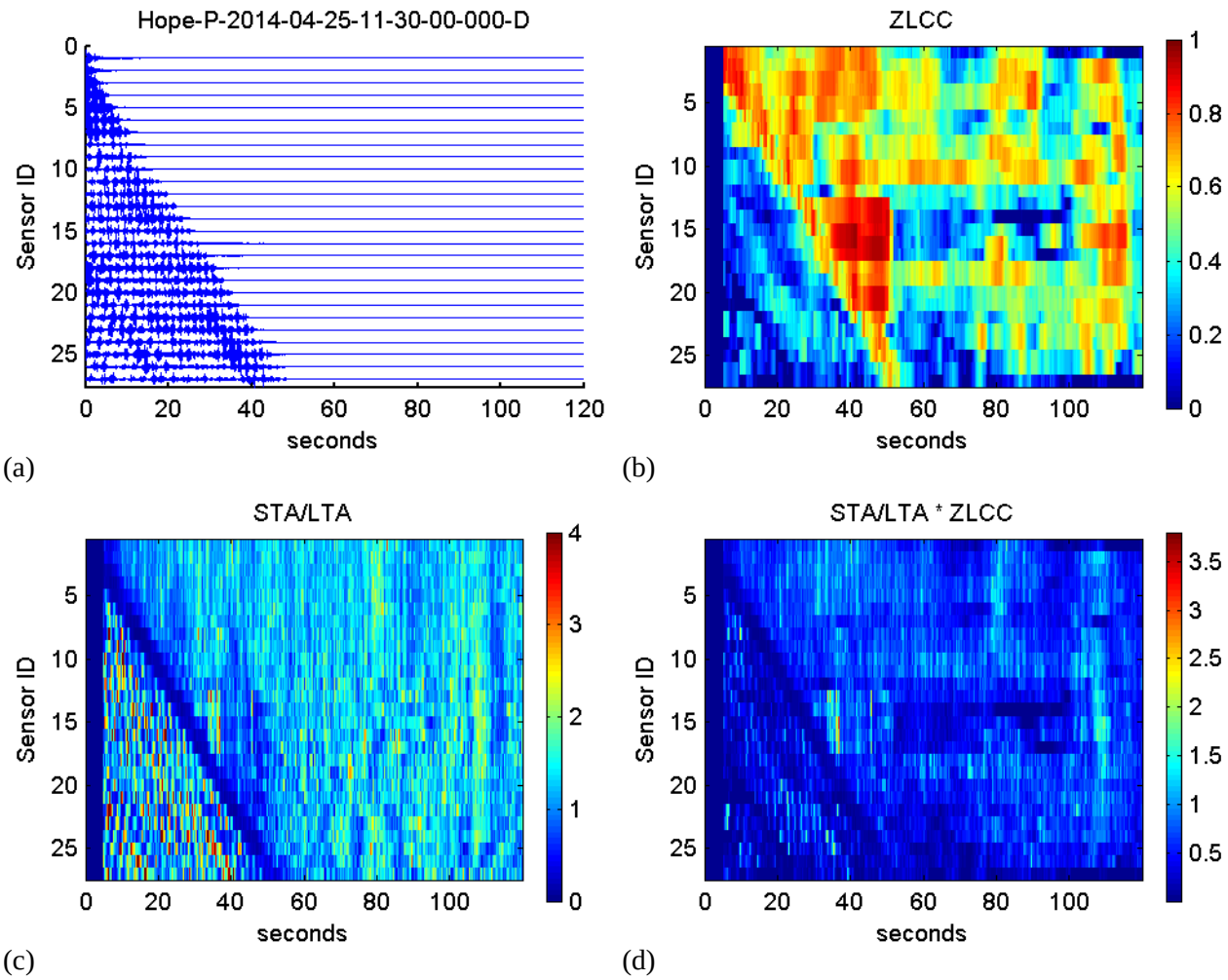

Figure C.6. Pattern recognition analysis of the train receding noise.

(a) Seismogram of a train which is leaving the site; (b) $\|R_{max}^{N}(t_i)\|$ matrix; (c) $\left\|\gamma_{STA/LTA}^{j}(t_i)\right\|$ matrix; (d) $\left\|H_{max}^{j}(t_i)\right\|$ matrix. Neither image (c) nor image (d) contains rockfall patterns.

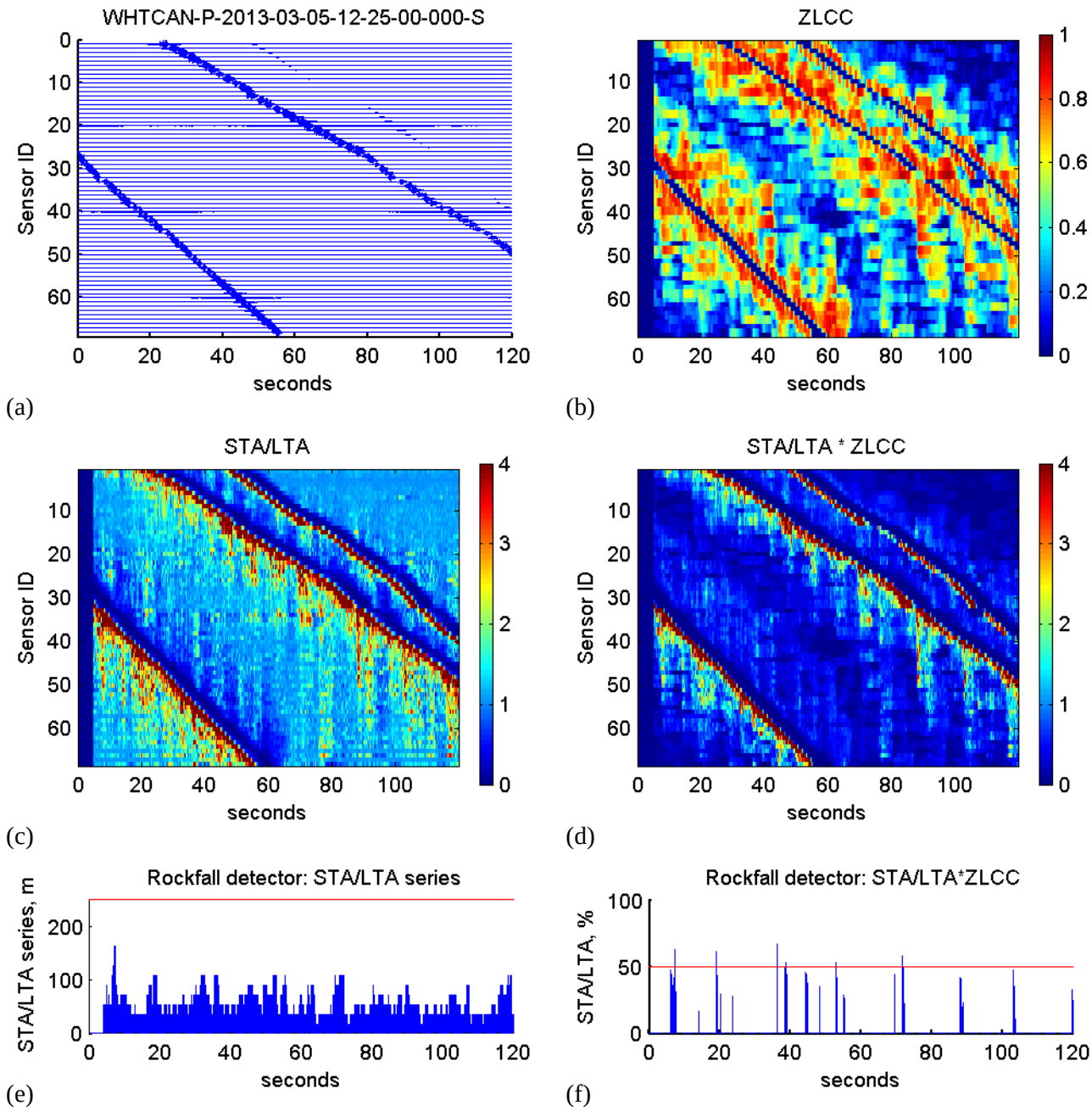

Figure C.7. Pattern recognition analysis of multiple high-rails.

(a) Seismogram of the high-rails; (b) $\|R^N_{max}(t_i)\|$ matrix; (c) $\left\|\gamma^j_{STA/LTA}(t_i)\right\|$ matrix; (d) $\|H^j_{max}(t_i)\|$ matrix. Plot (e) displays $D^{j,k}_{STA/LTA}(t_i)$; plot (f) displays $P^{j,k}_{STA/LTA}(t_i)$. Parameter $D^{j,k}_{STA/LTA}(t_i)$ remained below the threshold, and no array trigger was detected.

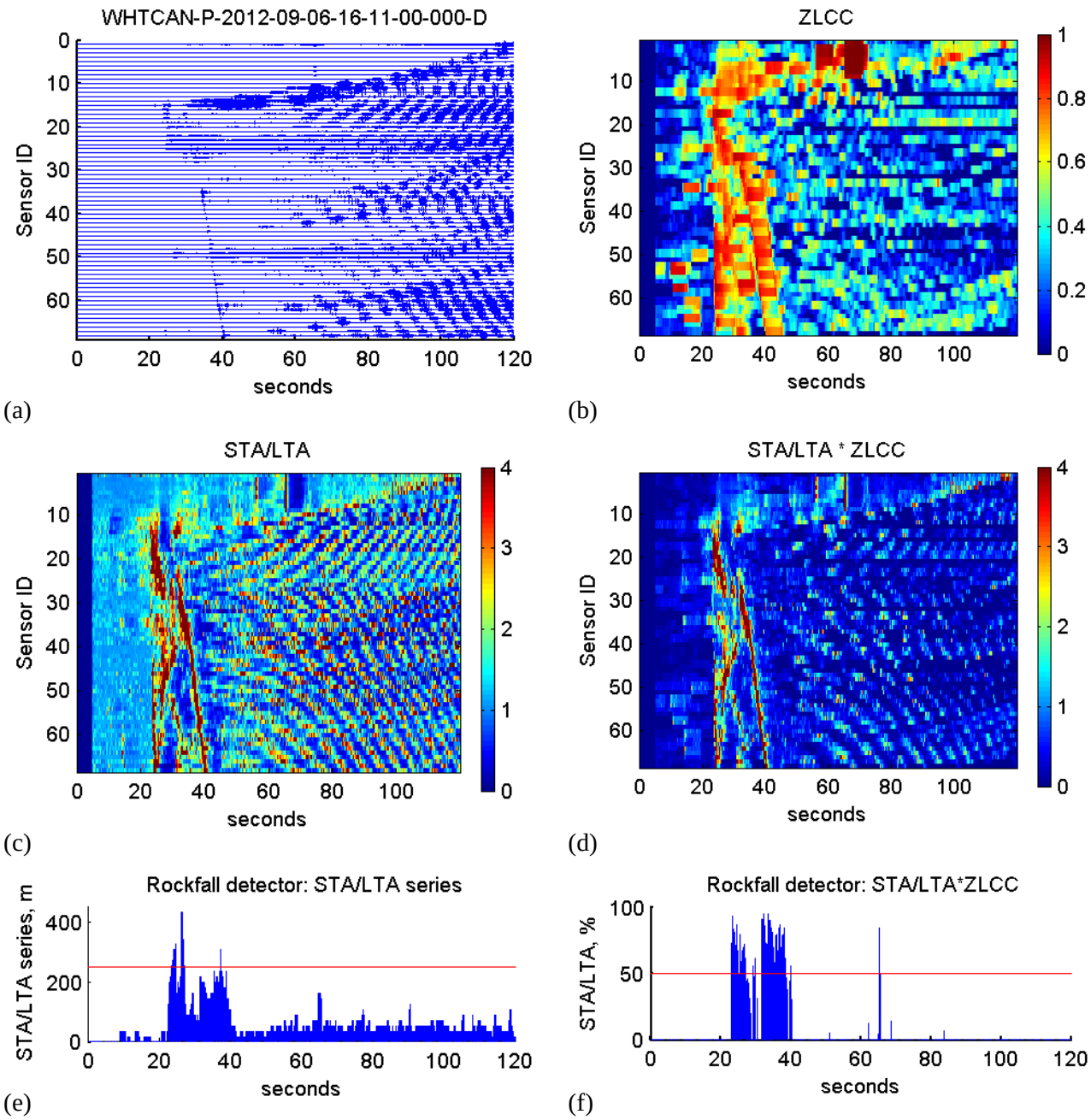

Figure C.8. Pattern recognition analysis of a starting train.

(a) Seismogram of the starting train; (b) matrix $\left\|\boldsymbol{R}^{N}_{max}(\boldsymbol{t}_i)\right\|$; (c) matrix $\left\|\boldsymbol{\gamma}^{j}_{STA/LTA}(\boldsymbol{t}_i)\right\|$; (d) zoomed-in view of $\left\|\boldsymbol{H}^{j}_{max}(\boldsymbol{t}_i)\right\|$ matrix. Plot (e) displays $\boldsymbol{D}^{j,k}_{STA/LTA}(\boldsymbol{t}_i)$; plot (f) displays $\boldsymbol{P}^{j,k}_{STA/LTA}(\boldsymbol{t}_i)$. Both criteria exceeded the thresholds at 25-35 s and and an array trigger was detected.

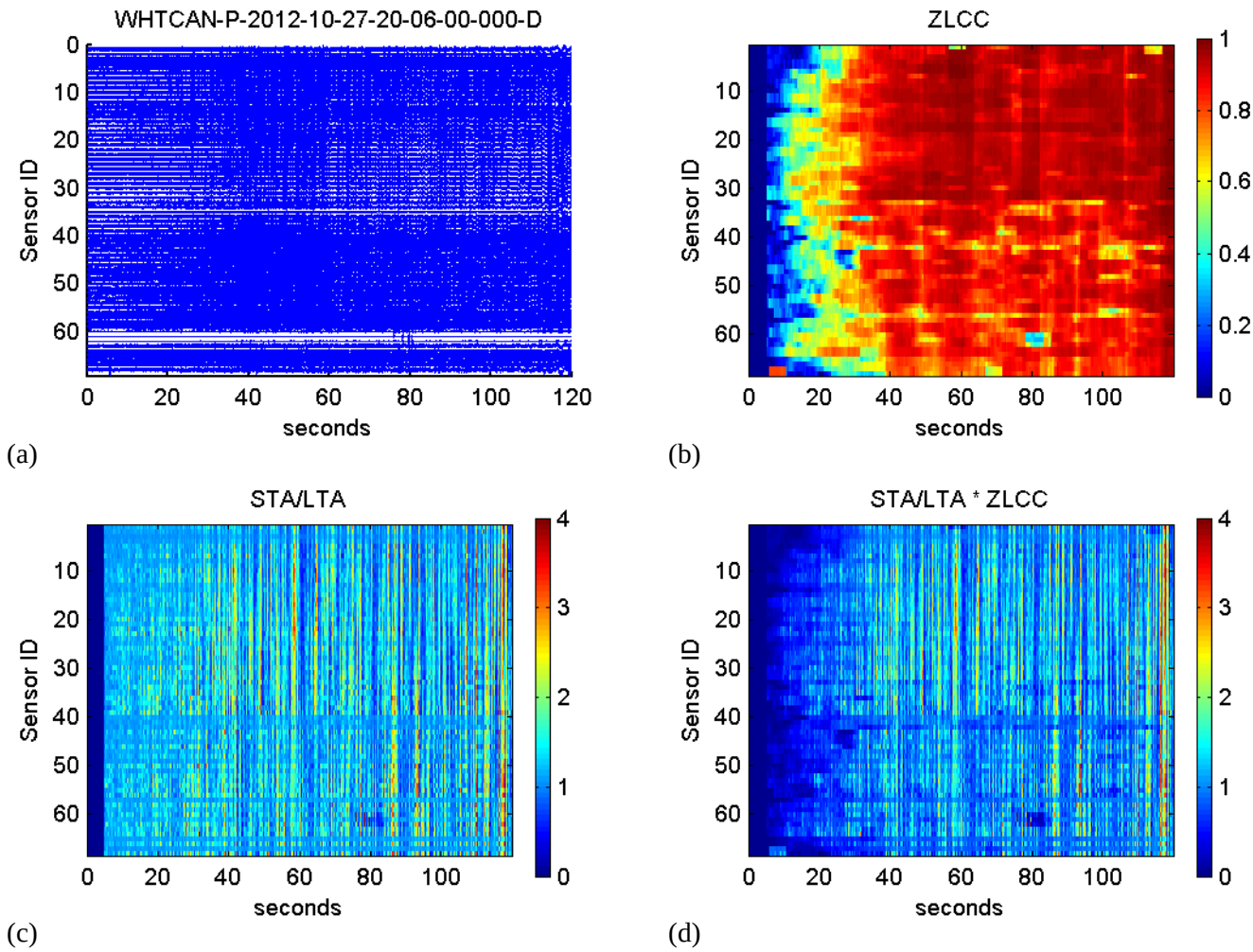

Figure C.9. Pattern recognition analysis of the October 27, 2012 Haida Gwaii M7.8 earthquake recorded by the White Canyon seismic array.

(a) Earthquake seismogram recorded with GS-32CT geophones; instrument correction was not performed; (b) matrix $\|R_{max}^{N}(t_i)\|$; (c) matrix $\left\|\gamma_{STA/LTA}^{j}(t_i)\right\|$; (d) matrix $\left\|H_{ma}^{j}(t_i)\right\|$. The earthquake induced coherent signals on all channels and resulted in a rockfall-like pattern in matrix $\|R_{max}^{N}(t_i)\|$. However, the relatively short LTA (5 seconds) kept the STA/LTA ratio low because of the earthquake's emergent signal. As a result, an array trigger was not detected.

Appendix D. Field reports on SDF activations at the Hope site

May 4, 2013 22:04 PST

In the computer modeling experiment (Chapter 5), this event was automatically identified as non-hazardous because the PGV did not exceed the system activation threshold (Figure D.1). According to the signal maintainer, '<...> the rockfall came from 20 to 25 feet[23] straight above the fence <…> it was a mass of shattered rock that came apart when it hit the fence and the ground <...> The largest intact piece of rock was about 5"x7"x16"[24].'

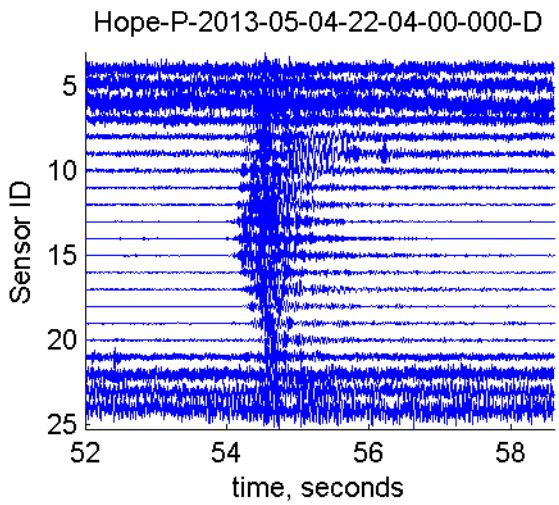

Figure D.1. Seismic record of the event which activated the SDF on May 4, 2013. Based on the seismic data, the wire was broken by non-hazardous rocks (smaller than 0.028 m^3).

[23] 7-8 m.
[24] 12.5 cm x 17.5 cm x 40 cm.

June 23, 2013 6:53 PST

Since this rockfall activated the Seismic Rockfall Detection System (Figure D.2) it appears that the wire was broken by rock(s), 0.028 m^3 or larger. According to the CP signal maintainer, 'the bottom 2 wires were broken; it was several rocks and the largest <…> was 12" x 8" x 6"[25].'

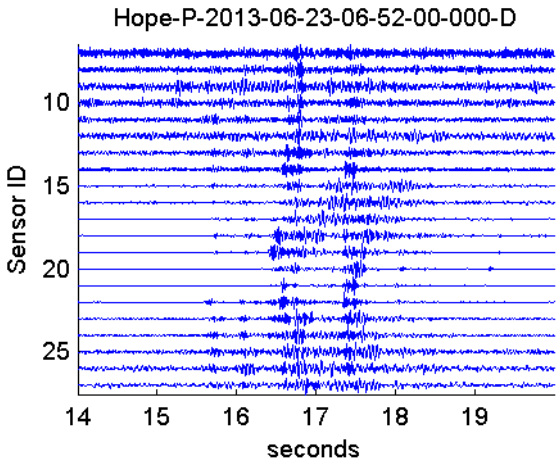

Figure D.2. Seismic record of the rockfall which activated the SDF at CASC 038.90 on June 23, 2013 at 06:53 PST.

June 16, 2013 13:59 PST

No seismic signal of significance was recorded by the Hope SRFDS at the time of SDF activation, and the SRFDS remained rearmed. Therefore, the SDF wire must have been broken by a non-hazardous rock. According to the CP signal maintainer, "<…> the wires were hit <…> by several smaller rocks that ripped the wires loose and wrapped the top 3."

[25] 30 cm x 20 cm x 15 cm.

July 24, 2013 23:37 PST

The event was detected only at three sensors and its peak amplitude was barely above the background noise level, too low to activate the SRFDS which ignored the event. The signal maintainer reported that he "never found the cause of this activation, it looked to me that the wire had just rotted out where it had been chaffing against the rock face".

November 27, 2014 21:09 PST

Based on the analysis of seismic data, the SDF was activated by a non-hazardous rock on November 27, 2014 which was ignored by the SRFDS. Several hours later, on November 28, 2014 while the SDF remained activated, it was damaged by a fallen tree which was confirmed later by CP S&C maintainers. The seismic record of the tree fall is illustrated in Figure D.3, together with a photo of the area which was about 40 meters away from the web camera. Based on the amplitude of the ground vibration generated by the tree, the SRFDS identified it as a hazardous rockfall.

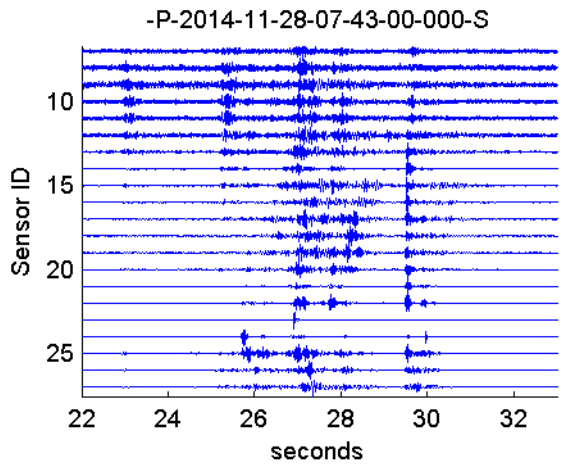

(a) (b)

Figure D.3. (a) Seismic record of a fallen tree which damaged the SDF and activated the seismic rockfall detection system; (b) the area where the tree fell photographed with the web camera. Pieces of the tree trunk are visible on the downhill side of the track.

Appendix E. Field reports on SDF activations at the White Canyon site

February 27, 2012 17:21:08 PST

One of the photos taken by the signal maintainer shows a rock large enough to derail a train (Figure E.1). However, no significant ground vibration was recorded at the time of SDF activation and the SRFDS did not activate. Based on the analysis of seismic data, the SDF wire was broken by animals, or the smaller of the two photographed rocks (Figure E.1(b)).

(a) (b)

Figure E.1. Photos taken by CN's signal maintainer at the location of the SDF break on February 27, 2012 (courtesy of CN).

The wire break was located by analyzing the ground vibrations induced by the signal maintainer and his high-rail when the SDF was repaired. The seismogram in Figure E.2 contains 120 seconds of continuous seismic data preceding the activation. Based on this record, prior to the time of the activation there was an animal in this area. The green arrows indicate a progression of quasi-periodic seismic signals from Z-01 to Z-05 which are characteristic of animal migration; the blue arrows indicate an approaching train. Several seconds after the wire was broken, a train arrived. The seismogram contains no signal patterns typical for falling rocks. Therefore, there is a possibility that the wire was broken by an animal, and the rocks fell afterwards and its signal was buried within the train's precursor/ receding noise. Alternatively, the rock(s) may have rolled down a talus slope visible on one of the photos and generated ground vibration with lower-than-expected amplitude.

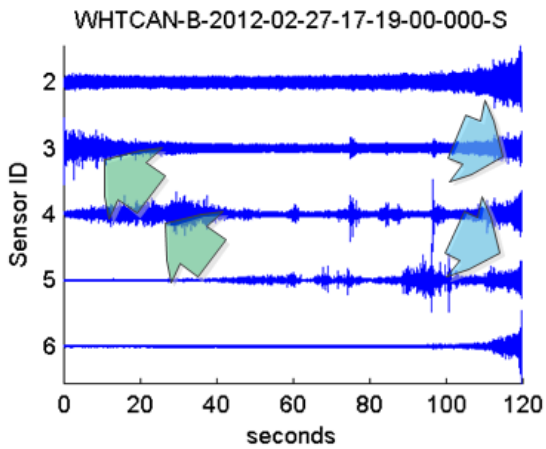

Figure E.2. Seismogram of the ground vibration near sensors Z-01 to Z-06 before the Lasha SDF was activated on February 27, 2012.

February 29, 2012 1:35:33 PST

The event data and location are illustrated in Figure E.3. The rock marked by the signal maintainer with a blue tie clip insulator is smaller than 0.028 m^3. The SRFDS computer model identified the rock as non-hazardous.

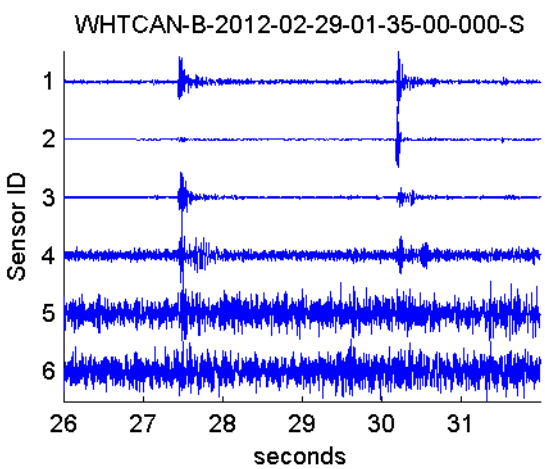

(a)

(b)

Figure E.3. (a) Seismic record of the February 29, 2012 1:35 PST event, and a photograph of (b) rocks which, in the opinion of the signal maintainer, may have caused this SDF activation (courtesy of CN).

February 29, 2012 11:47:55 PST

No big rocks were found at this location, according to the signal maintainer who reported that "<…> it looks like a collection of small rocks (shale) came down <…>". The White Canyon SRFDS identified the event as non-hazardous and it was ignored (Figure E.4).

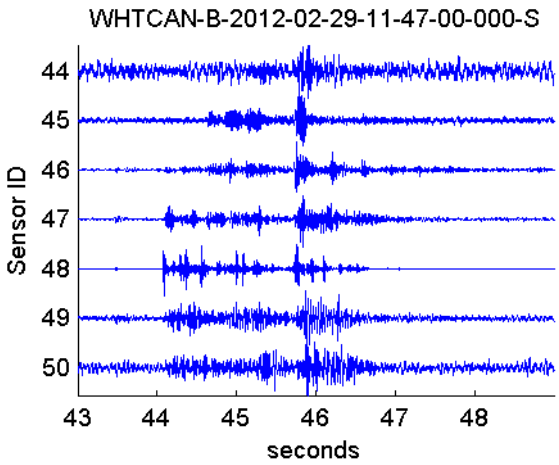

Figure E.4. Seismic record of the rockfall on February 29, 11:48 PST.
No photos are available for this event.

March 7, 2012 10:17:16 PST

At the time of the SDF activation a train was passing the area where the trip wire was broken; the area was identified when the signal maintainer arrived to repair the wires. Because the rockfall signal was buried in a strong train noise, the SRFDS did not trigger. The suspect rock was photographed by the signal maintainer (Figure E.5).

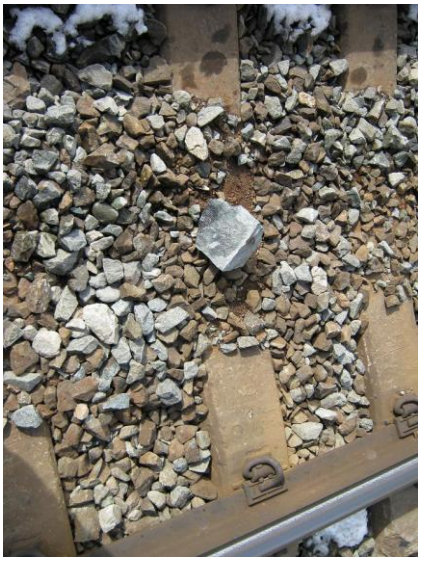

Figure E.5. Photo of the rock that, in the opinion of signal maintainer, activated the SDF on March 7, 2012 (courtesy of CN).

March 14, 2012 8:21:50 PST

According to CN, "the maintainer was not sure which rock broke the wire, so he took pictures of a few possibilities." (Figure E.6, Figure E.7). The SRFDS identified the event as non-hazardous and it was ignored. All rocks on the photos provided by the maintainer look smaller than 0.028 m^3.

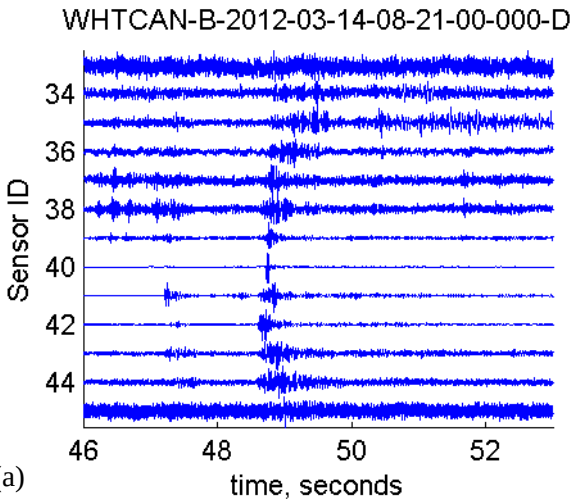

(a)

(b)

Figure E.6. (a) Seismic record of the event which occurred on March 16, 2012 at 8:21 PST and a photograph (b) of the location where the SDF wire was broken (courtesy of CN).

(a) (b)

Figure E.7. Photos of the location where the Lasha SDF was activated on March 16, 2012. Red arrows point at the rocks which, based on the seismic record, may have caused the alarms (courtesy of CN).

March 21, 2012 8:25:19 PST

The break was located by analyzing the ground vibration generated by the signal maintainer. At the time when the SDF was activated, a train was transiting the instrumented area which makes it impossible to identify a rockfall signal and estimate the rock size. In Figure E.8 green arrows indicate a progression of quasi-periodic seismic signals which are characteristic of animal migration; blue arrows indicate an approaching train. According to the S&C maintainer, the broken wire was located more than 25 feet above the ground which rules out wildlife as a possible cause of the SDF activation. The photo of the suspect rock is in Figure E.9.

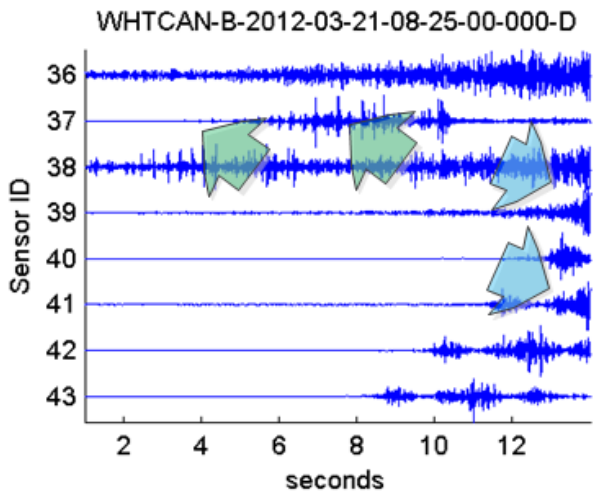

Figure E.8. Fifteen seconds of continuous seismic data acquired immediately before the SDF was activated on March 21, 2012.

Figure E.9. Photograph of the rock that, in CN's opinion, caused the March 21, 2012 SDF activation (courtesy of CN).

March 24, 2012 20:51:03 PST

Though the rockfall was detected 200 m away from the epicenter, it did not pass the system activation threshold because of the relatively low PGVs near the epicenter, and the SRFDS identified the event as non-hazardous.

Assuming that the S&C maintainer identified the rock correctly (on the photo in Figure E.10(b) the rock's size appears to be close to 0.028 m^3), it must have rolled down the slope because the event signal is 3 s

long (Figure E.10 (a)). At the sensor nearest to the epicenter the peak amplitudes occur at the end of the event signal; their timing coincided with the timing of the SDF activation.

Based on the analysis of the event's seismic signature and the timing of the SDF activation, it is hypothesized that the rock fell onto the ground several meters upslope from the track, where the impact was cushioned by talus deposits, and subsequently rolled downslope towards the geophone array and broke the SDF wires. This would explain the fact that the PGVs, that were induced in the beginning of the signal at the sensors closest to the impact location, are lower than the PGVs induced in the same area at the end of the signal.

This example brings up the concern of rocks falling onto soft talus slopes. This possibility needs to be taken into account when the applicability of the SRFDS is evaluated, and when the system calibration procedure is planned.

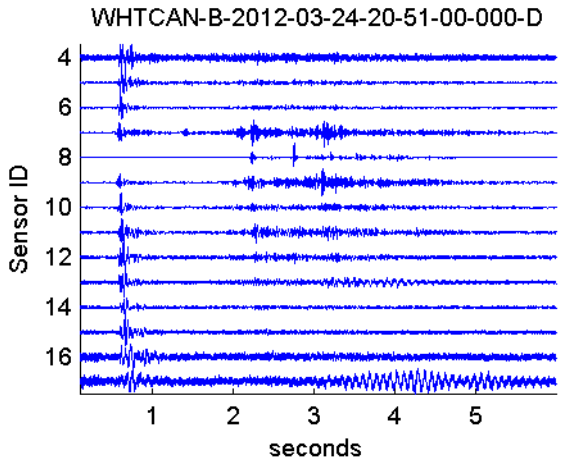

(a)

(b)

Figure E.10. (a) Seismic record of the event on March 24, 2012 20:51:03 PST, and a photograph of the rock (b) which, according to the signal maintainer, activated the slide fence. The rock is marked with the pliers (courtesy of CN).

March 25, 2012 9:37 PST

A large rockfall occurred in White Canyon on March 25, 2012 exactly where the SDF was activated the day before (Figure E.10); the signal maintainer repaired the SDF at 09:10 PST, 20 min before the rockfall started. Three SDF poles were broken (Figure E.11). Based on the analysis of seismic records, the event involved two rockfalls separated by six minutes, one at 09:31 PST at the beginning of the event (Figure

E.12), the other at 09:37 PST (Figure E.13), with a few relatively weak rockfalls in between. Precursor rocks activated the SDF at 09:30:59 PST. The SRFDS computer model was activated at 09:31 PST when the first of the two significant rockfalls occurred.

Figure E.11. The March 25, 2012 rockfall in White Canyon (courtesy of CN).

The seismogram in Figure E.12 shows the first 60 seconds of the event when the SRFDS model was activated. Figure E.13 shows the second rockfall which lasted 15 seconds. The seismic signature displays an emergent and constant energy release pattern which has been observed by other researchers (Vilajosana *et al*., 2008, Helmstetter and Garambois, 2010).

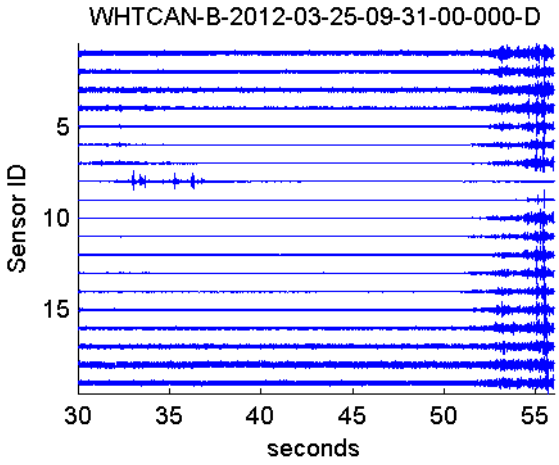

Figure E.12. Illustration of the first 60 seconds of the March 25, 2012 rockfall.

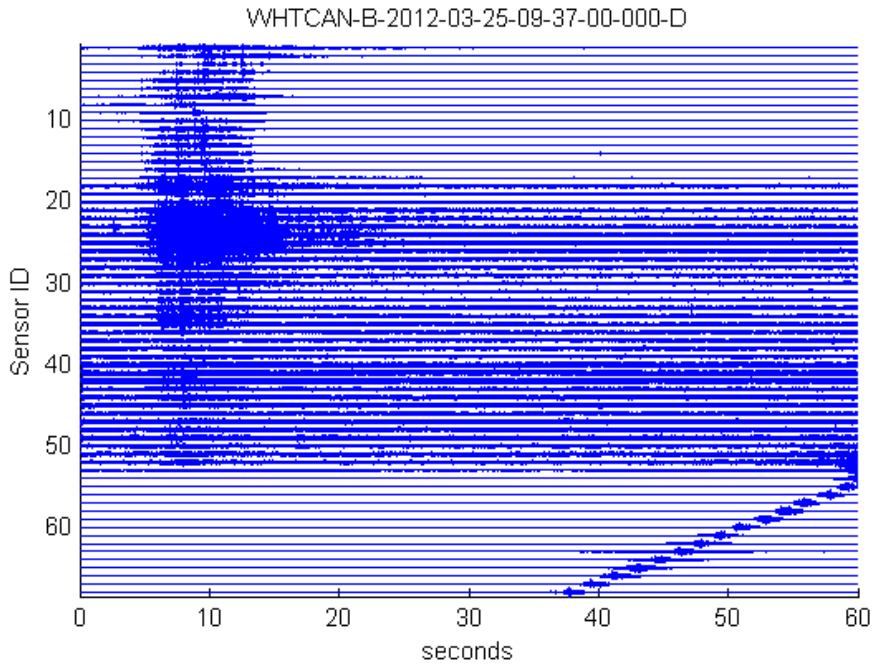

Figure E.13. Seismogram of the final rockfall in the series of rockfalls on March 25, 2012. The seismic record also contains the signal of a high-rail moving in the direction of the landslide (40 s to 60 s).

April 14, 2012 21:54 PST

Based on the PGV of the ground vibration generated by the rocks that broke the SDF wire, they must have been smaller than 0.028 m^3 (Figure E.14), and the SRFDS identified the event as non-hazardous.

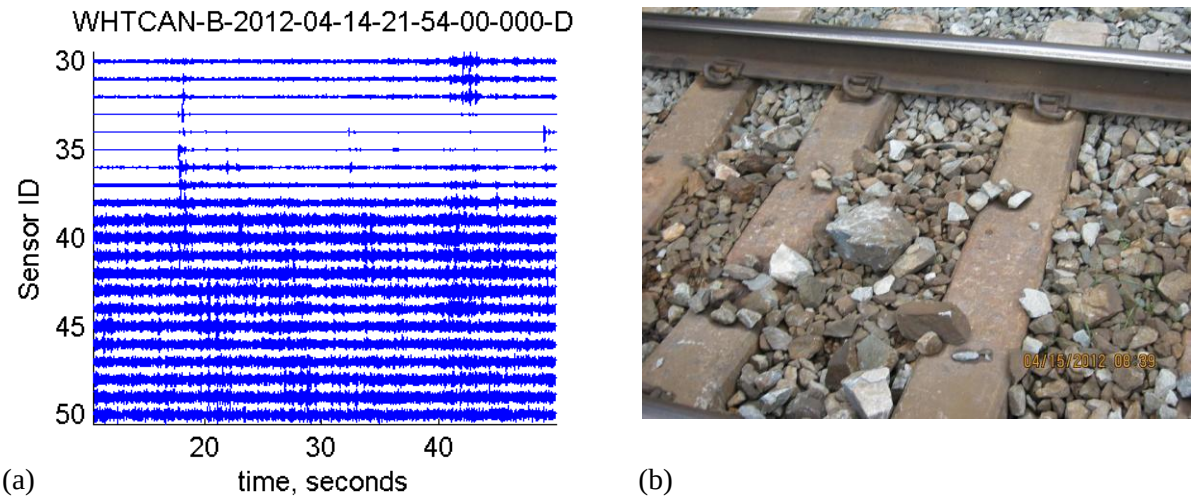

Figure E.14. (a) Seismic record of the April 14, 2012, 21:54 PST event; (b) photograph of the rocks which, according to the signal maintainer, broke the slide detector wire (courtesy of CN).

April 19, 2012 18:12:25 PST

The report of the CN's S&C maintainer said that "<…> it looked like the rocks rolled off the side of the rock shed…. The rocks were mostly approx 6-7 inch in diameter". Based on the peak ground velocities induced by the rocks, their size was smaller than 0.028 m^3, and the SRFDS identified them as non-hazardous (Figure E.15).

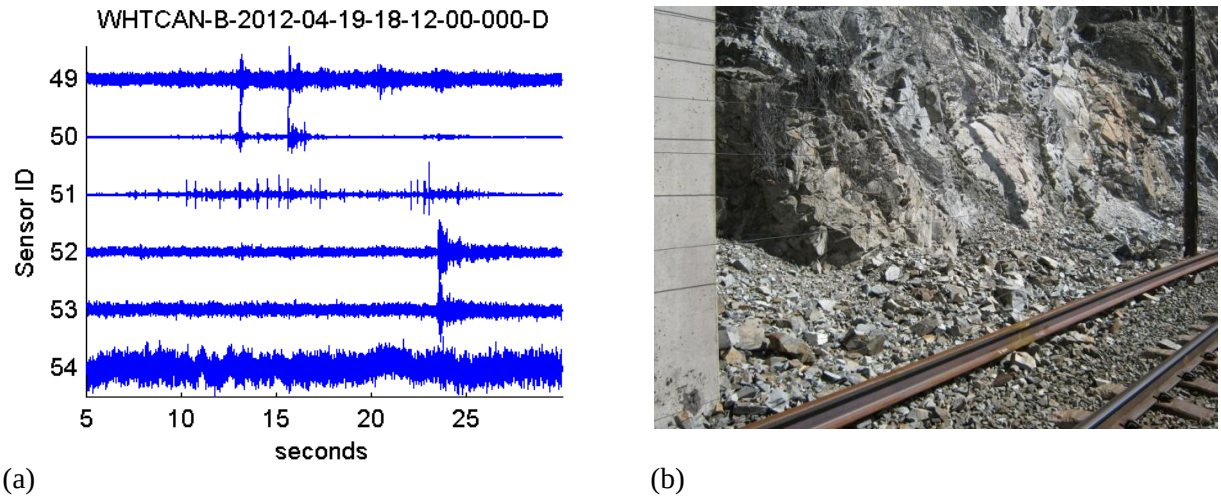

Figure E.15. (a) Seismic record of the April 19, 2012 event; (b) photograph of the area where the SDF was activated. In this area the slope is undergoing progressive continuous deterioration which is why the signal maintainer was unable to identify the rock(s) that broke the slide detector wire (courtesy of CN).

March 18, 2011 14:23 PST

The affected area and the seismic record of the event are in Figure E.16; the photo is courtesy of CN. The SRFDS computer model identified the event as hazardous.

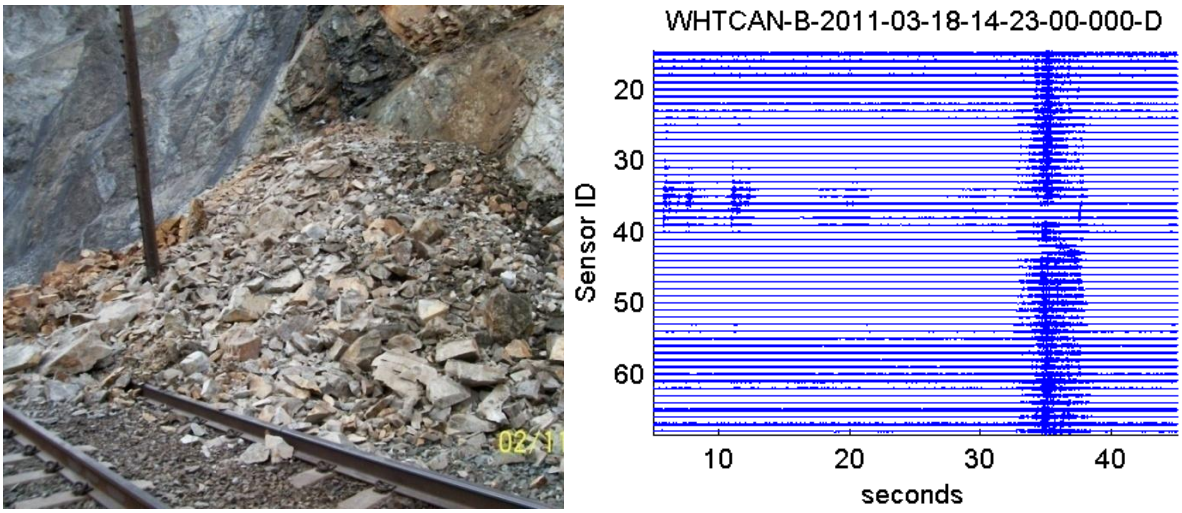

(a) (b)

Figure E.16. (a) Photograph of the March 18, 2011 rockfall (courtesy of CN); the time stamp is wrong due to incorrect camera settings; (b) seismogram of the event.